THE UNIVERSITY *of* EDINBURGH

Metal Complexes

Containing Non-Innocent Ligands

for Functional Materials

Maxwell James Reinhardt

Thesis submitted for the degree of PhD
to
The University of Edinburgh

2012

Declaration

I hereby declare that this thesis was composed by myself and that the work described within is my own, except where explicitly stated otherwise in acknowledgement reference or text. The work has not been submitted in whole or in part for any other degree, diploma or qualification.

Maxwell Reinhardt
September 2012

Acknowledgements

First thanks must be given to my supervisor Neil Robertson for the inspiration and opportunity to undertake this work towards the degree of PhD, as well as the wisdom and support he provided throughout the years.

Financial acknowledgements are paid to the EPSRC (UK) and the Japanese Science and Technology (JST) Agency for financial support through the joint EPSRC-JST programme, which also enabled my travels to Japan to carry out research through this collaboration. Thanks also to the COST network for the unique opportunity to present at one of its meetings.

My extreme gratitude is given to Kunio Awaga for twice welcoming me into his research group at Nagoya University in Japan. It provided me with a fantastic experience in addition to the scientific results, and a newfound appreciation of sushi. Many thanks must be paid to the other professors in the Awaga group, Michio Matsushita and Hirofumi Yoshikowa, for their scientific input and assistance. To the students of the Awaga group, thank you for your kindness and friendship. Additional acknowledgement must be given to Yoshiaki Shuku, who grew the crystals and solved the structure of CpCoDAnap, and made my visits all the more welcoming. Special thanks are given to Simon Dalgleish (previously of the Robertson group, now of the Awaga group) for the additional measurements on the CpCoDAnap compound, helping me adjust to the Japanese way and all the banter of yore.

Computation work was carried out with invaluable assistance from both Patricia Richardson and Michal Kochman.

Many, many thanks are offered to Gary Nichol and the University of Edinburgh Crystallography service for accepting my tiny crystals, collecting crystallographic data, solving a number of crystal structures and providing assistance when needed. Thanks also to past and present members of the Parsons and Moggach

groups, notably Fraser White, Nick Funnell and Alex Graham, for their patient assistance with my crystallography queries.

Mark Senn must be thanked for all of the PXRD work and the many tireless hours spent trying to fit my mostly poorly-diffracting data.

Hugh Vass of the School of Physics is acknowledged for his efforts in setting up the time-of-flight apparatus, which unfortunately never came to fruition. Enrico Mastropaolo and Tao Chen at the Scottish Microelectronics Centre are also noted in their assistance in carrying out the initial FET measurements and FET fabrication.

To the Robertson group past and present with whom I have spent the past few years, thanks for the friendship, biscuits, and good times. I give special thanks to Alex Sinclair for helping me through all of this, be it science related or others, and for all the awesome adventures. And to all the other chemists I have had the pleasure of working and playing with over the years, especially to those who never failed to "get the memo", I will always be grateful.

Final thanks must be given to my family; to my father who has been my academic inspiration, to Granda Betty for all her love and life lessons, and to my mother for never failing to support and believe in me…and of course for all the free lunches and "office cakes".

Structures

	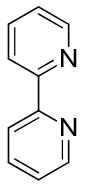 bpy	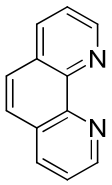 phen	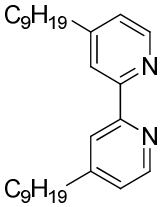 DNbpy	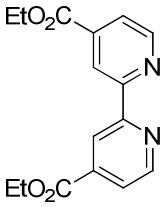 DECbpy
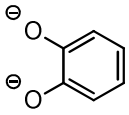 cat	Cu : **1a** Ni : **5a**	Cu : **2a** Ni : **6a**	Cu : **3a**	Cu : **4a**
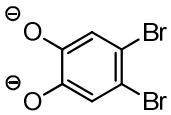 Br_2cat	Cu : **1b** Ni : **5b**	Cu : **2b** Ni : **6b**	Cu : **3b**	Cu : **4b**
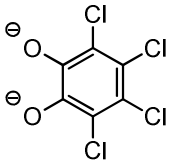 Cl_4cat	Cu : **1c** Ni : **5c**	Cu : **2c** Ni : **6c**	Cu : **3c**	Cu : **4c**
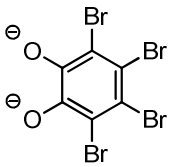 Br_4cat	Cu : **1d** Ni : **5d**	Cu : **2d** Ni : **6d**	Cu : **3d**	Cu : **4d**
	Chapter 3			
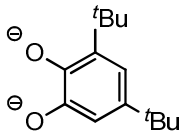 ^{t}Bu$_2$cat	Cu : **1e**	Cu : **2e**	Cu : **3e**	Cu : **4e**
		Chapter 4		

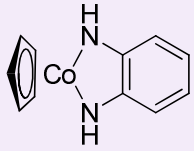 **7a**

CpCoDAbnz

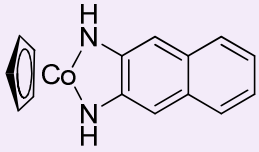 **7b**

CpCoDAnap

Chapter 5

Abbreviations

ARDF	Atomic radial distribution function
BCBG	Bottom-contact bottom gate
Bpy	2,2'-bipyridine
BO	Born-Oppenheimer
Br_2cat	4,5-Dibromocatechol
Br_4cat	Tetrabromocatechol
^{t}Bu$_2$cat	3,5-di-*tert*-butylcatechol
Cat	Catechol
CE	Counter electrode
cgs	Centimetres-grams-seconds
Cl_4cat	Tetrachlorocatechol
Cp	Cyclopentadiene
CT	Charge transfer
CV	Cyclic voltammetry
D	Drain electrode
DC	Direct current
DCM	Dichloromethane
DNbpy	4,4'-dinonyl-2,2'-bipyridyl
DECbpy	4,4'-diethoxydicarbonyl-2,2'-bipyridine
DFT	Density functional theory
DMF	Dimethyl formamide
DMSO	Dimethyl sulfoxide
DPV	Differential pulse voltammetry
DPPH	Diphenylpicrylhydrazyl
DPV	Differential pulse voltammetry
Et_2O	Diethyl ether
EtOAc	Ethyl acetate
EtOH	Ethanol
FAB	Fast atom bombardment
Fc	Ferrocene

FET	Field-effect transistor
HF	Hartree-Fock
HMDS	Hexamethyldisilane
HOMO	Highest occupied molecule orbital
LLCT	Intraligand charge transfer
LS	Least squares
LUMO	Lowest occupied molecular orbital
MeCN	Acetonitrile
MeOH	Methanol
MS	Mass spectrometry
NEt_3	Triethylamine
NIR	Near-infrared
NMR	Nuclear magnetic resonance
OFET	Organic field-effect transistor
OLED	Organic light-emitting diode
OTS	Octyltrichlorosilane
PAH(s)	Polycyclic aromatic hydrocarbon(s)
PCM	Polarisable continuum model
PEP	Pauli Exclusion Principle
PES	Potential electron surface
Phen	1,10-phenanthroline
PXRD	Powder X-ray diffraction
QCM	Quartz-crystal microbalance
QM	Quantum mechanics
RE	Reference electrode
Redox	Reduction and oxidation
RMS	Root mean square
RT	Room temperature
S	Source electrode
SAM	Self-assembled monolayer
SCFET	Single-crystal field-effect transistor
SEM	Scanning electron microscopy

SQUID	Superconducting quantum interference device
SOMO	Semi-occupied molecular orbital
TBA	Tetrabutylammonium
TD-DFT	Time-dependent density functional theory
THF	Tetrahydrofuran
TFT	Thin-film transistor
1,1,1-TCE	1,1,1-Trichloroethane
1,1,2-TCE	1,1,2-Trichloroethane
TTF	Tetrathiafulvalene
UV	Ultra-violet
Vis	Visible
WE	Working electrode
XRD	X-ray diffraction

Symbols

A	Area
B	Magnetic induction
C	Concentration
	Curie constant
C_i	Capacitance
D_0	Diffusion coefficient
ΔE	Peak-to-peak separation
$\Delta E_{p/2}$	Peak-to-peak at half-peak potential separation
E	Electrode potential
$E^{\circ\prime}$	Formal potential
$E_{1/2}$	Half-wave potential
E_{HOMO}	HOMO energy level
E_{LUMO}	LUMO energy level
E_{gap}	Energy gap
E_p	Peak potential
$E_{p/2}$	Peak potential at half-peak current
E_{pa}	Anodic peak potential
E_{pc}	Cathodic peak potential
ε	Molar extinction coefficient
F	Faraday constant
G	Gauss
H	Magnetic field
i_d	Diffusion current
I_D	Source-drain current
i_p	Peak current
i_{pa}	Anodic peak current
i_{pc}	Cathodic peak current
I_{sat}	Saturation current
J	Magnetic exchange
L	Channel gap length

λ_{max}	Absorption maximum position
M	Magnetisation
μ_{FET}	Field-effect mobility
μ_{lin}	Mobility measured from the linear regime
μ_{sat}	Mobility measured from the saturation regime
n	Number of moles
N	Avogadro's number
Ψ	Wavefunction
Q	Charge
R	Gas constant
	Resistance
R_S	Contact resistance at source electrode
ρ	Density
σ	Conductivity
T	Temperature
TIP	Temperature-independent paramagnetism
θ	Angle
	Weiss constant
υ	Scan rate
V	Potential
V_D	Source-drain potential
V_G	Gate potential
V_T	Threshold voltage
W	Channel width
χ_d	Diamagnetic susceptibility
χ_m	Magnetic susceptibility
χ_{meas}	Measured susceptibility
χ_p	Parmagnetic susceptibility

Contents

1. Introduction

The existence of complexes of that display non-innocence has been of interest in the field of coordination chemistry since the investigations of square-planar dithiolene complexes of the late transition metals in the 1960s.[1-4] The ligands used in these systems are termed "non-innocent" when bound to a number of the late transition metals, because the orbital energy levels are similar to those of the central metal ion. This allows there to be significant electron delocalisation over the complex with the potential for the complexes to exist in a number of electronic states due to the combined electrochemical activity.[5] In 1966, Jørgensen classified innocence as ligands that "allow oxidation states of the central atoms to be defined",[6] thus by this logic non-innocent ligands are defined as complexes where the precise oxidation states of the ligand and metal are ambiguously assigned. However it should be noted that no ligand is inherently non-innocent, but rather the ligand may behave in a non-innocent manner under the right circumstances. The qualification of non-innocence should therefore only be applied to combinations of metal and ligand that result in the aforementioned properties. In this thesis, the term "non-innocent" will be used to define ligands that often possess non-innocent behaviour when complexed to the metal centres they are bound to.

A general form of ligand that displays non-innocent behaviour is that of the 1,2-bidentate moiety with an unsaturated carbon backbone. The chelating donor groups (X) are either O, NH, S, or a combination of the three. The central transition metal is generally a late metal that favours a square-planar geometry, because the planarity of the complex is crucial for electron delocalisation within the molecule and molecular interactions in the solid material. When the metal is nickel or platinum for example, their square-planar complexes with such ligands have shown three-membered electron-transfer series (**Figure 1.1**).[7]

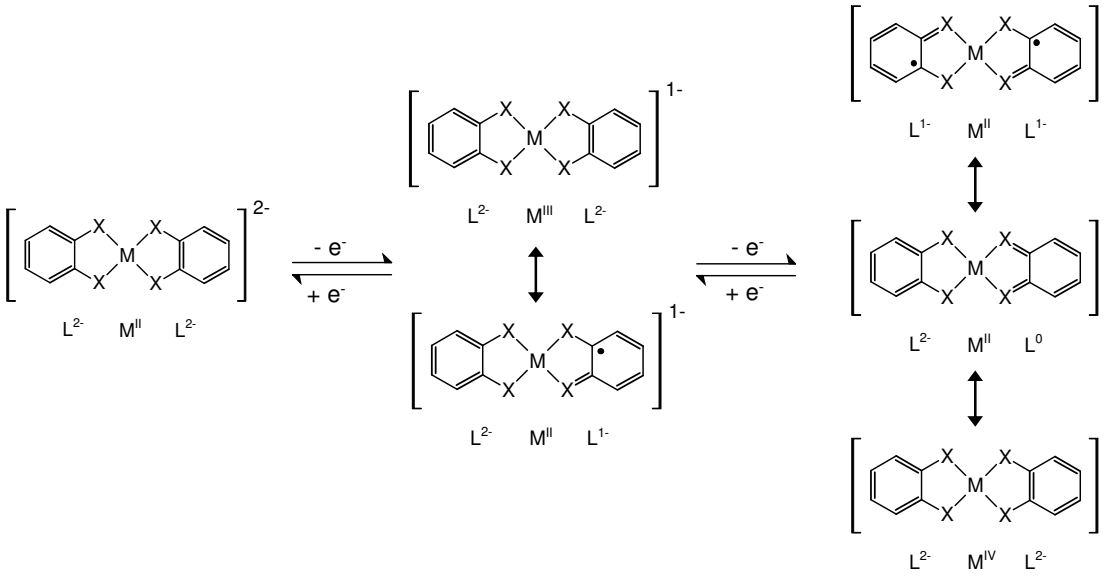

Figure 1.1. Schematic representation of the various electronic states that can exist in transition metal complexes with non-innocent ligands. The donor group 'X' often represents S, NH or O when this behaviour is observed, although more formal assignments of oxidation state are common when X = O.

Specific examples of ligands that have been shown to display non-innocent behaviour are those of catechol (1,2-dihydroxybenzene) and 1,2-diaminobenzene, where the unsaturated backbone is provided by a phenyl group. The electronic nature of these compounds has been extensively investigated by the groups of Pierpont[5,8-11] and Lever,[12,13] with focus on their redox and magnetic properties. The combined metal and ligand redox activity results in interesting magnetic behaviour, with potential for magnetic exchange interactions between a paramagnetic metal centre and the radical ligand or between two radical ligands mediated by a diamagnetic metal centre.[8,14,15] This research has been advanced by Wieghardt and co-workers who have performed experimental and theoretical examination of non-innocent complexes of 1,2-substituted phenyl chelates, where the donor group is a combination of O and NH.[7,16-21] These studies have focused on the understanding the nature of the metal-ligand interactions to apply to biological systems, such as those observed at the active site of enzymes that act upon molecules with similar moieties to the non-innocent ligands.

Compounds of catechol may be referred to as dioxolenes in analogy to the sulfur-based dithiolenes. The deprotonated, dianionic form of catechol is known as catecholate (cat), which can be readily oxidised to the monoanionic *o*-semiquinone (SQ) and neutral *o*-benzoquinone (Q) forms (**Figure 1.2**). It has been seen that catecholate compounds can be described by localised electronic states with defined oxidation states, unlike many of the dithiolene class of molecules.[5] However these states can exist in equilibrium with each other when the metal and ligand orbitals are close in energy, with differences in the charge and spin definition in what has been described as "valence tautomerism". Therefore, although the complexes may not be seen as non-innocent by definition that their oxidation states are not ambiguous, it is still a useful description due to the potential for easily accessible charge states.

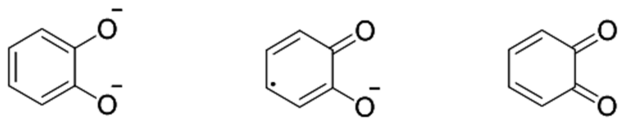

Figure 1.2. Oxidation states of catechol: cat = catecholate; SQ = semiquinone; BQ = benzoquinone.

Metal dithiolene complexes, where the metal is coordinated by one or more ligands with two S-donor atoms linked by a conjugated backbone, are one of the best researched of the non-innocent class of molecules. The square-planar *bis*-dithiolenes of the late transition metals have interesting magnetic, optical and electrical properties arising from the delocalised nature of the constituent metal and ligand orbitals,[22-24] which has enabled their use for a wide range of applications such as non-linear optics,[24,25] transistors[26] and near-infrared switches.[27] Of particular interest is the ability to fine tune the electrical properties to fit the application by changing the substituents on the core dithiolene moiety.[25] For example, Anthopoulos has shown that by lowering the energy of the lowest unoccupied molecular orbital (LUMO), stable *n*-channel conductivity can be observed in field-effect transistors (FETs).[28]

Materials based on square-planar non-innocent complexes have been tested in FETs,[26,29-32] and been seen to display field-effect mobilities as high as 10^{-2} cm^2 V^{-1} s^{-1} as with Ni bis(o-diiminobenzo-semiquinonate) complexes.[29] Most of these molecules are based on conjugated, chelating ligands such as 1,2-diaminobenzene and the dithiolene class of molecules. Field-effects have also been observed in square-planar Pt complexes, where the conductivity is thought to arise from beneficial Pt-Pt bonds in addition to the π-stacking between molecules.[32] Despite the similarity to the diaminobenzene and dithiolene counterpart, there are no reports of catechol-based materials displaying field-effect properties in the literature. Catechol compounds are well-researched in the field of biological chemistry due to the prevalence of the catechol moiety and enzymes with which it interacts in nature. However they have not been examined far beyond their simple coordination chemistry or chemical characterisation.[5,9-11,33,34]

Thesis content and chapter summary

Transition metal complexes have shown promise as electroactive materials when implemented into electronic devices. This is as a result of their structural and bonding diversity that can promote intermolecular interactions, increased stability and variation in the energy and location of the frontier orbitals. Complexes that have successfully exhibited functional electronic behaviour in the solid state have been planar structures based on conjugated, chelating ligands that are non-innocent in nature when complexed to a metal.

The work presented in this thesis is based on furthering the understanding of how the electronic structure and bonding of non-innocent and redox-active complexes can influence the solid-state structure and properties. The research is divided into two classes of compounds. The first is based on square-planar heteroleptic complexes of Cu(II) and Ni(II), which have been designed to study the influence of the electronic structure of simple derivatives of the catechol ligand. The second class of compounds is based on monometallic Co(III) half-sandwich compounds with 1,2-diamino-ligands, which were proposed due to their ease of

processability by solution and vapour methods, as well as their possession of stable redox processes.

The rest of this chapter presents discussion on the principles and applications of charge transport within molecular materials. The origin of electrical conductivity in molecular solids is described in addition to detailed discussion on their measurement. Particular attention is paid to the operation of field-effect transistors, and the various types of materials and processing techniques used to construct a device.

The experimental methods used in this thesis are described in Chapter 2, with the focus on electrochemistry, magnetometry and computational methods. A brief overview is given for each technique with the experimental aspects used to interpret the compounds.

Chapter 3 includes the molecular and structural investigations into a series of square-planar, heteroleptic compounds of copper and nickel that contain the aromatic and chelating ligands based on catechol and a bidentate N-donor ancillary ligand. Novel crystallisation techniques have yielded structures of this class of compounds that have never been obtained previously due to their lack of solubility. This has allowed detailed examination of how the intermolecular interactions and observed magnetism are influenced by the changing electronic properties.

To further investigate the chemical properties of the series of heteroleptic square-planar transition metal complexes as detailed in Chapter 3, two different types of modification were investigated in Chapter 4 that provide additional functionalisation to tune the frontier orbitals and increase solubility. This added solubility allowed further details about the nature of the electronic orbitals to be probed through the techniques of electronic absorption spectroscopy and electrochemical methods. Soluble compounds were also sought to allow solution

processability into thin films to be tested. Experimental observations are compared with solvent-based and time-dependent DFT calculations.

In Chapter 5, the molecular focus moves away from the purely planar structures in order to enhance the material processing, increase redox activity and study a different type of structure and its influence on the electronic behaviour. Two molecules that are based on organometallic "half-sandwich" structures of cobalt, which contain one 1,2-diamino-substituted aromatic ligand, are presented in detail. In addition to the molecular and structural characterisation, thin-film characterisation and field-effect transistor measurements are presented and discussed.

The main conclusions are summarised at the end of each results chapter, with discussion of where future investigations will lead to further advancement and understanding of the research area.

1.1 Introduction to molecular semiconductors

1.1.1 History

The electrical and photoconductive properties of molecular and polymeric materials have been investigated since the turn of the 20th century.[35] The potential application of these materials into electronic devices is great given the availability of inexpensive materials and processing techniques. At present, the field of molecular electronics (also referred to as organic or plastic electronics) has expanded almost exponentially, realising a range of electrical phenomena from a vast array of chemical families. The continuing research of these materials is paramount for further understanding of their underlying fundamental properties of charge generation and transport as well as for optimisation for potential technical applications in the field of electronics.[36-38]

1.1.2 Inorganic semiconductors

Electronic devices that rely on semiconductors as the active material have been dominated by traditional inorganic semiconductors for over 50 years. With the inception of the transistor in 1947 and the integrated circuit in 1958, inorganic semiconductors became the foundation of modern electronics, ultimately leading to the development of the microprocessor.[39] These devices were based on the semiconductors silicon and germanium, inorganic materials that can be processed and purified to a great degree of precision and purity. This is very important for the mass production of devices with reliable and reproducible electronic properties. In terms of performance, inorganic semiconductor devices possess electrical conductivities and switching speeds that are orders of magnitude greater than their molecular semiconductor counterparts. However, this performance comes at an expense with the high cost of fabrication plants, expensive sample preparation and device manufacture. The inorganic semiconductor industry has the goal of making

devices smaller and more efficient. In the field of molecular electronics the goal is to synthesise new materials and fabricate devices that have a sufficient charge mobility to merit their effectiveness, whilst remaining cheap and flexible enough to be used for a range of specialised applications.

1.1.3 Molecular semiconductors and device applications

Molecular semiconducting materials, based on either small molecules or polymers, have the potential for production of electronic devices at low cost and with wide-reaching functionality. The performance of molecular electronics has progressed significantly in recent years, with the advancements spurred on by demands for inexpensive electrical components, fundamental scientific interest and attractive potential applications. Photoconductivity, electroluminescence, metallic conductivity, superconductivity, semiconductivity and photovoltaic effects are all phenomena that have been observed in molecular materials.[40] Devices that utilise molecular materials as active elements include "organic" field-effect transistors (OFETs), light-emitting diodes (OLEDs), electrical rectifiers and photovoltaic cells (OPVs), amongst others, although it is the area of molecular semiconductors for use in FETs that will be discussed in detail in this chapter.

OFETs are the key components in the field of the molecular electronics, with applications in switching devices for (flexible) active matrix displays[41,42] and in integrated circuits as inexpensive memory elements for smart cards.[43] For low-end data storage devices like radio-frequency identification (RF-ID) tags, where the superior electrical performance of crystalline inorganics is not needed, the inexpensive fabrication onto plastic substrates is ideal.[44,45] Due to the relatively low charge mobility inherent in molecular semiconductor materials, OFETs can not compete with the performance and switching speeds of crystalline inorganic-based materials for high-performance applications. However, OFETs are suitable for applications where ease of processing, device flexibility and low overall cost are desired.[46] Active matrix displays currently use amorphous silicon as the

semiconducting material, the performance of which can be matched by organic devices. Therefore the benefits of light-weight, cheap and durable displays can be observed by implementing OFETs without a reduction in performance. However unlike inorganic semiconductors, molecular material devices are far more advanced technologically than scientifically, with many commercial applications in place before a full understanding of the physical origins of charge transport and trapping mechanisms has been discovered.

1.2 Conductivity and charge mobility

For the conduction of electric current in a material, charge carriers must exist that are able to carry this current. The conductivity, σ, is defined as the charge that is transported across a cross-sectional unit area per second per unit of electric field applied to the material. Thus the conductivity is proportional to the electric charge, e, the number of charge carriers, n, and the charge mobility, μ, as seen in **Equation 1.1** below. The mobility is defined as the velocity of the charge carrier in a unit field (**Section 1.2.2**).

$$\sigma = ne\mu \qquad \textbf{Equation 1.1}$$

In electronic conductivity the charge carriers are electrons or positively-charged holes. A free electron in this context is one that can transport current under the influence of an electric field. For an electron to be free there must be energy levels available into which it may move, so that the electron may gain energy from the electric field to carry current. This situation applies for positive holes as well. Therefore, the only charge carriers that can carry current and thus contribute to the conductivity in **Equation 1.1** are those that are free. However this is not entirely true for molecular materials as will be described later (**Section 1.5**).

The conductivity in elemental solid materials (e.g. silicon) can generally be described by band theory. Although the mechanism of charge transport in molecular materials is not completely understood and can be described by various models, it is inherently more anisotropic than that which exists in inorganic materials: the solid-state structure of molecular crystals dictates that the charge mobility and thus the conductivity is more often than not drastically different in different directions. Despite this difference it is useful to describe some of the basic concepts of solid state theory.

1.2.1 Band theory

In molecular orbital theory, as atoms of the same element are brought together their constituent atomic orbitals split into an equivalent number of molecular orbitals, which are divided into bonding and antibonding orbitals. Occupation of the bonding orbitals by the valence electrons leads to the formation of a covalent bond. In a bulk material, a very large number of atoms are held in close proximity in a lattice. Because the number of atoms is comparable to Avogadro's number (N_A), the spacing between individual energy levels becomes so small that they effectively form a continuous band of energy rather than discrete levels, as shown in **Figure 1.3**.

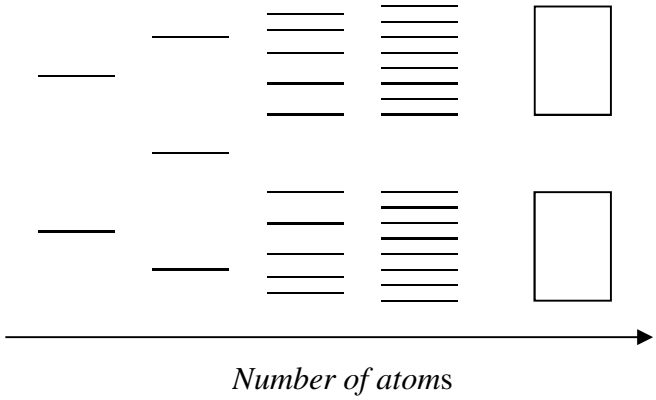

Figure 1.3. Coalescing of energy levels to form energy bands.

The bonding orbitals form the valence band that normally contains the electrons, and the antibonding orbitals form the conduction band that is generally unoccupied. The two energy bands are separated by an energy band gap in which no allowed states exist. The main difference between a material that is an insulator and one that is a semiconductor is the size of the band gap; a semiconductor has an energy gap in the range of a few electron volts that is suitable for exploitation in electronic devices. Compared to inorganic semiconductors, molecular semiconductors have a very small band width due to the weaker nature of the interactions between molecules in the solid state compared to the covalent bonding in the inorganic materials. Nevertheless, band theory can be applied to describe charge transfer in molecular crystals.[40]

1.2.2 Charge mobility in semiconductors

Current in a semiconductor can be generated by application of an externally-applied voltage, which creates an electric field that causes motion of the charge carriers. This is called the drift current. Thermal energy and random motion can also cause the movement of charge carriers from regions of high density to low density, resulting in what is termed the diffusion current. As the charge carriers accelerate under the influence of the applied field, a constant average velocity is eventually

reached due to a balance between the electric force and the increased lattice vibrations and collisions with impurities. The ratio of the average carrier velocity, v, to the applied electric field, E, is called the charge mobility, μ, as denoted in **Equation 1.2**:

$$\mu = v/E \qquad \textbf{Equation 1.2}$$

The common unit of measurement of mobility is $cm^2\ V^{-1}\ s^{-1}$, with the field represented by a potential gradient in $V\ cm^{-1}$. The relationship between drift current and mobility is shown in **Equation 1.3**:

$$I = nAF\mu \qquad \textbf{Equation 1.3}$$

where n is the number of charge carriers, A is the cross-sectional area of the sample and F is the electric force. The charge mobility is essentially a measure of how easily charge can move in response to an applied field to generate current. At high electric fields the saturation current is reached where the charge carrier velocity is no longer influenced by further increases in field. These relationships are characteristic of electrical conduction in the bulk of a material, however at the surface of a material there will be additional scattering mechanisms from surface states or interfaces that will lower charge mobility.

The number of charge carriers present to conduct electric current in an intrinsic semiconductor is dependent upon a balance between their generation and recombination mechanisms. Recombination is a process whereby electrons and holes annihilate each other by occupying the same state.[40] This process is mediated be so-called "traps", which are localised lower energy levels within the band structure of the material that charge carriers can "fall" into. Traps are normally caused by crystal imperfections such as defects or impurities, grain boundaries, interfaces or surface sites. When a carrier falls into a trap it is no longer free and able to transport electric current, therefore the effective mobility of the charge carrier is substantially lowered.

In addition, the probability of recombination with the opposing charge carrier is increased while in a trap.

The time that a carrier spends in a trap depends on the energy level, or depth, of the trap and the energy of the carrier. In most instances for a given material only one kind of charge carrier will be preferentially trapped, so the concentration of electrons and holes will not be equal and the current will be the result of transport of the majority charge carriers. If the energy difference between the trap level and the energy band from which the charge carrier was trapped is comparable to kT, then the trap is described as shallow. These traps are always filled to some degree at room temperature, in thermal equilibrium with the normal band occupation of the material. A deep trap has a depth that is much larger than kT, and the probability of escape is similar to the probability of the generation of a new electron-hole pair. It is the deep traps that are the major hindrance to charge mobility in molecular semiconductors.

1.2.3 Charge mobility in molecular semiconductors

Despite the ambiguity in the origins of electrical conduction in molecular semiconductors, there is a significant difference in the fundamentals of charge transport between thin films and highly-ordered single crystals. Charge transport in disordered semiconductors is normally explained by thermally-activated hopping of charges between localised neutral sites via a series of electron transfer reactions (the so called “hopping model”). On the other hand, highly-ordered molecular single crystals show a band-like transport.

In the hopping model, the charge transfer between molecules is considered to be a chemical process with an activation energy barrier, where charge mobility increases with temperature.[47] This model generally applies to organic materials with an effective charge mobility of less than 1 $cm^2\ V^{-1}\ s^{-1}$, where thermal fluctuations temporarily reduce the potential barrier to the movement of the electron. In the band model, the motion of charge carriers can be described in a similar fashion to those in

inorganic semiconductors with free charge carriers. In general, this model is used when the mobility is greater than 1 $cm^2 V^{-1} s^{-1}$, with the mobility increasing with decreasing temperature due to decreased phonon scattering.

However, there have been models proposed for charge transport in polycrystalline molecular thin films that sit in between the hopping and band models,[48] and so it seems that the degree to which a material fits a charge transport model depends on its degree of crystallinity and order, and is not described solely by either of the two models. Moreover, studies are now suggesting that due to the relatively weak interaction between molecules in a molecular crystal, thermal motion affects the electronic coupling and can lead to localised charges that would not be consistent with delocalised, band-like transport.[49]

For all forms of semiconducting material, purity is paramount to achieving high charge mobility, which is inversely proportional to the concentration of impurities and the depth of charge traps. At higher temperature, the charge carriers possess a greater thermal velocity that decreases the interaction time with and increases the probability of escaping from deep traps, thereby increasing mobility in disordered materials that obey the hopping model. The charge mobility is very much dependent upon the degree of molecular order in the semiconducting material, and charge traps can arise from grain boundaries in thin films or structural imperfections in single crystals. This is one of the main reasons why drastically different results for charge carrier mobility can be seen in OFETs composed of the same semiconductor.[50]

1.3 Field-effect transistors (FETs)

The first metal-oxide-semiconductor field-effect transistor (MOSFET) based on silicon was developed by Kahng and Atalla in 1960.[51] These devices were key to the advancement of the field of modern microelectronics, and remain the most

important components in the field. FETs based on organic semiconductors (OFETs) were realised about 10 years later,[52,53] and have since seen become a major area of research regarding functional materials. Devices have successfully utilised polymers and small conjugated molecules as the electroactive components. The performance of these devices is based on the key parameters of field-effect mobility (μ_{eff}), current on/off ratio (I_{on}/I_{off}) and threshold voltage (V_T), and is now comparable to that of commercial amorphous silicon thin-film transistors (TFTs).[54] For applications where low-cost and processability are key, OFETs have become a device of choice.

The FET is a class of transistor that, as the name implies, uses an electric field to control the conductivity of a channel of semiconducting material. The semiconducting material is deposited onto a gate electrode, which is separated from the material and the source (S) and drain (D) electrodes by a dielectric layer (**Figure 1.4**). The device depicted is of a bottom-gate bottom-contact (BGBC) architecture, where the semiconducting layer is deposited on top of the S-D electrodes. This FET design was employed for the measurements carried out during this thesis. The gate can be metallic or highly-doped silicon, which is coated with an insulating dielectric layer (e.g. SiO_2), however both the gate and insulator can be polymeric for use in flexible electronics.[55] The source and drain electrodes are generally vapour-deposited, high workfunction metals (e.g. Pt and Au), although conducting polymers can also be used for print-based fabrication methods. The semiconducting layer can be deposited from either the vapour or solution phase, as discussed in **Section 1.4**. The channel length between source and drain, *L*, is often 100 microns or less, and the channel width, *W*, can be orders of magnitude larger depending on the device construction.

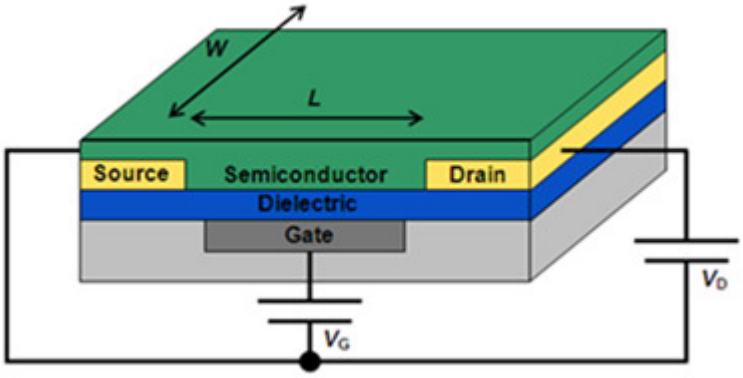

Figure 1.4. Basic structure of a bottom-gate bottom-contact (BGBC) OFET. V_D and V_G are the drain and gate voltages, respectively; W and L are the channel width and length, respectively.

1.3.1 FET operation

When a bias is applied to the gate electrode, a number of charge carriers of the opposite polarity are induced in the semiconductor at the dielectric interface.[56] This gate voltage (V_G) is applied between the gate and source electrodes, and together with the capacitance of the dielectric, effectively controls the density of charge carriers in the channel. The electric field produced by the applied V_G causes the semiconductor band energy levels to either shift up and accumulate holes in the valence band or shift down and accumulate electrons in the conduction band. The minimum potential needed for the semiconductor to accumulate charge between the S and D electrodes and switch the transistor into the on state is the threshold voltage (V_T). This parameter should be small to improve the efficiency and power consumption of the device. The presence of deep traps (that need to be filled before mobile charge carriers can be accumulated) also influences the size of V_T.

The induced charge carriers move in response to an applied source-drain voltage (V_D) between the source and drain electrodes, generating a source-drain current (I_D) that switches the transistor to the "on" state. In the linear regime at small V_D magnitudes, the I_D in the device is directly proportional to V_D (**Equation 1.4**). As V_D approaches the size of effective gate voltage ($V_G - V_T$), a space-charge limited saturation current (I_{sat}) comes into effect (**Equation 1.5**), with further increases in

source-drain voltage not significantly increasing the current in the channel. The characteristic linear and saturation regions are displayed in **Figure 1.5**.

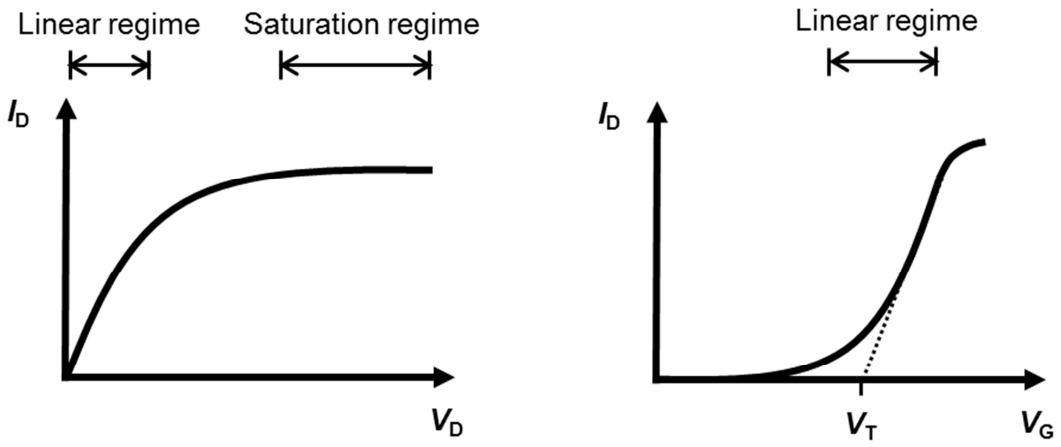

Figure 1.5. Output (left) and transfer (right) characteristics of an FET device.

Output characteristics

Linear regime $$I_{\mathrm{D}} = \left(\frac{W}{L}\right) \mu_{\mathrm{lin}} C_{\mathrm{i}} (V_{\mathrm{g}} - V_{\mathrm{T}}) V_{\mathrm{D}}$$ **Equation 1.4**

Saturation regime $$I_{\mathrm{D}} = \left(\frac{W}{2L}\right) \mu_{\mathrm{sat}} C_{\mathrm{i}} (V_{\mathrm{g}} - V_{\mathrm{T}})^2$$ **Equation 1.5**

Transfer characteristics

Linear regime $$\mu_{\mathrm{lin}} = \left(\frac{\partial I_{\mathrm{D}}}{\partial V_{\mathrm{G}}}\right) \cdot \left(\frac{L}{W C_{\mathrm{i}} V_{\mathrm{D}}}\right)$$ **Equation 1.6**

Saturation regime $$\mu_{\mathrm{sat}} = \left(\frac{\sqrt{\partial I_{\mathrm{D}}}}{\partial V_{\mathrm{G}}}\right)^2 \cdot \left(\frac{2L}{W C_{\mathrm{i}}}\right)$$ **Equation 1.7**

The mobility in the linear regime is represented as μ_{lin} and the mobility in the saturation regime μ_{sat}. When no gate voltage is applied, there should ideally be no more mobile charge carriers present to conduct electricity between the S and D electrodes, switching the transistor to the "off". The current on/off ratio (I_{on}/I_{off}) is the ratio of the drain current in the on-state to that in the off state, which governs the switching speed and contrast that can be achieved in a device. This measurement is determined from the transfer characteristics, where at a constant value of $V_{D,}$ the I_D is measured at a given V_G and compared with the I_D at V_G = 0. Often in devices

composed of molecular semiconductors, there will be a small amount of leakage current in the off-state due to charge carriers generated from thermal excitation from trap sites, thus lowering I_{on}/I_{off}. Furthermore it has been well documented that O_2 and H_2O from the air can negatively influence the device performance by the generation of surface states that can either dope or oxidise the material or create charge traps.[57]

The device characteristics are fundamentally dependent upon the contact resistance present for charge injection and ejection between the S-D electrodes and the semiconducting material.[58] This electrical property therefore governs the shape of the output and transfer characteristics that are experimentally observed. Contact resistance at the source electrode (R_S) will reduce the effective V_D and V_G applied to inject charge carriers. Hence the current observed in the linear and saturation regimes will also be reduced. Contact resistance at the drain electrode (R_D) does not influence the V_G, therefore will affect only the linear regime. As a consequence of this, the parameters derived from the output and transfer characteristics of field-effect mobility, on/off ratio and threshold voltage are all dependent upon the contact resistance.

The contact resistance, R, is linearly related to the gap length, L.[58] Therefore in addition to the inverse relationship between I_D and L that exists from **Equation 1.4** and **Equation 1.5**, decreasing the channel lengths should increase the current output and the on/off ratio. When applied to molecular semiconductors that often possess sub-micron grain sizes, the number of grain boundaries will decrease as the grain sizes become comparable in size to the gap length.[59] Therefore potentially higher field-effect mobilities should be observed. On the other hand, it has been seen in the literature that poor effective mobilities are observed when the more convenient BGBC FET architecture is used in conjunction with molecular semiconductors.[59] The benefit of having comparable grain sizes with the gap length is counteracted by crystal growth that is disrupted due to depositing onto an uneven surface with two different materials. Furthermore, the influences of these morphological changes have a greater influence on the short-channel devices, leading to non-Ohmic behaviour.

Surface treating the substrates with chemical reagents is one way of reducing the influence of this effect, which is detailed in Chapter 2.

General requirements for good performance of organic semiconductors in an OFET include: HOMO/LUMO levels at sufficient energy for the generation of charge carriers at modest values of applied electric field; strong intermolecular overlap of the frontier orbitals for efficient charge transport between molecules and through the solid material; a pure semiconductor to prevent charge traps due to impurities; and the molecules in the semiconducting layer orientated so that the direction of greatest intermolecular bonding (and hence greatest charge transport) is parallel to the device substrate and points between the source and drain electrodes.[60]

1.3.2 FETs performance and limitations

Due to the nature of molecular semiconductors, the field-effect charge mobility, μ_{FET} (also call the effective mobility, μ_{eff}) is mitigated by factors such as molecular vibrations, disordered films and large intermolecular distances. The major hindrance to charge carrier mobility in thin films of these materials is the presence of structural defects such as grain boundaries and interfacial sites generating charge carrier trap sites,[61,62] which also increases the threshold voltage and slows switching between on and off states of the transistor. In terms of the device fabrication, factors such as processing method, temperature, surface treatment, sample purity and device structure can all effect device performance by altering film morphology and molecular packing, and therefore the nature of structural order and extent of structural defects.[42] Therefore, it becomes difficult to determine the theoretical limit for performance in these types of materials.

Single crystal field-effect transistors (SCFETs) have been fabricated in the literature,[57,63-69] where grain boundaries between crystalline sites are eliminated, and charge-trap concentration is reduced and the variation in molecular order is minimised. SCFETs based on the organic polyacene derivative rubrene (**Figure 1.6**

(b)) have been observed with charge mobility up to 8 $cm^2 V^{-1} s^{-1}$ and near gate-voltage independence.[69] Nevertheless, structural defects still limit the study of material performance in SCFETs.[64,70,71] Contact effects at the interfacial sites will still occur that create a barrier to charge injection and limit performance. In addition, the measured charge mobility in an FET is an effective mobility measured in a narrow surface channel of semiconducting material, therefore if there are any trap states at the surface the mobility will be greatly affected. At the surface of a solid there is an abrupt termination of the crystal lattice. This lattice discontinuity leads to localised energy levels and can cause drastic distortions in the energy band structure as well as introduce traps.[40] Therefore, with the variation in performance that exists in the literature between OFETs, even those using the same molecular semiconducting material, care must be taken when comparing magnitudes of charge mobility. Despite being unable to measure the fundamental charge mobility inherent in the semiconducting material, the applicability of a given material for implementation into an FET device can be determined when the experimental parameters that give rise to the measured mobility are well defined.

1.4 Device processing

Most of the benefits of organic semiconductors originate from the ease and variety of their processability. Solution processing methods are ideal for low-cost applications such as RF-ID tags, and include inexpensive techniques such as spin- or drop-coating and inkjet printing. For small molecules that are not solution processable due to their solubility (oligothiophenes, polyacenes), other techniques such as vacuum- or vapour-deposition techniques are used. Generally the higher purity and molecular order that can be achieved via these methods results in higher charge mobilities than solution-based methods.[72] Fabrication at much lower temperatures than required for silicon-based devices allows a range of low-cost, flexible substrate materials to be exploited in addition to the lower energy running costs at reduced temperatures.[73] Low-temperature vacuum deposition and solution-

based printing onto flexible substrates via roll-to-roll processing has been realised, allowing for the mass production of light-weight, large-area displays.[74,75] The method of deposition of the semiconducting material is crucial to the final device performance, therefore control of the molecular order and the film morphology, thickness and coverage is very important.[74,76]

Vacuum deposition is a method that allows for the slow and precise growth of molecular thin films, leading to a good degree of molecular order in the film microstructure. The process involves thermally evaporating a pure source material in a vacuum chamber at very low pressures, resulting in the slow deposition of molecules onto a (relatively) cold substrate. The thickness of the thin films can be controlled to near monolayer accuracy by careful control of the temperature of the source material. Higher-quality films with a greater field-effect mobility are achieved when the growth process is sufficiently slow.[69]

Spin coating is one of the methods of choice for thin-film formation in the field of molecular electronics.[31,77-79] The semiconducting material is dissolved in a solvent to form a concentrated solution that is deposited onto the substrate. The substrate is accelerated to a high rotational spin speed, causing the solution to rapidly spread out and off the substrate edge due to centrifugal force, leaving a thin film adhered to the substrate surface. The thickness of the film is governed by properties of the solution such as concentration, viscosity and surface tension, as well as parameters from the spin-coating process such as spin speed and acceleration. These factors can be controlled to obtain a film of desired thickness.

1.5 Organic conducting materials

It was not until the middle of the 20th century that significant interest in the field of organic electronics was garnered by studies into the electronic conducting properties of conjugated molecular π-systems, such as phthalocyanines[80] and

polycyclic aromatic compounds.[81] Furthermore, following discoveries of insulator-metal transitions in linear polymers such as polyacetylene[82,83] and polypyrrole,[84] there was great fundamental and industrial interest in electronic materials based on organic polymers with extended π-systems. The common structural feature of organic semiconductors that have been studied so far is that they all possess a strong degree of π-conjugation. This conjugation is an important feature for charge transfer in organic species, because it increases delocalisation of electron density over individual molecules as well as improving the interactions between molecules. This leads to the dominant π- π intermolecular forces (weak in comparison to the strong covalent bonding that exist in inorganic semiconductors) determining the optical and electrical properties of the material.[60] Therefore, the macroscopic properties of organic semiconductors are controlled by their intrinsic molecular properties and interactions. A number of different classes of organic compounds that have been successfully implemented as the active layer in FETs are displayed in **Figure 1.6** and discussed below.

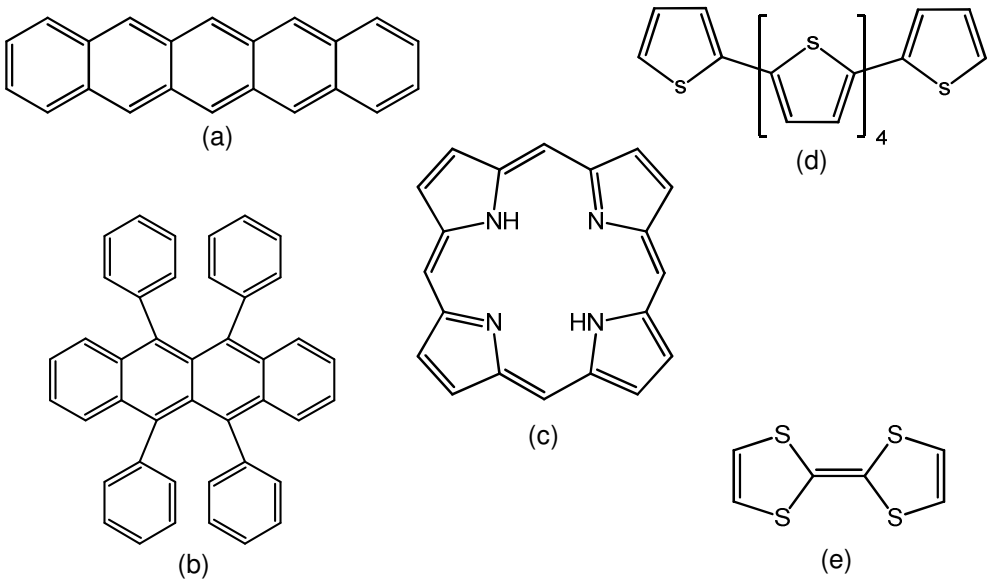

Figure 1.6. Organic semiconductor molecules: (a) pentacene (b) rubrene (c) porphyrin (d) sexithiophene (e) tetrathiafulvalene.

1.5.1 Polycyclic aromatic hydrocarbons (PAHs)

Polycyclic aromatic hydrocarbons (PAHs) are compounds that are composed solely of fused aromatic rings. A subset of the PAHs is the polyacenes (or oligoacenes), which are compounds made of linearly-fused benzene rings. The conductive properties of the polyacenes are well known, and are one of the most-heavily-researched classes of organic semiconductors for use in electronic devices due to the consistent and relatively-high charge mobility that can be achieved in thin-film FETs. Pentacene (**Figure 1.6** (a)) is still one of the most popular organic semiconductors being studied and optimised for devices,[43,44,66,74,85-88] with thin-film transistor hole mobilities comparable to amorphous silicon devices (> 1 $cm^2 V^{-1} s^{-1}$). Currently, pentacene remains a standard for the development of new organic semiconductors, with hole mobilities greater than 5 $cm^2V^{-1}s^{-1}$ in thin films[89,90] and 35 $cm^2 V^{-1} s^{-1}$ in room-temperature single crystals[57] being achieved.

The high charge mobility is a result of high molecular order and large grain sizes obtainable through vapour processing, which allows efficient charge

transport.[91] The disadvantages of pentacene are that it is highly insoluble and has a low environmental stability. SCFETs using rubrene (**Figure 1.6** (b)) have also shown effective hole charge mobilities up to 20 $cm^2 V^{-1} s^{-1}$ in the direction of strongest π-orbital overlap determined by the crystal structure.[92] The crystal packing in both pentacene and rubrene is herringbone in nature (**Figure 1.7**), with significant anisotropy in the strength of intermolecular interactions in the three different crystallographic axes.

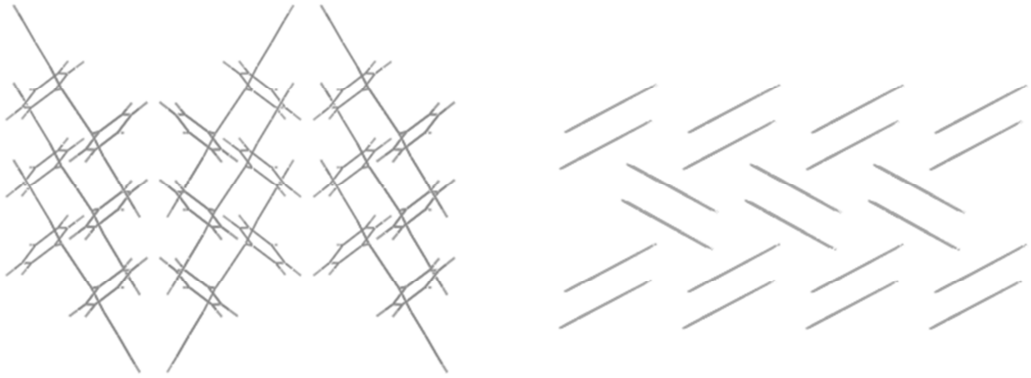

Figure 1.7. Herringbone crystal packing in rubrene (left) and pentacene (right) single crystals.[87]

1.5.2 Oligothiophenes

Oligothiophenes, such as sexithiophene (**Figure 1.6** (d)), are another important class of organic oligomer semiconductors based on the electron-rich thiophene ring, which have been the subject of much research for electronic applications such as OFETs. Pioneering studies on polycrystalline films of oligothiophenes for OFETs were among the first to show that using planar, conjugated compounds with close molecular packing is key to achieving a high charge mobility.[60,93] Oligomers containing up to 8 thiophene rings all display planar conformations with herringbone packing in the crystal structure like the polyacenes, with similar ordering in the crystalline sites of thin films.[94] The thiophene rings can be functionalised to increase solubility or increase the molecular ordering in the solid-state films, which is crucial to increasing charge mobility.[73] Through variation in the conjugation length and substitutions of the thiophene ring, there is an extensive

range of effective charge mobilities that have been measured in literature for this class of compound, again showing the importance of sample purity, device architecture and molecular order in the thin film.

1.5.3 Tetrathiafulvalene derivatives

A class of conducting organic materials also based on sulfur heterocycles are the tetrathiafulvalene (TTF) derivatives. The single-electron oxidation of the TTF unit leads to a remarkably stable radical cation, and has led to the observance of metallic conductivity, semiconductivity and superconductivity in the salts of oxidised TTF and its derivatives.[95-97] TTF can undergo two facile and reversible one-electron oxidations, with the oxidation of each ring leading to an aromatic, 6π-electron configuration (hence the stability). This behaviour also helps explain high conductivity of the TTF unit: high symmetry to allow strong charge delocalisation, and efficient π-π stacking due to planarity. Much of the research in the field of TTFs was driven by the pursuit of new superconducting materials, but there have been a number of examples of their use in FETs. Field-effect mobilities greater than 1 $cm^2 V^{-1} s^{-1}$ and current on/off ratios of 10^5 have been observed in SCFETs of TTF derivatives,[68] with crystals possessing a herringbone packing motif as seen in many of the other organic semiconducting crystals.

1.6 Transition-metal materials

Much of the focus of molecular semiconductors in the past has been concentrated on purely organic compounds such as the polyacenes and oligothiophenes, with research based on transition-metal complexes as conducting materials being very limited. However, in comparison to the research-dominating pure organic semiconductors, those based on transition-metal complexes can offer many advantages. There is an endless variety of starting materials and synthetic techniques available with which to modify molecular structure in organic

compounds, and this diversity can be augmented by the introduction of a transition metal centre that can offer variation in its coordination number, geometry, valence shell and interactions with the organic ligands.[29]

Compared to pure organic compounds, metal complexes can display a wide variety of redox potentials that are often facile and fully reversible, which is crucial to the generation and transport of electric charge in active semiconducting materials. In metal complexes, redox potentials can be adjusted systematically over a wide range through variation of the organic ligands and metal ion. The frontier orbitals can also be readily fine-tuned by modification of the interaction between the metal and ligand orbitals. This can be exploited to increase the strength of intermolecular interactions, to introduce ambipolar charge transport character, or to allow modification of the HOMO/LUMO gap to meet device requirements. Furthermore, the influence of paramagnetic species on charge transport can be investigated using transition-metal complexes, through the selection of paramagnetic transition metal ions and/or by the stabilisation of organic radical ligands.[98] With this novelty in mind, material properties such as processability, stability and charge-transport characteristics can be improved to allow for application-specific materials to be designed.[42]

1.6.1 Ambipolar devices

When incorporated into FETs most molecular semiconductors show predominantly hole-accumulation, or "*p*-type" behaviour.[99] Materials that can display stable "*n*-type" behaviour have been more difficult to achieve. A device that is able to operate in both *n*-channel and *p*-channel modes is termed "ambipolar". The charge mobility of electrons and holes in the semiconductor need to be of similar orders of magnitude to be of use in a device, with the maximum mobility of less importance. One of the main reasons that ambipolar characteristics may not translate into a device is that there are other factors than chemical structure that influence the accumulation and transport of charge, including processing methods, device

structure, electrode compositions and the nature of the gate dielectric.[99] It was discovered that significant electron trapping took place in devices that used SiO_2 as the gate dielectric due to the presence of reactive surface states as well as electron charge carriers reacting with atmospheric O_2 and H_2O.[100,101] For systems such as complementary circuits, OLEDs and some types of organic photovoltaics, semiconductors that can transport both electrons and holes are necessary. In OLEDs for example, the electrons and holes injected from the opposite electrodes need to have large and balanced mobilities so that they can recombine in the bulk to emit photons of light, and not recombine close to the electrode surfaces which would lead to electroluminescent quenching.[50]

The benefits of a single-component ambipolar semiconductor also include a more uniform thin film with fewer grain boundaries and a less complicated device fabrication.[98] Ambipolar behaviour has been reported in rubrene and other organic-based single crystal devices.[102] However the electron and hole mobilities are unbalanced in these materials, spanning two orders of magnitude due to the relatively wide band gap, leading to low-performance devices. Therefore metal complexes that can display a range of redox potentials with stable and readily-accessible anionic states are promising candidates for active materials in OFETs.[30] Through intelligent fine-tuning of electronic structure, there are currently examples of materials based on transition-metal complexes (detailed below) that have the potential to exhibit stable electron-mobility or a good balance between electron and hole mobilities for ambipolar behaviour in an OFET.

1.6.2 Non-innocent complexes

A number of metal-based compounds have now been investigated for use in OFETs. Molecules based on the macromolecules phthalocyanine and the porphyrins possessing a transition metal ion at the centre have and continue to be studied,[103] but much of the redox chemistry in these systems is largely ligand-based and not involving the metal centre.[31] A class of metal coordination compounds that have

shown promise are those based on late transition metals possessing aromatic chelating ligands, with some examples shown in **Figure 1.8**. These complexes have shown ambipolar behaviour in devices,[26,30,98] and despite the low values for the respective charge mobilities, these devices show good performance due to the balanced magnitude of the hole and electron mobilities.

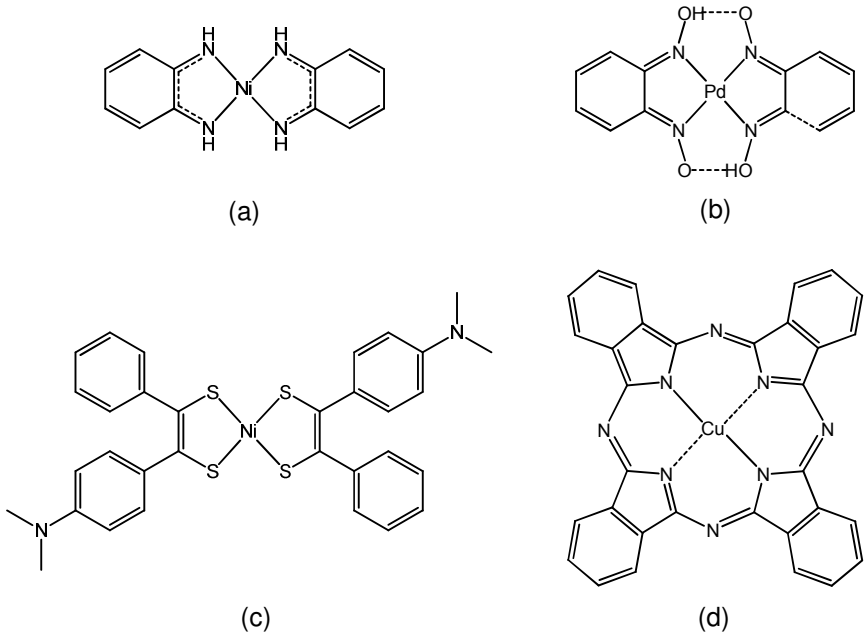

Figure 1.8. Metal complexes that have been used in FETs: (a) bis(*o*-diiminobenzo-semiquinonate) nickel;[29] (b) bis(benzoquinonedioximato) platinum;[32] (c) bis(4-dimethylaminodithiobenzyl) nickel;[26] (d) Copper phthalocyanine,[103] a well-known hole-conducting material.

1.7 References

(1) Schrauzer, G. N.; Mayweg, V. *Journal of the American Chemical Society* **1962**, *84*, 3221.

(2) Davison, A.; Edelstein, N.; Holm, R. H.; Maki, A. H. *Journal of the American Chemical Society* **1963**, *85*, 2029.

(3) Gray, H. B.; Williams, R.; Bernal, I.; Billig, E. *Journal of the American Chemical Society* **1962**, *84*, 3596.

(4) McCleverty, J. A. *Progress in Inorganic Chemistry* **1968**, *10*, 49.

(5) Pierpont, C. G. *Coordination Chemistry Reviews* **2001**, *216-217*, 99.

(6) Jørgensen, C. K. *Coordination Chemistry Reviews* **1966**, *1*, 164.

(7) Ray, K.; Weyhermuller, T.; Neese, F.; Wieghardt, K. *Inorganic Chemistry* **2005**, *44*, 5345.

(8) Lange, C. W.; Conklin, B. J.; Pierpont, C. G. *Inorganic Chemistry* **1994**, *33*, 1276.

(9) Lange, C. W.; Pierpont, C. G. *Inorganica Chimica Acta* **1997**, *263*, 219.

(10) Lynch, M. W.; Buchanan, R. M.; Pierpont, C. G.; Hendrickson, D. N. *Inorganic Chemistry* **1981**, *20*, 1038.

(11) Buchanan, R. M.; Fitzgerald, B. J.; Pierpont, C. G. *Inorganic Chemistry* **1979**, *18*, 3439.

(12) Lever, A. B. P.; Masui, H.; Metcalfe, R. A.; Stufkens, D. J.; Dodsworth, E. S.; Auburn, P. R. *Coordination Chemistry Reviews* **1993**, *125*, 317.

(13) Santana da Silva, R.; Gorelsky, S. I.; Dodsworth, E. S.; Tfouni, E.; Lever, A. B. P. *Journal of the Chemical Society, Dalton Transactions* **2000**, 4078.

(14) Razuvaev, G. A.; Teplova, I. A.; Shalnova, K. G.; Abakumov, G. A. *Journal of Organometallic Chemistry* **1978**, *157*, 353.

(15) Abakumov, G. A.; Cherkasov, V. K.; Bubnov, M. P.; Éllert, O. G.; Rakitin, Y. V.; Zakharov, L. N.; Struchkov, Y. T.; Saf'yanov, Y. N. *Russian Chemical Bulletin* **1992**, *41*, 1813.

(16) Chaudhuri, P.; Verani, C. N.; Bill, E.; Bothe, E.; Weyhermuller, T.; Wieghardt, K. *Journal of the American Chemical Society* **2001**, *123*, 2213.

(17) Chun, H.; Verani, C. N.; Chaudhuri, P.; Bothe, E.; Bill, E.; Weyhermuller, T.; Wieghardt, K. *Inorganic Chemistry* **2001**, *40*, 4157.

(18) Herebian, D.; Bothe, E.; Bill, E.; Weyhermuller, T.; Wieghardt, K. *Journal of the American Chemical Society* **2001**, *123*, 10012.

(19) Bachler, V.; Olbrich, G.; Neese, F.; Wieghardt, K. *Inorganic Chemistry* **2002**, *41*, 4179.

(20) Herebian, D.; Wieghardt, K. E.; Neese, F. *Journal of the American Chemical Society* **2003**, *125*, 10997.

(21) Ray, K.; Petrenko, T.; Wieghardt, K.; Neese, F. *Dalton Transactions* **2007**, 1552.

(22) Cho, J.-Y.; Domercq, B.; Jones, S. C.; Yu, J.; Zhang, X.; An, Z.; Bishop, M.; Barlow, S.; Marder, S. R.; Kippelen, B. *Journal of Materials Chemistry* **2007**, *17*, 2642.

(23) Mueller-Westerhoff, U. T.; Vance, B.; Ihl Yoon, D. *Tetrahedron* **1991**, *47*, 909.

(24) Deplano, P.; Pilia, L.; Espa, D.; Mercuri, M. L.; Serpe, A. *Coordination Chemistry Reviews* **2010**, *254*, 1434.

(25) Curreli, S.; Deplano, P.; Faulmann, C.; Ienco, A.; Mealli, C.; Mercuri, M. L.; Pilia, L.; Pintus, G.; Serpe, A.; Trogu, E. F. *Inorganic Chemistry* **2004**, *43*, 5069.

(26) Anthopoulos, T. D.; Setayesh, S.; Smits, E.; Cölle, M.; Cantatore, E.; de Boer, B.; Blom, P. W. M.; de Leeuw, D. M. *Advanced Materials* **2006**, *18*, 1900.

(27) Mueller-Westerhoff, U. T. In *Comprehensive Coordination Chemistry*; Wilkinson, G., Ed.; Pergamon Press: Oxford, 1987, p 595.

(28) Anthopoulos, T. D.; Anyfantis, G. C.; Papavassiliou, G. C.; de Leeuw, D. M. *Applied Physics Letters* **2007**, *90*, 122105.

(29) Noro, S.; Chang, H. C.; Takenobu, T.; Murayama, Y.; Kanbara, T.; Aoyama, T.; Sassa, T.; Wada, T.; Tanaka, D.; Kitagawa, S.; Iwasa, Y.; Akutagawa, T.; Nakamura, T. *Journal of the American Chemical Society* **2005**, *127*, 10012.

(30) Taguchi, T.; Wada, H.; Kambayashi, T.; Noda, B.; Goto, M.; Mori, T.; Ishikawa, K.; Takezoe, H. *Chemical Physics Letters* **2006**, *421*, 395.

(31) Cho, J. Y.; Domercq, B.; Jones, S. C.; Yu, J.; Zhang, X.; An, Z.; Bishop, M.; Barlow, S.; Marder, S. R.; Kippelen, B. *Journal of Materials Chemistry* **2007**, *17*, 2642.

(32) Sakai, K.-i.; Hasegawa, T.; Ichikawa, M.; Taniguchi, Y. *Chemistry Letters* **2006**, *35*, 302.

(33) Buchanan, R. M.; Wilsonblumenberg, C.; Trapp, C.; Larsen, S. K.; Greene, D. L.; Pierpont, C. G. *Inorganic Chemistry* **1986**, *25*, 3070.

(34) Pierpont, C. G.; Buchanan, R. M. *Coordination Chemistry Reviews* **1981**, *38*, 45.

(35) Pochettino, A. *Academy Lincei Rendus* **1906**, *15*, 355.

(36) Pope, M.; Swenberg, C. E. *Electronic Processes in Organic Crystals and Polymers, Second Edition*, 1999.

(37) Garnier, F.; Yassar, A.; Hajlaoui, R.; Horowitz, G.; Deloffre, F.; Servet, B.; Ries, S.; Alnot, P. *Journal of the American Chemical Society* **2002**, *115*, 8716.

(38) Shirota, Y.; Kageyama, H. *Chemical Reviews* **2007**, *107*, 953.

(39) Gorton, W. S. *Proceedings of the IEEE* **1998**, *86*, 50.

(40) Gutmann, F.; Lyons, L. E. *Organic Semiconductors*; Wiley: New York, 1967.

(41) Huitema, H. E. A. *Nature* **2001**, *414*, 599.

(42) Reese, C.; Bao, Z. N. *Materials Today* **2007**, *10*, 20.

(43) Gelinck, G. H.; Huitema, H. E. A.; Van Veenendaal, E.; Cantatore, E.; Schrijnemakers, L.; Van der Putten, J.; Geuns, T. C. T.; Beenhakkers, M.; Giesbers, J. B.; Huisman, B. H.; Meijer, E. J.; Benito, E. M.; Touwslager, F. J.; Marsman, A. W.; Van Rens, B. J. E.; De Leeuw, D. M. *Nature Materials* **2004**, *3*, 106.

(44) Dimitrakopoulos, C. D.; Brown, A. R.; Pomp, A. *Journal of Applied Physics* **1996**, *80*, 2501.

(45) Baude, P. F. *Applied Physics Letters* **2003**, *82*, 3964.

(46) Dimitrakopoulos, C. D.; Purushothaman, S.; Kymissis, J.; Callegari, A.; Shaw, J. M. *Science* **1999**, *283*, 822.

(47) Li, L.; Meller, G.; Kosina, H. *Journal of Applied Physics* **2007**, *101*, 033716.

(48) Sirringhaus, H. *Advanced Materials* **2005**, *17*, 2411.

(49) Troisi, A.; Orlandi, G. *The Journal of Physical Chemistry A* **2006**, *110*, 4065.

(50) Brédas, J. L.; Calbert, J. P.; da Silva Filho, D. A.; Cornil, J. *Proceedings of the National Academy of Sciences of the United States of America* **2002**, *99*, 5804.

(51) Kahng, D.; Atalla, M.; Bell Telephone Lab Inc: United States, 1960.

(52) Barbe, D. F.; Westgate, C. R. *Journal of Physics and Chemistry of Solids* **1970**, *31*, 2679.

(53) Ebisawa, F.; Kurokawa, T.; Nara, S. *Journal of Applied Physics* **1983**, *54*, 3255.

(54) Shur, M. *Physics of Semiconductor Devices*; Prentice-Hall: Englewood Cliffs, NJ, 1990.

(55) Bao, Z. N.; Rogers, J. A.; Katz, H. E. *Journal of Materials Chemistry* **1999**, *9*, 1895.

(56) Newman, C. R.; Frisbie, C. D.; da Silva, D. A.; Bredas, J. L.; Ewbank, P. C.; Mann, K. R. *Chemistry of Materials* **2004**, *16*, 4436.

(57) Jurchescu, O. D.; Baas, J.; Palstra, T. T. M. *Applied Physics Letters* **2004**, *84*, 3061.

(58) Melzer, C.; Seggern, H.; Grasser, T., Meller, G., Li, L., Eds.; Springer Berlin / Heidelberg: 2010; Vol. 223, p 189.

(59) Zaumseil, J.; Baldwin, K. W.; Rogers, J. A. *Journal of Applied Physics* **2003**, *93*, 6117.

(60) Facchetti, A. *Materials Today* **2007**, *10*, 28.

(61) Horowitz, G. *Advanced Materials* **1998**, *10*, 365.

(62) Horowitz, G. *Advanced Functional Materials* **2003**, *13*, 53.

(63) Reese, C.; Bao, Z. N. *Journal of Materials Chemistry* **2006**, *16*, 329.

(64) Briseno, A. L.; Mannsfeld, S. C. B.; Ling, M. M.; Liu, S. H.; Tseng, R. J.; Reese, C.; Roberts, M. E.; Yang, Y.; Wudl, F.; Bao, Z. N. *Nature* **2006**, *444*, 913.

(65) Briseno, A. L.; Tseng, R. J.; Ling, M. M.; Talcao, E. H. L.; Yang, Y.; Wudl, F.; Bao, Z. N. *Advanced Materials* **2006**, *18*, 2320.

(66) Butko, V. Y.; Chi, X.; Lang, D. V.; Ramirez, A. P. *Applied Physics Letters* **2003**, *83*, 4773.

(67) de Boer, R. W. I.; Gershenson, M. E.; Morpurgo, A. F.; Podzorov, V. *Physica Status Solidi A* **2004**, *201*, 1302.

(68) Mas-Torrent, M.; Durkut, M.; Hadley, P.; Ribas, X.; Rovira, C. *Journal of the American Chemical Society* **2004**, *126*, 984.

(69) Podzorov, V.; Sysoev, S. E.; Loginova, E.; Pudalov, V. M.; Gershenson, M. E. *Applied Physics Letters* **2003**, *83*, 3504.

(70) Roberson, L. B.; Kowalik, J.; Tolbert, L. M.; Kloc, C.; Zeis, R.; Chi, X. L.; Fleming, R.; Wilkins, C. *Journal of the American Chemical Society* **2005**, *127*, 3069.

(71) Podzorov, V.; Gershenson, M. E.; Kloc, C.; Zeis, R.; Bucher, E. *Applied Physics Letters* **2004**, *84*, 3301.

(72) Halik, M.; Klauk, H.; Zschieschang, U.; Schmid, G.; Radlik, W.; Ponomarenko, S.; Kirchmeyer, S.; Weber, W. *Journal of Applied Physics* **2003**, *93*, 2977.

(73) Murphy, A. R.; Frechet, J. M. J. *Chemical Reviews* **2007**, *107*, 1066.

(74) Gundlach, D. J.; Jia, L. L.; Jackson, T. N. *IEEE Electron Device Letters* **2001**, *22*, 571.

(75) Irimia-Vladu, M.; Marjanovic, N.; Vlad, A.; Ramil, A. M.; Hernandez-Sosa, G.; Schwoödiauer, R.; Bauer, S.; Sariciftci, N. S. *Advanced Materials* **2008**, *20*, 3887.

(76) Sirringhaus, H.; Brown, P. J.; Friend, R. H.; Nielsen, M. M.; Bechgaard, K.; Langeveld-Voss, B. M. W.; Spiering, A. J. H.; Janssen, R. A. J.; Meijer, E. W.; Herwig, P.; de Leeuw, D. M. *Nature* **1999**, *401*, 685.

(77) Handa, S.; Miyazaki, E.; Takimiya, K. *Chemical Communications* **2009**, 3919.

(78) Watanabe, M.; Chao, T.-H.; Liu, S.-W.; Chien, C.-T.; Chang, Y. J.; Yuan, C.-H.; Huang, K.-C.; Chien, S.-H.; Shinmyozu, T.; Chow, T. J. *Journal of Materials Chemistry* **2011**, *21*, 11317.

(79) Sonar, P.; Singh, S. P.; Williams, E. L.; Li, Y.; Soh, M. S.; Dodabalapur, A. *Journal of Materials Chemistry* **2012**.

(80) Eley, D. D. *Nature* **1948**, *162*, 819.

(81) Akamatu, H.; Inokuchi, H.; Matsunaga, Y. *Nature* **1954**, *173*, 168.

(82) McGinness, J.; Corry, P.; Proctor, P. *Science* **1974**, *183*, 853.

(83) Chiang, C. K.; Fincher, C. R.; Park, Y. W.; Heeger, A. J.; Shirakawa, H.; Louis, E. J.; Gau, S. C.; MacDiarmid, A. G. *Physical Review Letters* **1977**, *39*, 1098.

(84) Bolto, B. A.; McNeill, R.; Weiss, D. E. *Australian Journal of Chemistry* **1963**, *16*, 1090.

(85) Gundlach, D. J.; Klauk, H.; Sheraw, C. D.; Chung-Chen, K.; Jiunn-Ru, H.; Jackson, T. N. In *Electron Devices Meeting, 1999. IEDM Technical Digest. International* 1999, p 111.

(86) Ostroverkhova, O.; Cooke, D. G.; Hegmann, F. A.; Anthony, J. E.; Podzorov, V.; Gershenson, M. E.; Jurchescu, O. D.; Palstra, T. T. M. *Applied Physics Letters* **2006**, *88*, 162101.

(87) Mannsfeld, S. C. B.; Virkar, A.; Reese, C.; Toney, M. F.; Bao, Z. *Advanced Materials* **2009**, *21*, 2294.

(88) Tang, Q. X.; Li, H. X.; Liu, Y. L.; Hu, W. P. *Journal of the American Chemical Society* **2006**, *128*, 14634.

(89) Kelley, T. W.; Baude, P. F.; Gerlach, C.; Ender, D. E.; Muyres, D.; Haase, M. A.; Vogel, D. E.; Theiss, S. D. *Chemistry of Materials* **2004**, *16*, 4413.

(90) Lee, S.; Koo, B.; Shin, J.; Lee, E.; Park, H.; Kim, H. *Applied Physics Letters* **2006**, *88*, 162109.

(91) Heringdorf, F. J. M. Z.; Reuter, M. C.; Tromp, R. M. *Nature* **2001**, *412*, 517.

(92) Menard, E.; Podzorov, V.; Hur, S.-H.; Gaur, A.; Gershenson, M. E.; Rogers, J. A. *Advanced Materials* **2004**, *16*, 2097.

(93) Garnier, F.; Horowitz, G.; Fichou, D.; Yassar, A. *Synthetic Metals* **1996**, *81*, 163.

(94) Lovinger, A. J.; Davis, D. D.; Dodabalapur, A.; Katz, H. E. *Chemistry of Materials* **1996**, *8*, 2836.

(95) Ferraris, J.; Cowan, D. O.; Walatka, V.; Perlstein, J. H. *Journal of the American Chemical Society* **1973**, *95*, 948.

(96) Bendikov, M.; Wudl, F.; Perepichka, D. F. *Chemical Reviews* **2004**, *104*, 4891.

(97) Yamada, J.-i.; Akutsu, H.; Nishikawa, H.; Kikuchi, K. *Chemical Reviews* **2004**, *104*, 5057.

(98) Noro, S.; Takenobu, T.; Iwasa, Y.; Chang, H. C.; Kitagawa, S.; Akutagawa, T.; Nakamura, T. *Advanced Materials* **2008**, *20*, 3399.

(99) Zaumseil, J.; Sirringhaus, H. *Chemical Reviews* **2007**, *107*, 1296.

(100) Dimitrakopoulos, C. D.; Malenfant, P. R. L. *Advanced Materials* **2002**, *14*, 99.

(101) Chua, L.-L.; Zaumseil, J.; Chang, J.-F.; Ou, E. C. W.; Ho, P. K. H.; Sirringhaus, H.; Friend, R. H. *Nature* **2005**, *434*, 194.

(102) Takahashi, T.; Takenobu, T.; Takeya, J.; Iwasa, Y. *Applied Physics Letters* **2006**, *88*, 033505.

(103) Bao, Z.; Lovinger, A. J.; Dodabalapur, A. *Applied Physics Letters* **1996**, *69*, 3066.

2. Experimental techniques

2.1 Characterisation methods

Mass spectrometry experiments were carried out using an MS50 instrument, with a 3-NOBA matrix for the fast atom bombardment (FAB) experiments. Elemental analyses were performed by Mr. Stephen Boyer at London Metropolitan University or Donna McColl at St. Andrews University. Infrared spectroscopy measurements were performed on KBr disks on a JASCO FT/IR-410 spectrophotometer. ^{1}H-NMR and ^{13}C-NMR experiments were performed on either a Bruker 400 MHz or 500 MHz Fourier transform spectrometer. The electronic absorption spectra were recorded with a Jasco V-570 UV/Vis/NIR spectrophotometer running Spectra Manager software. Solution spectra were measured in a 1 cm path length quartz cell. Diffuse reflectance spectra were obtained using an integrating sphere attachment of the spectrophotometer, with samples prepared by dilution with barium sulfate ($BaSO_4$) powder. Thin film absorption measurements were recorded by placing the film normal to the incident beam, flush with the sample holder. Details of single crystal structure refinements are given in the experimental section of each chapter.

2.2 Electrochemistry

Potentiometry is a technique for measuring the potential of an electrochemical cell under conditions of no current flow. For a general reduction or oxidation (redox) reaction

$$a\mathrm{A} + n\mathrm{e}^{-} \Leftrightarrow b\mathrm{B}$$

The standard potential of the reaction is related to the concentration of the reactants (A) and products (B) at the electrode/solution interface according to the Nernst equation (**Equation 2.1**)

$$E = E^{0'} - \frac{2.303RT}{nF}\log\frac{[\mathrm{B}]^b}{[\mathrm{A}]^a} \qquad \textbf{Equation 2.1}$$

where E is the applied electrode potential, $E^{0'}$ is the formal potential, R is the universal gas constant (8.3145 J K^{-1} mol^{-1}), T is temperature, n is the number of moles of electrons involved in the reaction and F is the Faraday constant (96,485 C mol^{-1} of electrons). The notation $[B]^b/[A]^a$ represents the ratio of the concentrations of products to reactants raised to their stoichiometric powers, used in place of an activity term when the concentration is sufficiently low (< 0.1 mol dm^{-3}). Under standard conditions of temperature and pressure (298 K, 1 atmosphere), the Nernst equation can be written as

$$E = E^{0'} - \frac{0.0591}{n}\log\frac{[\mathrm{B}]^b}{[\mathrm{A}]^a} \qquad \textbf{Equation 2.2}$$

where the parameters have the same meanings. When the reaction kinetics of electron transfer at the electrode surface are sufficiently fast, the concentration of oxidised and reduced species is in equilibrium and reaction is said to be reversible in nature. The conditions that determine whether or not the Nernst equation is obeyed depend on the system being studied as well as the experimental conditions.

Voltammetry is a general term used to describe methods where the potential between two electrodes is varied, resulting in an observed current response that is dependent not only on the concentration of the redox species (the analyte) at the electrode surface being studied, but on the relative electrode potentials. The current generated is a result of electron transfer between the redox species and the electrode in a heterogeneous process, and is carried through the solution by the migration of ions. This process forms an electrical double layer at the surface of the electrode.

This layer is composed of ions and orientated electric dipoles that serve to counteract the charge on the electrode, and acts like a capacitor of charge. The formation of this double layer is complex and not detailed in this thesis, but its presence is acknowledged for the influence it has on the electrochemical studies.

The measured current at the working electrode is dependent upon a combination of Faraday's law and Fick's first law of diffusion:

$$i_{\mathrm{d}} = nFAD_0\left(\frac{\partial C_0}{\partial x}\right)_0 \qquad \textbf{Equation 2.3}$$

where i_{d} is the diffusion-limited current, n is the number of electrons, F is Faraday's constant, A is the electrode area, D_0 is the diffusion coefficient of the analyte and $(\partial C_0/\partial x)_0$ is concentration gradient at the electrode surface. The product $D_0(\partial C_0/\partial x)_0$ is equivalent to the flux (mol cm^{-2} s^{-1}) of analyte to the electrode surface. Therefore, the current is directly proportional to the concentration of analyte and its diffusion across the concentration gradient at the electrode surface. A greater concentration gradient leads to greater diffusion and a higher current, so to observe Nernstian behaviour, the diffusion layer must be sufficiently thin. To the solution of analyte is added a large molar excess of inert ions. The purpose of this supporting electrolyte is to provide ionic strength to the solution, which decreases the thickness of the double layer and ensures a potential drop to within nanometres (nm) of the working electrode surface. This in turn ensures that the electric field is uniform and close to zero throughout the bulk solution, allowing the current response at the electrode surface to be well-defined (*vide infra*).[1]

Two methods of voltammetric analysis were used during this PhD; the swept method of cyclic voltammetry (CV) and the stepped method of differential pulse voltammetry (DPV), which are described below.

2.2.1 Cyclic voltammetry (CV)

Cyclic voltammetry is a useful technique in quickly determining information about the thermodynamics of redox processes and the kinetics of electronic-transfer reactions. The experiment involves linearly scanning the potential of the working electrode and measuring the resulting current response. The process is termed cyclic because the potential can be swept between two predefined values (switching potentials) multiple times during a scan. The resulting plot is called a cyclic voltammogram, an example of which is displayed in **Figure 2.1** for the oxidation of ferrocene to ferrocenium (Fc/Fc^+). Ferrocene is an organometallic complex that is often used as an internal reference standard due to its facile and stable one-electron redox process and its relatively inert nature.

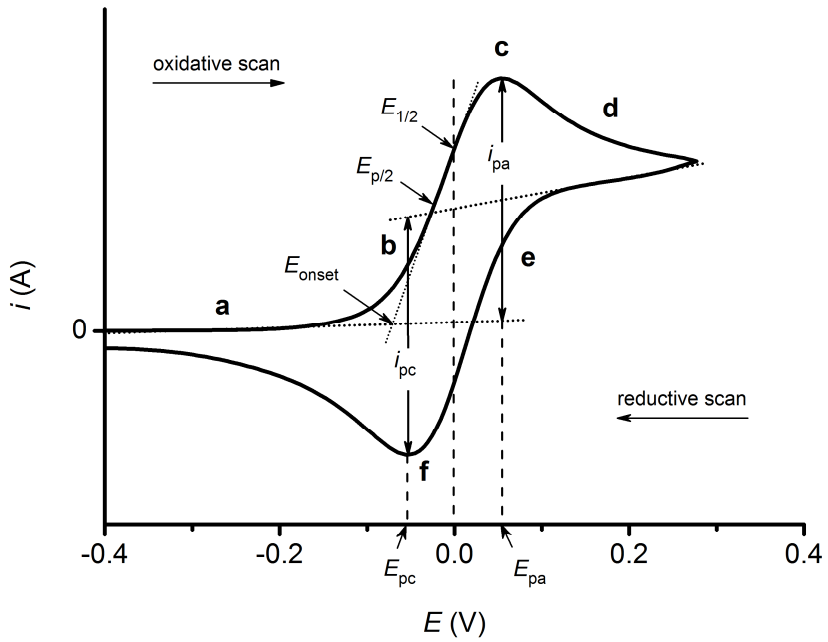

Figure 2.1. Schematic of a typical cyclic voltammogram for an electrochemically-reversible one-electron redox process. This example is of the oxidation of ferrocene with the potentials referenced *vs.* the ferrocene/ferrocenium (Fc/Fc^+) redox couple.

Initially during the oxidative scan (to positive potentials) the potential is not sufficient to oxidise Fc to Fc^+ (**Figure 2.1**, **a**). As the potential becomes more positive and the onset (E_{onset}) of oxidation is reached, the current starts to exponentially increase (**b**) as Fc is being oxidised at the working electrode surface.

As the current linearly increases with potential the process is under electrochemical control, dependent upon the concentration gradient of Fc near the electrode surface within the diffusion layer. As the analyte is depleted and the diffusion layer grows the current reaches peak maximum (anodic peak (i_{pa}) for oxidation at the anodic peak potential (E_{pa}) point **c**. The process is under mixed control at this point, with a balance between further increases in current due to the increasing reaction rate, and decreasing flux of analyte to the electrode surface from further and further distances. After this point the current becomes limited by the mass transport of molecules of analyte from the bulk to the diffuse layer interface, which is slow on the electrochemical timescale and therefore does not satisfy the Nernst equation. This results in a decrease in current (**d**) as the potentials are scanned more positive until a steady-state is reached where further increases in potential no longer has an effect.

Scan reversal to negative potentials (reductive scan) continues to oxidise Fc to Fc^+ until the applied potential reaches the point where the Fc^+ accumulated at the electrode surface can re-reduce to Fc (**e**). The process for re-reduction follows that for the initial oxidation, only with an opposite scan direction and a cathodic peak (i_{pc}) at the cathodic peak potential (E_{pc}) (**f**). The anodic and cathodic peak currents should be of equal magnitude but opposite sign provided the process is reversible (*vide infra*). The peak current, i_p, of the reversible redox process is described by the Randles-Sevcik equation,[2] which at 298 K is:

$$i_p = (2.69 \times 10^5) n^{3/2} A C D^{1/2} v^{1/2} \qquad \textbf{Equation 2.4}$$

where n is the number of electrons, A the electrode area (cm^2), C the concentration (mol cm^{-3}), D the diffusion coefficient (cm^2 s^{-1}), and v the potential scan rate (V s^{-1}). An important result of this equation is that the peak current, i_p, is directly proportional to the concentration of analyte and the square root of the scan rate, $v^{1/2}$ for an electrochemically-reversible process. Further tests with which to validate the reversibility of a redox process are shown in **Table 2.1**. It should be noted that all of these conditions need to be met in order to fully qualify reversibility.

Table 2.1. Characteristics of electrochemical reversibility of a redox process.[3]

- Peak-to-peak potential separation, $\Delta E = |E_{pa} - E_{pc}| \approx 59/n$ mV
- Anodic-to-cathodic peak ratio, $|i_{pa}/i_{pc}| = 1$
- $i_p \propto v^{1/2}$
- E_p is independent of v

The current peaks are experimentally measured from the peak position vertically to the intercept with an extrapolated baseline of the background current that precedes the onset of the redox process, as shown in **Figure 2.1**. Also included in the figure is the mid-peak potential, $E_{1/2}$, which is determined by the following equation:

$$E_{1/2} = (E_{pa} + E_{pc}) / 2 \qquad \textbf{Equation 2.5}$$

$E_{1/2}$ is closely-related to the formal potential, E^0, but is often used instead to define all of the electrochemical processes in the voltammogram. This is because the formal potential can only be accurately defined when a redox process is truly electrochemically reversible.

When the electron transfer rate at the electrode surface is slow in comparison to the rate of mass transport, the cyclic voltammogram shape is altered and electrochemical irreversibility is exhibited. This is characterised by smaller peak height, a wider peak-to-peak separation and a shift in peak potential with scan rate. A quasi-reversible system is defined as having an electron-transfer rate that is comparable in magnitude to the rate of mass transport. By reducing the scan rate one can switch from an irreversible to reversible system. Completely irreversible systems are characterised by a complete absence of a reverse peak in the CV due to an irreversible electron transfer process that may be caused by a slow reaction rate, a geometry change or a proceeding chemical reaction involving the charged species. Full explanations of the equations and conditions that govern irreversibility can be

found in the literature, but only qualitative descriptions are needed here for the reader to interpret the voltammograms described later in this thesis.

In cases where a return peak of a redox process is not observed, too weak or not assignable, it may be convenient to define the $E_{1/2}$ relative to the half-peak potential, $E_{p/2}$:

$$E_{1/2}^{ox/red} = (E_p + E_{p/2}) / 2 \quad \textbf{Equation 2.6}$$

$$\Delta E_{p/2} = |E_p - E_{p/2}| = 56.5/n \text{ (mV)} \quad \textbf{Equation 2.7}$$

where $E_{p/2}$ is defined as the potential at half-peak current (**Figure 2.1**). In the discussion of CV of irreversible redox processes, it is this definition of $E_{1/2}$ that is used.

2.2.2 Differential pulse voltammetry

Different pulse voltammetry is a pulsed technique that has enhanced sensitivity as compared with cyclic voltammetry. The potential is stepped between two values in a pulsed manner, with each fixed, short pulse superimposed on a slowly-swept base potential. A profile of this potential versus time waveform is shown in **Figure 2.2**. The current is measure twice during a single pulse: once just before the application of a pulse (τ') and once at the end of a pulse (τ). The difference between the current values is plotted against the base potential giving a voltammogram that displays redox processes with a characteristic peak shape. This process allows the faradaic current to be measured by allowing for the decay of the double layer charging current. Characteristic information obtainable from a DPV experiment include the $E_{1/2}$ value, which is equivalent to E_p in DPV when scanning from zero to more oxidising or reducing potentials.

The peak-to-peak separation in DP for a reversible redox process should be zero. For electrochemically-irreversible processes, the return peak will be shifted to

more extreme potentials (e.g. more oxidative potentials for an oxidative scan), with a smaller and broader peak current. Due to the sensitivity of DPV, redox processes may be observed that were not observed with swept techniques such as CV. Processes regarded as irreversible during CV may be observed to display quasi- or fully-electrochemically-reversible behaviour in DPV.

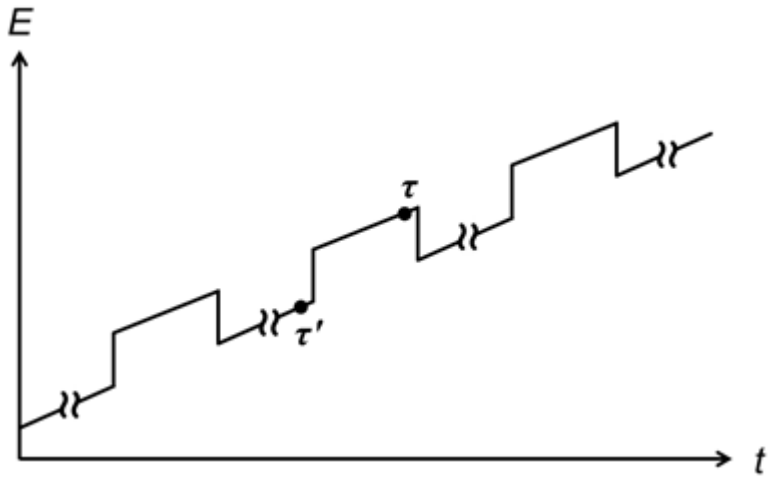

Figure 2.2. Potential-time waveform for DPV.

2.2.3 Relationship to material properties

The information gained from CV and DPV can yield important information about the location and energy of the frontier molecular orbitals. In general, the first oxidation process takes place from the HOMO and the first reduction from the LUMO. From CV, the energy of these respective orbitals can be estimated from the potential of the first redox processes ($E_{1/2}$), or in DP from the first peak potentials (E_p). From these measurements, the HOMO-LUMO gap (E_{gap}) can be calculated:

$$E_{\text{gap}} = |E_{\text{HOMO}} - E_{\text{LUMO}}| = |E_{1/2}^{ox} - E_{1/2}^{red}| \quad \text{(CV)} \qquad \textbf{Equation 2.8}$$

$$E_{\text{gap}} = |E_{\text{HOMO}} - E_{\text{LUMO}}| = |E_{pa} - E_{pc}| \quad \text{(DP)} \qquad \textbf{Equation 2.9}$$

which is measured in units of electron Volts (eV). The electron volt is defined as the energy gained by the charge of a single electron that is moved across a potential

difference of one volt (V). It is a commonly used unit of measurement for energy gaps because it is a linear scale (therefore directly comparable to V) that is comparable to the values obtained using other methods. The values of E_{gap}, E_{HOMO} and E_{LUMO} can provide a qualitative estimate of the respective energy levels in the solid state. On the other hand, comparisons of the kinetic stability of charged species in the solid state and in solution should be done with caution, because electron-transfer processes in the solid state are many orders of magnitude faster than the scan rates used in CV.

2.2.4 Experimental setup

In the standard 3-electrode cell, the roles of referencing the potentials applied and balancing the current produced are split between three electrodes; potential difference is applied between the working electrode (WE) and reference electrode (RE), and the current is passed between the working and counter electrodes (CE). To control the application of the potential difference, the potential of the working electrode is varied whilst the potential of the reference is kept at constant, defined value. The fixed potential of the reference electrode is created by a well-defined electrochemical reaction involving an excess of reagents. Meanwhile, the current passed at the working electrode is balanced by that at the counter electrode, which is designed to have a large surface area in order to ensure that current is only passed between the working and counter electrodes. The 3-electrode cell was constructed using customised glassware with fittings designed to accommodate the multiple electrodes and gas-flow adapters (**Figure 2.3**).

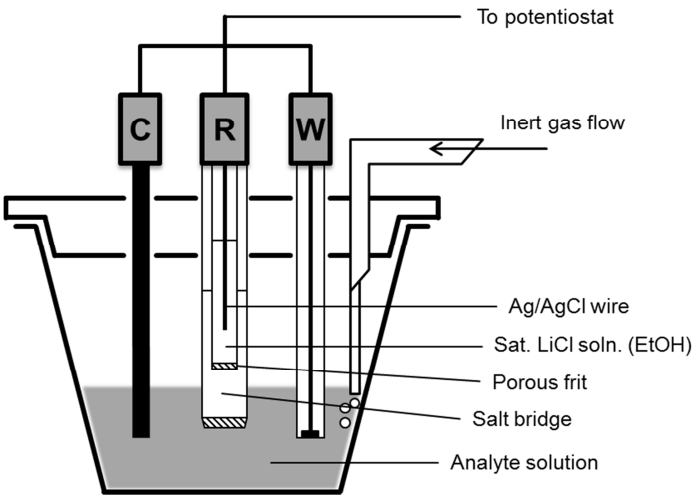

Figure 2.3. Three-electrode electrochemical cell setup.

2.2.5 Experimental parameters

Electrochemical experiments were performed with a standard three-electrode configuration with a μAutolab PGSTAT 30 Type III potentiostat with GPES 4.8 software. Pt working and counter electrodes were used, with the working electrode polished before each experiment. Two different working electrodes were used depending on the experiment: for better signal-to-noise ratio, a large-area Pt working electrode with a disk of surface area of *ca.* 3 mm^2 was used to allow a high current to pass; for scan rate studies, the working electrode was homemade, constructed from a 0.5 mm diameter platinum wire sealed in a glass capillary connected to a Cu electrode. In both cases the surface was polished between experiments. The reference electrode was a double-junction cell of Ag/AgCl. This consists of a Ag wire coated in AgCl in a glass tube surrounded by saturated LiCl in EtOH solution. This forms the inner element, which is connected to an outer solution of supporting electrolyte via a porous frit. This outer solution forms a "salt bridge" that is in contact with the analytical solution via a second porous frit. Tetrabutylammonium tetrafluoroborate ($TBABF_4$), used as a supporting electrolyte, was prepared from tetrafluoroboric acid and tetrabutyl ammonium hydroxide. The solid electrolyte was recrystallised from hot methanol before the addition of diethyl ether and cooled in a freezer to yield large crystals. The reference electrode was calibrated by the addition of ferrocene at

the end of the experiments, to allow for the use of the ferrocenium/ferrocene redox couple as an internal potential reference. All solutions were degassed with nitrogen for 15 minutes before experimental analysis.

Due to the sensitivity of most voltammetric techniques the presence of even tiny quantities of electroactive impurities can be detected, therefore clean glassware, pure and dry solvents and polished electrodes are needed. Removing dissolved oxygen (O_2) is also necessary if negative potentials will be applied. O_2 will be reduced at relatively modest negative potentials (around -0.33 *vs*. Ag/AgCl). Not only will this result in a rogue cathodic peak in the voltammogram, but it results in the formation of radical species that can subsequently react with the analyte. Dissolved oxygen can be removed by bubbling an inert gas such as nitrogen (N_2) through the solution prior to analysis in a process commonly known as degassing. During the experiment, a positive pressure of the inert gas is kept above the solution to prevent oxygen redissolving.

2.3 SQUID magnetometry

Magnetic measurements in this thesis were performed using a superconducting quantum interference device (SQUID). This is an extremely sensitive device that can accurately detect the magnetic moment of a sample by the small perturbations to the current flowing through its superconducting detection coils as the sample is moved through it. The SQUID itself is a closed, superconducting loop circuit that is housed within a large superconducting magnet. The role of the superconducting magnetic is to generate the magnetic fields necessary to induce uniform magnetisation of the sample, which is required to induce the currents in the detection coils as well as studying the magnetic field effect on the magnetic ordering.

The magnetic measurements described in this thesis are defined using the Gaussian “cgs” (centrimeter-gram-second) system opposed to the International

System of Units (SI), as they are the most common observed in the literature. The magnetic field applied by the external superconducting magnetic, *H*, is related to the magnetic induction (or net field), *B*, by the sample magnetisation, *M*, in the following equation

$$B = 4\pi H + M \qquad \textbf{Equation 2.10}$$

B has units of G (gauss) in cgs units, and is a response to the *M* of a material as the sample is moved through the SQUID pickup coils. *M* is the total sum of all the magnetic moments in a sample and is measured in units of emu (electromagnetic units). It is often more convenient to represent the magnetic moment with respect to relevant parameters such as the volume, mass or number of moles of a sample. When considering the molar magnetisation, the direct relationship between *M* and *H* is

$$M = \chi_m H \qquad \textbf{Equation 2.11}$$

where χ_m is the molar magnetic susceptibility with units of emu mol^{-1}. Compounds with a positive value of χ_m are called "paramagnetic", where the unpaired electrons are present in a randomly-orientated fashion. Compounds with a negative value of χ_m are called "diamagnetic" and possess no unpaired electrons. Therefore paramagnetic materials are attracted to an externally-applied magnetic field, whereas diamagnetic ones repel the magnetic field. At low temperatures, paramagnetic materials can undergo phase transitions where the magnetic moments align in a cooperative fashion.[4] In this thesis, the magnetic behaviour of materials is examined by studying how the magnetisation (or specifically the magnetic susceptibility) changes as a function of temperature at a fixed value of *H*.

2.3.1 Paramagnetism

The most basic form of paramagnetism is that of a Curie-type paramagnet, which consists of a system with random and non-interacting magnetic moments

$$\chi = C/T \qquad \textbf{Equation 2.12}$$

C is the Curie constant that contains a relationship to the magnetic moment. A plot of $1/\chi$ *vs*. *T* will give a straight line of gradient *C* that intercepts at the origin: at high *T* the magnetic moments are randomly orientated with respect to the applied field due to thermal energy. As *T* approaches zero, the moments will align parallel with the field, resulting in a χ that approaches infinity.

Temperature also has influence on interactions that may exist between magnetic moments on different atoms, as described by the Curie-Weiss Law

$$\chi = C/(T - \theta) \qquad \textbf{Equation 2.13}$$

where θ is Curie-Weiss temperature (commonly referred to as the Weiss Constant), which is related to the magnetic moment interactions: interactions where the moments are aligned in the same direction are termed "ferromagnetic" with $\theta > 0$; interactions where the moments are aligned anti-parallel to each other are termed "antiferromagnetic" with $\theta < 0$. The antiferromagnetic interactions are of particular relevance to the compounds studied in this thesis, and are described in greater detail in Chapter 3 (**Section 3.2.8**).

A final form of paramagnetism that is of relevance to this thesis is the Van Vleck paramagnetism, which is related to the population of low-lying magnetic orbitals by thermal excitations. This temperature-independent paramagnetism (*TIP*) is relatively small, but often needs to be accounted for during interpretation of magnetic data for certain systems.

2.3.2 Diamagnetism

Diamagnetism exists in all atoms and molecules, including those that possess unpaired electrons. Therefore the total measured magnetic susceptibility, χ_{meas}, is a combination of both the diamagnetic (χ_d) and paramagnetic susceptibilities (χ_p)

$$\chi_{meas} = \chi_d + \chi_p \qquad \textbf{Equation 2.14}$$

Therefore the total diamagnetic susceptibility needs to be subtracted from the experimentally measured values of χ to determine the true paramagnetic susceptibility of a sample. The diamagnetism of atoms and specific bonding types can be accounted from experimentally-derived corrections known as Pascal's constants.[5]

2.3.3 Experimental parameters

Variable-temperature direct current (DC) magnetic susceptibility measurements were recorded down to 1.8 K on a Quantum Design MPMS-XL SQUID magnetometer equipped with a 7 Tesla (T) DC magnet, equipped with MPMS MultiVu Application software for data processing. Powder samples of approximately 10 to 20 mg were placed inside gelatine capsules that were mounted inside the centre of plastic drinking straws. Experiments were carried out at a DC field of 0.1 T and a temperature range of 1.8 to 300 K. Corrections were applied to the measured magnetic susceptibility data to correct for diamagnetism using Pascal's constants,[5] and for a temperature-independent paramagnetism (*TIP*) of Cu(II).[6]

2.4 Computational methods

The basis for most computational chemistry calculations used today is quantum mechanics. The mathematical models allow for the calculation of a range of molecular properties such as molecular geometry, the energy of molecular orbitals

and the origin of spectroscopic transitions. It is necessary to use high-performance computers to perform these calculations, and still the time required to solve these calculations is often excessive. To meet this challenge, approximations have been developed to simplify the mathematical models as much as possible, efficient computational methods have been designed to save time and computational resources. It is important to understand the origins and limits of computational models to ensure the data extracted from their experiments are meaningful. A brief description of the computational theory used to interpret the results in this thesis is given, and more detailed explanations can be found elsewhere.[7]

The basis of all quantum mechanical (QM) calculations is finding a solution to the time-independent Schrödinger equation

$$\hat{H}\Psi = E\Psi \qquad \textbf{Equation 2.15}$$

where Ψ is the wavefunction, E is the energy and $\hat{H}$ is the Hamiltonian operator. A Ψ is a combination of mathematical functions that describes the position of an electron. the $\hat{H}$ is a mathematical operation that contains all the potential and kinetic energy terms that operates on the wavefunction in order to generate the energy of a given electron. The time-independent Schrödinger equation relies on the description of wavefunctions as stationary states, or orbitals, with every orbital described by a separate Ψ. A common way to construct the wavefunction is to reproduce the atomic radial distribution function (ARDF), which describes how the density of a given atomic orbital varies with distance from the nucleus. Because these RDFs are approximately Gaussian in shape, they can be reproduced by summing a series of Gaussian functions together with varying exponents and weighting applied. The collection of these functions that describes the position of electrons in the system is termed the "basis set", which is detailed below. The functions that best describe the Ψ will result in a minimum energy of the system.

2.4.1 Density functional theory

Density function theory (DFT) is a computational method of solving the Schrödinger equation by using electron density, originally formulated by Hohenberg and Kohn.[8] It defines the ground-state energy as the global minimum of a single universal functional for energy that is based on using the electron density. This is a massive simplification in computational complexity that models the energy remarkably accurately, which has led to the popularity of this method especially for large systems of many atoms. Due to the nature of the calculation however, crucial quantum mechanical interactions are not accounted for, and approximations are needed. The Pauli Exclusion Principle (PEP) dictates that two particles cannot exist in exactly the same quantum state. This results in an exchange interaction in the QM calculations that prevents electrons of the same spin occupying the same space at the same time, resulting in an effective repulsion between electrons with parallel spins. The correlation interaction is the result of the coulombic repulsion that exists between electrons, where their motion of one electron is correlated with the motion of all the others in the system.

2.4.2 Level of theory

In this thesis, hybrid DFT functionals were used that include a component of the exact electron exchange energy as calculated using the *ab initio* method of Hartree-Fock (HF) theory. There are many functionals that exist that have been created to model specific systems by altering the proportion of HF and DFT contributions. In general, it is best practice to employ functionals that have been trained on a set of molecules similar to those that you are trying to investigate. It was found that the B3LYP set of functionals, using the Becke 3-parameter exchange functional[9] and the Lee, Yang and Parr correlation functional,[10] which is known to produce descriptions of reaction profiles for transition metal-containing compounds, proved to be satisfactory for the molecules investigated in this thesis.

There are many basis sets in existence, and the type and number of functions used within them are important factors when running a calculation. Large basis sets may give a more accurate description of your system but are more computationally expensive. A balance is often reached where the molecular description is sufficiently accurate given the computational cost. Split-valence basis sets are almost universally used, where the valence electrons are treated separately from the core electrons. The core electrons can be modelled with less accuracy because they have little influence on the observed molecular properties of a system, whilst the valence orbitals are described by more functions to give better flexibility. Pseudopotentials can be used to replace the core electrons completely with a single function, and are often used when large atoms are present. This greatly reduces the computational cost without negatively affecting the result. In this thesis the basis set 6–31G(d,p) was used to describe all non-metal and non-heavy atoms of the systems studied. The hyphen '–' indicates that a split-valence description is used. 6 contracted functions are used to describe the core electrons, 3 to describe the inner valence orbitals and 1 to describe the outer valence orbitals. The term '(d,p)' indicates the presence of polarisation functions, which are orbital descriptions with higher angular momentum to better model the position of the electrons. This is important for systems where the atoms are interacting with larger atoms such as transition metals, which can polarise the interacting valence orbitals.

2.4.3 Calculated properties

2.4.3.1 Geometry optimisation

Geometry optimisation is a method whereby the positions of atoms in molecules are iteratively adjusted until a stationary point on the potential energy surface (PES) is reached. This method makes use of the Born-Oppenheimer (B-O) approximation, where the nuclei are considered to be approximately stationary with respect to the fast movement of electrons. The energy of an input molecular geometry is calculated by optimising the basis set. The forces on all atoms are then

calculated to determine the gradient of energy with respect to their position. The B-O approximation is temporarily lifted and atoms are moved along this gradient to a potentially lower energy configuration and the energy is calculated for this new geometry as before. If the new geometry is of a lower energy, the calculation is continued. If a stationary point is reached, the calculation is stopped.

It should be noted that the stationary point which is reached may not be the global minimum of the system, and may in fact be a local minimum or saddle point on the PES. This is confirmed by the use of a frequency calculation, which computes the force constants of the system. A minimum is indicated by the absence of any negative frequencies. To determine whether the local minimum is a global minimum, the calculated geometry should be converged upon by using one of several different starting geometries. It may be the case that the PES is very flat around the minimum as well, and therefore its exact location is difficult to pinpoint. In these instances negative frequencies may be found that are very small (< 10 cm^{-1}), arising often from rotations of peripheral groups in the molecule. When the magnitude of the force is this weak, it is safe to proceed with further analysis of the molecular properties.

Generally geometry optimisations are initially performed with single molecules in the gas phase. To compare the calculation more accurately with experiment results, the geometry can be optimised in the presence of a solvent. In this thesis the polarisable continuum model (PCM) was used to model the solvent. The PCM describes a sphere of solvent around the molecule with a given density and dielectric field. The PCM therefore does not model any potential dipolar interactions of the solvent with the molecule being optimised, which can be problematic for structures with strong dipole moments and optimisations with polar or hydrogen-bonding solvents.[11]

2.4.3.2 Time-dependent DFT (TD-DFT)

By observing how the solvent-optimised ground-state wavefunctions vary with time in response to an oscillating electromagnetic field, the electronic transitions in the system can be modelled. This is referred to as time-dependent DFT (TD-DFT), and is useful for predicting the appearance and origins of the electronic absorption peaks that are observed experimentally in the electronic absorption spectrum. The percentage contribution of molecular orbitals is given for each calculated electronic transition, which can be qualitatively compared with the experimental data. As with the PCM geometry optimisations, the single-point TD-DFT calculations have associated problems in the treatment of the solvent molecules. For molecules that possess a strong dipole moment and exhibit charge-transfer absorptions in the electronic spectra, the electronic distribution in the molecule changes significantly on the absorption of a photon of electromagnetic radiation. The quantitative energy of the calculated transitions therefore may be significantly different from the values obtained experimentally. Nevertheless, qualitative information about the origin of the transitions can still be gained as well as qualifying trends exhibited within a series of compounds.

2.4.4 Computational details

All calculations were carried out using the GAUSSIAN 09 package,[12] using resources provided by the EaStCHEM Research Computing Facility. Single-molecule gas-phase calculations were used to determine the ground state molecular geometry and to calculate the frontier orbitals. The B3LYP[9,10] hybrid DFT functional and the 6-31G(d,p) basis set were used for all atoms apart from the metal atoms and Br, which used the LANL2DZ[13-15] pseudopotentials to model core electrons. Unrestricted calculations were carried out for the Cu(II) compounds. Geometry optimisations generated the expected square-planar geometry for all compounds. Initial geometries were generated using Arguslab software [16] or taken from the single-crystal structures. Frequency calculations were run on all optimised structures to ensure they represented the global minimum energy geometry. Isosurfaces of the

molecule orbitals were generated using the GAUSSIAN 09 cubegen utility and Arguslab software to generate the images that were subsequently rendered using POV-RAY.[17] Simulated absorption spectra calculated from TD-DFT were generated using GaussSum 2.2 software[18] by a convolution of the energy of the calculated transitions.

2.5 FET structure

For electrical characterisation, the FET substrates were of the bottom-contact, bottom gate (BCBG) configuration. The gate electrode is *n*-doped silicon, which is separated from the source-drain (S-D) electrodes by a 300 nm layer of thermally-grown silicon dioxide (SiO_2) that acts as the gate dielectric. The interdigitated S-D electrodes composed of either gold or platinum were deposited by standard photolithographic techniques at S-D distances of 2, 5, 10, 20 and 50 μm. A 10 nm adhesion layer of titanium was used prior to gold electrode deposition to improve the strength of the contact to the substrate.

2.6 Thin-film processing

Details of vacuum sublimation are given in the experimental section of Chapter 3, and details of vacuum depositions onto FET substrates are presented in Chapter 5. Details of solution processing methods that have been attempted are also given in the relevant chapters (4 and 5).

2.6.1 Surface modifications

The use of substances that alter the surface of the device substrate before deposition of the semiconducting layer have become a popular method of improving

device performance.[19] In particular, organosilanes (with the general formula of $RSiX_3$ for the precursor, where X = Cl, OMe or OEt and R = alkyl group) have been shown to passivate the SiO_2 dielectric layer of FETs, with the potential to not only improve performance by reducing charge trap sites on the dielectric but also to improve film morphology.[20] These precursors react to form a self-assembled monolayer (SAM) of siloxanes on the surface by reacting with the silanol (Si-OH) groups on the surface of SiO_2. These reactions happen readily due to the driving force of forming very strong Si-O bonds. Organosilanes implemented in this work include hexamethyldisilane (HMDS), which possesses short, bulky alkyl chains, and octyltrichlorosilane (OTS), where each Si atom is bonded to a long, octyl chain. The details of the surface functionalisation are given in the experimental section Chapter 4 and 5.

2.7 References

(1) Dickinson, E. J. F.; Limon-Petersen, J. G.; Rees, N. V.; Compton, R. G. *The Journal of Physical Chemistry C* **2009**, *113*, 11157.

(2) Sevćik, A. *Collection of Czechoslovak Chemical Communications* **1958**, *13*, 349.

(3) *Instrumental methods in electrochemistry*; Kemp, T. J., Ed.; Ellis Horwood Limited, 1985.

(4) Likhtenshtein, G. I.; Yamauchi, J.; Nakatsuji, S. i.; Smirnov, A. I.; Tamura, R. In *Nitroxides*; Wiley-VCH Verlag GmbH & Co. KGaA: 2008, p 1.

(5) Bain, G. A.; Berry, J. F. *Journal of Chemical Education* **2008**, *85*, 532.

(6) Grove, H.; Julve, M.; Lloret, F.; Kruger, P. E.; Törnroos, K. W.; Sletten, J. *Inorganica Chimica Acta* **2001**, *325*, 115.

(7) Atkins, P.; Friedman, R. *Molecular quantum mechanics*; Oxford University Press: Oxford, 2005.

(8) Hohenberg, P.; Kohn, W. *Physical Review* **1964**, *136*, B864.

(9) Becke, A. D. *The Journal of Chemical Physics* **1993**, *98*, 1372.

(10) Lee, C.; Yang, W.; Parr, R. G. *Physical Review B* **1988**, *37*, 785.

(11) Magyar, R. J.; Tretiak, S. *Journal of Chemical Theory and Computation* **2007**, *3*, 976.

(12) Frisch, M. J.; Trucks, G. W.; Schlegel, H. B.; Scuseria, G. E.; Robb, M. A.; Cheeseman, J. R.; Scalmani, G.; Barone, V.; Mennucci, B.; Petersson, G. A.; Nakatsuji, H.; Caricato, M.; Li, X.; Hratchian, H. P.; Izmaylov, A. F.; Bloino, J.; Zheng, G.; Sonnenberg, J. L.; Hada, M.; Ehara, M.; Toyota, K.; Fukuda, R.; Hasegawa, J.; Ishida, M.; Nakajima, T.; Honda, Y.; Kitao, O.; Nakai, H.; Vreven, T.; Montgomery, J. A.; Peralta, J. E.; Ogliaro, F.; Bearpark, M.; Heyd, J. J.; Brothers, E.; Kudin, K. N.; Staroverov, V. N.; Kobayashi, R.; Normand, J.; Raghavachari, K.; Rendell, A.; Burant, J. C.; Iyengar, S. S.; Tomasi, J.; Cossi, M.; Rega, N.; Millam, J. M.; Klene, M.; Knox, J. E.; Cross, J. B.; Bakken, V.; Adamo, C.; Jaramillo, J.; Gomperts, R.; Stratmann, R. E.; Yazyev, O.; Austin, A. J.; Cammi, R.; Pomelli, C.; Ochterski, J. W.; Martin, R. L.; Morokuma, K.; Zakrzewski, V. G.; Voth, G. A.; Salvador, P.; Dannenberg, J. J.; Dapprich, S.; Daniels, A. D.; Farkas; Foresman, J. B.; Ortiz, J. V.; Cioslowski, J.; Fox, D. J. In *Gaussian 09, Revision B.01, Gaussian, Inc., Wallingford CT* Wallingford CT, 2009.

(13) Hay, P. J.; Wadt, W. R. *The Journal of Chemical Physics* **1985**, *82*, 270.

(14) Hay, P. J.; Wadt, W. R. *The Journal of Chemical Physics* **1985**, *82*, 299.

(15) Wadt, W. R.; Hay, P. J. *The Journal of Chemical Physics* **1985**, *82*, 284.

(16) Thompson, M. A.; 4.0.1 ed.; Planaria Software LLC: Seattle, WA.

(17) 3.6 ed.; Persistence of Vision Pty. Ltd.: Williamstown, Victoria, Austrailia, 2004.

(18) O'Boyle, N. M.; Tenderholt, A. L.; Langer, M. M. *Journal of Computational Chemistry* **2008**, *29*, 839.

(19) Gundlach, D. J.; Klauk, H.; Sheraw, C. D.; Chung-Chen, K.; Jiunn-Ru, H.; Jackson, T. N. In *Electron Devices Meeting, 1999. IEDM Technical Digest. International* 1999, p 111.

(20) DiBenedetto, S. A.; Facchetti, A.; Ratner, M. A.; Marks, T. J. *Advanced Materials* **2009**, *21*, 1407.

3. Square-planar catecholate complexes of copper and nickel

3.1 Introduction

Research on transition metal-based compounds as the active materials in electronic devices has been growing due to their potential advantages in comparison to purely organic materials, increased stability, stronger intermolecular interactions and a greater variation in the energy and location of the frontier orbitals.[1] Materials based on square-planar molecules of the late transition metals have been tested in FETs, with molecules that are based on conjugated, chelating ligands that can be non-innocent in nature when complexed to a metal.[2-5] For efficient charge transport in the solid state, good molecular order and strong intermolecular interaction is paramount. Generally, high purity, good molecular order and film reproducibility can be achieved via vapour deposition methods of small molecules.[6] Cu phthalocyanine (CuPc) is a well-known molecule that forms vapour-deposited materials with semiconducting properties.[7] The influence of paramagnetic species on charge transport can also be investigated using transition metal complexes, through the selection of paramagnetic transition metal ions and/or by the stabilisation of organic radical ligands.[3] In this context, the packing of neutral, planar transition-metal complexes to form magnetically-interacting molecular stacks becomes notably relevant.

This chapter includes molecular and structural investigations of a series of square-planar, heteroleptic Cu and Ni compounds that contain aromatic and chelating ligands based on catechol and a bidentate N,N'-donor ancillary ligand. Four catechol ligands have been investigated: catechol (cat), tetrachlorocatechol (Cl_4cat), 4,5-dibromocatechol (Br_2cat) and tetrabromocatechol (Br_4cat). The N-chelate ancillary ligand is either 2,2'-bipyridine (bpy) or 1,10-phenanthroline (phen) (**Chart 3.1**). This

family of M-diimine catechates has not been paid much attention in the literature, but merit investigation given their similarity to the diamino- and dithio-compounds that have been seen to display interesting electronic properties (**Section 1.6.2**). The varying degree and type of halogenation of the catecholates should provide insight into how changing the electronic properties of the compounds affect the material properties. The compounds have been formulated to be charge neutral to enable the possibility for the compounds to be vapour processed. Novel crystallisation techniques have yielded new crystal structures of these compounds, which allows detailed examination of the intermolecular interactions and observed magnetism.

Chart 3.1. Ligands and complexes presented in this chapter are highlighted in black.

	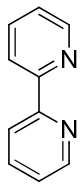 bpy	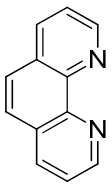 phen	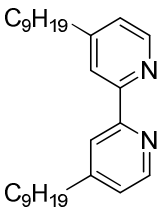 DNbpy	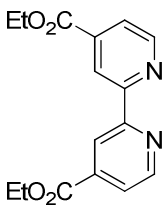 DECbpy
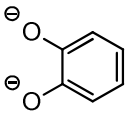 cat	Cu : **1a** Ni : **5a**	Cu : **2a** Ni : **6a**	Cu : **3a**	Cu : **4a**
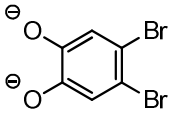 Br_2cat	Cu : **1b** Ni : **5b**	Cu : **2b** Ni : **6b**	Cu : **3b**	Cu : **4b**
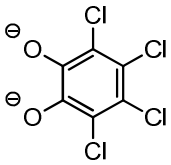 Cl_4cat	Cu : **1c** Ni : **5c**	Cu : **2c** Ni : **6c**	Cu : **3c**	Cu : **4c**
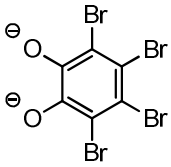 Br_4cat	Cu : **1d** Ni : **5d**	Cu : **2d** Ni : **6d**	Cu : **3d**	Cu : **4d**
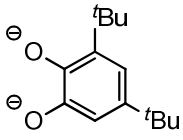 ^{t}Bu$_2$cat	Cu : **1e**	Cu : **2e**	Cu : **3e**	Cu : **4e**

3.2 Results and discussion

3.2.1 Remarks on synthesis

Unless otherwise stated, all reactions were performed under an inert atmosphere of N_2 and using degassed solvents, due to the potential for the catechol moiety to oxidise and/or decompose by interacting with O_2 in the presence of a Cu species and base when in solution (**Section 3.2.1.1**). All chemicals were reagent grade purchased from Sigma Aldrich and used without further purification, apart from catechol which was purified by sublimation before use.

The synthetic routes to the mixed-ligand complexes are a variation on that described by Brown et al.,[8] and involve mixing together molar ratios of the appropriate ligands and Cu(II) salt in polar solvents, whereupon the neutral compounds precipitate out of solution upon the addition of two molar equivalents of base with respect to the catechol ligand. The Cu complexes of catechol and tetrachlorocatechol with both the 2,2'-bipyridine and 1,10-phenanthroline ligands have been synthesised previously but were not examined beyond their electronic spectra.[8] The solid products are stable in air, however many of these mixed-ligand complexes are known to be hygroscopic or retain waters of crystallisation, therefore rigorous drying conditions may be needed.

The general procedure for the synthesis of all of the metal complexes reported was the same. To a stirred solution of the metal sulfate salt (5 mmol) in deionised water (3 ml) was added a solution of the catechol ligand (5 mmol) in 50% ethanol (5 ml), a solution of the ancillary N-donor ligand (5 mmol) in ethanol (5 mmol) and a solution of potassium hydroxide (0.4 M, 5 ml, 10 mmol). The resulting precipitate was collected by filtration and washed with deionised water and ethanol to remove any salts or unreacted ligand, before drying in a vacuum desiccator.

3.2.1.1 Oxidation of catechol

Molecules and complexes of catechol (or pyrocatechol as it was previously known) are known to undergo oxidation under a range of reaction conditions. Some examples from the literature are shown in **Scheme 3.1**. There are specific enzymes in nature that oxidise catechol-containing species via a transition metal-based active site to benzoquinone, in a process that is accelerated under more basic conditions.[9] Solid catechol will itself undergo a slow oxidation in air to the brown compound benzoquinone, therefore should be sublimed prior to use. There are other enzymes that induce irreversible C-C bond cleavage of the aromatic ring to other organic products.[10] The presence of molecular oxygen is not necessary to oxidise the catechol however, as demonstrated by the anaerobic oxidation of catechol by Cu(II) ions in basic methanolic solution.[11] It is hypothesised that it is actually the metal centres that induce oxidation, and it is the role of molecular oxygen to reoxidise the reduced metal ion to the oxidation state needed to continue the reaction cycle.

In light of these studies, care was taken to limit the exposure of O_2 during synthesis that involved the unsubstituted catechol ligand. Also, the reactions were formulated to ensure that catechol was the last reagent added before product precipitation, as the catechol compounds are stable in the solid state.

Nevertheless, three compounds of catechol in this chapter, **2a**, **5a** and **6a**, were not pure as shown by elemental analysis. The compounds **2b** and **6b** (containing the Br_2cat ligand) were also found to be impure. Therefore, these compounds were not studied by more sensitive techniques such as powder EPR and SQUID magnetometry, and their discussion in this chapter will be limited to electronic spectroscopy and molecular orbital relationships.

Scheme 3.1. Oxidation pathways of catechol and its complexes.

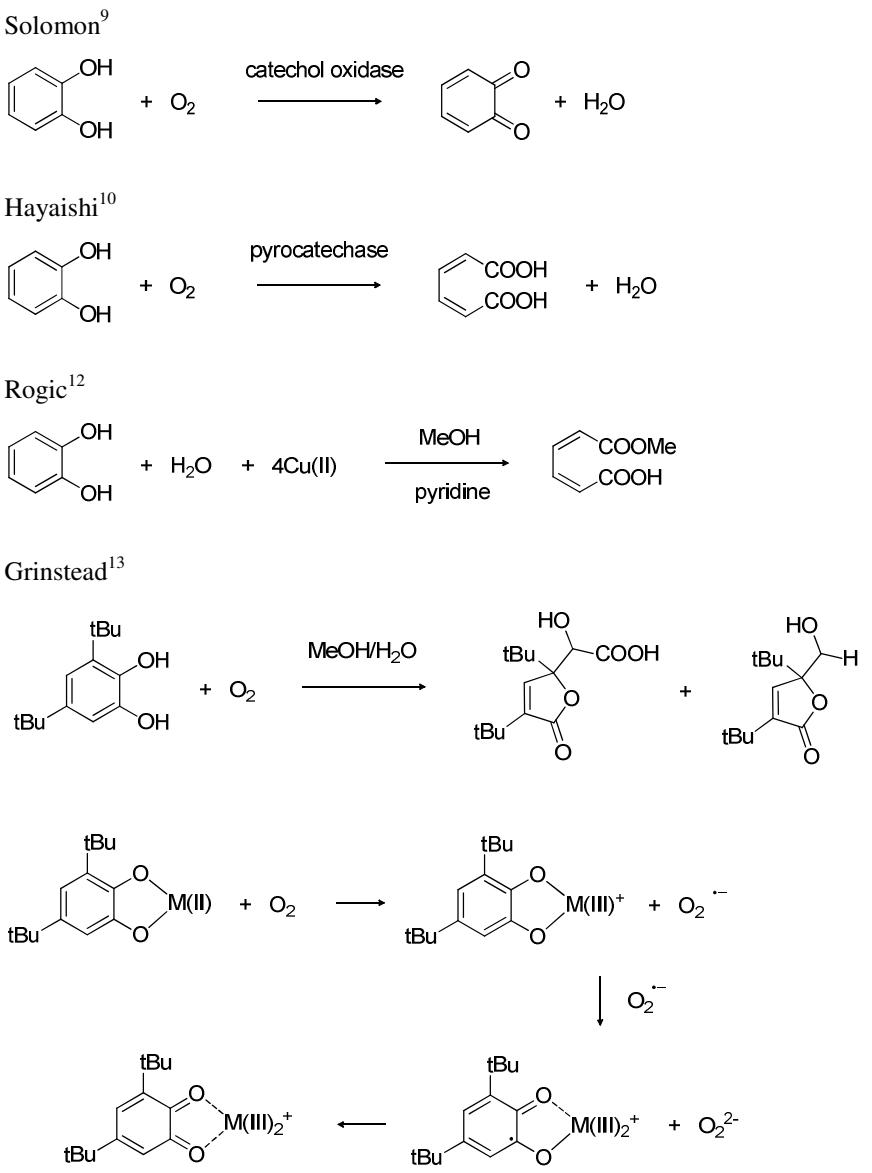

3.2.2 Electronic spectroscopy

The electronic absorption maxima for all the reported complexes have been determined from reflectance spectroscopy (**Table 3.1**). Each compound displays absorptions in the UV, visible and NIR regions of the spectrum. The reflectance spectra for the two classes of Cu and Ni compounds are shown in **Figure 3.1**. The

UV absorptions do not vary within a series of compounds with the same N-chelate. Intense absorptions in this region are commonplace for aromatic compounds, and can be assigned to intraligand π-π* transitions. The absorption peak in the visible region is assigned to the HOMO to LUMO ligand-to-ligand charge transfer, which is explained in Chapter 4 (**Section 4.2.3**). From the onset of this transition, an estimate of the band gap of the material can be determined. The lowest energy transitions may originate from solid-state interactions that are not observed as strongly in solution spectra of analogous compounds described in Chapter 4.

Within a series with the same N-chelate compound, the absorption maxima positions for both the visible (400 to 500 nm) and NIR (700 to 830 nm) absorptions shift when substituting the catecholate ligands. The absorption peak positions shift to shorter wavelengths following the general trend of increasing electron-withdrawing ability of the substituents on the catechol ligand, from catechol complexes at the longest wavelengths to tetrachlorocatechol complexes at the shortest wavelengths. This agrees with the stabilisation of the HOMO based on the catecholates leading to larger HOMO-LUMO gaps as seen from the DFT calculations (**Section 3.2.9**). Changing the N-chelate ligand has less of an effect on the absorption maxima energy of complexes, which is understandable given only the slight difference in structure of the two N-chelates.

Table 3.1. Absorption maxima (nm) for Cu and Ni catecholate complexes determined from diffuse reflectance spectroscopy.[†]

	Absorption maxima (nm)						Absorption maxima (nm)				
			Cu						**Ni**		
1a	254	305	514	840	[1150]	**5a**	235	269	795		
1b	254	309	491	780	[1110]	**5b**	250	306	520	900	[1225]
1c	255	310	436	710	[950]	**5c**	243	303	483	960	[1200]
1d	240	310	432	714	[935]	**5d**	245	301	472	1020	[1190]
2a	232	270	476	820	[1180]	**6a**	231	269	798		
2b	230	271	454	808	[1060]	**6b**	231	271	500	1100	[1215]
2c	230	270	420	754	[1030]	**6c**	230	269	420	1025	[1185]
2d	234	270	440	755	[1035]	**6d**	235	272	460	1050	[1180]

[†]The onset of the low-energy NIR absorption is represented within the square brackets.

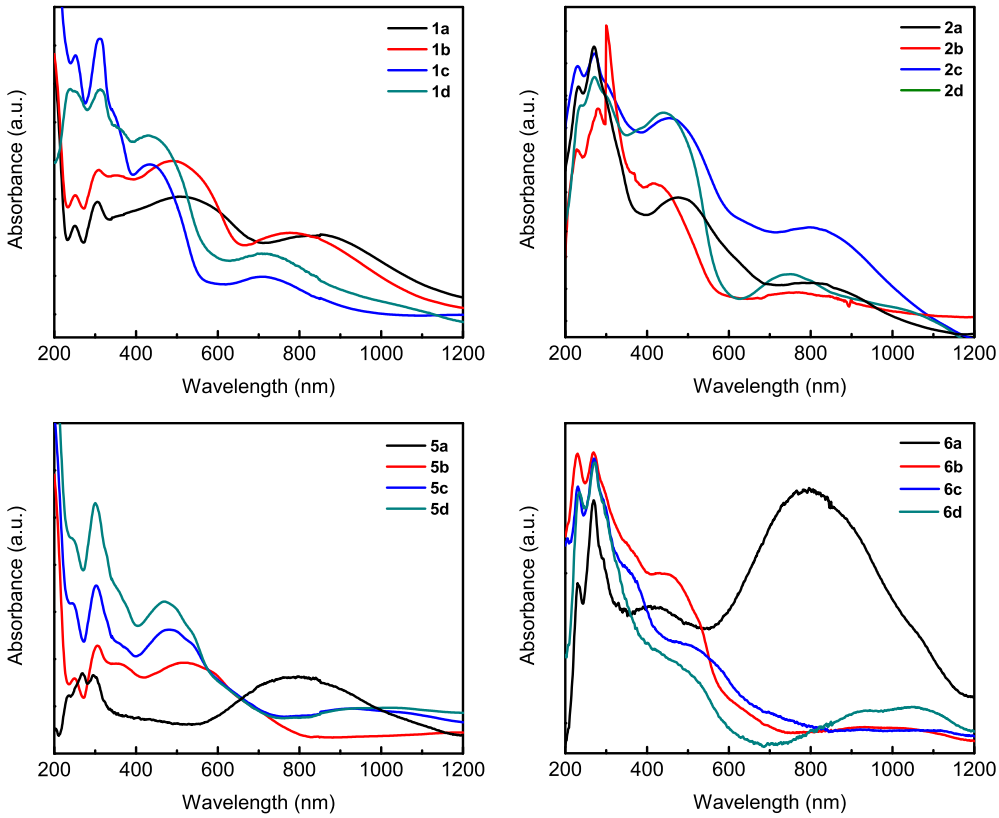

Figure 3.1. Diffuse reflectance spectra of Cu bpy (top left), Cu phen complexes (top right), Ni bpy complexes (bottom left) and Ni phen complexes (bottom right).

The lowest energy NIR peak is the weakest intensity peak in the absorption spectrum for all of the compounds measured apart from the catechol compounds of Ni, **5a** and **6a**, and is very broad in the range of 600 to 1100 nm. For the Ni complexes **5c**, **5d**, **6b**, **6c** and **6d** one can observe two peaks in this range of similar, yet weak, intensity. With comparisons drawn from the absorption spectra in Chapter 4 (**Section 4.2.3**) it is hypothesised that the NIR band may arise from intermolecular interactions in the solid state (i.e. weakly-associated dimers).

3.2.3 Powder EPR spectroscopy

Room-temperature powder EPR measurements were carried out on the six Cu complexes that were pure by elemental analysis, **1a**, **1c**, **2c**, **1b**, **1d** and **2d**. This gives an accurate confirmation of the *g*-value, which is important when determining the

magnetic properties of these materials (**Section 3.2.7**). Three complexes containing the bpy ancillary ligand **1a**, **1c**, and **1b**, were also studied using variable-temperature EPR measurements down to temperatures of 5 K. The general shape of the spectra are depicted at 10 K (**Figure 3.2** (left)). The shape of the spectra is typical for square-planar Cu(II) complexes,[14] but appears roughly isotropic with a only a shoulder visible on the low-field side of the first-derivative absorption peak. This indicates that there is a lack of resolution to resolve the anisotropy of the axial symmetry expected, and only an isotropic *g*-factor could be determined. The experimental values are in agreement with other Cu(II) square-planar compounds in the range of 2.0 to 2.2.[15-17]

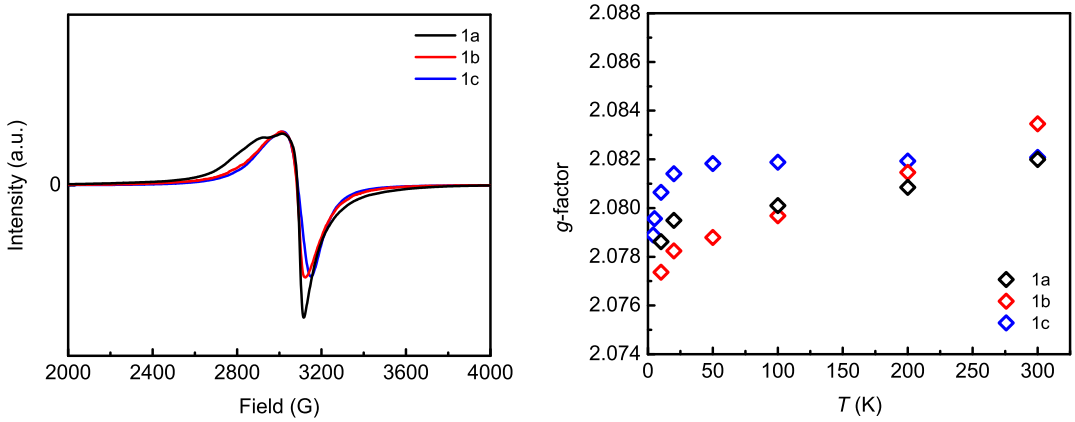

Figure 3.2. Powder EPR spectra of **1a, 1b** and **1c** at 10 K (left) and variable-temperature powder EPR spectrum of **1a, 1b** and **1c** depicting how the *g*-factor is affected by changing temperature (right).

Variable-temperature measurements were carried out between 4 and 300 K to discover how the *g*-factor changes as the strength of magnetic interactions between the Cu centres in different molecules becomes comparable with thermal energy (**Figure 3.2** (right)). The *g*-factor gradually decreases for all compounds as the temperature decreases below about 10 K, suggesting the potential presence of antiferromagnetic interactions.

3.2.4 Reactant diffusion crystallisations

Structural data is needed in order to determine the nature of intermolecular interactions and how the magnetic properties are influenced by molecular geometry. Initially, crystals suitable for single crystal X-ray diffraction (SCXRD) were attempted to be grown by the method of vacuum sublimation (**Section 3.2.10.2**). However, due to the limited ability of this series of compounds to sublime at the pressures achieved, another method was needed.

The technique of reactant diffusion to grow crystals of insoluble or sparingly-soluble compounds has been known for almost 100 years, but is often overlooked. Initial successes of the technique were with the diffusion of ions in aqueous or gelatinous media to form crystals of insoluble salts.[18,19] The aim of this technique is not only in the understanding of the solid state structure, but also in achieving a greater degree of substance purity. In order to favour a large particle size, one must optimise the reaction conditions to favour very slow product formation. This will guarantee that molecules of the desired compound will form in low concentrations and thus enable fewer nucleation sizes and larger crystal grains.

There were various methods employed with this technique in the literature, such as placing the reactant solutions in small vessels that were submerged in the diffusion medium. Other methods included the slow siphoning of reactant solutions through capillaries into the diffusion medium.[18] The use of silica gels as a diffusion medium have become popular,[20-22] as it greatly slows down the reaction time, yielding crystals in a timeframe of a number of weeks to months. Ionic crystals that show electroactive behaviour (such as optoelectronics, piezoelectrics and ferroelectrics) have been successfully produced using this method.[23]

Nevertheless, to the best of the author's knowledge this technique has been limited to reactions of ionic species and those involving the mixture of only two reactant solutions, and often takes a period of weeks to months for suitably-sized

crystals to form. Examples exist of charge-neutral species being generated from ion exchange in an H-cell, but took over 2 months to form.[24] Reactions involving relatively non-polar reactants or those involving the combination of multiple reactants have not been explored to a great extent in the literature.

For reactions involving the compounds detailed in this chapter, four separate reagents are required to be mixed together in order to form the desired product. This understandably introduces a greater deal of difficulty when assembling the diffusion reaction. For example, one must consider the order in which reactant solutions must be mixed to avoid unwanted species being formed. Furthermore, the solubility of the reactants and the density of the solvent in which they are dissolved are crucial factors in not only the rate of crystallisation, but also in preventing side products. Finally, the components must come together at a rate slow enough to form crystals but not so slow that the reactants precipitate from solution; a reactant may precipitate out of the reaction if the composition of the solvent is changed by too great an extent. For example, a metal salt dissolved in water will crystallise out of solution once enough organic solvent has diffused in.

3.2.4.1 Testing of reactant solution order

Initial tests were required to determine the order in which the reactant solutions needed to be mixed to avoid precipitation of other products. The metal salt used was $CuSO_4 \cdot 5H_2O$ and the catechol used was Cl_4cat for reasons of stability. Preliminary tests showed that if the base were to contact the metal salt, copper hydroxide and other copper sulfates and hydroxysulfates would form. Also when the N-chelate ligand was mixed with the metal salt it would induce precipitation of $[Cu(\text{n-chelate})_n(OH_2)_n(SO_4)]$ compounds.[25]

It was determined that the copper salt needs to first react with either the catechol solution followed by the N-chelate ligand or a mixture of both ligands to form the protonated precursor complex $[M(\text{N-chelate})(\text{catechol}H_2)]^{2+}$. However this process needs to be slow, because the precursor may precipitate out at higher

concentrations. Therefore a diffusion solvent must be present between the metal salt solution and ligand solutions. The metal salt is most soluble in polar, dense solvents and the ligands are soluble in less polar and less dense solvents. Therefore the metal salt solution should be placed at the bottom of the reaction, separated from the ligand solutions by a diffuser solvent of a density that is between both solutions. The base should be added on top to react last. A schematic of the setup is shown in **Figure 3.3**. Each layer was added carefully by needle to prevent premature mixing. This is another reason why choice of solvent is important, as certain solvents layer better than others. Precipitation generally took place near the initial interface of the metal salt with the diffuser.

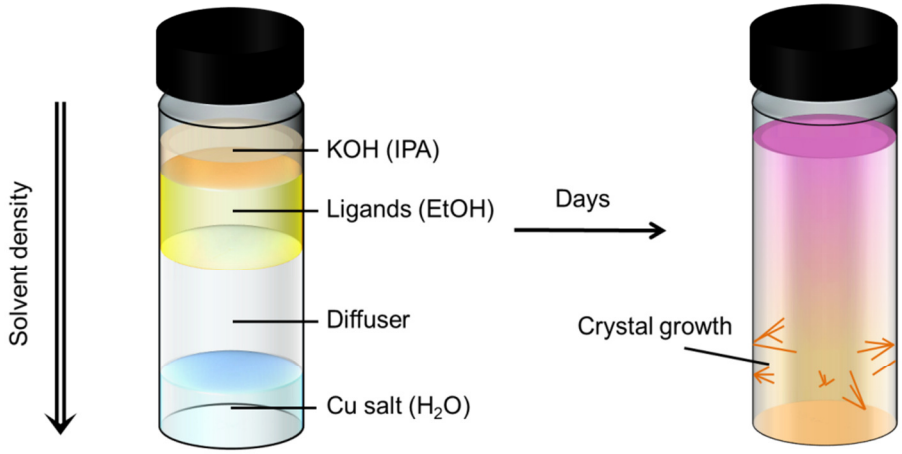

Figure 3.3. Layering system used to grow crystals of insoluble compounds. The solvent density and ordering of reactant solutions are important for single crystal growth and to avoid precipitation.

Tests were carried out by changing one of the following variables: reaction vessel length and diameter; nature and volume of diffuser solvent; concentration and molar ratio of reactant solutions; metal salt; base. All combinations of ligands were also tested. A list of different reaction conditions that have been tested in every combination is shown in **Table 3.2**. For the reaction vessel, the narrower the diameter for the solvents to diffuse through the slower the diffusion will be. However, if the diameter is too narrow the passage can get blocked by precipitate. As a compromise, glass vials a height of 7.5 cm and a diameter of 1.25 cm were

employed. For the reactant solutions, volumes of approximately 1 ml were used (within the given molar ratio constraints of the reaction).

Table 3.2. Variable reactants and conditions used in reactant diffusions. All ligands from **Chart 3.1** have been tested.[†]

Copper salt (H_2O)	$CuSO_4 \cdot 5H_2O$ // $CuCl_2 \cdot 2H_2O$ // Cu(acetate)$_2 \cdot H_2O$ // $[Cu(NH_3)_4]^{2+}$			
Nickel salt (H_2O)	$NiSO_4 \cdot 6H_2O$ // $NiCl_2 \cdot 6H_2O$			
Conc. of reactant solutions (mol dm^{-3}) [‡]	0.01 // 0.02 // 0.04 // 0.10			
Molar ratios	M	: catechol	: N-chelate	: base
	1.0	: 1.0	: 1.0	: 2.0
	1.0	: 1.0	: 1.0	: 2.0
	1.0	: 1.0	: 1.0	: 1.9
	0.9	: 1.2	: 1.0	: 2.0
	0.9	: 1.4*	: 1.0	: 2.0
Diffuser (3-10 ml)	DMF // EtOAc // DMF+EtOAc // THF // EtOAc: ^{i}PrOH (10:1, 5:1, 1:1)$^{\infty}$			
Base	KOH (EtOH) // KOH (^{i}PrOH) // NH_3 // NEt_3 // $^{i}Pr_2NH$ // pyridine			

[†]The solvents in parenthesis indicate the solvent used to dissolve the given reactant; EtOH was used as the solvent for both ligands. [‡]Concentration of base solutions was always twice that of the other reactants. *Higher molar catechol ratio used only when premixing Br_4cat solution with $CuCl_2$ solution. $^{\infty}$Used explicitly in Ni salt crystallisations.

3.2.4.2 Copper reactant diffusion crystallisations

In general for the Cu reactant diffusions the best conditions for single crystal growth were using DMF as the diffuser and KOH (^{i}PrOH) as the base. With these components crystal needles of the greatest thickness and length were produced. EtOAc and THF as the diffusion medium both produced crystals that were far too fine. The nitrogen-based bases produced either too many nucleation sites or crystals that were very rough and branched.

Rather than detail the results of every diffusion reaction, only the reactions from which single crystals suitable for XRD were obtained are presented in **Table 3.3**. Single crystals structures of **1c**, **2c** and **1d** were obtained from vials with a larger volume of diffusion solvent, often 6-8 ml of DMF. This does not mean however that other vials did not contain crystals that were suitable for XRD.

In an attempt to reduce the quantity of impurities precipitating or crystallisation from solution, which could lead to smaller or contaminated crystals of product, a modified reaction scheme was used. This differed from the normal method detailed in **Figure 3.3** by first mixing the metal salt and catechol ligand solutions, before layering with the diffuser and other solutions as normal. This technique was used in the crystallisation of **1d** from $CuCl_2$ solution reactions, and did result in no visible blue, crystalline impurities. It must be said that this procedure did not succeed with all metal salts, catechols or combinations of their solutions.

3.2.4.3 Nickel reactant diffusion crystallisations

For the Ni(II) salts a different diffuser was needed, because they formed an insoluble precipitate when DMF was added. EtOAc did not produce these precipitates, so this solvent was used in addition to mixtures with ^{i}PrOH. EtOAc is immiscible with H_2O, but the reactant solutions in alcohols are still able to diffuse through. This may have the added benefit of slower diffusion of the ligands into this layer due to its lower polarity relative to EtOH, and thus lower solubility of the ligands. However, these experiments led only to formation of precipitates at the interface of the initially-immiscible layers. Mixtures of EtOAc:IPA layer well on top of H_2O and become totally miscible over time and did prove to work better than pure EtOAc. Testing the v/v ratios of EtOAc:IPA, from 10:1 to 5:1 to 1:1 there was increasing crystal size and decreasing bulk purity.

The Ni-based reactions produced less crystalline product and less overall product yield than the corresponding Cu-based reactions. The difficulty in obtaining large single crystals of Ni complexes was illustrated by the presence of only one crystal structure, that of Ni(Cl_4cat)(bpy) (**5c**).

Table 3.3. Specific reactant diffusions that yielded single crystals suitable for XRD.

0.04 M solutions:
$CuSO_4.5H_2O$ (H_2O) + 7 ml DMF + Cl_4cat (EtOH) + bpy (EtOH) + 1.8 N × KOH (EtOH)
➔ Cu(Cl_4cat)(bpy) single crystal structure
$CuSO_4 \cdot 5H_2O$ (H_2O) + 8 ml DMF + Cl_4cat (EtOH) + phen (EtOH) + KOH (^{i}PrOH)
➔ Cu(Cl_4cat)(phen) single crystal structure
$NiSO_4 \cdot 6H_2O$ (H_2O) + (1:1)EtOAc:IPA + Cl_4cat (EtOH) + bpy (EtOH) + KOH (IPA)
➔ Ni(Cl_4cat)(bpy) single crystal structure
0.01 M solutions:
[$CuCl_2 \cdot 2H_2O$ + Br_4cat(DMF)] + 6 ml DMF + bpy (EtOH) + KOH (^{i}PrOH)
➔ Cu(Br_4cat)(bpy) single crystal structure

3.2.4.4 Testing impurity phases

The origin of the blue impurity was tested to see if it was a result of individual combinations of reactant solutions. The reactants (and solvents) used were $CuSO_4 \cdot 5H_2O$ (H_2O), Cl_4cat (EtOH), bpy (EtOH) and KOH (^{i}PrOH), and the diffusion medium was DMF.

By carrying out the procedure with a blank EtOH layer where the ligands solutions would normally be present, there was a decreasing presence of light blue precipitate as the DMF volume increased. This may indicate that the light blue precipitate is in fact copper hydroxide created by the reaction of the base with the metal salt. The procedure was carried out again without the Cl_4cat solution present, 7 ml DMF, with and without KOH solution. Without KOH present, needle-like light blue crystals formed, with a colourless solution remaining. With KOH present, very small blue crystals formed near the bottom of the vial with a faint bed of precipitate-like solid present in a pale green solution. The exact nature of the impurities was not investigated, only optimising the conditions to prevent their occurrence. It is likely that there may be a variety of species, such as copper hydroxysulfates and hydrated

sulfate salts of the Cu(N-chelate). These products could be also forming to some degree in the general synthetic procedures to produce powder, polycrystalline samples of the complexes, as indicated in the powder diffraction patterns (see **Section 3.2.6**).

3.2.4.5 Reactant diffusions summary

The following general trends were observed when increasing the volume of the diffusion medium: the size of crystals increased; the quantity of crystals decreased; the degree of cluster formation and branching of the crystals increased; the visible presence of blue, crystalline impurities increased. Therefore as the speed of ligand diffusion decreases, the number of nucleation sites is decreased resulting in fewer but larger crystals and a greater possibility of impurity formations. In the reactions with small volumes of diffusion solvent, the crystallised material can be almost powder-like in appearance. One finds that although the crystals may be too small for single crystal diffraction, under an optical microscope these crystals are single and of good quality. On the other hand, the large crystal growths are subject to branching meaning a lower percentage of quality single crystals.

3.2.5 Structure

Crystal structures were obtained for the complexes **1c**, **2c**, **1d** and **5c**. All four complexes crystallise with one molecule in the asymmetric unit apart from complex **1d**, which crystallises with two (**Figure 3.4**). There are no solvents of crystallisation present in any of the structures. Each molecule in the structures can be related to a dimeric pair via an inversion centre, although the strength of interaction with the nearest neighbour varies across the structures (see below). The complexes that contain the Cl_4cat ligand, **1c**, **2c** and **5c**, are all monoclinic and possess a similar packing arrangement. Complexes **1c** and **5c**, differing only in the central metal ion present, are isomorphous and crystallise in the $P2_1/n$ space group. The most dimerised structure, **2c**, crystallises in $P2_1/c$ (**Figure 3.5**). Although

complex **1d** crystallises in the triclinic P-1 space group, the molecules pack in a comparable fashion to the structures of the other three complexes.

All of the complexes possess a central metal(II) ion coordinated by two oxygen atoms of the catecholate and two nitrogen atoms of the ancillary ligand (either bpy or phen), in a general square-planar geometry. Relevant intramolecular bond lengths and angles are listed below (**Table 3.4**). The intramolecular Cu-O bond lengths in complexes **1c**, **2c** and **1d** range between 1.91 and 1.92 Å and compare well with those observed in other analogous square-planar copper complexes in the range 1.87-1.93 Å.[26,27] The Cu-N bond lengths range between 1.98-1.99 Å. The intramolecular Ni-O and Ni-N bond lengths in **5c** are all significantly shorter than in the Cu complexes, with larger bite angles of the coordinated ligands than in the copper analogues.

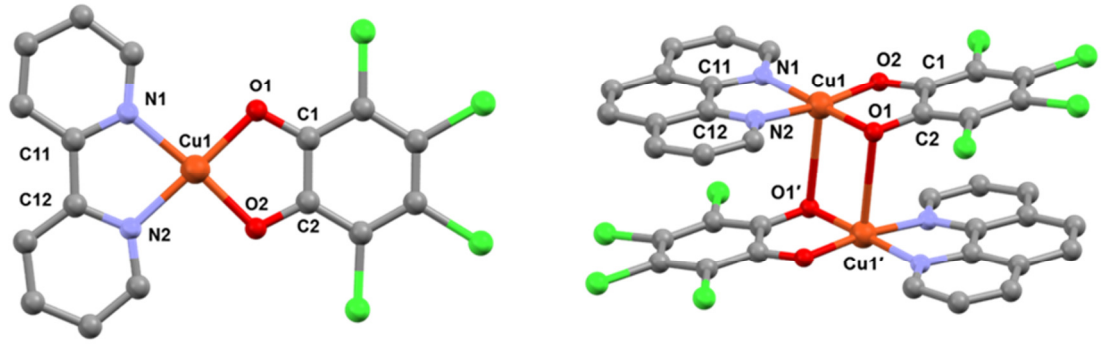

Figure 3.4. Asymmetric units of **1c** (left) and **2c** (right) with atomic numbering scheme used in all complexes, which shows the square planar geometry of the molecules and the dimerisation of **2c**.

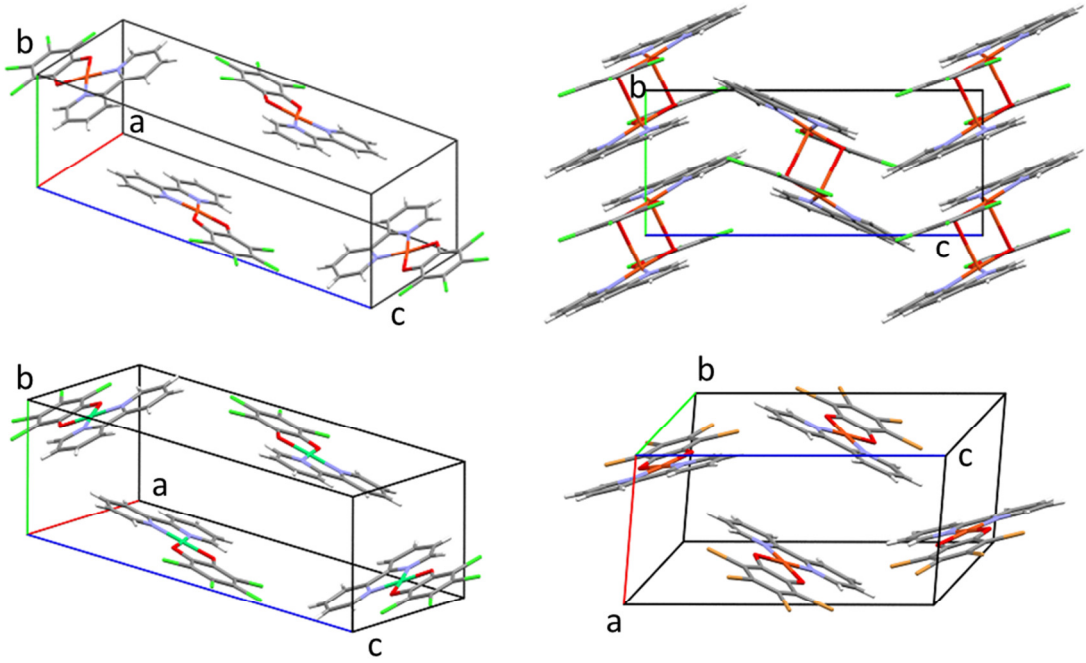

Figure 3.5. Unit cells of **1c** (a), **2c** (b), **1d** (c) and **5c** (d). The crystallographic cell axes *a*, *b* and *c* are red, green and blue respectively.

Table 3.4. Selected interatomic distances (Angstroms), bond angles (degrees) and torsion angles (degrees) for **1c**, **5c**, **2c** and **1d**. The terms '**i**' and '**ii**' describe the two different molecules in the asymmetric unit of **1d**.

Parameter	**1c**	**2c**	**1d-i**	**1d-ii**	**5c**
M-O1	1.910(1)	1.920(1)	1.918(7)	1.906(7)	1.839(2)
M-O2	1.907(2)	1.909(2)	1.914(7)	1.907(7)	1.844(2)
M-N1	1.975(1)	1.997(2)	1.975(9)	1.985(7)	1.879(2)
M-N2	1.977(2)	1.992(2)	1.982(8)	1.977(9)	1.882(2)
O1-C1	1.320(3)	1.330(3)	1.314(2)	1.329(3)	1.325(3)
O2-C2	1.321(2)	1.322(2)	1.313(3)	1.314(4)	1.332(3)
O1-M-O2	87.63(6)	87.4(7)	87.5(3)	87.0(3)	89.1(8)
O1-M-N1	93.25(6)	96.0(7)	95.4(3)	95.1(3)	92.7(8)
O1-M-N2	175.23(7)	177.0(8)	176.2(3)	176.7(3)	176.6(8)
O2-M-N1	176.53(6)	172.4(8)	176.8(3)	176.3(3)	178.2(8)
O2-M-N2	97.13(6)	94.1(8)	94.9(3)	96.2(3)	94.0(8)
N1-M-N2	81.98(6)	82.2(8)	82.1(3)	81.7(3)	84.2(8)
O1-C1-C2-O2	2.5(3)	2.8(3)	1.2(1)	2.2(1)	0.47(3)
N1-C11-C12-N2	0.9(2)	0.4(3)	2.2(11)	1.3(1)	0.21(3)

The packing of the molecules can be described as a regular array of molecules stacked in an alternating fashion (head to tail) in the crystallographic *b*-axis (apart from complex **1d** which is triclinic), promoting a face-to-face π-π interaction between the electron-rich aromatic ring of the catechol and one of the relatively electron-deficient aromatic rings of the bpy. Selected intermolecular distances and short contacts are displayed in **Table 3.5**. The distance between least-squares (LS) planes of individual molecules (calculated through all non-H atoms) is between 3.2 and 3.4 Å for all complexes, with the largest distances between molecules of **1d**. Along the crystallographic *c*-axis there are also C-H···X intermolecular hydrogen bonds of less than 3 Å linking the stacks of molecules together, where X = Cl or Br. The shortest of these contacts are listed in **Table 3.5**.

The degree of planarity in the molecules is given by the root mean square (RMS) deviation of the atoms from the LS plane, which in turn is related to the degree of planarity in the basal plane of the $N_2O_2^{2-}$ metal coordination sphere. The most planar structure is the Ni complex **5c**, where the distance between the metal centre and the nearest O atom of a neighbouring molecule, Ni1-O1′, is the longest at 3.328(2) Å. Little interaction with this O atom is indicated, as it is displaced by only 0.002 Å from the LS plane. By contrast, in the Cu complexes there is an apical interaction of the out-of-plane O atom, O1′, which can distort the square-planar geometry about the Cu centre. This interaction is weak in **1c** at 3.035(1) Å and **1d** at 3.088(7) and 3.103(7) Å, but significant enough to displace O1′ from the LS plane by 0.143 Å in **1c** and 0.161 and 0.164 Å in **1d**. This is a common interaction observed in Cu(II) square-planar complexes,[28,29] owing to the Lewis acidity of the metal centre,[30] but is too slight in these structures to cause any significant distortion in the square-planar geometry. In compound **2c** however, the Cu-O1′ out-of-plane distance is short enough at 2.726(6) Å to form a weakly-bonded dimer. The Cu and O1 atoms are displaced towards each other from the LS planes by 0.226 Å and 0.367 Å respectively, completing a distorted square-pyramidal coordination about the Cu centre. This Cu atom displacement from the basal plane towards the apical oxygen atom is similar to that observed in other elongated square-pyramidal copper

dimers.[31-33] Despite the stronger dimerisation in **2c**, the LS planes are closer in **1c**. This is due to a greater degree of planarity, as indicated by the much smaller root RMS deviation of the atoms from the LS plane of 0.047 Å in **1c** compared to 0.138 Å in **2c**. The distortion from perfect square-planar geometry is also indicated by the trans-atom angle in the metal coordination, O1-M-N2 and O2-M-N2. This angle is less than 180° in all complexes, decreasing from 178.2(8)° in the most planar Ni complex, **5c**, to 172.4(8)° in the most distorted geometry of **2c**.

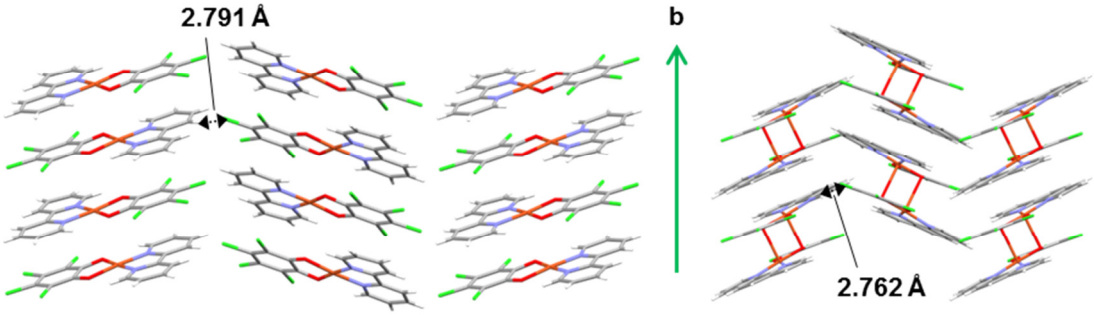

Figure 3.6. Packing pattern in the crystal structures of **1c** (left) and **2c** (right) along the crystallographic *c*-axis. Alternating molecules stack along the *b*-axis with close C-H···Cl contacts between stacks of less than 3 Å. There is very weak dimerisation between molecules along the *b*-axis of **1c**, and stronger dimerisation in **2c**.

Table 3.5. Selected intermolecular distances (Å), angles (°) and displacements Δ (Å) from least-squares (LS) planes of square-planar molecules defined by all non-H atoms in the square-planar unit (molecule) or the N_2O_2 basal plane (basal). Atoms in nearest neighbour molecules are denoted by a single prime (′) and next nearest neighbour molecules by a double prime (″).

	1c	**5c**	**2c**	**1d-i**	**1d-ii**
M1···M1′	3.4858(4)	3.5996(6)	3.329(5)	3.505(2)	3.493(2)
M1···M1″	4.3377(4)	4.3696(6)	3.911(5)	4.096(2)	4.079(2)
M1···O1′	3.035(1)	3.328(2)	2.726(1)	3.088(7)	3.103(7)
M1···O2″	3.547(1)	3.544(2)	4.526(2)	3.619(7)	3.594(8)
M1-O1-M1′	86.54(5)	83.0(6)	89.8(6)	85.6(2)	84.8(2)
X···H	Cl1···H141′	Cl1···H141′	Cl4···H8′	Br2···H131′	Br7···H261′
	2.791	2.848	2.762	2.868	2.919
LS→LS′	3.238	3.294	3.286	3.341	3.360
[a]$RMS_{molecule}$	0.047	0.040	0.138	0.070	0.078
$\Delta M1_{basal}$	0.028	0.010	0.079	0.035	0.033
$\Delta M1_{molecule}$	0.082	0.018	0.226	0.110	0.115
$\Delta O1_{molecule}$	0.143	0.002	0.367	0.164	0.161

[a]$RMS_{molecule}$ is the root mean square deviation of atoms from the LS plane through the molecule.

3.2.6 Powder X-ray diffraction

Powder XRD measurements were carried out on bulk polycrystalline samples of **1c**, **2c** and **1d** in order to qualify phase purity, which is important for interpretation of the results obtained from the magnetic measurement (**Section 3.2.7**). Data were collected out to a 2θ value of 30°, because data collected beyond this value were not strong enough to distinguish accurately from the noise. Rietveld refinements were carried out using structural parameters from the single crystal structures as a starting point (**Figure 3.7**), with the results of the refinement shown in **Table 3.6**. Despite relatively broad peaks, the compounds all show a favourable comparison between experimental and calculated peaks. There are only a few potential impurity phases observed in the patterns of **2c** and **1d**. This is confirmed by the relatively low R_p and goodness-of-fit (χ^2) parameters of **1c** and **1d**, and slightly higher values for **2c**. R_p is generally comparable to the *R*-factor in single-crystal structure analysis. The χ^2 parameter is determined by the square of the ratio of the weighted *R*-factor (R_{wp}) and the expected *R*-factor (R_{exp}),[34] and a value of less than 6 is generally regarded as a quality fit.[35]

The strong impurity peak at 2θ = 12.3° in **1d** matches the (0,1,1) peak of the powder pattern of *cis*-[Cu(bpy)$(OH_2)_2(SO_4)$].[36] This sulfate-linked one-dimensional chain Cu(II) structure slowly formed from DMF solutions containing Cu(II), bpy and sulfate species, and also matches the habit of the blue needle crystals occasionally observed in the reaction diffusion crystallisations with DMF as a diffusion solvent (**Section 3.2.4**). However, the intensity of diffraction peaks in powder diffraction pattern are dependent on many more factors than simply the mass of sample being irradiated, so it is not a good measure of quantity of impurity. Because the goodness-of-fit of the data is suitable and the elemental analysis of the powder sample shows good purity, the quantity of this impurity is likely very small.

The unit cell parameters could not be accurately refined to an appreciable standard in **2c**, which may be an indication in least-square Rietveld refinement that

unmodelled contributions from the impurity phase have too great of an influence.[37] The impurity peaks in the powder pattern of **2c** occur at 2θ = 22.8, 24.3 and 25.9°, which is large angle for peaks of their relative intensity.[38] Given this information, it is likely that these peaks arise from a by-product with a different chemical composition rather than from a polymorph of the intended product. The impurity does not match the powder patterns of anterlite or brochantite, two mineral Cu hydroxysulfates,[39] nor the phen analogue of the potential impurity discovered in **1d** however.[40] Furthermore, factors such as preferred orientation, peak broadening due to crystallite size and strains can lead to inability to refine powder patterns. Given the nature of precipitation of the compounds, it is understandable that there will be variations in crystallite size and strain.

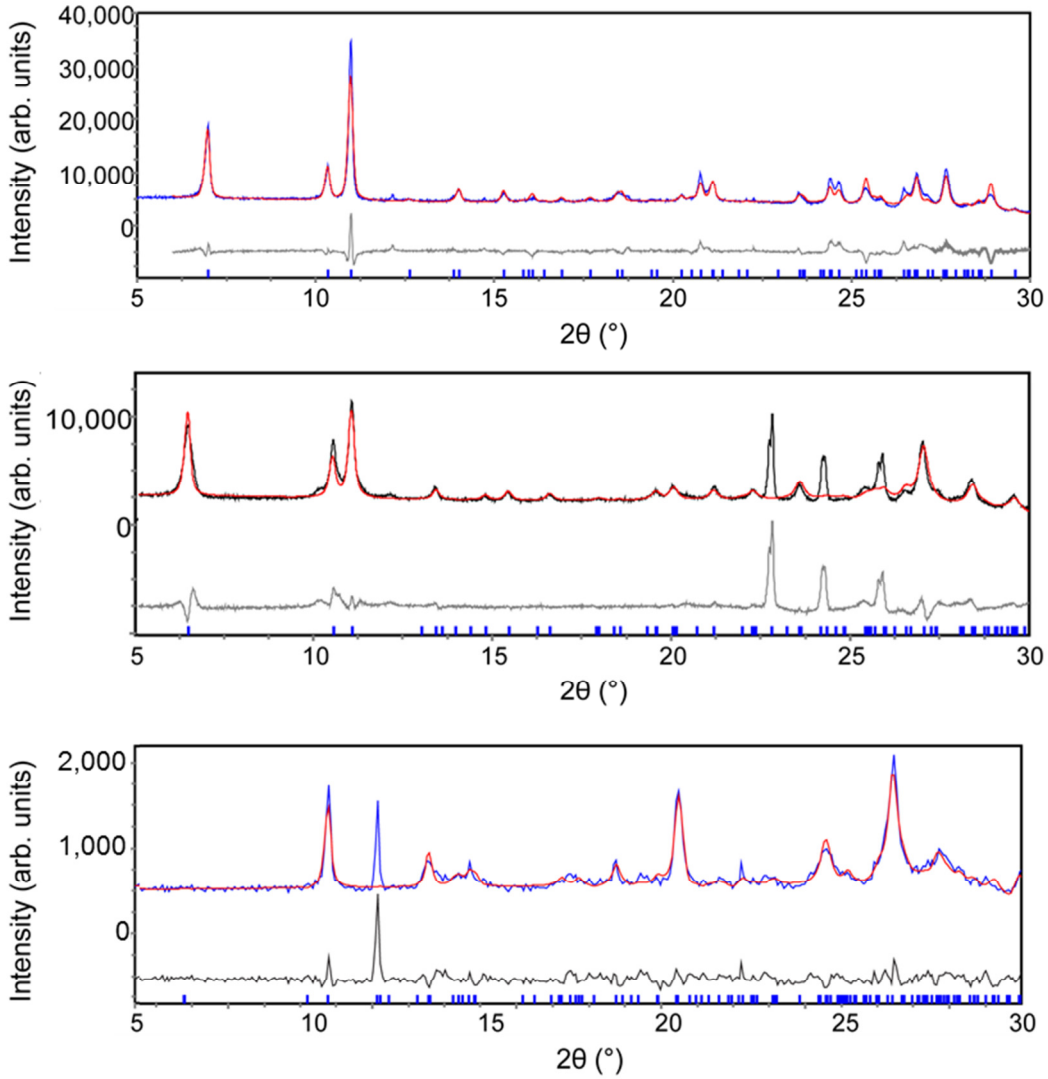

Figure 3.7. Rietveld fit profile for powder sample of **1c** (top), **2c** (middle) and **1d** (bottom). Observed data (blue line) at 298 K is compared with the calculated pattern (red line), with starting parameters derived from the single crystal structure measured at 120 K. The difference between the two patterns (grey line) is also shown along with the predicted Bragg peaks for the calculated space group (blue tick marks). There are impurity peaks at 2θ = 22.8, 24.3 and 25.9° in **2c** and one strong impurity peak at 2θ = 12.3° in **1d**.

Table 3.6. Unit cell parameters and reliability factors obtained from Rietveld refinement of powder data of **1c**, **2c** and **1d**. The cell parameters in **2c** were not refined but simply taken from the single crystal structure.

	1c	**2c**	**1d**
a / Å	8.8040(2)	13.9350	7.4587(8)
b / Å	7.2883(1)	7.16319	14.1976(4)
c / Å	25.3589(6)	17.2033	18.1791(5)
α / °	90.000	90.000	112.6086(6)
β / °	95.5617(12)	103.0592	100.2374(9)
γ / °	90.000	90.000	91.53573(9)
V / Å^3	1619.533(5)	1672.804	1739.251(4)
2θ range (°)	2-30	2-30	2-30
λ (Å)	1.54058	1.54058	1.54058
R_p (%)	5.072	8.969	5.902
R_{wp} (%)	7.661	15.383	8.749
R_{exp} (%)	1.369	1.858	3.706
χ^2 (GoF)	5.595	8.281	2.361

3.2.7 Magnetic measurements

Magnetic susceptibility data for the pure complexes **1a**–**1d**, **2c** and **2d** were measured on polycrystalline powder samples as a function of temperature from 1.8 to 300 K and an applied field of 0.1 T. Plots of the magnetic data are shown in **Figure 3.8** for the bpy compounds **1a**-**1d** and **Figure 3.9** for the phen compounds **2c** and **2d**, with the product of the molar magnetic susceptibility and temperature, $\chi_M T$, plotted against T. For all of the compounds analysed, the magnetic susceptibility deviates from typical Curie behaviour, with $\chi_M T$ decreasing from a constant value sharply at temperatures below about 20 K. The compounds display Curie-Weiss behaviour between about 20 – 300 K with small, negative Weiss constants, which is indicative of very weak antiferromagnetic interactions between the Cu(II) centres.

Due to the dimeric nature of the compounds determined by the single crystal structures, the data were analysed by best-fit curves calculated from the Bleaney-Bowers equation (**Equation 3.1**). This equation was initially formulated for a pair of

coupled Cu(II) ions based on Van Vleck's model of isotropic spin-exchange between magnetic centres

$$\chi_m = \frac{g^2\beta^2 N}{3kT}[1 + (1/3)e^{(-2J/kT)}]^{-1} + TIP \qquad \textbf{Equation 3.1}$$

where χ_M is the molar magnetic susceptibility, J is the exchange coupling constant, *TIP* is the temperature independent paramagnetism and the other constants with their usual meaning.[41] This equation was derived from the simple isotropic Hamiltonian $\hat{H} = -2JS_1 \cdot S_2$ where J is the exchange coupling parameter and $S_1 = S_2 = 1/2$ (interacting local spins). The values of parameters g and J were extracted from the least-squares fit of the magnetic data to the Bleaney-Bowers equation and are shown in **Table 3.7** The agreement between the experimental data and the calculated fit is given by a sum of squares method, which will equal one for a perfect fit of the data

$$R = (\Sigma_i[(\chi_m T)_{\mathrm{obs(i)}} - (\chi_m T)_{\mathrm{calc(i)}}]^2 / \Sigma_i[(\chi_m T)_{\mathrm{obs(i)}}]^2)^{1/2} \qquad \textbf{Equation 3.2}$$

The calculated fits are in good agreement with the experimental data, as indicated by values of R very close to one. Other models such as the Heisenberg model of infinite 1-D chains and the Bonner-Fisher model of anisotropic coupling within 1-D chains were also both fitted to the data,[42] but the Bleaney-Bowers model gave the best result. This is further evidence that the dimer formulation is an accurate one. The calculated g-values from the plots are between 2.0 and 2.2, which are in agreement with the experimentally-determined EPR values and those observed in the literature.[15-17] The J values are relatively small, ranging between about -0.8 and -1.6 cm^{-1}, but are expected due to the nature of the orientation of and the angle between the magnetic orbitals. Further explanation of the magnetic data and its relationship with molecular structure is given in **Section 3.2.8** below.

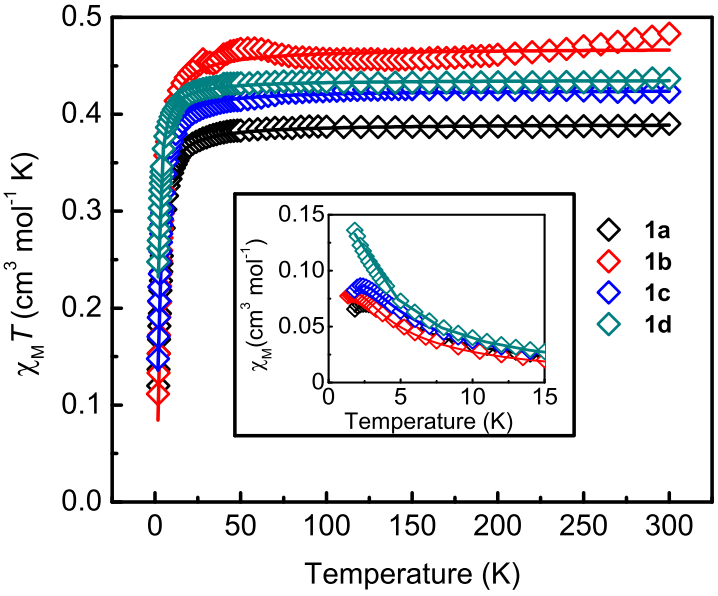

Figure 3.8. Plot of $\chi_M T$ vs. T for Cu bpy compounds **1a**, **1b**, **1c** and **1d** in the range of 1.8 to 300 K. The data were fitted with the Bleaney-Bowers equation (**Equation 3.1**) after removal of the temperature-independent factors. Inset: plot of χ_M vs. T from 0 – 20 K with data fit to the Bleaney-Bowers equation.

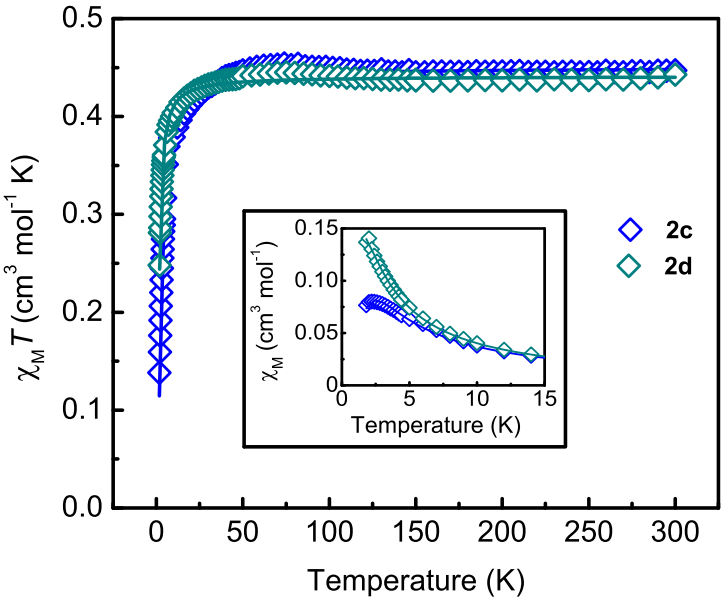

Figure 3.9. Plot of $\chi_M T$ vs. T for Cu phen compounds **2c** and **2d** in the range of 1.8 to 300 K. The data were fitted with the Bleaney-Bowers equation (Equation **3.1**) after removal of the temperature-independent factors. Inset: plot of χ_M vs. T from 0 – 20 K with data fit to the Bleaney-Bowers equation.

Table 3.7. Magnetic properties derived from Bleaney-Bowers fits to Cu magnetic data (except **2a** and **2b**).

Complex	*g*-value			*J* / cm^{-1}		*TIP* / cgs	$^{\dagger}R$
	$\chi_M T$ vs. *T*	χ_M vs. *T*	EPR	$\chi_M T$ vs. *T*	χ_M vs. *T*		
1a	2.040	1.989	2.080	-1.55	-1.46	Measured	0.9985
1b	2.128	2.061	2.082	-1.52	-1.39	157×10^{-6}	0.9928
1c	2.122	2.086	2.081	-1.40	-1.31	356×10^{-6}	0.9975
1d	2.155	2.090	2.077	-0.95	-0.85	-165×10^{-6}	0.9961
2c	2.190	2.053	2.084	-1.59	-1.39	-212×10^{-6}	0.9912
2d	2.169	2.127	2.077	-0.91	-0.83	10×10^{-6}	0.9920

†Residual adjusted mean-square fit of data to the Bleaney-Bowers equation.

3.2.8 Magneto-structural correlations

Many different parameters have been explored in the literature to explain the magnetic interactions between Cu centres in either binuclear or dimerised mononuclear structures with bridging O atoms. One of the most notable of these parameters is the Cu-O-Cu bridging angle, originally postulated to be of importance by Hatfield and co-workers with their investigation of di-hydroxo-bridged binuclear Cu(II) complexes.[43] Other influential factors may include the Cu-O bridge distance, Cu···Cu separation distance and the geometry of the Cu centres.[44,45] It is generally accepted however, that valid comparisons should only be made between systems that are similar with respect to the nature of the coordinating atom, the coordination geometry of the magnetic centres and the orientation of the magnetic planes.[46] For example, the Cu-O-Cu bridging angle relationship that was popularised by Goodenough,[47] alone does not explain the magnetic interactions observed in alkoxo-bridged binuclear complexes.[48]

Within the bpy series of compounds, the calculated value of *J* is seen to increase as the size of the catecholate ligand increases: cat < Br_2cat < Cl_4cat < Br_4cat. The values of *g* and *J* also follow this trend for the phen complexes, although only two compounds were measured. These trends do correlate in the same order with increasing Cu1···O1′ distance, decreasing Cu1-O2-Cu1′ angles and increasing Cu1···Cu′ distance as displayed in **Figure 3.10**, which are potentially relevant

crystallographic distances and angles in terms of magnetic correlation. There appears to be a strong correlation of J with the Cu1-O2-Cu1′ bridging angle, and weaker correlations with the interatomic distances. However, with only three crystal structures to fit comparisons to, it may be naïve to draw strong conclusions from these correlations.

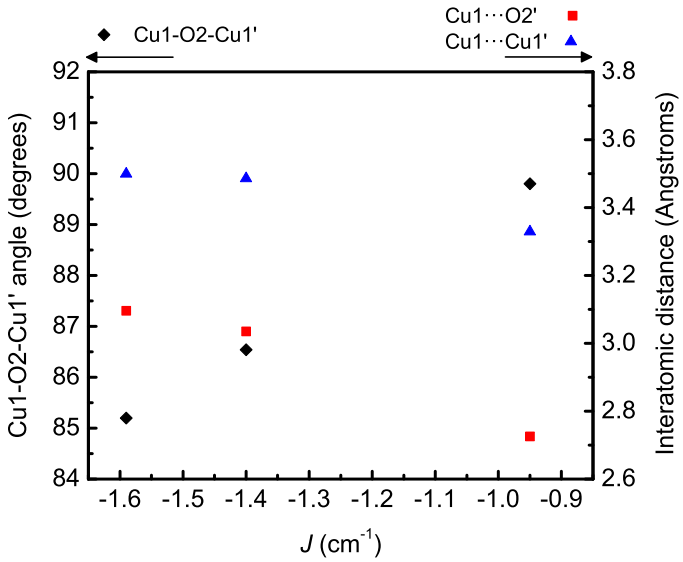

Figure 3.10. Correlations of various structural parameters of 1c, 2c and 1d with the value of J calculated by the magnetic fitting in **Section 3.2.7**.

For 5-coordinate Cu centres, a distorted-square-pyramidal geometry is most commonly observed. Dimers can be constructed by joining the individual square-pyramidal units by the basal edge with two equatorial bridging ligands (C_i or C_{2h} symmetry) or by joining two staggered, square-planar units to form a centrosymmetric dimer where the bridging atom is equatorial to one Cu centre and axial to the other. The latter case is observed in the crystal structures presented in this chapter, therefore the bridging mode is 'axial-equatorial'. In the strongest example of this interaction in **2c**, one can form a triangle with sides of Cu1-O1 at 1.920(1) Å, Cu1′-O1 at 2.725(1) Å, Cu1···Cu1′ at 3.329(5) Å and an internal Cu1-O1-Cu1′ angle of 89.8(6)°.

The angle between the N_2O_2 basal plane of the Cu centre and the Cu_2O_2 bridging plane is Cu1-O1-Cu1′, which is smaller than 90° for all of the structures reported. The magnetic plane is defined as the plane in which the unpaired electron is occupied, which is the N_2O_2 basal plane of the four strongest-bound ligands with consideration paid to the EPR and computational findings (**Section 3.2.9**). For the complexes reported, the structure is described by magnetic planes that lie approximately parallel to each other. Therefore the magnetic interaction in compounds with this orientation is expected to be weak; superexchange through the bridging O atoms is prevented due to the normal out-of-plane interaction of one of the O1 *p*-orbitals with the Cu magnetic orbital.[49] This is observed with values of *J* in the range of 0 to -2 cm^{-1}. Examples of similar systems with weakly-bridged, parallel magnetic planes described by Hatfield and co-workers also exhibit this weak out-of-plane coupling, whether it is ferromagnetic or antiferromagnetic.[17,43,50]

3.2.9 DFT calculations

Single-molecule gas-phase calculations were used to determine the ground state molecular geometry, as well as the shape and energy of the frontier orbitals of all the compounds detailed in this chapter. The B3LYP hybrid DFT functional was used with a 6-31G(d,p) basis set for all atoms apart from Cu and Br, which used the LANL2DZ pseudopotentials to model core electrons. Geometry optimisations generated the expected square-planar geometry for all compounds.

Determining the true electronic structure of Cu(II) species from DFT calculations has proven difficult in the literature. It has been shown that the nature of the functionals applied have a significant influence on the ordering of the valence orbitals.[51-54] For square-planar Cu(II) systems, the single-occupied molecule orbital (SOMO) where the unpaired electron resides is always calculated to exist in a molecular orbital based primarily on the $d_{x^2-y^2}$ orbital. This agrees with experimental EPR results[55-57] and with the commonly accepted position of the unpaired electron from ligand-field theory.[58] However, this orbital is seen to vary in position from

within the HOMO-LUMO gap to levels which are below that of the HOMO depending on the computational methods implemented.

A systematic study by Whyte and co-workers[59] explored many different combinations of levels of theory and basis set, and discovered that pure DFT functionals placed the SOMO within the HOMO-LUMO gap, whereas hybrid DFT functionals (B3LYP) that include correlation functionals, placed the SOMO below the energy of the HOMO. It has been suggested that it is the inherent self-interaction error in DFT calculations that is the issue, destabilising orbitals that are more localised in nature.[51] Therefore it is in fact the hybrid functionals, which reduce the self-interaction error, that give a more accurate representation of the orbital energies. Therefore the calculation of the SOMO to be below the energy level of the HOMO is fundamentally correct. It may seem surprising, but the existence of this buried SOMO is corroborated by methods such as photoelectron spectroscopy[51,54] and electrochemistry.[59,60]

The percentage occupancies of the HOMO, LUMO and SOMO for the Cu complexes are shown in **Table 3.8**. In calculations of both Ni and Cu compounds, the HOMO was localised primarily on the catechol ligands and the LUMO on the ancillary N-chelate ligands. There is little mixing of the frontier orbitals with the central metal ion, which is confirmation that the primary electronic absorption in the visible absorption spectrum is due to a LLCT between HOMO and LUMO. Examination of the SOMO for each compound shows that the largest single atom contributor is unsurprisingly the Cu atom, however the overall majority of the electron spin density is located on the coordinating O and N atoms of the catechol and N-chelate respectively.

For the Cu compounds in this chapter, the unrestricted calculations placed the spin density largely on the copper centre in the $d_{x^2-y^2}$ orbital. This is confirmed by the magnetic measurements (**Section 3.2.7**) and also by EPR measurements of soluble analogues in the next chapter (**Section 4.2.4**). The SOMO was calculated at a

position of HOMO-2, below two filled π-orbitals of the catechol ligand. The orbital energy level diagrams for all of the Ni, Cu bpy and Cu phen compounds are depicted in **Figure 3.11**, **Figure 3.12** and **Figure 3.13** respectively. In these figures, the red lines represent orbitals based primarily on the metal centre, whereas the black and blue lines represent orbitals primarily located on the catechol and N-chelate ligand respectively. It can be seen that the lone unpaired electron sits in a metal-based orbital below two occupied catechol-based orbitals for the Cu compounds. The values for the energy levels displayed in these figures are given in **Table 3.9**. The calculated HOMO-LUMO gap energies are given with comparison to those calculated from the onset of the low-energy absorption ($E_{\mathrm{gap}}^{\mathrm{Refl}}$) in the diffuse reflectance spectra. Despite the fact that DFT cannot predict the exact energy of the molecular orbitals, and the difficulty of estimating the onset of a broad, low-intensity band in the reflectance spectra, the HOMO-LUMO gap energies compare rather favourably for the Cu compounds.

Table 3.8. Calculated percentage contributions to selected molecular orbitals of Cu complexes.

Complex	Orbital	Orbital locations (%)				
		Cu	Catechol		N-chelate	
1a	HOMO	4.82	Molecule	86.72	Molecule	8.48
			O atoms	32.52	N atoms	0.68
	LUMO	1.46	Molecule	4.58	Molecule	93.96
			O atoms	2.72	N atoms	25.98
	SOMO	24.73	Molecule	50.25	Molecule	25.05
			O atoms	42.48	N atoms	10.66
1b	HOMO	4.19	Molecule	92.42	Molecule	3.39
			O atoms	29.96	N atoms	0.28
	LUMO	1.51	Molecule	3.31	Molecule	95.18
			O atoms	1.90	N atoms	26.22
	SOMO	22.01	Molecule	56.32	Molecule	21.67
			O atoms	37.90	N atoms	9.74
1c	HOMO	3.74	Molecule	91.73	Molecule	4.53
			O atoms	29.40	N atoms	0.12
	LUMO	1.62	Molecule	2.41	Molecule	95.97
			O atoms	1. 46	N atoms	26.28
	SOMO	21.74	Molecule	55.76	Molecule	22.50
			O atoms	29.48	N atoms	9.60
1d	HOMO	3.63	Molecule	92.08	Molecule	4.26
			O atoms	28.62	N atoms	0.10
	LUMO	1.63	Molecule	2.31	Molecule	96.07
			O atoms	1.40	N atoms	26.30
	SOMO	21.06	Molecule	57.14	Molecule	21.82
			O atoms	32.42	N atoms	9.92
2a	HOMO	4.86	Molecule	89.62	Molecule	5.54
			O atoms	32.64	N atoms	0.59
	LUMO	1.49	Molecule	5.22	Molecule	93.24
			O atoms	2.60	N atoms	11.81
	SOMO	23.98	Molecule	51.52	Molecule	24.48
			O atoms	42.82	N atoms	3.13
2b	HOMO	4.01	Molecule	92.64	Molecule	3.34
			O atoms	28.18	N atoms	0.34
	LUMO	1.55	Molecule	3.34	Molecule	95.14
			O atoms	1.86	N atoms	27.42
	SOMO	17.73	Molecule	63.88	Molecule	18.38
			O atoms	32.10	N atoms	7.04
2c	HOMO	3.76	Molecule	94.14	Molecule	2.10
			O atoms	29.50	N atoms	0.12
	LUMO	1.68	Molecule	2.41	Molecule	95.91
			O atoms	1.36	N atoms	27.50
	SOMO	20.80	Molecule	57.05	Molecule	22.15
			O atoms	39.48	N atoms	8.20
2d	HOMO	3.64	Molecule	94.36	Molecule	1.98
			O atoms	28.76	N atoms	0.10
	LUMO	1.68	Molecule	2.28	Molecule	96.02
			O atoms	1.30	N atoms	27.50
	SOMO	20.63	Molecule	58.16	Molecule	21.22
			O atoms	33.34	N atoms	8.70

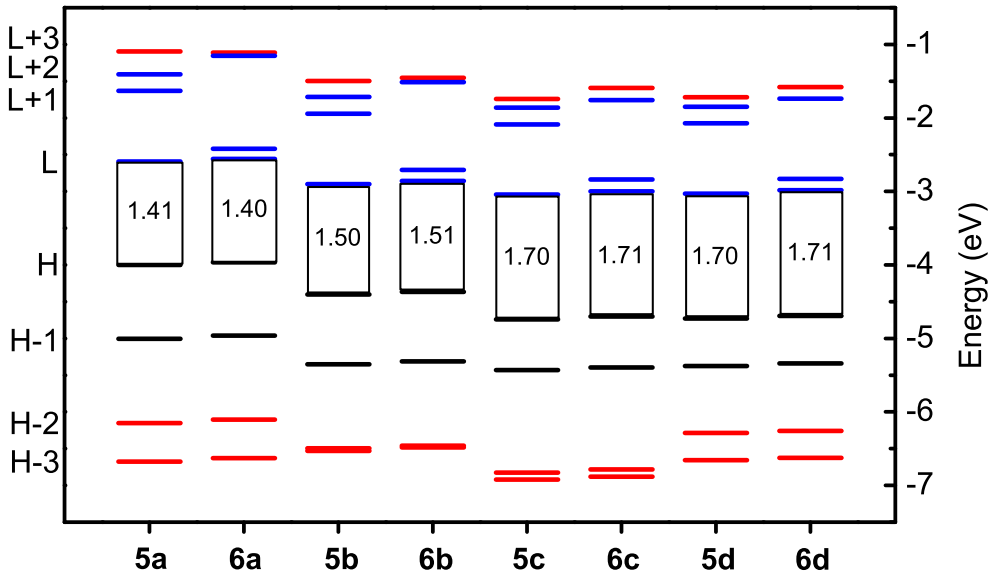

Figure 3.11. Calculated orbital energies for all Ni complexes with the calculated HOMO-LUMO energy gap. Line colours represent orbitals with majority contributions from the metal centre (red), catecholate (black) and N-chelate (blue).

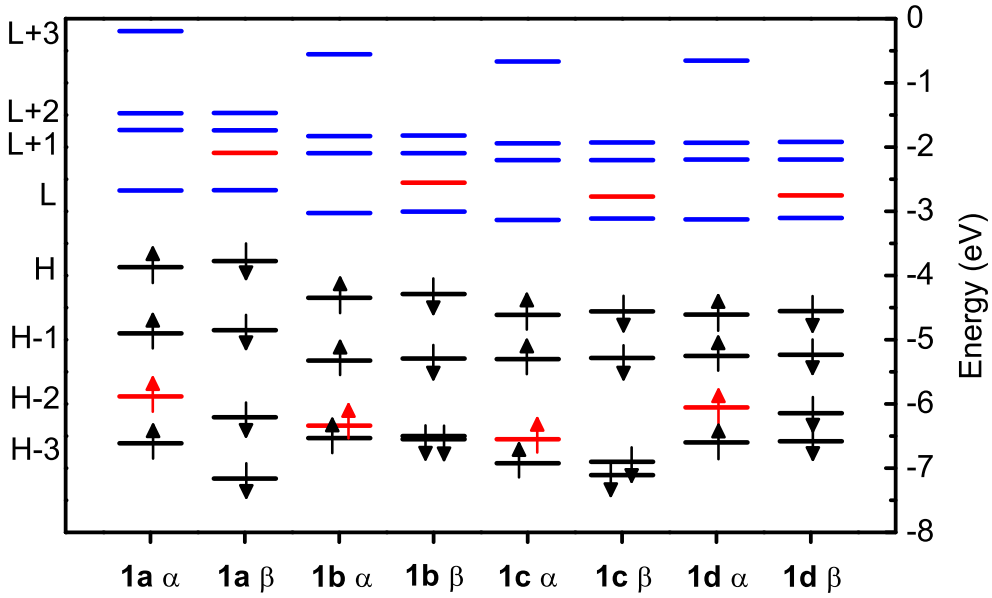

Figure 3.12. Calculated α (↑) and β (↓) orbital energies for all Cu bpy complexes. Line colours represent orbitals with majority contributions from the metal centre (red), catecholate (black) and N-chelate (blue).

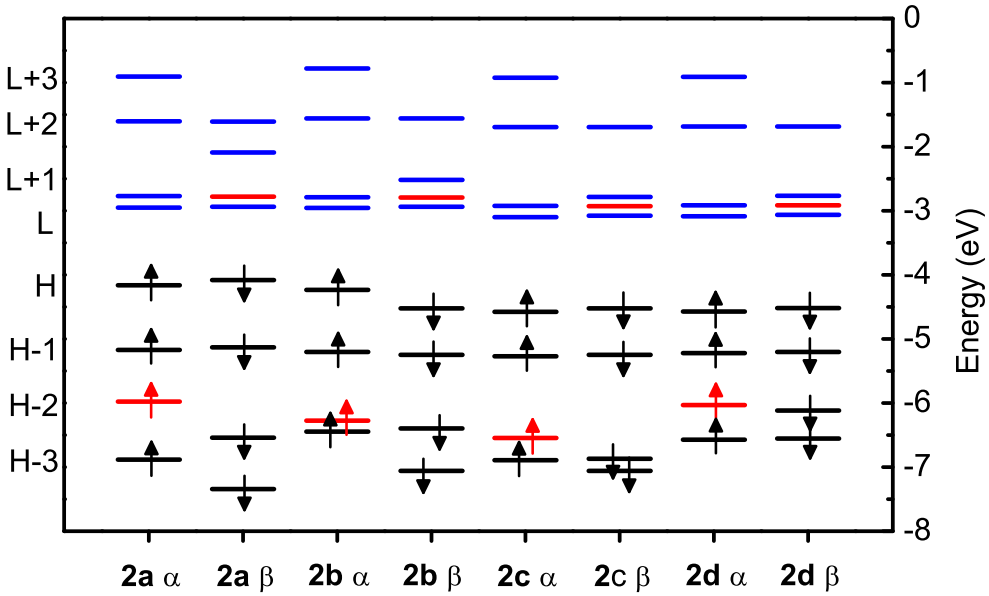

Figure 3.13. Calculated α (↑) and β (↓) orbital energies for all Cu phen complexes. Line colours represent orbitals with majority contributions from the metal centre (red), catecholate (black) and N-chelate (blue).

Table 3.9. Energy levels of frontier orbitals of Cu and Ni complexes calculated by hybrid DFT.

Complex	HOMO (eV)	LUMO (eV)	SOMO (eV)	E_{gap}^{DFT} (eV)	E_{gap}^{Refl} (eV)
Copper					
1a	α = -3.87	α = -2.67	-5.88	α = 1.20	1.08
	β = -3.77	β = -2.67		β = 1.10	
1b	α = -4.35	α = -3.02	-6.34	α = 1.32	1.12
	β = -4.29	β = -3.01		β = 1.28	
1c	α = -4.61	α = -3.13	-6.55	α = 1.48	1.31
	β = -4.56	β = -3.11		β = 1.44	
1d	α = -4.61	α = -3.12	-6.05	α = 1.48	1.33
	β = -4.55	β = -3.10		β = 1.45	
2a	α = -3.83	α = -2.65	-5.88	α = 1.18	1.05
	β = -3.74	β = -2.64		β = 1.09	
2b	α = -4.23	α = -2.96	-6.27	α = 1.28	1.17
	β = -4.17	β = -2.94		β = 1.23	
2c	α = -4.58	α = -3.10	-6.55	α = 1.48	1.20
	β = -4.52	β = -3.07		β = 1.45	
2d	α = -4.57	α = -3.09	-6.03	α = 1.49	1.20
	β = -4.52	β = -3.06		β = 1.46	
Nickel					
5a	- 4.00	- 2.59	*n/a*	1.41	-
5b	- 4.40	- 2.90	*n/a*	1.50	1.01
5c	- 4.74	- 3.04	*n/a*	1.70	1.03
5d	- 4.73	- 3.03	*n/a*	1.70	1.04
6a	- 3.96	- 2.56	*n/a*	1.40	-
6b	- 4.37	- 2.86	*n/a*	1.51	1.02
6c	- 4.70	-3.00	*n/a*	1.71	1.05
6d	-4.69	-2.98	*n/a*	1.71	1.05

3.2.10 Thin-film processing

In order to test the potential conducting properties of the compounds detailed in this chapter, they would need to be processed into uniform materials. Methods such as spin coating, drop casting, and vapour methods are commonly used for this purpose, but due to the discovered lack of solubility and volatility of the compounds these methods are be limited. To work around this problem the method of psuedo-drop casting was employed and is detailed below.

3.2.10.1 FET measurements

Measurements were conducted on pseudo-dropcast films: a drop of a concentrated suspension of the insoluble material in DCM was placed onto the inter-digitated electrode surface of the FET substrate; the DCM evaporated in a matter of seconds leaving a thick film which appeared uniform but amorphous via optical microscopy. Gate voltages (V_G) were varied between -50 and 50 V and source drain (V_D) voltages between -10 and 10 V. No gate dependence was seen for the drain current (I_D) and insulator-type behaviour was observed. This is not surprising given the potential number of grain boundaries and lack of long-range order in the amorphous film. Attempts to deposit the materials onto FETs via vapour methods are ongoing.

3.2.10.2 Vapour processing

Testing was carried out in a tube furnace to determine whether the compounds would sublime under dynamic vacuum and thus be suitable for vacuum deposition onto FET substrates. For each compound the source material was seen to decompose on heating without any noticeable sublimation. However sublimation was witnessed inside a melting point capillary tube during the melting point determination of compound **2c**. Repeating the heating within the tube furnace, and setting the temperature 10 °C below the sublimation/decomposition temperature, a thin film of **2c** was successfully sublimed (**Figure 3.14**). It should be noted also that this was achieved with a medium vacuum of approximately 2×10^{-2} mbar (2 Pa), and therefore it stands to prove the other compounds may yet be sublimable given a stronger vacuum/lower pressures.

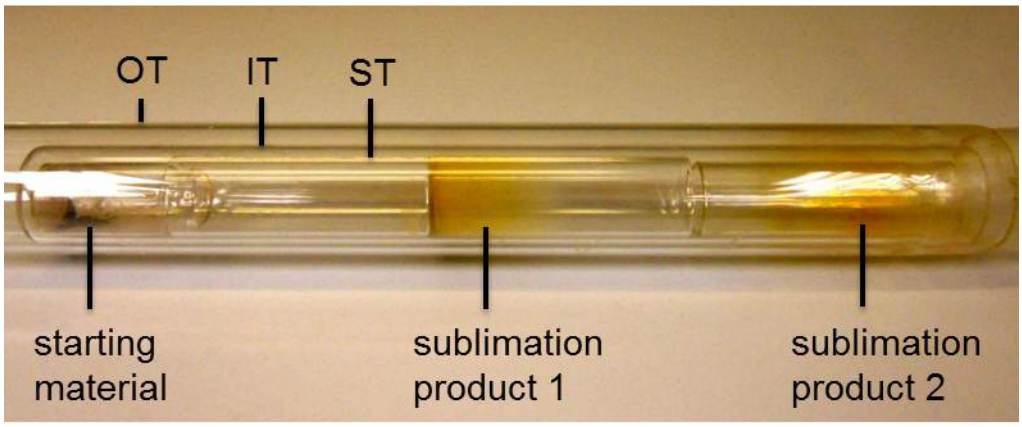

Figure 3.14. Result of vacuum sublimation of **2c** at 240 °C. OT = outer tube, IT = inner tube, ST = sample tubes.

On cleaning the glass sublimation tubes, the thin film dissolved in acetone. Solution absorption spectroscopy of a dissolved film of sublimed Cu(Cl_4cat)(phen) is shown in **Figure 3.15** below. There is a strong absorption at λ_{max} = 283 nm and a very weak absorption at λ_{max} = 283 nm that closely match those observed by Brown in a weak DMSO solution.[8]

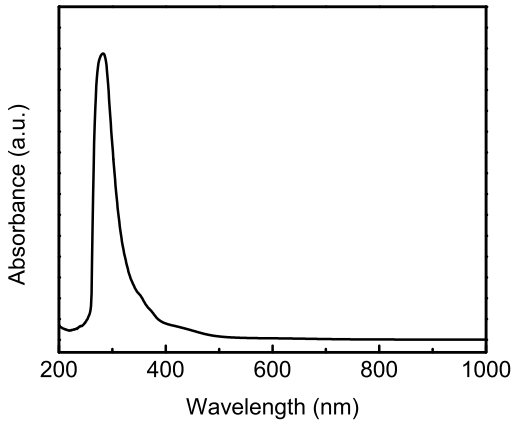

Figure 3.15. Result of vacuum sublimation of **2c** at 240 °C. OT = outer tube, IT = inner tube, ST = sample tubes.

3.3 Conclusions

A series of previously understudied heteroleptic square-planar Cu and Ni complexes with diimine and catecholate ligands has been investigated with regard to their electronic, magnetic and structural properties. The four catecholate molecules that were employed had varying degrees of halogenation, which was seen to influence the electronic structure. The DFT calculations have confirmed the orbital assignment of the solid state absorptions of HOMO-LUMO and their relative energies in the visible spectrum, showing how the frontier orbitals are altered through variation of the ligands. As the donor ability of the catecholate was reduced (through addition of halogen atom substituents on the aromatic ring), the HOMO-LUMO gap was seen to increase. This also has an influence on the compound stability, which is probed further in Chapter 4.

Through the methods of powder EPR, magnetometry and DFT calculations, the unpaired electron of the Cu complexes is confirmed to be localised primarily on the metal atom. Despite existing in a localised charge state, the non-innocent nature of these complexes is confirmed by the calculated location of this unpaired electron in SOMO that is buried beneath two catechol-based π orbitals. This has been subsequently proven by electrochemical experiments in Chapter 4. There are significant contributions to this orbital from the coordinating O and N atoms of the ligands.

Finally, crystal structures previously unattainable by traditional methods were grown by a novel reactant diffusion technique, which allowed investigation into how the geometry and intermolecular interactions of these compounds influenced their solid state and magnetic properties.

3.4 Experimental

Tetrachlorocatechol (Cl_4catH_2). Synthesis adapted from that of Lübbecke et al.[61] Catechol (4.02 g, 36.5 mmol) was stirred in glacial acetic acid (40 ml) and hydrochloric acid (HCl) (36%, 200 ml) until dissolved. The acidic solution was cooled to 0-5 °C in an ice bath before adding hydrogen peroxide (H_2O_2) (30%, 16 ml) in 1 ml aliquots over the course of 2 h. The solution colour turned from light brown to dark orange once all H_2O_2 was added. The solution was left to warm to room temperature whereupon a pale precipitate formed, leaving a red solution. The product was collected by filtration and was washed with cold glacial acetic acid and deionised water. The yield of crude product, a mix of orange, crystalline material and less crystalline, tan powder was 8.941 g (99%). The crude product was recrystallised from 1:2 ethanol:water to give a total yield of 5.56 g (61%) of fine, tan-coloured needles. Calculated (found) for $C_6H_2Cl_4O_2$: C, 29.07 (28.95); H, 0.81 (0.93), N 0.00 (0.00). ^{13}C-NMR (500MHz, d_6-DMSO): δ 119.33 (2 × *C*-Cl), 120.96 (2 × *C*-Cl), 143.53 (2 × *C*-OH).

Tetrabromocatechol (Br_4catH_2). The synthesis was carried out as above for tetrachlorocatechol, only using hydrobromic acid (HBr) (48%, 250 ml) in place of hydrochloric acid. The yield of crude product was 15.251 g (98%), which was recrystallised from 1:2 ethanol:water to give a total yield of 12.05 g (78%) of dark tan needles. Calculated (found) for $C_6H_2Br_4O_2$: C, 16.93 (16.86); H, 0.47 (0.50), N 0.00 (0.00). MS (+EI): *m/z* (%) = 425.6 (100%) [M^+]. ^{13}C-NMR (500MHz, d_6-DMSO): δ 112.62 (2 × *C*-Br), 118.52 (2 × *C*-Br), 141.35 (2 × *C*-OH).

Catecholato(2,2'-bipyridyl)Cu(II), [Cu(cat)(bpy)] (1a). To a stirred solution of $CuSO_4 \cdot 5H_2O$ (1.248 g, 5 mmol) in deionised water (5 ml) under N_2 was added a solution of 1,10-phenanthroline (0.904 g, 5 mmol) in 50% ethanol (5 ml), forming a light blue precipitate. A solution of catechol (0.551 g, 5 mmol) in 50 % ethanol (5 ml) was added to the stirred mixture with no significant colour change. The pH was adjusted to neutral by addition of 2N equivalents of KOH solution,

which led to the formation of a brown precipitate in a clear solution. The product was filtered under vacuum and washed with several times with deionised water and acetone, before drying under vacuum to yield a solid brown product (1.45 g, 87%). Calculated (found) for $C_{16}H_{12}CuN_2O_2$: C, 58.62 (58.51); H, 3.69 (3.60); N, 8.55 (8.46). MS (EI): *m/z* (%) = 327.02 (6.33%) [M^+]. IR ν (powder, cm^{-1}): 1517 (w), 1506 (w), 1478 (s), 1452 (s), 1445 (s), 1254 (s), 1157 (w), 1104 (w), 1056 (w), 1031 (m), 861 (w), 836 (w), 790 (m), 789(m), 765 (s), 744 (s), 737 (s), 729 (m), 613 (s).

Catecholato(1,10-phenanthrolino)Cu(II), [Cu(cat)(phen)] (2a). Solid red-brown product (1.58 g, 90%). Calculated (found) for $C_{18}H_{12}CuN_2O_2$: C, 61.44 (57.67); H, 3.44 (3.30); N, 7.96 (7.30). IR ν (powder, cm^{-1}): 1519 (w), 1479 (s), 1444 (m), 1427 (w), 1254 (s), 1165 (s), 1097 (s), 1044 (s), 1032 (m), 1001 (w), 857 (s), 843 (w), 786 (w), 766 (w), 739 (m), 725 (s), 717 (m), 667 (w), 651 (w), 640 (w), 619 (s), 598 (w), 566 (s), 542 (s), 530 (s), 512 (s).

4,5-Dibromocatecholato(2,2'-bipyridyl)Cu(II), [Cu(Br_2cat)(bpy)] (1b). Solid brown product (2.185 g, 90%). Calculated (found) for $C_{16}H_{10}Br_2CuN_2O_2$: C, 39.57 (39.18); H, 2.08 (1.78); N, 5.77 (5.69). MS (+EI): *m/z* (%) = 482.84 (5.60%) [M^+]. IR ν (KBr disk, cm^{-1}): 3416 (m, b), 1604 (s), 1575 (w), 1566 (w), 1468 (s), 1449 (s), 1349 (m), 1314 (m), 1254 (s), 1225 (m), 1159 (w), 1084 (m), 1053 (w), 1033 (m), 847 (w), 839 (w), 820 (m), 762 (s), 727 (m), 676 (w), 666 (w), 653 (s).

4,5-Dibromocatecholato(1,10-phenanthrolino)Cu(II), [Cu(Br_2cat)(phen)] (2b). Solid red-brown product (2.348 g, 92%). Calculated (found) for $C_{18}H_{10}N_2O_2CuBr_2$: C, 42.42 (38.31); H, 1.98 (1.06); N, 5.50 (4.47). IR ν (powder, cm^{-1}): 1522 (w), 1479 (s), 1452 (m), 1428 (m), 1349 (w), 1316 (w), 1267 (m), 1256 (s), 1224 (w), 1187 (w), 1170 (m), 1164 (m), 1154 (w), 1104 (m), 1093 (s), 1049 (s), 1043 (s), 1031 (m), 996 (w), 973 (w), 961 (w), 927 (w), 876 (w), 868 (w), 858 (s), 840 (m), 822 (w), 786 (w), 766 (w), 740 (w), 725 (m), 718 (s), 682 (w), 650 (m), 626 (m), 618 (m), 593 (s), 567 (m), 559 (w), 538 (s), 527 (s).

Tetrachlorocatecholato(2,2'-bipyridyl)Cu(II), [Cu(Cl$_4$cat)(bpy)] (1c). Solid yellow product (2.058 g, 88%). Calculated (found) for $C_{16}H_8Cl_4CuN_2O_2$: C, 41.27 (40.98); H, 1.73 (1.47); N, 6.02 (5.71). MS (EI): *m/z* (%) = 464.86 (7.35%) [M^+]. IR ν (KBr disk, cm^{-1}): 3550 (m), 3474 (m), 3416 (m), 1630 (w), 1617 (w), 1587 (w), 1519 (m), 1451 (s), 1429 (s), 1374 (m), 1257 (m), 1109 (w), 973 (m), 837 (m), 804 (m), 788 (m), 717 (m).

Tetrachlorocatecholato(1,10-phenanthrolino)Cu(II), [Cu(Cl$_4$cat)(phen)] (2c). Solid dark yellow product (2.060 g, 87%). Calculated (found) for $C_{18}H_8Cl_4CuN_2O_2$: C, 44.15 (44.08); H, 1.65 (1.55); N, 5.72 (5.61). IR ν (KBr disk, cm^{-1}): 3550 (m), 3473 (s), 3415 (s), 1612 (m), 1604 (m), 1472 (m), 1458 (s), 1448 (s), 1376 (m), 1317 (m), 1292 (s), 1260 (m), 1160 (w), 972 (m), 804 (m), 788 (m), 759 (s), 728 (m).

Tetrabromocatecholato(2,2'-bipyridyl)Cu(II), [Cu(Br$_4$cat)(bpy)] (1d). Solid yellow brown product (2.897 g, 91%). Calculated (found) for $C_{16}H_8Br_4CuN_2O_2$: C, 29.87 (30.02); H, 1.25 (1.17); N, 4.35 (4.26). Mp = 250 °C (dec). IR ν (KBr disk, cm^{-1}): 3468 (m), 3413 (s), 3108 (w), 3034 (w), 2523 (w), 2034 (w), 1638 (w), 1611 (m), 1604 (m), 1576 (w), 1568 (w), 1516 (w), 1497 (w), 1472 (s), 1445 (s), 1352 (w), 1315 (m), 1263 (s), 1240 (m), 1169 (m), 1158 (m), 1138 (m), 1058 (w), 1036 (w), 1024 (w), 972 (w), 926 (m), 769 (m), 755 (s), 727 (s), 667 (w), 651 (w), 618 (m), 570 (m), 489 (w), 415 (m).

Tetrabromocatecholato(1,10-phenanthrolino)Cu(II), [Cu(Br$_4$cat)(phen)] (2d). Solid dark yellow product (2.784 g, 83%). Calculated (found) for $C_{18}H_8Br_4CuN_2O_2$: C, 32.39.15 (32.46); H, 1.21 (1.14); N, 4.20 (4.16). Mp = 305 °C (subl.). IR ν (powder, cm^{-1}): 1519 (w), 1444 (s), 1427 (m), 1346 (w), 1263 (m), 1241 (w), 1165 (w), 1107 (w), 1094 (w), 1043 (w), 1030 (w), 925 (w), 835 (s), 747 (m), 739 (m), 724 (m), 716 (s), 641 (w), 619 (m), 610 (m), 594 (w), 567 (s), 547 (w).

Catecholato(2,2'-bipyridyl)nickel(II), [Ni(cat)(bpy)] (5a). Solid green yellow product (0.985 g, 61%). Calculated (found) for $C_{16}H_{12}NiN_2O_2$: C, 59.50 (49.17); H, 3.74 (3.94); N, 8.67 (5.34). IR ν (powder, cm^{-1}): 1472 (m), 1452 (s), 1429 (m), 1314 (w), 1264 (w), 1251 (w), 1154 (w), 1095 (w), 1021 (w), 863 (w), 809 (w), 759 (m), 735 (w), 701 (w), 667 (w), 654 (w), 628 (w), 594 (w), 566 (m), 548 (w), 539 (m), 529 (m), 518 (w), 510 (s), 502 (s), 490 (s), 482 (s), 476 (s), 467 (s), 464 (s).

Catecholato(1,10-phenanthrolino)nickel(II), [Ni(cat)(phen)] (6a). Solid green product (1.535 g, 88%). Calculated (found) for $C_{18}H_{12}NiN_2O_2$: C, 62.30 (46.67); H, 3.49 (3.72); N, 8.07 (5.00). IR ν (powder, cm^{-1}): 1458 (s), 1429 (m), 1373 (w), 1345 (w), 1263 (m), 1104 (w), 1093 (w), 982 (w), 958 (w), 849 (m), 835 (w), 804 (m), 771 (m), 758 (m), 746 (w), 726 (m), 713 (w), 645 (w), 625 (w), 610 (w), 591 (w), 575 (w), 565 (m), 538 (m), 531 (m), 525 (m), 517 (m), 512 (s), 502 (s), 492 (s), 486 (s), 474 (s), 467 (s).

4,5-Dibromocatecholato(2,2'-bipyridyl)nickel(II), [Ni(Br_2cat)(bpy)] (5b). Solid red brown product (2.182 g, 91%). Calculated (found) for $C_{16}H_{10}Br_2NiN_2O_2$: C, 39.97 (39.83); H, 2.10 (2.33); N, 5.83 (5.92). IR ν (powder, cm^{-1}): 1470 (m), 1451 (m), 1348 (w), 1314 (w), 1257 (m), 1169 (w), 824 (w), 807 (w), 761 (m), 736 (w), 720 (w), 664 (w), 653 (w), 625 (w), 607 (w), 575 (m), 566 (m), 539 (m), 530 (m), 514 (s), 506 (s), 487 (s), 478 (s), 469 (s), 463 (s).

4,5-Dibromocatecholato(1,10-phenanthrolino)nickel(II), [Ni(Br_2cat)(phen)] (6b). Solid dark brown product (2.272 g, 90%). Calculated (found) for $C_{18}H_{10}N_2O_2NiBr_2$: C, 42.83 (40.31); H, 2.00 (0.89); N, 5.55 (4.69). IR ν (powder, cm^{-1}): 1517 (w), 1451 (m), 1427 (m), 1379 (w), 1346 (w), 1262 (w), 1104 (w), 870 (w), 843 (m), 809 (w), 759 (w), 725 (m), 646 (w), 626 (w), 599 (w), 575 (m), 565 (m), 542 (m), 518 (s), 499 (s), 486 (m), 482 (m), 468 (s), 459 (s).

Tetrachlorocatecholato(2,2'-bipyridyl)nickel(II), [Ni(Cl_4cat)(bpy)] (5c). Solid red brown product (2.050 g, 89%). Calculated (found) for $C_{16}H_8Cl_4NiN_2O_2$: C,

41.71 (41.41); H, 1.75 (1.48); N, 6.08 (5.97). IR ν (powder, cm^{-1}): 1470 (m), 1451 (m), 1378 (w), 1314 (w), 1264 (w), 983 (w), 804 (m), 759 (m), 739 (w), 722 (w), 653 (w), 626 (w), 604 (m), 590 (w), 566 (s), 538 (m), 514 (s), 507 (s), 503 (s), 489 (s), 485 (s), 474 (s), 466 (s).

Tetrachlorocatecholato(1,10-phenanthrolino)nickel(II), [Ni(Cl_4cat)(phen)] (6c). Solid light brown product (2.060 g, 87%). Calculated (found) for $C_{18}H_8Cl_4NiN_2O_2$: C, 44.60 (45.15); H, 1.66 (1.85); N, 5.78 (5.98). IR ν (powder, cm^{-1}): 1458 (s), 1377 (w), 1345 (w), 1263 (m), 982 (w), 957 (w), 849 (w), 835 (w), 805 (m), 771 (m), 758 (m), 726 (m), 713 (w), 667 (w), 645 (w), 610 (w), 592 (w), 576 (w), 565 (s), 555 (w), 531 (m), 525 (m), 512 (s), 502 (s), 486 (s), 474 (s), 467 (s).

Tetrabromocatecholato(2,2'-bipyridyl)nickel(II), [Ni(Br_4cat)(bpy)] (5d). Solid brick red product (2.760 g, 87%). Calculated (found) for $C_{16}H_8Br_4NiN_2O_2$: C, 30.09 (30.19); H, 1.26 (1.15); N, 4.39 (4.47). IR ν (powder, cm^{-1}): 1450 (s), 1348 (w), 1314 (w), 1281 (w), 1238 (w), 1158 (w), 1058 (w), 1021 (w), 930 (w), 805 (w), 756 (s), 736 (m), 722 (m), 653 (w), 625 (w), 598 (m), 565 (m), 548 (m), 531 (s), 525 (s), 513 (s), 498 (s), 486 (s), 478 (s), 462 (s).

Tetrabromocatecholato(1,10-phenanthrolino)nickel(II), [Ni(Br_4cat)(phen)] (6d). Solid light brown product (2.835 g, 86%). Calculated (found) for $C_{18}H_8Br_4NiN_2O_2$: C, 32.63 (32.74); H, 1.22 (1.14); N, 4.23 (4.14). IR ν (powder, cm^{-1}): 1519 (w), 1451 (s), 1347 (w), 1314 (w), 1263 (w), 1238 (w), 1104 (w), 931 (w), 843 (w) 804 (w), 747 (s), 724 (m), 619 (w), 595 (w), 566 (m), 550 (m), 538 (m), 531 (s), 519 (s), 513 (s), 503 (s), 498 (s), 486 (s), 476 (s), 467 (s).

Variable temperature powder EPR spectra were collected using a JEOL X-band JES-FA200 spectrometer. The samples were sealed in quartz tubes under an inert atmosphere of helium. Measurement was carried out between 4 and 300 K at a center field of 320 mT with a sweep width of 10 mT.

3.4.1 Vacuum sublimation

Vacuum sublimation was carried out using a Thermo Scientific Thermolyne F21130-33 tube furnace. The reactor tube containing the sample was evacuated using a vacuum capable of pressures below 10^{-2} mbar. The temperature of the furnace was set at 200°C and increased by steps of 10°C every hour whilst under the dynamic vacuum until signs of either sublimation or decomposition were observed. Decomposition was indicated by the presence of small, white nucleations of free ligand within the glass tube outside of the tube furnace. The source material would also be heavily darkened or black in colour after decomposition.

A thin film of **2c** was produced in a tube furnace by heating a 30 mg sample in a glass tube (sealed at one end) to 240 °C for 24 h under a dynamic vacuum. The thin film was deposited in two regions around the circumference of the inner glass tube: 10 cm and 25 cm from the source material. Both thin films of product were about 5 cm in length. The film closest to the source material was opaque and thicker in appearance than the film furthest from the source material, which was translucent and had a slightly darker yellow colour. At the very end of the glass tube there had grown over 12 nucleations of red, square crystals, which are awaiting structural analysis.

3.4.2 X-ray crystallography

The structure refinements of **1c**, **2c**, **1d** and **5c** were carried out by the author. Single crystal data were collected on an Agilent Technologies SuperNova diffractometer, using Cu-Kα radiation and graphite monochromator at 100 or 150 K. Data collection, cell refinement and data reduction were carried out using CrysAlis PRO[62] software. The structures were solved using SIR92 direct methods,[63] giving the positions of all non-hydrogen atoms. The structures were refined using CRYSTALS[64] software and the CAMERON[65] structure visualiser and using a full-matrix least-squares refinement procedure, with non-hydrogen atoms refined

anisotropically and hydrogen atoms placed at calculated positions. Full details of the structure refinement are given in **Table 3.10**. Molecular graphics were constructed using Mercury software.[66]

Powder XRD was carried out using the in-house Bruker D8 Advance Powder X-ray diffractometer by Mark Senn, who also carried out the Rietveld refinements of the measured powder diffraction data. The diffractometer was operating in flat-plate mode with monochromated Cu-Kα1 radiation (λ = 1.54046 Å). The data were collected over a range of 6 to 40° over a period of 6 hours. The Rietveld refinements were carried out using TOPAS software.[67]

Table 3.10. Crystallographic data and structure refinement details.

	1c	2c	1d	5c
Chemical formula	$C_{16}H_8Cl_4Cu_1N_2O_2$	$C_{18}H_8Cl_4Cu_1N_2O_2$	$C_{16}H_8Br_4Cu_1N_2O_2$	$C_{16}H_8Cl_4N_2\ Ni_1O_2$
Dimensions / mm	0.47 × 0.05 × 0.03	0.07 × 0.04 × 0.02	0.36 × 0.03 × 0.02	0.18 × 0.03 × 0.02
Morphology	Orange blade	Brown block	Orange block	Brown block
Fw	465.61	489.63	643.41	460.77
Crystal system	Monoclinic	Monoclinic	Triclinic	Monoclinic
Space group	$P2_1/n$	$P2_1/c$	P -1	$P2_1/n$
a / Å	8.77158(13)	13.9350(3)	7.2738(3)	8.7791(3)
b / Å	7.21907(12)	7.16320(16)	14.1625(8)	7.3176(3)
c / Å	25.1149(5)	17.2033(3)	17.8965(8)	24.7544(10)
α / °	90	90	111.891(5)	90
β / °	96.0621(16)	103.0592(18)	99.752(4)	95.694(3)
γ / °	90	90	92.581(4)	90
V / Å^3	1581.45(5)	1672.81	1674.10(15)	1582.43(11)
Z	4	4	4	4
T / K	120	150	120	150
λ(Cu-Kα) / Å	1.54184	1.54184	1.54184	1.54184
Calc. density / g cm^{-3}	1.956	1.944	2.553	1.934
θ range / °	3.540 to 76.323	3.256 to 70.885	3.387 – 74.132	3.589 to 73.961
Limiting indices	-11 ≤ h ≤ 10	-16 ≤ h ≤ 16	-8 ≤ h ≤ 7	-10 ≤ h ≤ 10
	-9 ≤ k ≤ 7	-6 ≤ k ≤ 8	-17 ≤ k ≤ 17	-9 ≤ k ≤ 8
	-31 ≤ l ≤ 31	-20 ≤ l ≤ 21	-22 ≤ l ≤ 22	-30 ≤ l ≤ 30
Refinement method	full-matrix least-squares on F^2	full-matrix least-squares on F^2	full-matrix least-squares on F	full-matrix least-squares on F^2
R_{int}	0.070	0.040	0.055	0.045
Measured reflections	13313	12513	25156	12391
Independent reflections	3264	3183	6645	3140
Observed reflections [$I > 2\sigma(I)$]	3086	2641	5817	2731
Parameters / restraints	226 / 0	224 / 0	451 / 0	226 / 0
R [$I > 2\sigma(I)$]	0.0260	0.0286	0.0853	0.0281
R (all data)[a]	0.0274	0.0365	0.0907	0.0340
R_w (all data)[b]	0.0509	0.0769	0.0631	0.0522
GOF (all data)	1.0035	0.950	1.117	1.031

[a] $R = \Sigma||F_o| - |F_c||/\Sigma|F_o|$. [b] $R_w = [\Sigma w(|F_o| - |F_c|)^2/\Sigma w|F_o|^2]^{1/2}$.

3.4.2.1 Pseudo-dropcasting

The traditional method of dropcasting involves making a saturated solution of the compound of interest in a relatively volatile solvent and placing a drop of it directly on top of the electrode region of a substrate. Once the solvent has evaporated you are left with a thin film of your material. Pseudo-dropcasting differs only in making a fine suspension of the compound of interest rather than a solution. A much thicker film will be formed as a result (**Figure 3.16**).

Figure 3.16. Image of a pseudo-dropcast film of **1c** on the interdigitated electrode region of an FET substrate.

3.5 References

(1) Reese, C.; Bao, Z. N. *Materials Today* **2007**, *10*, 20.

(2) Noro, S.; Chang, H. C.; Takenobu, T.; Murayama, Y.; Kanbara, T.; Aoyama, T.; Sassa, T.; Wada, T.; Tanaka, D.; Kitagawa, S.; Iwasa, Y.; Akutagawa, T.; Nakamura, T. *Journal of the American Chemical Society* **2005**, *127*, 10012.

(3) Noro, S.; Takenobu, T.; Iwasa, Y.; Chang, H. C.; Kitagawa, S.; Akutagawa, T.; Nakamura, T. *Advanced Materials* **2008**, *20*, 3399.

(4) Anthopoulos, T. D.; Setayesh, S.; Smits, E.; Cölle, M.; Cantatore, E.; de Boer, B.; Blom, P. W. M.; de Leeuw, D. M. *Advanced Materials* **2006**, *18*, 1900.

(5) Anthopoulos, T. D.; Anyfantis, G. C.; Papavassiliou, G. C.; de Leeuw, D. M. *Applied Physics Letters* **2007**, *90*, 122105.

(6) Halik, M.; Klauk, H.; Zschieschang, U.; Schmid, G.; Radlik, W.; Ponomarenko, S.; Kirchmeyer, S.; Weber, W. *Journal of Applied Physics* **2003**, *93*, 2977.

(7) Bao, Z.; Lovinger, A. J.; Dodabalapur, A. *Applied Physics Letters* **1996**, *69*, 3066.

(8) Brown, D. G.; Reinprecht, J. T.; Vogel, G. C. *Inorganic and Nuclear Chemistry Letters* **1976**, *12*, 399.

(9) Solomon, E. I.; Chen, P.; Metz, M.; Lee, S.-K.; Palmer, A. E. *Angewandte Chemie International Edition* **2001**, *40*, 4570.

(10) Hayaishi, O.; Hashimoto, K. *The Journal of Biochemistry* **1950**, *37*, 371.

(11) Demmin, T. R.; Swerdloff, M. D.; Rogic, M. M. *Journal of the American Chemical Society* **2002**, *103*, 5795.

(12) Rogic, M. M.; Demmin, T. R.; Hammond, W. B. *Journal of the American Chemical Society* **1976**, *98*, 7441.

(13) Grinstead, R. R. *Biochemistry* **1964**, *3*, 1308.

(14) Abakumov, G. A.; Cherkasov, V. K.; Bubnov, M. P.; Éllert, O. G.; Rakitin, Y. V.; Zakharov, L. N.; Struchkov, Y. T.; Saf'yanov, Y. N. *Russian Chemical Bulletin* **1992**, *41*, 1813.

(15) Buchanan, R. M.; Wilsonblumenberg, C.; Trapp, C.; Larsen, S. K.; Greene, D. L.; Pierpont, C. G. *Inorganic Chemistry* **1986**, *25*, 3070.

(16) Hasty, E. F.; Colburn, T. J.; Hendrickson, D. N. *Inorganic Chemistry* **1973**, *12*, 2414.

(17) Inman, G. W.; Hatfield, W. E.; Drake, R. F. *Inorganic Chemistry* **1972**, *11*, 2425.

(18) Johnston, J. *Journal of the American Chemical Society* **1914**, *36*, 16.

(19) Bridle, C.; Lomer, T. R. *Acta Crystallographica* **1965**, *19*, 483.

(20) Ezhil Raj, A. M.; Jayanthi, D. D.; Jothy, V. B.; Jayachandran, M.; Sanjeeviraja, C. *Inorganica Chimica Acta* **2009**, *362*, 1535.

(21) Quasim, I.; Firdous, A.; Want, B.; Khosa, S. K.; Kotru, P. N. *Journal of Crystal Growth* **2008**, *310*, 5357.

(22) Hidalgo-López, A.; Veintemillas-Verdaguer, S. *Journal of Crystal Growth* **1997**, *178*, 559.

(23) Torres, M. E.; Lopez, T.; Peraza, J.; Stockel, J.; Yanes, A. C.; Gonzalez-Silgo, C.; Ruiz-Perez, C.; Lorenzo-Luis, P. A. *Journal of Applied Physics* **1998**, *84*, 5729.

(24) Kushch, L. A.; Nikolaev, A. V.; Yagubskii, E. B.; Simonov, S. V.; Shibaeva, R. P.; Sadakov, A. V.; Omel'yanovskii, O. E.; Mironov, V. S. *Inorganic Chemistry Communications* **2012**, *21*, 57.

(25) Xu, F.; You, W.; Huang, W. *Acta Crystallographica Section E* **2009**, *65*, m129.

(26) Itoh, S.; Takayama, S.; Arakawa, R.; Furuta, A.; Komatsu, M.; Ishida, A.; Takamuku, S.; Fukuzumi, S. *Inorganic Chemistry* **1997**, *36*, 1407.

(27) Shimazaki, Y.; Huth, S.; Hirota, S.; Yamauchi, O. *Inorganica Chimica Acta* **2002**, *331*, 168.

(28) Bevan, J. A.; Graddon, D. P.; McConnell, J. F. *Nature* **1963**, *199*, 373.

(29) Robertson, I.; Truter, M. R. *Journal of the Chemical Society A: Inorganic, Physical, Theoretical* **1967**, 309.

(30) Bencini, A.; Dei, A.; Sangregorio, C.; Totti, F.; Vaz, M. G. F. *Inorganic Chemistry* **2003**, *42*, 8065.

(31) Bhadbhade, M. M.; Srinivas, D. *Inorganic Chemistry* **1993**, *32*, 6122.

(32) Luo, H.; Lo, J.-M.; Fanwick, P. E.; Stowell, J. G.; Green, M. A. *Inorganic Chemistry* **1999**, *38*, 2071.

(33) Xu, G.-J.; Yan, S.-P.; Liao, D.-Z.; Jiang, Z.-H.; Cheng, P. *Acta Crystallographica Section E* **2005**, *61*, m933.

(34) Toby, B. H. *Powder Diffraction* **2006**, *21*, 67.

(35) *The Rietveld method. (IUCr Monograph on Crystallography, No. 5)*; Young, R. A., Ed.; Oxford University Press: Oxford, 1993.

(36) K. Chattopadhyay, S.; C.W. Mak, T. *Inorganic Chemistry Communications* **2000**, *3*, 111.

(37) David, W. I. F. *Journal of Research of the National Institute of Standards and Technology* **2004**, *109*, 107.

(38) *The Basics of Crystallography and Diffraction (IUCr Texts on Crystallography, No. 5)*; 2nd Edition ed.; Hammond, C., Ed.; Oxford University Press: Oxford, 2001.

(39) Vilminot, S.; Richard-Plouet, M.; AndrÃ©, G.; Swierczynski, D.; BourÃ©e-Vigneron, F.; Marino, E.; Guillot, M. *Crystal Engineering* **2002**, *5*, 177.

(40) Xu, L.; Wang, E.; Peng, J.; Huang, R. *Inorganic Chemistry Communications* **2003**, *6*, 740.

(41) Bleaney, B.; Bowers, K. D. *Proceedings of the Royal Society of London. Series A. Mathematical and Physical Sciences* **1952**, *214*, 451.

(42) Bonner, J. C.; Fisher, M. E. *Physical Review* **1964**, *135*, A640.

(43) Hatfield, W. E. *Inorganic Chemistry* **1972**, *11*, 216.

(44) Chaudhuri, P.; Verani, C. N.; Bill, E.; Bothe, E.; Weyhermuller, T.; Wieghardt, K. *Journal of the American Chemical Society* **2001**, *123*, 2213.

(45) Carlin, R. L. *Magnetochemistry*; Springer-Verlag: Heidelberg, **1986**.

(46) Lintvedt, R. L.; Glick, M. D.; Tomlonovic, B. K.; Gavel, D. P.; Kuszaj, J. M. *Inorganic Chemistry* **1976**, *15*, 1633.

(47) Goodenough, J. B. *Physical Review* **1955**, *100*, 564.

(48) Mikuriya, M.; Toriumi, K.; Ito, T.; Kida, S. *Inorganic Chemistry* **1985**, *24*, 629.

(49) Grove, H.; Julve, M.; Lloret, F.; Kruger, P. E.; Törnroos, K. W.; Sletten, J. *Inorganica Chimica Acta* **2001**, *325*, 115.

(50) Singh, P.; Jeter, D. Y.; Hatfield, W. E.; Hodgson, D. J. *Inorganic Chemistry* **1972**, *11*, 1657.

(51) Marom, N.; Hod, O.; Scuseria, G. E.; Kronik, L. *The Journal of Chemical Physics* **2008**, *128*, 164107.

(52) Aristov, V. Y.; Molodtsova, O. V.; Maslyuk, V. V.; Vyalikh, D. V.; Zhilin, V. M.; Ossipyan, Y. A.; Bredow, T.; Mertig, I.; Knupfer, M. *The Journal of Chemical Physics* **2008**, *128*, 034703.

(53) Vázquez, H.; Jelínek, P.; Brandbyge, M.; Jauho, A.; Flores, F. *Applied Physics A* **2009**, *95*, 257.

(54) Westcott, B. L.; Gruhn, N. E.; Michelsen, L. J.; Lichtenberger, D. L. *Journal of the American Chemical Society* **2000**, *122*, 8083.

(55) Roberts, E. M.; Koski, W. S. *Journal of the American Chemical Society* **1960**, *82*, 3006.

(56) Hathaway, B. J.; Billing, D. E. *Coordination Chemistry Reviews* **1970**, *5*, 143.

(57) Calle, C.; Schweiger, A.; Mitrikas, G. *Inorganic Chemistry* **2007**, *46*, 1847.

(58) Griffith, J. S.; Orgel, L. E. *Quarterly Reviews, Chemical Society* **1957**, *11*, 381.

(59) Whyte, A. M.; Roach, B.; Henderson, D. K.; Tasker, P. A.; Matsushita, M. M.; Awaga, K.; White, F. J.; Richardson, P.; Robertson, N. *Inorganic Chemistry* **2011**, *50*, 12867.

(60) King, E. R.; Betley, T. A. *Journal of the American Chemical Society* **2009**, *131*, 14374.

(61) Lübbecke, H.; Boldt, P. *Tetrahedron* **1978**, *34*, 1577.

(62) *CrysAlis PRO*; Agilent Technologies UK Ltd: Yarnton, England, 2011.

(63) Altomare, A.; Cascarano, G.; Giacovazzo, C.; Guagliardi, A.; Burla, M. C.; Polidori, G.; Camalli, M. *Journal of Applied Crystallography* **1994**, *27*, 435.

(64) Betteridge, P. W.; Carruthers, J. R.; Cooper, R. I.; Prout, K.; Watkin, D. J. *Journal of Applied Crystallography* **2003**, *36*, 1487.

(65) Watkin, D. J.; Prout, K.; Pearce, L. J.; Chemical Crystallography Laboratory, University of Oxford: Oxford, UK, **1996**.

(66) Macrae, C. F.; Bruno, I. J.; Chisholm, J. A.; Edgington, P. R.; McCabe, P.; Pidcock, E.; Rodriguez-Monge, L.; Taylor, R.; van de Streek, J.; Wood, P. A. *Journal of Applied Crystallography* **2008**, *41*, 466.

(67) Coelho, A. *Journal of Applied Crystallography* **2003**, *36*, 86.

4. Square-planar catecholate complexes of copper with solubilising ligands

4.1 Introduction

To further investigate the chemical properties of the series of heteroleptic square-planar transition-metal complexes as detailed in Chapter 3, the core structure of these M(N-chelate)(catecholate) compounds was modified with two different methods of ligand functionalisation that would enable solubility in common organic solvents (**Chart 4.1**). The first class of compounds introduces the modified catecholate 3,5-di-^{t}butylcatechol (^{t}Bu$_2$cat), and uses the N-chelates of either 2,2'-bipyridine (bpy) or 1,10-phenanthroline (phen) as before. The compound Cu(^{t}Bu$_2$cat)(bpy) has been synthesised previously and the crystal structure determined,[1] however the compounds were not studied beyond their electronic absorption[2] and EPR spectra and are found to be relatively unstable (**Section 4.2.1**). The second class is composed of molecules that include a solubilising functionality on the N-chelate ligand. In this way the series of halogenated catecholates from Chapter 3 could be utilised in the structures. The N-chelates for this class of compounds are the alkyl-substituted 4,4'-dinonyl-2,2'-bipyridyl (DNbpy) and the ester-substituted 4,4'-diethoxydicarbonyl-2,2'-bipyridine (DECbpy). The opposing influence of these two substituents on the energy level of the LUMO also allows further tunability of the frontier orbitals.

Therefore by altering the substituents on the constituent ligands, their influence on electronic and solid-state structure can be further investigated. The added solubility will allow further details about the nature of the electronic orbitals to be probed through the techniques of electronic absorption spectroscopy, solution EPR and electrochemical methods, in addition to correlation with computational studies. Soluble compounds were also sought because this will allow the solution

processability into thin films to be tested, an aspect important in the field of molecular electronics.

Chart 4.1. Ligands and complexes presented in this chapter are highlighted in black.

	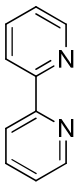 bpy	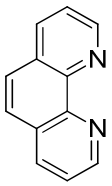 phen	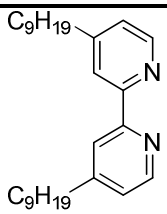 DNbpy	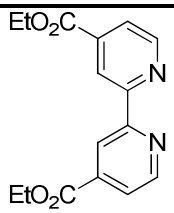 DECbpy
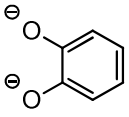 cat	Cu : **1a** Ni : **5a**	Cu : **2a** Ni : **6a**	Cu : **3a**	Cu : **4a**
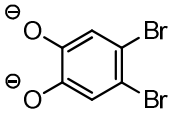 Br_2cat	Cu : **1b** Ni : **5b**	Cu : **2b** Ni : **6b**	Cu : **3b**	Cu : **4b**
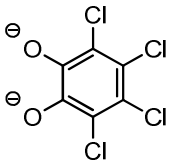 Cl_4cat	Cu : **1c** Ni : **5c**	Cu : **2c** Ni : **6c**	Cu : **3c**	Cu : **4c**
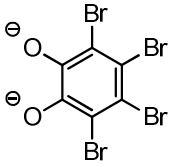 Br_4cat	Cu : **1d** Ni : **5d**	Cu : **2d** Ni : **6d**	Cu : **3d**	Cu : **4d**
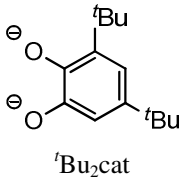 ^{t}Bu$_2$cat	Cu : **1e**	Cu : **2e**	Cu : **3e**	Cu : **4e**

4.2 Results and discussion

4.2.1 Remarks on synthesis

In addition to the catechol oxidation reactions mentioned in Chapter 3 (**Section 3.2.1.1**), square-planar transition-metal complexes of electron-rich catecholates have been seen to undergo an additional type of reaction leading ultimately to their decomposition. Cu(II) complexes of 3,5-Di-^{t}butylcatechol (^{t}Bu$_2$cat) with an ancillary N-chelate of 2,2'-bpyridine and 1,10-phenanthroline (compounds **1e** and **2e** in this chapter) have been shown in the literature to abstract halogen atoms from halogenated solvents resulting in the replacement of the catecholate with two chloride ligands.[3] An example is shown in **Scheme 4.1** with carbon tetrachloride (CCl_4). This reaction is accelerated by the presence of O_2 but occurs even in its absence. The light green Cu(N-chelate)Cl_2 products were formed in quantitative yield.

Scheme 4.1. Halogen atom abstraction of Cu(^{t}Bu$_2$cat)(phen) adapted from Brown.[3]

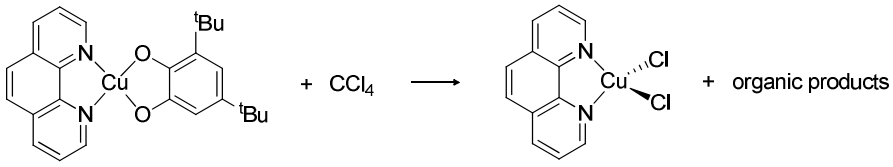

All reactions that used the catechol and 3,5-di-^{t}butylcatechol ligands were performed under an inert atmosphere of N_2 and using degassed solvents, due to the potential for decomposition. Solid compounds of these ligands are stable once dry. All chemicals were reagent grade purchased from Sigma Aldrich and used without further purification, apart from catechol which was purified by sublimation before use.

The general synthetic route to compounds in this chapter is the same as that in Chapter 3. The Cu complexes of 3,5-di-^{t}butylcatechol with 2,2'-bipyridine and

1,10-phenanthroline have been synthesised previously.[1,4] Despite the propensity for decomposition, a crystal structure has been obtained for the 2,2'-bipyridine complex (**1e**) following crystallisation from DCM solution.[1] This literature structure will be used in comparison with the crystal structures determined this thesis.

4.2.2 Structure

Crystalline material was grown for all of the complexes that are stable in solution (e.g. non-cat and $^{t}Bu_2$cat complexes). Of these complexes, single-crystal structures suitable for XRD were obtained for **3b**, **3c**, **3d**, **4c** and **4d**. Previously only one crystal structure of this class of compounds has been obtained,[1] which was that of **1e** despite the difficulties with solution stability. Therefore, together with the structures obtained in Chapter 3, a greater understanding of the influence of the solid state structure to the molecular and material properties can be obtained.

The general numbering scheme used for the compounds in this chapter is given by **Figure 4.1** from the asymmetric unit of **3b**, with the structures of all of the asymmetric units shown in **Figure 4.2**. The compounds containing the DNbpy ligand are nominally formulated as dimers due to the short Cu1-O2′/ Cu1′-O2 bond lengths in the crystal structure (**Table 4.2**), whereas the compounds containing the DECbpy ligand are formulated as monomers. However, as with the compounds in Chapter 3 each molecule in the structures can be related to a dimeric pair via an inversion centre. All of the complexes possess a central Cu(II) ion coordinated by two O atoms of the catecholate and two N atoms of the ancillary ligand. The relevant intramolecular bond lengths and angles are listed below (**Table 4.1**). The intramolecular Cu-O bond lengths in all complexes are between 1.90-1.93 Å. The Cu-N bond lengths are all between 1.97 and 1.99 Å.

In the DNbpy compounds the Cu(II) centre is coordinated by an O atom of the dimer pair, O2′, through an inversion centre, forming a distorted square pyramidal geometry with an elongated apical Cu-O bond. This Cu1···O2′ bond is

between 2.41 and 2.50 Å for all the DNbpy compounds (**Table 4.2**), which is notably shorter than the corresponding distance for **2c** of 2.73 Å (Cu1-O1′, Chapter 3), but longer than that for the strongly-dimerised structure of **1e** of 2.33 Å.[1] The length of this bond increases as the bulk of the catechol ligand increases from Br_2cat to Cl_4cat to Br_4cat. For the DECbpy compounds this interaction is much weaker at 2.831(1) and 2.869(2) for **4c** and **4d** respectively, but stronger than that observed for the unsubstituted bpy complexes **1c** and **1d**, which are between 3.0 and 3.1 Å, in Chapter 3. As a result the geometry of these complexes is square planar, with an RMS deviation from the LS mean plane of less than 0.07 Å for both complexes.

The structures of **3c**, **3d** and **4c** all belong to the monoclinic $P2_1/c$ space group, possessing unit cells with long *a* and *c* axes (**Table 4.17**). The packing is described by alternating stacks of molecules or dimers in the crystallographic *b*-axis. The structures of **3b** and **4d** belong to the triclinic *P*-1 space group, with unit cells with one relatively long axis. In these triclinic structures, the molecular/dimer stacks all orientated at the same angle (**Figure 4.5** and **Figure 4.6**). The stacking is different in nature between the dimers in the DNbpy structures and the molecules in the DECbpy structures; the molecules in **4c** and **4d** stack in a head-to-tail fashion infinitely up the alternating chain (**Figure 4.7** and **Figure 4.8**), whereas the head-to-tail dimers are slipped to promote π-π interactions between the DNbpy ligands (**Figure 4.9**). The bpy-bpy π-stacking distance in the *b*-axis is 3.233 Å, 3.328 Å and 3.314 Å for **3b**, **3c** and **3d** respectively. This results in a significant shifting of the position of Cu centres between dimers with respect to each other (intradimer Cu···Cu′ = 3.1-3.2 Å, interdimer Cu···Cu″ = 5.4-5.5 Å). The long, flexible alkyl chains of the DNbpy complexes pack in the same direction, with one of the chains bending towards the other to form a hydrophobic region within the crystal structure, separating the dimer stacks. The CO_2Et_2 groups of the DECbpy promote short C-H···O contacts between the molecules of 2.5 Å.

Table 4.1. Selected interatomic distances (Å), bond angles (°) and torsion angles (°) for **3b**, **3c**, **3d**, **4c** and **4d**. O2 is the atom that forms an elogated Cu-O bond to the form the dimeric pair.

Parameter	**3b**	**3c**	**3d**	**4c**	**4d**
Cu-O1	1.918(2)	1.913(2)	1.905 (4)	1.908 (1)	1.907 (2)
Cu-O2	1.929(2)	1.932(2)	1.927 (4)	1.904 (1)	1.900 (2)
Cu-N1	1.989(2)	1.969(3)	1.973 (5)	1.972 (2)	1.971 (3)
Cu-N2	1.993(3)	1.982(3)	1.985 (5)	1.990 (2)	1.977 (3)
O1-C1	1.328(4)	1.327(4)	1.321 (8)	1.324 (2)	1.322 (4)
O2-C2	1.347(4)	1.338(4)	1.336 (8)	1.331 (2)	1.330 (4)
O1-Cu-O2	87.5(1)	86.9(1)	86.6 (2)	87.6 (1)	87.69 (0)
O1-Cu-N1	96.3(1)	94.8(1)	94.8 (2)	96.1 (1)	95.99 (1)
O1-Cu-N2	162.8(1)	166.5(1)	167.1 (2)	173.0 (1)	173.52 (2)
O2-Cu-N1	175.0(1)	175.0(1)	175.2 (2)	175.5 (1)	175.85 (1)
O2-Cu-N2	94.8(1)	96.2(1)	96.7 (2)	94.0 (1)	94.35 (1)
N1-Cu-N2	80.6(1)	81.1(1)	81.0 (2)	82.0 (1)	81.79 (2)
O1-C1-C2-O2	1.4(4)	2.2(5)	4.2(8)	3.5(3)	3.3(5)
N1-C11-C12-N2	2.4(4)	0.6(4)	0.6(8)	0.6(3)	1.7(4)

Table 4.2. Selected intermolecular and interplanar distances (Å), angles (°) and displacements Δ (Å) from least-squares (LS) planes. Atoms in nearest neighbour molecules are denoted by a single prime (′) and next nearest neighbour molecules by a double prime (″). [a]$RMS_{molecule}$ is the root mean square deviation of atoms from the LS plane through the molecule.

	3b	**3c**	**3d**	**4c**	**4d**
Cu1···Cu1′	3.1767(6)	3.1295(6)	3.113(1)	3.3547(4)	3.3734(8)
Cu1···Cu1″	5.5088(6)	5.4144(6)	5.491(1)	3.8488(4)	4.9436(9)
Cu1···O2′	2.414(2)	2.475(2)	2.495(4)	2.831 (1)	2.869(2)
Cu1···O″	6.161(2)	6.101(3)	6.185(4)	4.718(1)	5.021(3)
Cu1-O2-Cu1′	93.35(8)	89.62(9)	88.5(2)	87.97(5)	87.58(9)
LS→LS′	3.516	3.575	3.562	3.229	3.062
LS→LS″	2.920	2.972	3.027	3.246	3.180
[a]$RMS_{molecule}$	0.226	0.278	0.284	0.067	0.068
$\Delta Cu1_{basal}$	0.168	0.149	0.142	0.062	0.141
$\Delta Cu1_{molecule}$	0.475	0.504	0.487	0.161	0.087
$\Delta O2_{molecule}$	0.632	0.609	0.601	0.250	0.142

1e[1]: Cu1···Cu1′ = 3.0742(8), Cu1···O2′ = 2.330(2), Cu1-O2-Cu1′ = 92.5(1)

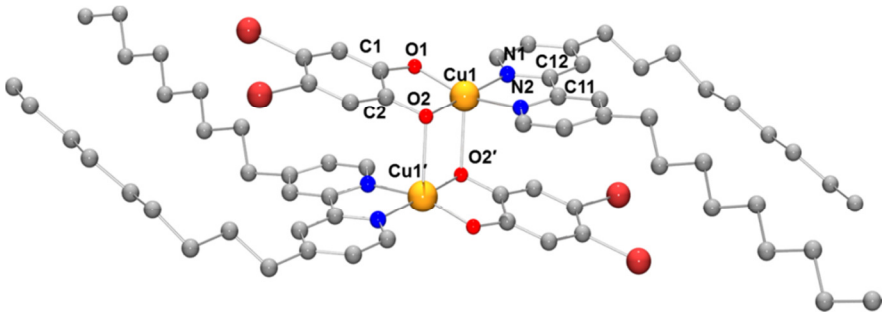

Figure 4.1. General numbering scheme of the compounds in this chapter as represented by the dimer unit of **3b**.

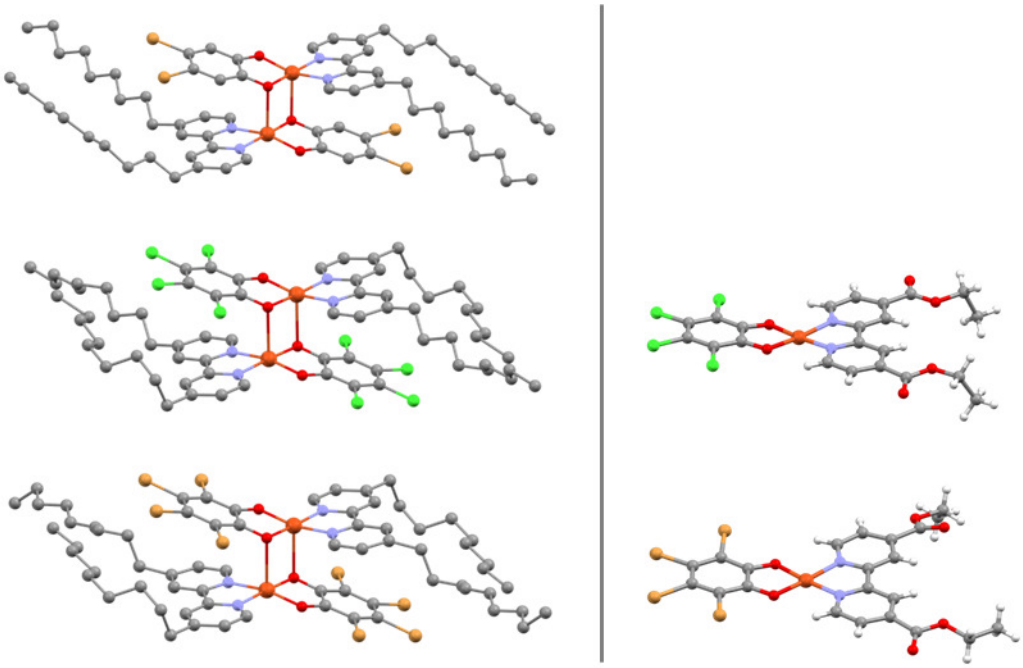

Figure 4.2. Structures of the dimers of **3b** (top left), **3c** (middle left) and **3d** (bottom left) and monomers of **4c** (middle right) and **4d** (bottom right). H atoms are omitted from the DNbpy structures.

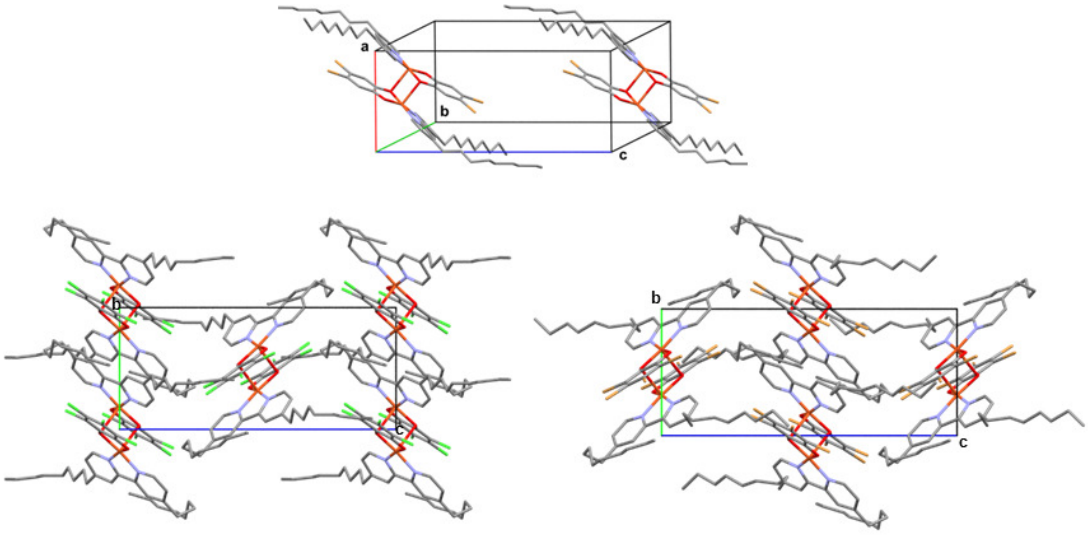

Figure 4.3. Unit cell diagrams for **3b** (top), **3c** (bottom left) and **3d** (bottom right). H atoms are omitted.

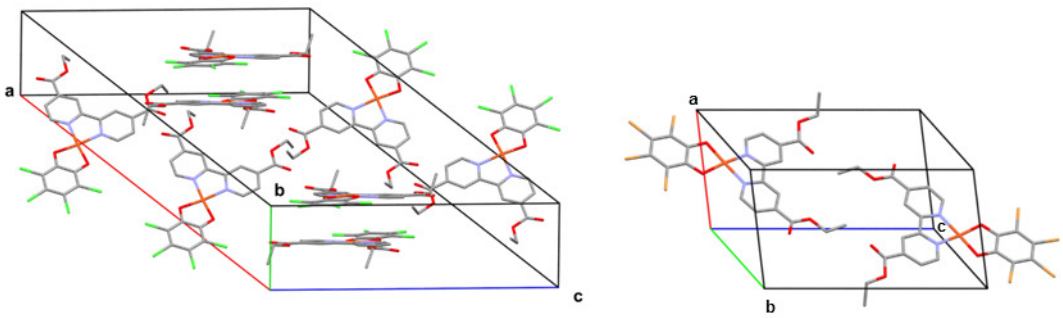

Figure 4.4. Unit cell diagrams of **4c** (left) and **4d** (right). H atoms are omitted.

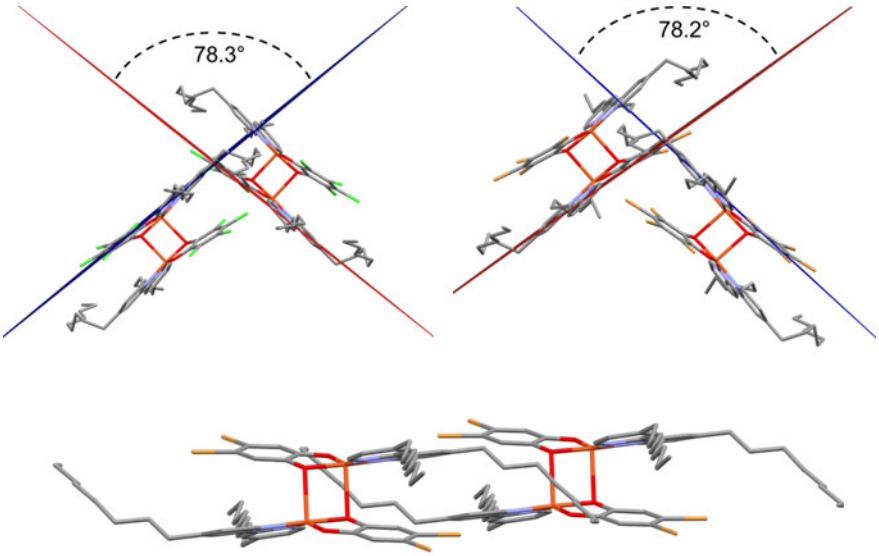

Figure 4.5. Alignment of dimer stacks in DNbpy complexes: there is an angle between adjacent dimer stacks of 78.3° in **3c** (top left) and 78.2° in **3d** (top right), whereas the dimers are coplanar in **3b** (bottom).

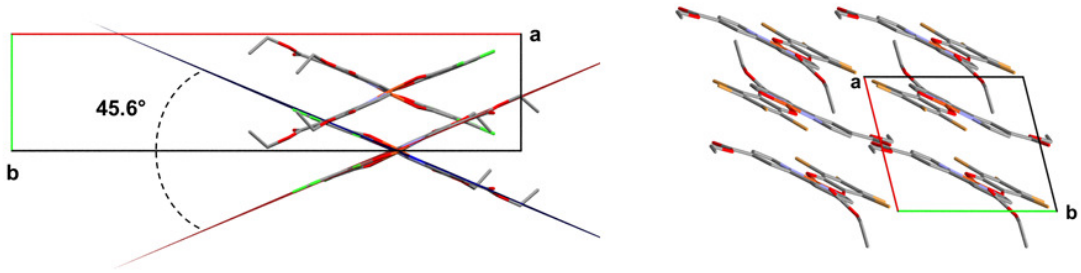

Figure 4.6. Alignment of dimer stacks in DECbpy complexes **4c** (left) and **4d** (right). There is a 45.6° angle between adjacent dimer stacks in **4c**, whereas the dimers are coplanar in **4d**.

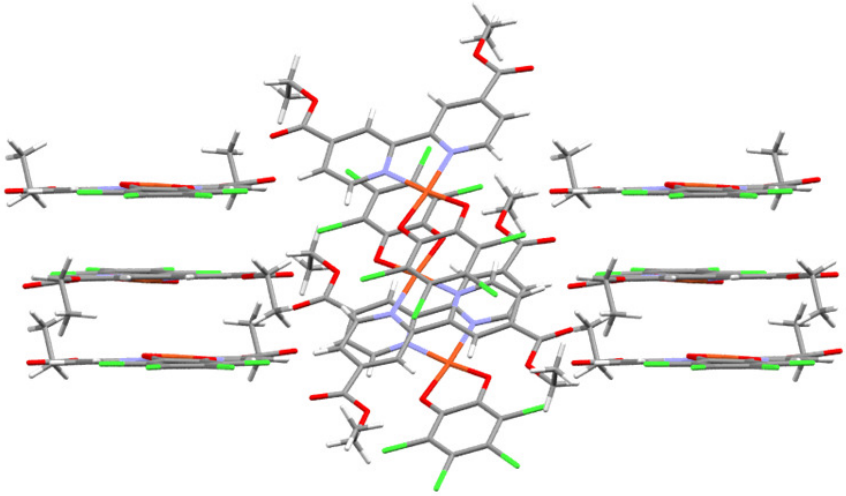

Figure 4.7. Crystal packing of **4c**.

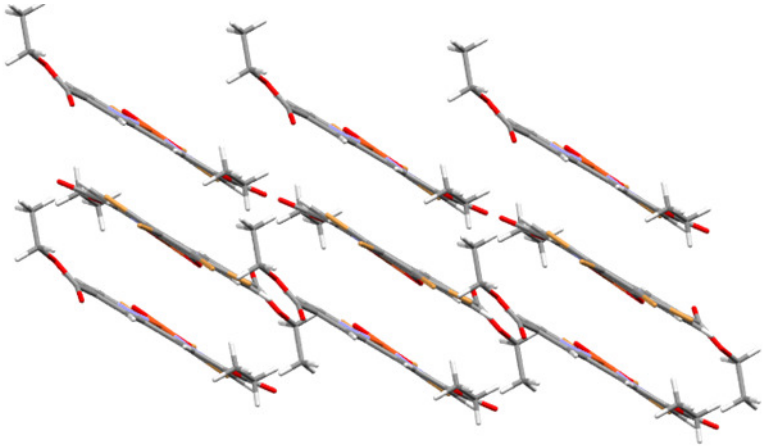

Figure 4.8. Crystal packing of **4d**.

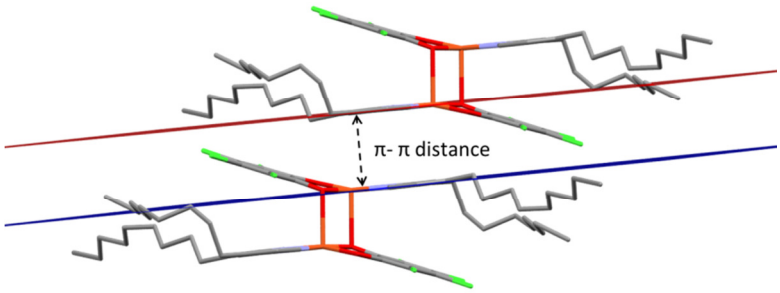

Figure 4.9. Example of interdimer π-stacking between the DNbpy ligands in the stacking direction of the crystal structures of DNbpy complexes, represented by **3c**.

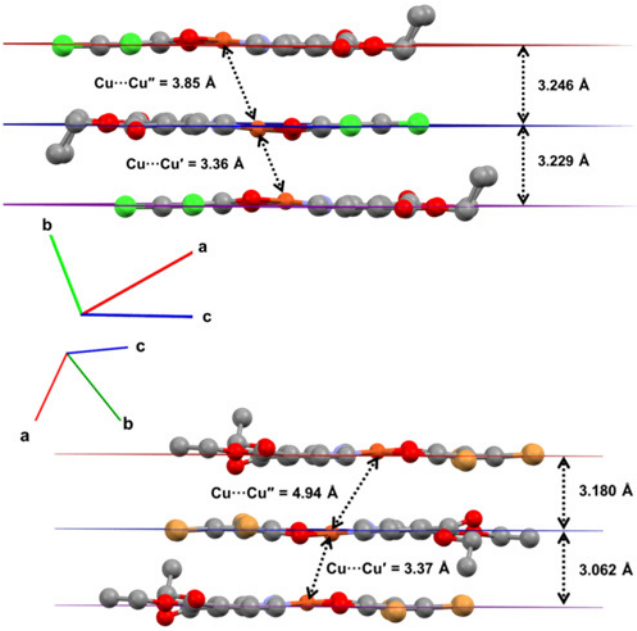

Figure 4.10. Interdimer and interplanar distances in **4c** (top) and **4d** (bottom).

4.2.3 Electronic absorption spectroscopy

Information about the nature of the electronic structure is obtainable by studying the electronic absorption spectra in solution. The complexes analysed are square planar and heteroleptic (3-series compounds are dimers in the solid state), containing one readily-oxidisable donor catecholate ligand and one bidendate, heteroaromatic acceptor ligand with low-energy, empty π*-orbitals. Square-planar complexes of this type in the literature are characterised by charge transfer (CT) absorptions in the visible region of the absorption spectrum that are primarily interligand (or ligand-to-ligand) in nature (LLCT),[2,5-7] from the HOMO that is primarily based on the donor ligand, to the LUMO that is based on the acceptor ligand.[5] This assignment is confirmed by studying the systematic effect of changing the donor ligand, acceptor ligand and central metal ion; it is found that both donor and acceptor ligands need to be present, whereas the metal ion has little influence on the absorption. In cases where the HOMO does have significant contributions from the metal ion, such as in some Group 10 dithiolenes, the CT transition is regarded as having metal-to-ligand and ligand-to-ligand contributions.[7] These systems also show

strong negative solvatochromism, where the peak absorption wavelength increases with increasing solvent polarity.

The solution absorption and powder reflectance spectra for all reported complexes have been measured in the UV/Vis/NIR region of the electromagnetic spectrum, typically in the range of 200-1200 nm for solution spectra and 200-2000 nm for powder spectra. The absorption data from all of the measured spectra are included in **Table 4.3**. All the complexes display the same general features. There are at least two intense absorptions (molar absorptivities, $\varepsilon > 17{,}000$ mol^{-1} cm^3 cm^{-1}) in the UV region of the spectrum. The peak absorption position does not change with changing catecholate, and is very similar to the respective uncoordinated N-chelate ligands. Therefore these absorptions have been assigned to intraligand π-π^* transitions of the N-chelate. There is one strong absorption band in the visible region of the solution spectrum ($\varepsilon \approx 1000 - 1700$ mol^{-1} cm^3 cm^{-1}), which depends significantly on the nature of the catechol ligand within a series of compounds that have the same N-chelate. This absorption is assigned to a LLCT from the catecholate to N-chelate, which is further validated by the electrochemical (**Section 4.2.5**) and DFT (**Section 4.2.6**) results, which both confirm the origin of the HOMO to be catecholate in nature and the origin of the LUMO to be N-chelate in nature.

The visible absorption spectra for **1e** and **2e** are shown in **Figure 4.11** (left). Both complexes have an absorption peak at 550 nm, but the peak in both complexes at higher energy around 410-430 nm is not observed in the literature.[2] This absorption actually corresponds with the start of the compound decomposition in DCM solution, as confirmed by a UV/Vis stability study of **2e** over the course of a few hours (**Figure 4.11** (right)). The absorption at 550 nm decreases and the absorption at 430 nm increases, corresponding with a colour change from dark blue to bright green. There is an isosbestic point at around 490 nm indicating clean conversion between two products. As detailed in **Section 4.2.1**, these compounds are known to react in the presence of halogenated solvents to form green Cu(N-chelate)Cl_2, therefore it is likely that Cu(phen)Cl_2 is being formed. The high-energy

N-chelate intraligand π-π^* bands remain essentially unchanged and are not shown in the spectra. A similar decomposition for catechol compounds of DNbpy and DECbpy was also observed (*vide infra*).

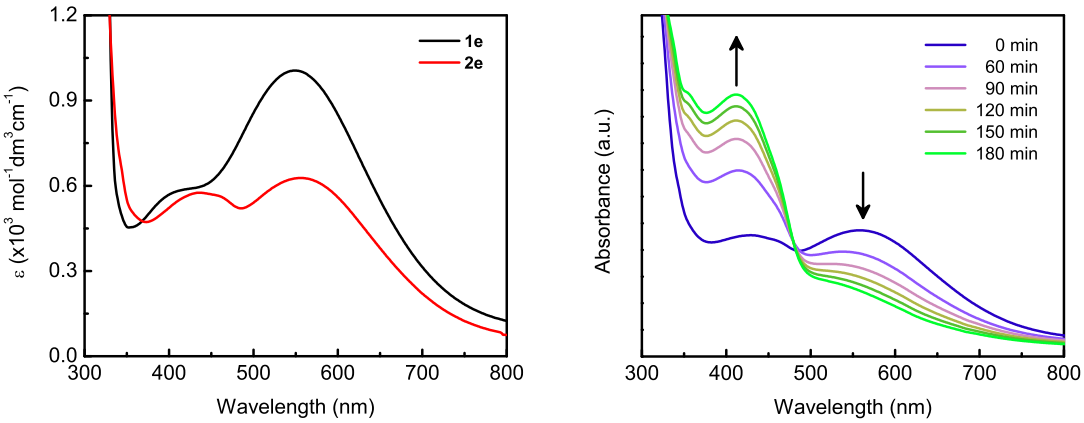

Figure 4.11. Left: absorption spectra of **1e** and **2e** in DCM. Right: oxidation of a DCM solution of **2e** in a sealed cuvette that has been exposed to air.

The absorption spectra of all DNbpy and DECbpy compounds are shown in **Figure 4.12**. Both sets of compounds display the LLCT band in the visible region of the spectrum, between 410 and 470 nm for the DNbpy compounds and 430 and 520 nm for the DECbpy compounds (**Table 4.3**). The DNbpy compounds display additional weak-intensity absorptions in the NIR region. The molar absorptivities for these absorptions are about 50 to 60 mol^{-1} dm^3 cm^{-1}. No similar absorption was observed for the DECbpy compounds. However, there are NIR absorptions in the diffuse reflection spectra of all of the compounds reported (*vide infra*). It is possible that the origin of this solution-based NIR peak is from intermolecular interactions: the DNbpy compounds are dimeric in the solid state whereas the DECbpy compounds are not. Therefore the presence of this very weak NIR absorption peak in the solution spectra of the DNbpy compounds may in fact be caused by a proportion of molecules that are dimerised even in solution. The peak absorption obeyed the Beer-Lambert Law indicating it was not due to aggregation.

As mentioned above, solutions of catechol compounds **3a** and **4a** are prone to decomposition. A stability experiment was carried out on a 0.25 mM solution of **3a** in 1,1,2'-trichloroethane (1,1,2'-TCE) (**Figure 4.13** (left)). The charge-transfer band around 480 nm very rapidly decreases in intensity within the first 5 minutes, and the absorption bands at 386 and 680 nm gradually increase over the course of an hour. By contrast, the compounds of the catecholates Br_2cat, Cl_4cat, and Br_4cat remain stable in solution indefinitely, as indicated by the absorption spectrum of **3c** in 1,1,2-TCE solution after 0 and 72 hours (**Figure 4.13** (right)).

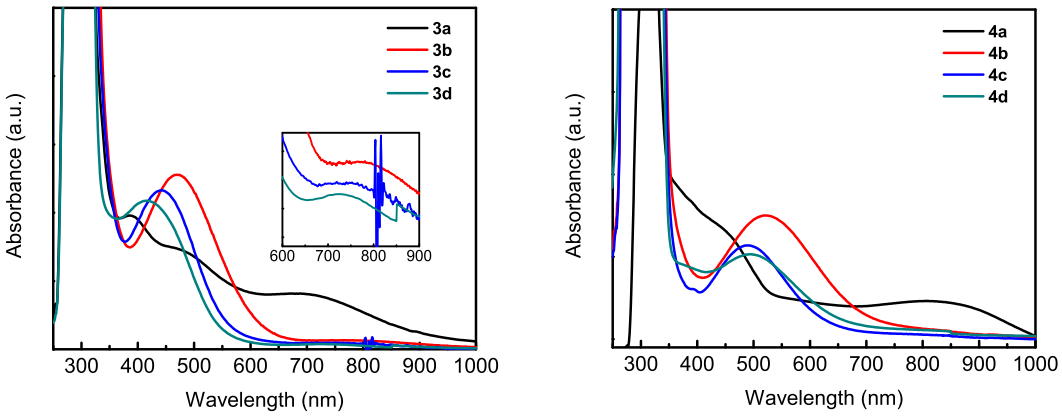

Figure 4.12. Absorption spectra of DNbpy compounds in THF solution (left) and DECbpy compound in DMF solution (right). The y-axis is represented by absorbance with arbitrary units because of the instability of the catechol compounds **3a** and **4b**. The spectra are measured from solutions of the same approximate concentration and molar absorptivities (where given) are presented in **Table 4.3**.

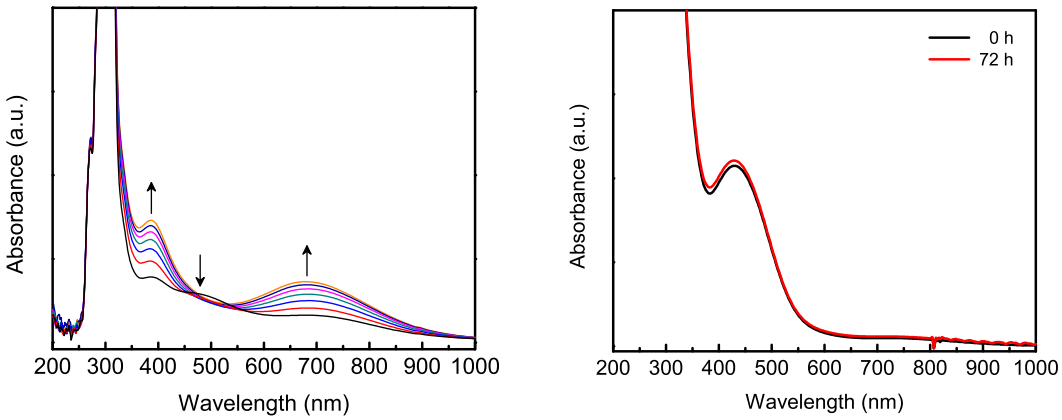

Figure 4.13. Stability of Cu DNbpy compounds. Left: decomposition of a 1,1,2-TCE solution of **3a** in a sealed cuvette that has been exposed to air over 1 h; scans were 1 minute in duration and were taken every 5 minutes. Right: air stability of **3c** in 1,1,2-TCE solution over 72 h.

In addition, the absorbance spectra obtained by diffuse reflectance spectroscopy of powder samples can lead to an understanding of the electronic structure in the solid state. The diffuse reflectance spectra were measured for all the compounds in the range of 200 to 1200 nm, with details of the UV/Vis/NIR solid state absorptions listed in **Table 4.3**. The spectra for all DNbpy and all DECbpy are displayed in **Figure 4.14**. As with the solution spectra, the absorptions in the UV region of the spectrum from about 200 to 320 nm do not change with different catechol ligands. The same general trend that is observed in Chapter 3 is observed with the compounds in this chapter, with the peak positions of the visible and NIR absorption maxima blueshifting with increasingly-stabilised catechol ligands. The absorption peak ranges of compounds from all four different series of N-chelate compounds (with two from Chapter 3) are compared in **Table 4.4**. The peak absorption positions for compounds with a given catecholate ligand generally increase in wavelength in the following order, DNbpy < phen ≈ bpy < DECbpy. Considering the position of the LUMO and the nature of the transitions, this trend agrees with the energy level considerations of the substituents on the N-chelate molecule: the alkyl groups on the DNbpy ligand destabilise the LUMO causing it to raise in energy; the ester groups on the DECbpy on the other hand stabilise the LUMO and thus lower it in energy. These results are confirmed by the energy level positions that have been calculated by DFT methods (**Section 4.2.6**).

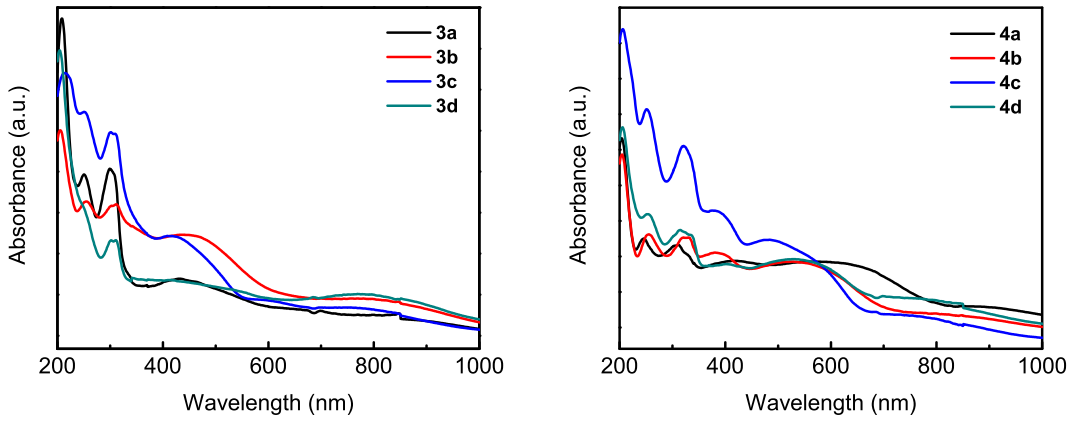

Figure 4.14. Diffuse reflectance spectra of DNbpy (left) and DECbpy (right) compounds.

Table 4.3. Absorption maxima (nm) of Cu catecholate complexes from absorption and diffuse reflectance spectroscopy.[†]

Solution absorption maxima (nm) (onset (nm))						
1e				550 [1040]		
2e				550 [1710]		
3a	272	301	308	470		
3b		300 [19,000]	308 [21,700]	460 [1275]	(610)	770 [65]
3c		300 [21,700]	306 [20,100]	434 [1063]	(560)	730 [50]
3d	272	301 [20,790]	310 [17,700]	413 [1475]	(550)	726 [60]
4a			324	437	(530)	806
4b	269		316	520	(685)	
4c	269		316	489	(635)	
4d	265		313 [16,900]	494 [990]	(650)	

Reflectance absorption maxima (nm) (onset (nm))						
1e	211	251	304	395	596	
2e	210	250	320	392	600	
3a	209	250	299	308	450 (640)	800
3b	206	255	302	311	438 (615)	780
3c	212	250	301	310	410 (550)	760
3d	204	249	302	311	413 (570)	770
4a	205	246	312	417	568 (790)	870
4b	205	255	321	382	535 (700)	797
4c	206	251	321	377	483 (660)	711
4d	206	251	321	403	510 (670)	725

[†]The numbers in square brackets represent the molar extinction coefficient measured in units of mol^{-1} dm^3 cm^{-1}.

Table 4.4. Summary of absorption maxima peak ranges for different series of N-chelate complexes measured from diffuse reflectance spectroscopy.

N-chelate series	Wavelength range of absorption maxima (nm)	
	Visible band	NIR band
DNbpy	410 - 450	760 - 800
[†]phen	420 - 480	750 - 820
[†]bpy	430 - 500	700 - 820
DECbpy	480 - 570	710 - 870

[†]Summarised from values in Chapter 3.

4.2.4 EPR spectroscopy

Room-temperature solution EPR measurements were recorded on **1e** and **2e** in dichloromethane (DCM). These compounds were the most soluble and therefore formed the strongest concentrations that would give a well-resolved EPR spectrum.

This gives accurate information about the the *g*-value, which is important for formulating the location of spin density and when determining the magnetic properties of these materials (**Section 0**). Despite potential instability in solution, the compounds were not seen to decompose throughout the experiment (evidenced by the lack of solution colour change or variation in the EPR signal). Both compounds showed nearly identical spectra, and are in agreement with that recorded by Buchanan for **1e**.[1] The spectrum of **1e** is shown in **Figure 4.15** with a four-line splitting pattern typical of a monomeric Cu(II) species. There is hyperfine coupling (*A*) to the two N atoms of the N-chelate ligand, which is observable at the high-field end of the spectra. The line pattern was simulated to obtain values of g_{iso} = 2.10, A (1 × $^{63/65}$Cu) = 90.0/97.0 × 10^{-4} cm^{-1} and A(2 × ^{14}N) = 10.5 × 10^{-4} cm^{-1}. The *g* factor was corrected with respect to DPPH, and agrees well with other Cu(II) square-planar compounds in the range of 2.0 to 2.2.[1,8,9]

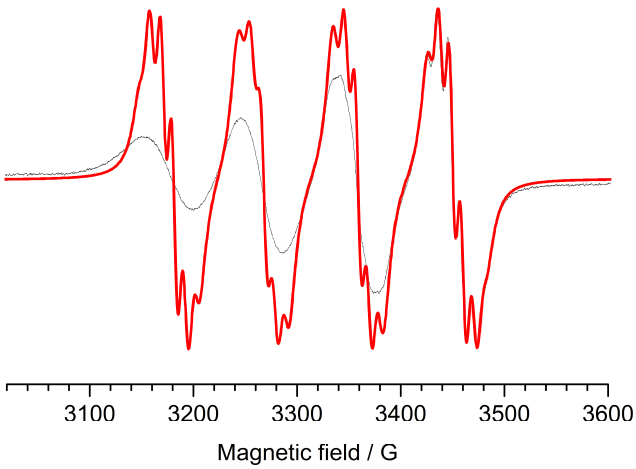

Figure 4.15. Black line: experimental EPR spectrum of **2e** in DCM at 298 K (9.51 GHz). Red line: simulated EPR spectrum of **2e** with calculated parameters g_{iso} = 2.09865, A (1 × $^{63/65}$Cu) = 90.0/97.0 G, A (2 × ^{14}N) = 10.5 G.

4.2.5 Electrochemistry

The electrochemical properties of all of compounds apart from **3a** (due to instability) were investigated using the techniques of cyclic voltammetry (CV) and differential pulse voltammetry (DPV). These experiments can lead not only to

information about the electrical and chemical stability of the compounds, but also to the experimental determination of the energy and location of the frontier orbitals. In particular, information can be gained about how the individual HOMO and LUMO orbitals are altered through variation within the molecular species, which is useful in assessing the potential use of materials as conducting materials in electronic devices. Qualifications regarding electrochemical reversibility are considered according to values of the anodic peak to cathodic peak separation potential, ΔE, and ratio of anodic and cathodic peak currents, $|i_{pa}/i_{pc}|$, which are set out in Chapter 2 (**Section 2.2.1**).

Cyclic voltammograms of **1e** and **2e** were measured in a DCM solution with 0.3 M $TBABF_4$ supporting electrolyte, with the data displayed in **Table 4.5**. The CV scans for **1e** and **2e** are shown in **Figure 4.16**, scanning initially to oxidative potentials. The potentials are referenced to the Fc/Fc^+ redox couple to allow comparison between voltammograms. At reductive potentials there is a single, irreversible cathodic peak (E_{pc}) for both compounds at approximately -1.5 V and -1.7 V for **1e** and **2e** respectively. These reduction peaks can be assigned to a LUMO orbital primarily located on the N-chelate ligand by analogy with other square-planar systems with bpy or phen ligands that possess low-lying empty π^* orbitals. This assignment is also in agreement with the DFT calculations that place the LUMO energy level of **1e** lower than that of **2e** (**Section 4.2.6**). Initial oxidative scans of **1e** result in a broad, anodic process at approximately -0.27 V, which is coupled to a cathodic process at about -0.5 V. Given the broad peak shapes and peak-peak separation, this process may correspond to a two-electron oxidation of the complex. This is reasonable given the propensity of catechol to undergo a two-electron oxidation to benzoquinone, and the electron-rich nature of the $^tBu_2$cat ligand that may make this process even more facile. Furthermore, the scanning to positive potentials of **2e** results in two resolved anodic peaks at -0.32 and -0.04 V that span the broad anodic peak of **1e**. These peaks are also coupled to a cathodic process at about -0.5 V. This is further proof of the correct assignment of the HOMO to the catecholate moiety of the compounds.

The redox activity was further examined using DPV, which identified the same redox processes as CV but with arguably better clarity. Potentials were scanned from a potential of zero *vs*. Ag/AgCl to positive and negative potentials respectively, and subsequently referenced to Fc/Fc^+, in order to create the voltammograms displayed in **Figure 4.17**. The first oxidation process occurs at $E_{1/2}$ = -0.42 V *vs*. Fc/Fc^+ for both compounds (**Table 4.6**), which is indicative of the HOMO assignment to the ^{t}Bu$_2$cat ligand that is present in both compounds. Compound **2e** displays an addition anodic peak at -0.12 V, whereas the area underneath first oxidation peak of **1e** integrates to a current that is equal to both of the first two oxidation peaks of **2e**. This is further emphasis that these oxidations are catechol based to form the benzoquinone form of the ligand. Once the catecholate has been oxidised to the benzoquinone, the now neutral donor ligand may induce decomplexation, resulting in the weak current response of the reverse DPV scans.

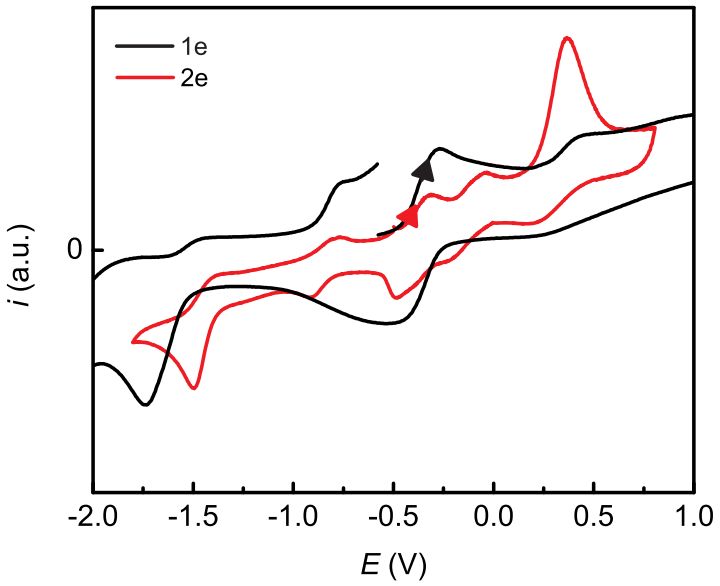

Figure 4.16. Cyclic voltammograms of **1e** and **2e** in 0.3 M $TBABF_4$ DCM solution. Current values are normalised for peak comparison as different scan rates were used (1.0 V s^{-1} for **1e** and 0.1 V s^{-1} for **2e**). Potentials are referenced *vs*. Fc/Fc^+.

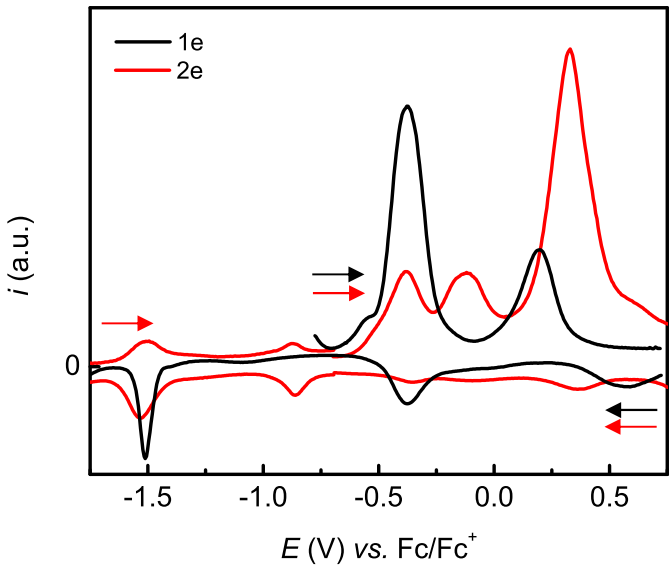

Figure 4.17. Differential pulse voltammograms of **1e** and **2e** in 0.3M $TBABF_4$ in DCM solution. Current values are normalised for peak comparison. Potentials are referenced *vs.* Fc/Fc^+: $E_{1/2}$ = 0.576 V for **1e** and 0.498 V for **2e**. Arrows indicate the starting potential and scan direction of the DP scans.

Table 4.5. Selected electrochemical values observed from CV for **1e** and **2e** in DCM solution of 0.3 M $TBABF_4$ supporting electrolyte. Scan rate = 0.1 V s^{-1}. Potentials are referenced *vs.* Fc/Fc^+, where ΔE = 100 mV.[†]

Complex	$E_{1/2}^{red}$ (V)	ΔE (mV)	$\lvert i_{pa}/i_{pc} \rvert$	$E_{1/2}^{ox}$ (V)	ΔE (mV)	$\lvert i_{pa}/i_{pc} \rvert$	E_{gap} (eV)
1e	-1.65[C]	115	*n/a*	-0.42[B]	-145	0.94	1.08
2e	-1.47[C]	55	*n/a*	-0.42[B]	-163	0.84	1.05

[†]Definition of terms in the table are given in Chapter 2. For processes defined as irreversible, $E_{1/2}^{red/ox} = (E_p + E_{p/2})/2$ and $\Delta E_{p/2} = (E_p - E_{p/2})$, where $E_{p/2}$ is the half-peak potential. [A]Electrochemically-reversible redox process. [B]Partially-reversible redox process (presence of redox activity within 200 mV of the peak potential). [C]Electrochemically-irreversible redox processs.

Table 4.6. Selected electrochemical values observed from DPV for **1e** and **2e** in DCM solution of 0.3 M $TBABF_4$ supporting electrolyte. Potentials are referenced *vs.* Fc/Fc^+.

Complex	$E_{1/2}^{red}$ (V)	ΔE (mV)	$\lvert i_{pa}/i_{pc} \rvert$	$E_{1/2}^{ox}$ (V)	ΔE (mV)	$\lvert i_{pa}/i_{pc} \rvert$	E_{gap} (eV)
[†]**1e**	-1.51[C]	-	-	-0.38[B]	2	4.93	-1.13
2e	-1.52[B]	26	0.50	-0.37[B]	29	6.13	-1.15

[†]The return scan for **1e** from 2 to 0 V was not measured. [A]Electrochemically-reversible redox process. [B]Partially-reversible redox process (presence of redox activity within 200 mV of the peak potential). [C]Electrochemically-irreversible redox processs.

Further examination of these first oxidation processes at varying scan rates was carried out for **1e** and **2e** (**Figure 4.18**). By studying the peak process over a narrow scan range and with different scan rates, one can determine if the process is indeed electrochemically reversible. This process can be classified as reversible confirmed by a number of factors: the plot of current (i) against the square root of scan rate ($v^{1/2}$) is a straight line through the origin; the ratio of the oxidation current (i_{ox}) to the reduction current (i_{red}) is constant at around a value of 1; the anodic and cathodic peak potentials (E_{pa} and E_{pc}) do not move with increasing scan rate. However, judging by the separation between the two half-wave potentials (ΔE) compared to that of the Fc/Fc^+ couple of 100 mV, the process is not likely electrochemically reversible. It should be noted that the second redox process is very close to the first for **2e**, and may actually be unresolved in **1e**. If two redox processes are too close together, electrochemical reversibility cannot be experimentally measured, as is the case if there is a second redox process or if scan is truncated within 400 mV of the first peak.

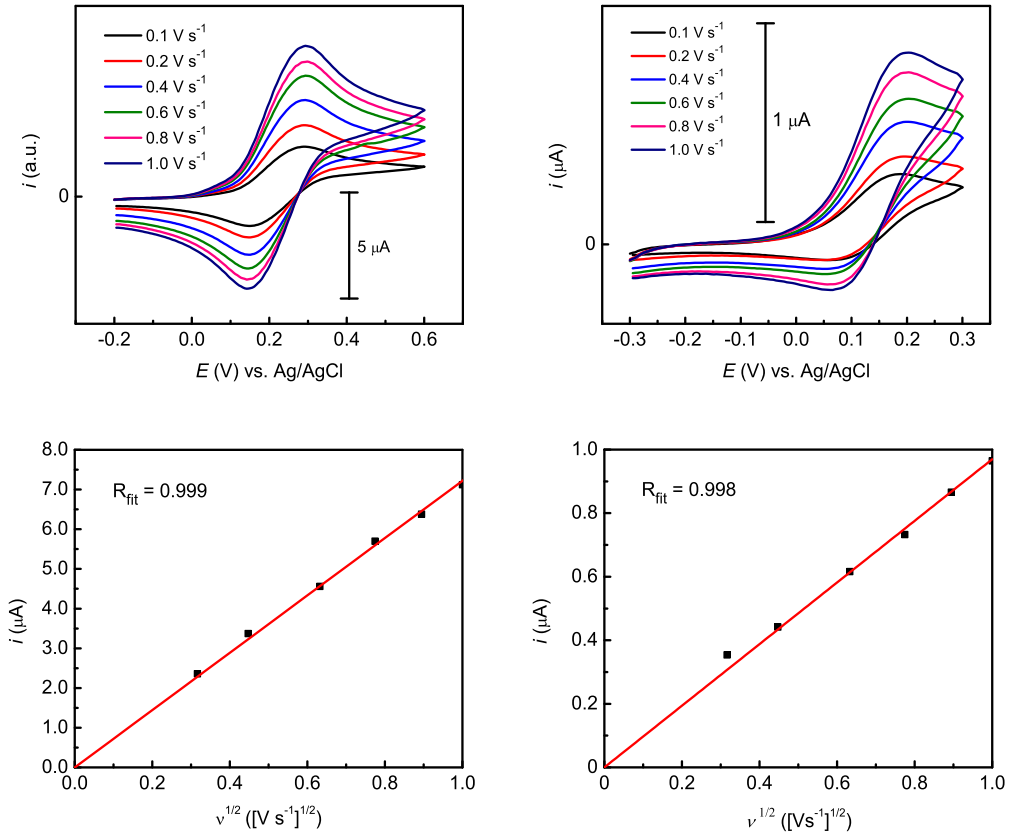

Figure 4.18. Cyclic voltammetry scan rate study for first redox process at oxidative potentials **1e** (top left) and **2e** (top right) in 0.3M $TBABF_4$ DCM solution, with plots of the peak anodic current (i_{pa}) vs. the square root of scan rate ($\nu^{1/2}$) for **1e** (bottom left) and **2e** (bottom right). The peak anodic (E_{pa}) and cathodic (E_{pc}) positions due not shift with scan rate, and the ratio of $| i_{pa}/i_{pc} |$ is approximately unity.

The DNbpy complexes **3b**, **3c** and **3d** were examined by CV and DPV, with the voltammograms displayed in **Figure 4.19** and **Figure 4.20** respectively. Cycling to oxidative potentials results in a first oxidation process with $E_{1/2}^{ox}$ (calculated from half-peak potential) between about -0.1 and 0.2 V vs. Fc/Fc^+ (**Table 4.7**). This process occurs at increasingly positive potentials for the complexes of cat, Cl_4cat and Br_4cat. These oxidation processes appear electrochemically irreversible for **3b** and **3c** but reversible for **3d**. Scanning to negative potentials leads to the appearance of a first reduction process of $E_{1/2}^{red}$ (calculated from half-peak potential) between -1.4 and -1.5 V. However, given the peak shape and potential, these peaks are not expected to be the reduction of the LUMO orbital based on the DNbpy ligand; this ligand is destabilised to reduction due to the alkyl substituents, so is expected at more

negative potentials. This hypothesis is confirmed from the presence of cathodic peaks at potentials below -2 V in the DP voltammograms (**Figure 4.20**).

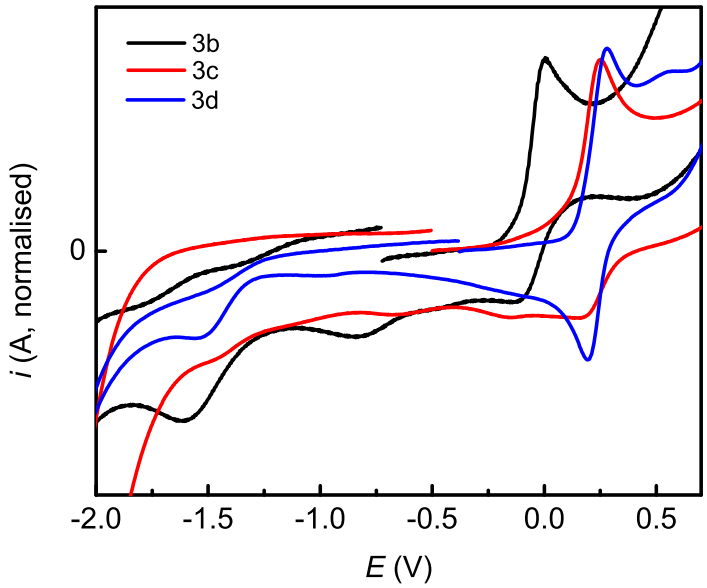

Figure 4.19. Cyclic voltammograms of **3b**, **3c** and **3d** in 0.3 M $TBABF_4$ DCM solution. The current representing the y-axis has been normalised to allow comparison of peak potentials. Potentials are referenced *vs*. Fc/Fc^+.

Table 4.7. Selected electrochemical values observed from CV for **3b**, **3c** and **3d** in DCM with 0.3 M $TBABF_4$ supporting electrolyte.[†] Scan rate = 0.1 V s^{-1}. Potentials are referenced *vs*. Fc/Fc^+.

Complex	$E_{1/2}^{red}$ (V)	$\Delta E_{p/2}$ (mV)	ΔE_p (mV)	$E_{1/2}^{ox}$ (V)	$\Delta E_{p/2}$ (mV)	ΔE_p (mV)
3b	-1.51[C]	165	*n/a*	-0.09[C]	65	109
3c	-1.44[C]	70	*n/a*	0.16[C]	60	132
3d	-1.41[C]	140	*n/a*	0.18[A]	70	90

[†] $E_{1/2}^{red/ox} = (E_p + E_{p/2})/2$, $\Delta E_{p/2} = (E_p - E_{p/2})$, $\Delta E_p = (E_{pa} - E_{pc})$. [A]Electrochemically-reversible redox process. [B]Partially-reversible redox process (presence of redox activity within 200 mV of the peak potential). [C]Electrochemically-irreversible redox processs.

The DPV measurements display the same first oxidation processes as observed during CV, as well as finding the expected reduction potentials based on the DNbpy ligand at potentials between -2.0 and -2.5 V *vs*. Fc/Fc^+. The relevant data for the first observed positive and negative redox processes are shown in **Table 4.8**.

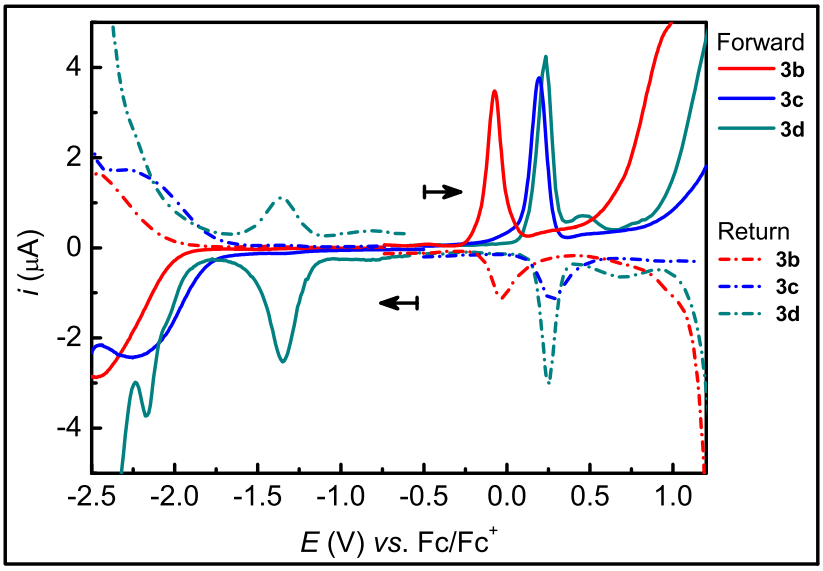

Figure 4.20. Differential pulse voltammograms for DNbpy compounds **3b**, **3c** and **3d** in DCM with 0.3 M $TBABF_4$. Potentials are referenced *vs.* Fc/Fc^+.The solid lines represent the scans from zero (*vs.* Ag/AgCl reference electrode) and the dot-dash lines represent the return scans from more extreme potentials back to zero.

Table 4.8. Selected electrochemical values observed from DPV for DNbpy compounds **3b**, **3c** and **3d** in a DCM solution of 0.3 M $TBABF_4$ supporting electrolyte. Potentials are referenced *vs.* Fc/Fc^+.

Complex	$E_{1/2}^{red}$ (V)	ΔE (mV)	$\lvert i_{pa}/i_{pc} \rvert$	$E_{1/2}^{ox}$ (V)	ΔE (mV)	$\lvert i_{pa}/i_{pc} \rvert$	E_{gap} (eV)
3b	-2.46[B]	11	0.77	-0.05[C]	40	2.28	2.41
3c	-2.27[B]	10	0.87	0.23[C]	76	2.34	2.46
3d	-2.18	*n/a*	*n/a*	0.24[B]	15	1.40	2.42

[†]Definition of terms in the table are given in Chapter 2. For processes defined as irreversible, $E_{1/2} = E_p$. [A]Electrochemically-reversible redox process. [B]Partially-reversible redox process. [C]Electrochemically-irreversible redox processs.

The electrochemical activity of the DECbpy complexes was examined by CV and DPV, with the voltammograms displayed in **Figure 4.21** and **Figure 4.22** respectively. During CV, cycling initially to oxidative potentials resulted in a first oxidation process with $E_{1/2}^{ox}$ (calculated from half-peak potential) between about -0.3 and 0.0 V *vs.* Fc/Fc^+ (**Table 4.9**). This process occurs at higher potentials for complexes with more stabilised catecholate ligands. These oxidation processes appear partially-reversible, with broad or additional nearby anodic peaks that may hinder observation of electrochemical reversibility. Scanning to negative potentials

results in the first reduction process of $E_{1/2}^{red}$ (calculated from half-peak potential) between -2.0 and -2.1 V. There is little variation in the cathodic peak position of this process within the compound series. This is to be expected with the assignment of the LUMO to the DECbpy of these complexes. This reduction process has a coupled re-oxidation, which occurs at increasingly negative potentials moving from approximately -0.20 V in **4a** to -0.44 V in **4d**.

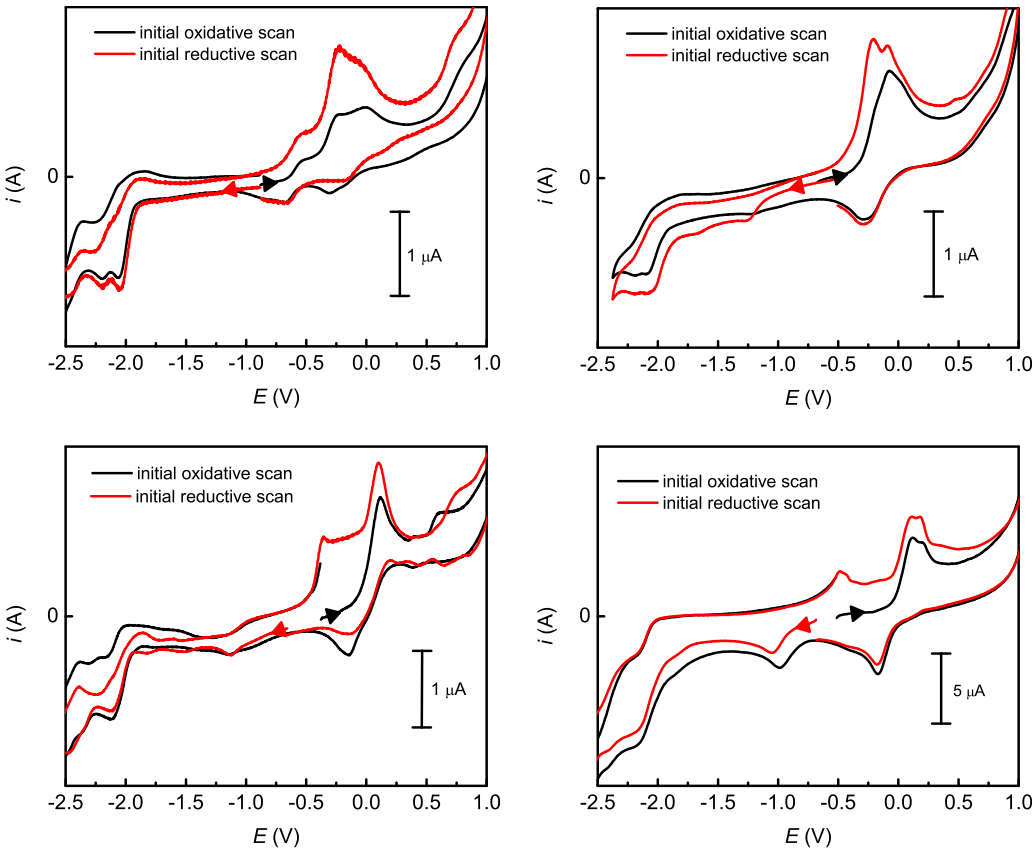

Figure 4.21. Cyclic voltammograms of DECbpy complexes in DMF solution of 0.1 M $TBABF_4$ supporting electrolyte: **4a** (top left), **4b** (top right), **4c** (bottom left) and **4d** (bottom right), with scans to initial oxidative potentials (black lines) and scans to initial reductive potentials (red lines). Scan rate = 0.1 V s^{-1}. Potentials are referenced *vs*. Fc/Fc^+.

Table 4.9. Selected electrochemical values observed from CV for all DECbpy compounds in DMF solution of 0.1 M $TBABF_4$ supporting electrolyte.[†] Scan rate = 0.1 V s^{-1}. Potentials are referenced *vs.* Fc/Fc^+ for which ΔE = 83 mV (**4a**), 103 mV (**4a**), 103 mV (**4c**) and 100 mV (**4d**).

Complex	$E_{1/2}^{red}$ (V)	$\Delta E_{p/2}$ (mV)	ΔE_p (mV)	$E_{1/2}^{ox}$ (V)	$\Delta E_{p/2}$ (mV)	ΔE_p (mV)
4a	-2.02[C]	73	102	-0.33[B]	69	90
4b	-2.04[C]	77	98	-0.23[B]	122	217
4c	-2.05[C]	100	120	0.01[B]	75	260
4d	-2.08[C]	108	136	0.00[B]	85	287

[†] $E_{1/2}^{red/ox} = (E_p + E_{p/2})/2$, $\Delta E_{p/2} = (E_p - E_{p/2})$, $\Delta E_p = (E_{pa} - E_{pc})$. [A]Electrochemically-reversible redox process. [B]Partially-reversible redox process (presence of redox activity within 200 mV of the peak potential). [C]Electrochemically-irreversible redox processs.

The DPV measurements display similar results to CV in regard to the positions of the first oxidation and reduction potentials. **Table 4.10** displays the relevant data for the first observed positive and negative redox processes. The first reduction potential for the DECbpy compounds occurs just after -2 V *vs.* Fc/Fc^+, and appears reversible for **4b**, **4c** an **4d** from considerations of the ΔE and $|i_{pa}/i_{pc}|$ values. The first oxidation processes on the other hand appear only partially reversible in nature, with either additional anodic processes at similar potentials or peak intensities which integrate to indicate 2 electrons involved in the process. Many additional peaks are visible at negative potentials after the first reduction process, of which a number appear to be electrochemically reversible.

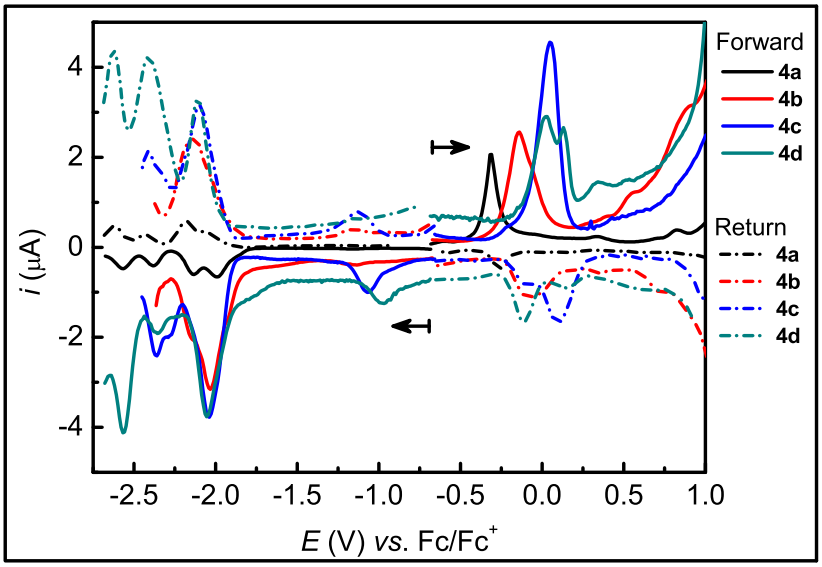

Figure 4.22. Differential pulse voltammograms for all Cu DECbpy compounds (**4a** to **4d**) in a DMF solution of 0.1 M $TBABF_4$ supporting electrolyte. Potentials are referenced *vs*. Fc/Fc^+.

Table 4.10. Selected electrochemical values observed from DPV for **DECbpy** compounds in a DMF solution of 0.1 M $TBABF_4$ supporting electrolyte. Potentials are referenced *vs*. Fc/Fc^+.

Complex	$E_{1/2}^{red}$ (V)	ΔE (mV)	$\lvert i_{pa}/i_{pc} \rvert$	$E_{1/2}^{ox}$ (V)	ΔE (mV)	$\lvert i_{pa}/i_{pc} \rvert$	E_{gap} (eV)
4a	-2.04[B]	87	0.52	-0.29[C]	51	4.32	1.75
4b	-2.08[B]	98	0.77	-0.11[B]	60	2.28	1.97
4c	-2.07[A]	61	0.84	0.07[B]	49	2.73	2.00
4d	-2.08[A]	56	0.88	-0.04[B]	140	1.75	2.04

[†]Definition of terms in the table are given in Chapter 2. For processes defined as irreversible, $E_{1/2} = E_p$. [A]Electrochemically-reversible redox process. [B]Partially-reversible redox process. [C]Electrochemically-irreversible redox processs.

What is very clear in the DP voltammograms is visualisation of the experimental HOMO-LUMO gap (E_{gap}^{DPV}). This value is tabulated for all of the compounds analysed with other experimentally-derived estimations of the HOMO-LUMO gap from electronic absorption spectra as well as values determined from DFT calculations (**Table 4.11**). For the DNbpy and DECbpy compounds there is good qualitative and quantitative agreement between the experimental and calculated bandgap energies.

Table 4.11. Frontier orbitals and band gap energies determined by various methods.† $E_{1/2}^{ox}$ and $E_{1/2}^{red}$ potentials are obtained by DPV and referenced *vs.* Fc/Fc^{+}.

	$E_{1/2}^{ox}$ (V)	$E_{1/2}^{red}$ (V)	E_{gap}^{DPV} (eV)	E_{gap}^{Abs} (eV)	E_{gap}^{Refl} (eV)	‡E_{gap}^{DFT} (eV)
1e	-0.38	-1.51	1.13	1.75	1.93	α = 1.91 β = 1.88
2e	-0.38	-1.50	1.12	1.73	-	α = 1.93 β = 1.88
3b	-0.07	-2.47	2.40	2.03	2.02	α = 2.36 β = 2.11
3c	0.19	-2.26	2.46	2.22	2.26	α = 2.60 β = 2.17
3d	0.23	-2.18	2.41	2.26	2.16	α = 2.63 β = 2.21
4b	-0.14	-2.03	1.89	1.81	1.77	α = 2.02 β = 1.99
4c	0.05	-2.04	2.09	1.97	1.88	α = 2.21 β = 2.13
4d	0.03	-2.06	2.08	1.91	1.85	α = 2.29 β = 2.19

† E_{gap}^{DPV} = electrochemical band gap calculated from the difference in the oxidation ($E_{1/2}^{ox}$) and reduction ($E_{1/2}^{red}$) peak potential values, E_{gap}^{Abs} = optical band gap determined by onset of LLCT solution absorption band, E_{gap}^{Refl} = optical band gap determined by onset of LLCT diffuse reflectance absorption band, E_{gap}^{DFT} = computationally-determined energy gap.

‡Calculations optimised with a polarisable continuum solvent model: **3b** – THF; **1e**, **2e** and **3c** – DCM; **3d** – 1,1,2-TCE; **4b**, **4c** and **4d** - DMF.

4.2.6 DFT calculations

Single-molecule gas-phase calculations were used to determine the ground-state molecular geometry and to calculate the frontier orbitals of all the compounds detailed in this chapter. The compounds of catechol, **3a** and **4a**, failed to optimise to an energy minimum ground-state structure and therefore are not included. Compounds **1e** and **2e** failed to minimise during gas-phase calculations but energy minima were reached when using a solvent model. As in Chapter 3, the B3LYP hybrid DFT functional and the 6-31G(d,p) basis set were used for all atoms apart from Cu and Br, which used the LANL2DZ pseudopotentials to model core

electrons. Geometry optimisations generated the expected square-planar geometry for all calculated compounds.

The percentage occupancies of the HOMO, LUMO and SOMO for the optimised complexes are shown in **Table 3.8**, which are very similar to the equivalent orbitals of the bpy and phen complexes of Chapter 3. The ordering of the calculated orbital energy levels from gas-phase geometry optimisations of the DNbpy and DECbpy series of complexes are displayed in **Figure 4.23** and **Figure 4.24** respectively, with the visual representation of these MOs given in **Figure 4.25**. The calculated energies of these orbitals are presented in **Table 4.13**. Comparing the energies of the frontier orbitals within each series of compounds, the energy of the HOMO and LUMO decrease in the following order of catechol ligands: Br_2cat > Cl_4cat > Br_4cat. The LUMO decreases less in energy than the HOMO, resulting in an increase in the calculated HOMO-LUMO bandgap in the same order. The same trend is observed for the complexes in Chapter 3. Overall, the energy of the LUMO orbitals for each N-chelate set of compounds (including those from Chapter 3) follows the order of decreasing energy determined by absorption spectroscopy (**Section 4.2.3**), which is: DNbpy > phen ≈ bpy > DECbpy.

Table 4.12. Calculated percentage contributions to selected molecular orbitals of Cu complexes.

Complex	Orbital	Orbital locations (%)				
		Cu	Catechol		N-chelate	
1e	HOMO	4.14	Molecule	94.65	Molecule	1.18
			O atoms	29.90	N atoms	0.00
	LUMO	1.86	Molecule	1.55	Molecule	96.54
			O atoms	1.02	N atoms	26.75
	SOMO	23.84	Molecule	52.24	Molecule	23.94
			O atoms	37.90	N atoms	11.60
2e	HOMO	4.13	Molecule	94.69	Molecule	1.15
			O atoms	29.96	N atoms	0.00
	LUMO	1.93	Molecule	1.44	Molecule	96.59
			O atoms	0.94	N atoms	27.92
	SOMO	23.17	Molecule	52.61	Molecule	24.21
			O atoms	37.94	N atoms	10.24
3b	HOMO	4.18	Molecule	92.74	Molecule	3.06
			O atoms	0.00	N atoms	0.00
	LUMO	1.41	Molecule	2.90	Molecule	95.70
			O atoms	1.68	N atoms	23.94
	SOMO	22.95	Molecule	53.80	Molecule	23.24
			O atoms	39.24	N atoms	10.20
3c	HOMO	3.73	Molecule	94.20	Molecule	2.04
			O atoms	29.76	N atoms	0.00
	LUMO	1.52	Molecule	2.22	Molecule	96.25
			O atoms	1.28	N atoms	24.02
	SOMO	22.02	Molecule	55.18	Molecule	22.84
			O atoms	39.46	N atoms	9.84
3d	HOMO	3.80	Molecule	94.36	Molecule	1.80
			O atoms	30.96	N atoms	0.00
	LUMO	1.55	Molecule	1.92	Molecule	96.53
			O atoms	1.14	N atoms	24.04
	SOMO	20.24	Molecule	58.90	Molecule	20.86
			O atoms	30.00	N atoms	9.84
4b	HOMO	4.18	Molecule	90.28	Molecule	5.50
			O atoms	0.00	N atoms	0.68
	LUMO	1.73	Molecule	5.10	Molecule	93.18
			O atoms	2.70	N atoms	26.56
	SOMO	20.20	Molecule	58.68	Molecule	21.12
			O atoms	34.40	N atoms	9.20
4c	HOMO	3.79	Molecule	92.37	Molecule	3.80
			O atoms	28.54	N atoms	0.38
	LUMO	1.80	Molecule	4.02	Molecule	94.12
			O atoms	2.10	N atoms	26.69
	SOMO	21.22	Molecule	56.38	Molecule	22.38
			O atoms	38.54	N atoms	9.36
4d	HOMO	3.85	Molecule	93.01	Molecule	3.13
			O atoms	29.82	N atoms	0.24
	LUMO	1.83	Molecule	3.25	Molecule	94.90
			O atoms	1.78	N atoms	26.78
	SOMO	20.78	Molecule	57.55	Molecule	21.66
			O atoms	31.92	N atoms	9.82

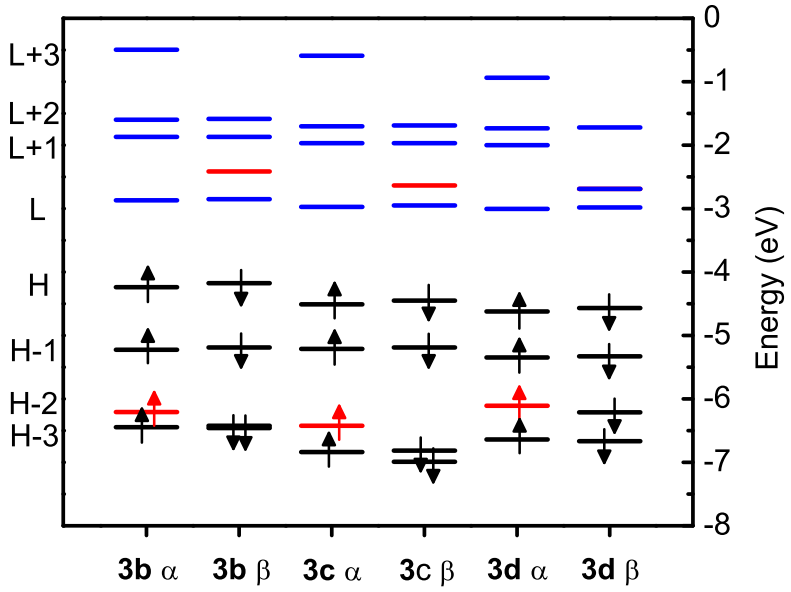

Figure 4.23. Calculated α (↑) and β (↓) orbital energies for the Cu DNbpy complexes **3b**, **3c** and **3d**. Lines colours represent orbitals with majority contributions from the Cu(II) centre (red), catecholate (black) and DNbpy (blue).

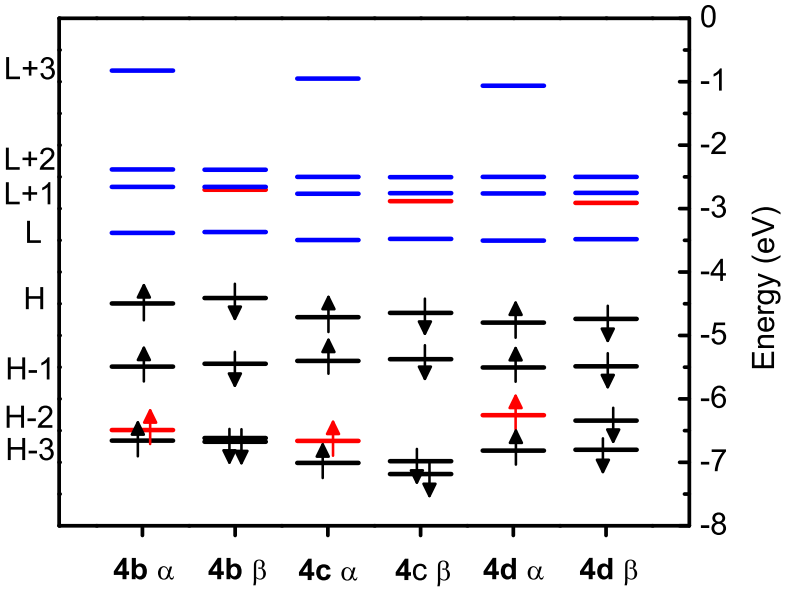

Figure 4.24. Calculated α (↑) and β (↓) orbital energies for the Cu DECbpy complexes **4b**, **4c** and **4d**. Lines colours represent orbitals with majority contributions from the Cu(II) centre (red), catecholate (black) and DECbpy (blue).

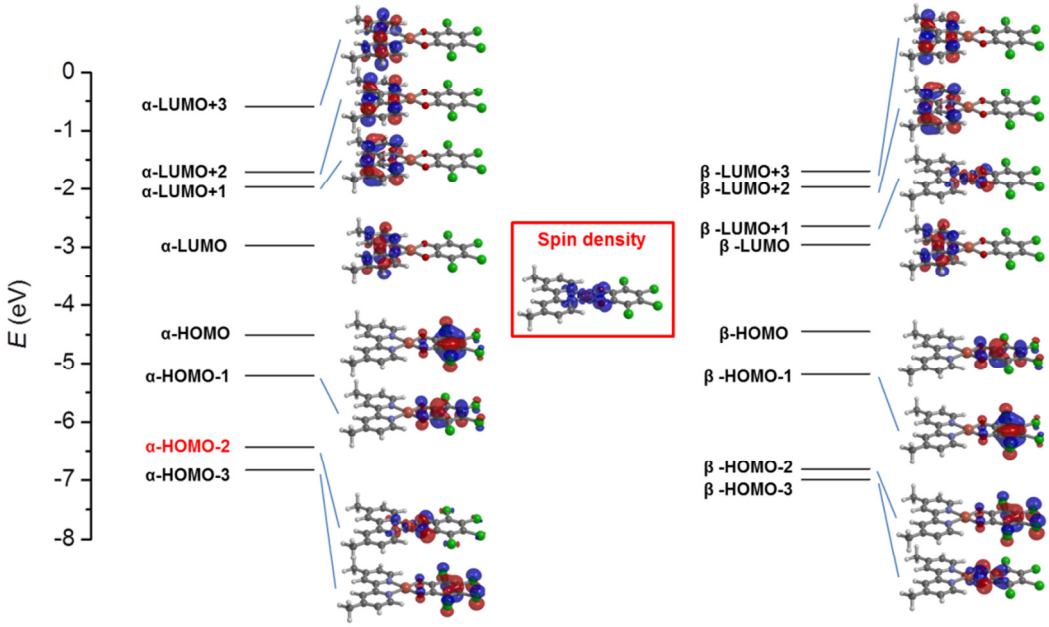

Figure 4.25. Calculated alpha and beta orbital energy levels of 3c (with nonyl chains replaced by methyl groups to reduce computational cost) calculated with B3LYP/6-31G(d,p) level of theory for all atoms apart from Cu (B3LYP/LANL2DZ). The calculated spin density of located on alpha HOMO-2 orbital.

Table 4.13. Energy levels of frontier orbitals of Cu complexes calculated by hybrid DFT.

Complex	HOMO (eV)	LUMO (eV)	SOMO (eV)	E_{gap}^{DFT} (eV)
DNbpy				
3b	α = -4.24	α = -2.87	-6.21	α = 1.37
	β = -4.18	β = -2.85		β = 1.33
3c	α = -4.51	α = -2.97	-6.42	α = 1.53
	β = -4.45	β = -2.95		β = 1.50
3d	α = -4.62	α = - 3.00	-6.11	α = 1.62
	β = -4.57	β = -2.98		β = 1.59
DECbpy				
4b	α = -4.50	α = -3.38	-6.49	α = 1.11
	β = -4.41	β = -3.37		β = 1.04
4c	α = -4.71	α = -3.50	-6.66	α = 1.21
	β = -4.65	β = -3.48		β = 1.17
4d	α = -4.80	α = -3.51	-6.26	α = 1.29
	β = -4.74	β = -3.48		β = 1.26

Calculations were also carried out using the Polarisable Continuum Model (PCM) to model the influence of solvent on the orbital energy levels. This allows a

better comparison to be made with experimental data measured from solution such as UV/Vis/NIR absorption and electrochemistry. Calculated values of the frontier orbitals of the α and β electrons using this model are detailed in **Table 4.14**. The bandgaps (E_{gap}^{DFT}) calculated using this method are approximately 1 eV greater than the corresponding values in the gas-phase calculations, and closely match those determined experimentally as compared in **Table 4.11**.

Table 4.14. Energy levels of frontier orbitals of Cu complexes calculated by hybrid DFT with PCM to model solvation: **3b** = THF; **3c** = DCM; **3d** = 1,1,2-TCE; **4b**, **4c** and **4d** = DMF.

Complex	HOMO (eV)	LUMO (eV)	SOMO (eV)	E_{gap}^{DFT} (eV)
$^{t}Bu_2$cat				
1e	α = -4.34	α = -2.43	-6.14	α = 1.91
	β = -4.28	β = -2.40		β = 1.88
2e	α = -4.33	α = -2.41	-6.17	α = 1.93
	β = -4.28	β = -2.40		β = 1.88
DNbpy				
3b	α = -4.81	α = -2.45	-6.52	α = 2.36
	β = -4.76	β = -2.65		β = 2.11
3c	α = -5.09	α = -2.49	-6.76	α = 2.60
	β = -5.04	β = -2.87		β = 2.17
3d	α = -5.15	α = -2.52	-6.67	α = 2.63
	β = -5.10	β = -2.89		β = 2.21
DECbpy				
4b	α = -5.01	α = -3.00	-6.74	α = 2.02
	β = -4.96	β = -2.97		β = 1.99
4c	α = -5.25	α = -3.04	-6.96	α = 2.21
	β = -5.20	β = -3.07		β = 2.13
4d	α = -5.34	α = -3.04	-6.87	α = 2.29
	β = -5.29	β = -3.09		β = 2.19

4.2.6.1 TD-DFT

Single-point time-dependent DFT (TD-DFT) calculations were calculated from the solvent model geometry-optimised structures to provide further confirmation of the origins of the observed electronic transitions. The calculations predict a strong absorption peak for each complex in the visible or NIR region that is mostly HOMO-LUMO in nature (**Table 4.15**). The predicted energy of peak absorptions are underestimated, placing the peaks on average to 200 nm longer

wavelengths than are observed from solution spectra. Details of the predicted transitions compared with experimental values are displayed in wavenumbers (cm^{-1}) to provide a linear unit of comparison (**Table 4.3**). However the energies of charge transfer transitions are known to be poorly predicted due to the nature of the TD calculation.[10,11] What is important though is the nature of the transition that has been determined, and the qualitative agreement that is shown within each series of compounds.

Table 4.15. Calculated TD-DFT excitation energies and assignments of low-energy transitions and experimental absorption maxima from solution spectra.[†]

Complex	Energy (cm^{-1})		Majority orbital contribution
	Experimental	TD-DFT	
1e	18,180 (1040)	11,600 (0.061)	HOMO(α)->LUMO(α) (64%) HOMO(β)->LUMO(β) (36%)
2e	18,180 (1710)	11,710 (0.060)	HOMO(α)->LUMO(α) (66%) HOMO(β)->L+1(β) (34%)
3b	21,740 (1275)	15,110 (0.052)	HOMO(α)->LUMO(α) (71%) HOMO(β)->L+1(β) (29%)
3c	23,040 (1060)	16,980 (0.044)	HOMO(α)->LUMO(α) (73%) HOMO(β)->L+1(β) (27%)
3d	24,210 (1475)	17,270 (0.045)	HOMO(α)->LUMO(α) (75%) HOMO(β)->L+1(β) (25%)
4b	17,540	13,740 (0.064)	HOMO(α)->LUMO(α) (66%) HOMO(β)->LUMO(β) (34%)
4c	19,230	14,000 (0.053)	HOMO(α)->LUMO(α) (68%) HOMO(β)->L+1(β) (31%)
4d	20,240 (99)	14,600 (0.052)	HOMO(α)->LUMO(α) (70%) HOMO(β)->L+1(β) (29%)

[†]Molar absorptivities (mol^{-1} dm^3 cm^{-1}) of experimental absorptions and calculated oscillator strengths of calculated absorptions are given in parentheses.

4.2.7 Thin-film processing

Unlike the compounds in Chapter 3, the presence of the solubilising ligands should allow the compounds detailed in this chapter to be solution processed into thin films rather than by vapour techniques. Ultimately this would enable much cheaper and easier processing of thin films for applications purposes.

Using the technique of spin coating, extensive testing was carried out with the stable DNbpy compounds **3b**, **3c** and **3d** to find the conditions best suited to producing a homogenous thin film. The variables that were investigated included the solvent used, solution volume and spin speed, acceleration and duration. The films were spin-coated onto FET substrates, which were either untreated or coated with a surface-modifying layer such as octadecyltrichlorosilane (OTS) or hexamethyldisilizane (HMDS). It was hoped that in addition to the beneficial influence to the electronic properties of the devices they coated, the surface-modifying layers may also induce an ordering of the molecules within the film. For example, the long alkyl chains of OTS and the nonyl chains of the DNbpy ligand may interact while the complex is in solution. This could also help align the molecules so that they are ordered between the FET electrodes in the direction of maximum orbital overlap.

Beneficial qualities of the solvent for spin coating are that it forms concentrated solutions with the compounds to be processed, that it is viscous and ideally non-volatile. The solvents tested during spin coating were low- to middle-polarity organic solvents such as DCM, $CHCl_3$, chlorobenzene, 1,1,1-TCE, 1,1,2-TCE, toluene and carbon disulfide (CS_2). Difficulty was encountered however due to the low solubility of complexes in all the solvents tested, with a maximum concentration of about 1 mM being obtained. In most instances, concentrations of at least 10-20 mM are needed to achieve a quality thin film.[12] Perhaps the strength of dimerisation in the compounds has an adverse effect on their solubility.

4.2.7.1 FET measurements

Measurements were conducted using the FETs with the best looking thin films of **3c** visible to the eye (in terms of uniformity and coverage) deposited on top of them. Positive and negative gate voltages were applied, from -60 to 60 V, but no gate dependence was observed. Due to the problems associated with the thin film deposition it is difficult to conclude whether or not the compounds are poor

conductors. Nevertheless, further molecular modifications would be needed in order to increase the solubility enough to enable effective solution processing.

4.2.8 Magnetic measurements

Magnetic susceptibility data for the complexes **1e** (**Figure 4.26**), **3b** to **3d** (**Figure 3.8**) and **4a** to **4d** (**Figure 4.27**) were measured on polycrystalline powder samples as a function of temperature from 1.8 to 300 K and an applied field of 0.1 T. The data are presented as plots of the $\chi_M T$ and χ_M plotted against T. As with the compounds in Chapter 3, all of the DNbpy and DECbpy compounds analysed deviate from Curie behaviour at low temperatures, with $\chi_M T$ decreasing from a constant value decreasing sharply below 20 K and χ_M below 4 K, indicating antiferromagnetic interactions. The data were also analysed by application of the Bleaney-Bowers equation (**Equation 3.1**), to which the least-squares fit of the data proved accurate with agreement factors very close to unity (**Table 3.7**).

Compound **1e** does not show the same sharp decrease in magnetic susceptibility in the χ_M vs. T plot, but does show a downturn in the $\chi_M T$ vs. T plot that deviates from that of non-interacting paramagnetic centres (**Figure 4.26**). Buchanan and co-workers observed magnetic coupling in the powder EPR data of Cu(^{t}Bu$_2$cat)(bpy) but could not quantify or qualify its origin.[1]

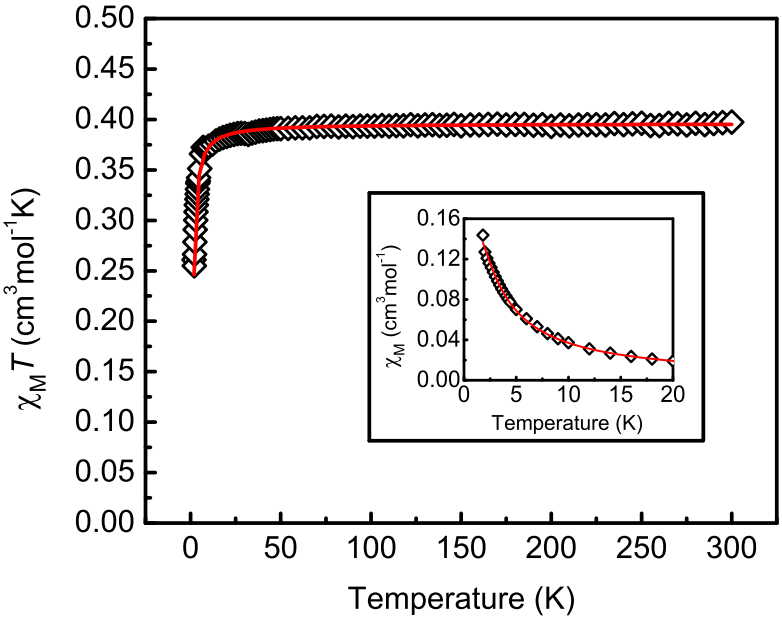

Figure 4.26. Magnetic susceptibility data for **1e** with $\chi_M T$ plotted as a function of temperature from 1.8 to 300 K. The data were fitted with the Bleaney-Bowers equation with g = 2.05 and J = -0.78 cm^{-1} after removal of the temperature-independent paramagnetism (TIP) (-165 × 10^{-6} cm^3mol^{-1}). Inset: plot of χ_M vs. T from 0 to 20 K with data fit to the Bleaney-Bowers equation.

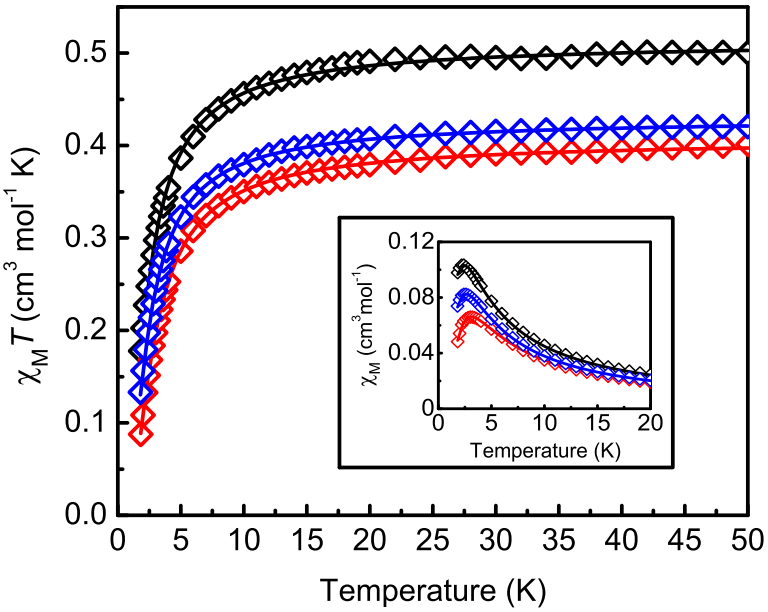

Figure 4.27. Magnetic susceptibility data for **3b** (black)**, 3c** (red) **and 3d** (blue) with $\chi_M T$ plotted as a function of temperature from 1.8 to 50 K. The data were fitted with the Bleaney-Bowers equation after removal of the *TIP*. Inset: plot of χ_M vs. T from 0 to 20 K fit to the Bleaney-Bowers equation.

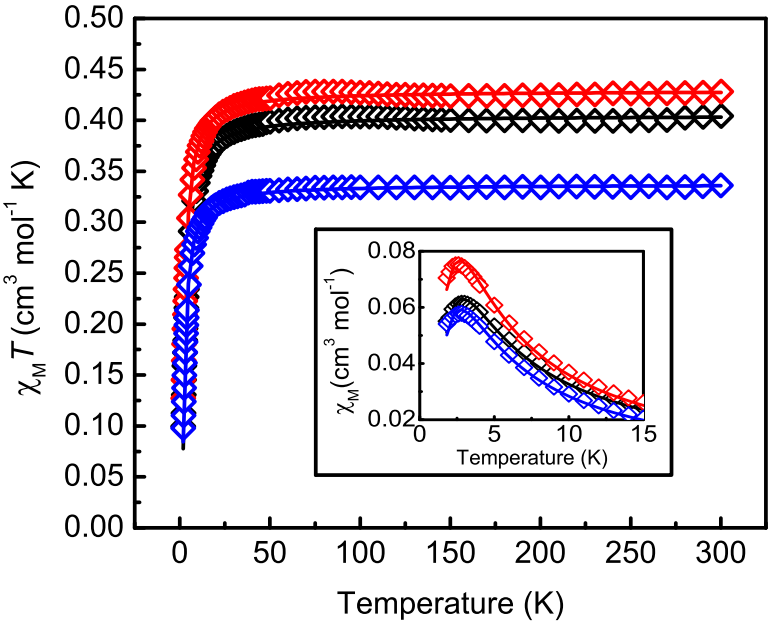

Figure 4.28. Magnetic susceptibility data for **4b** (black)**, 4c** (red) and **4d** (blue) with $\chi_M T$ plotted as a function of temperature from 1.8 to 300 K. The data were fitted with the Bleaney-Bowers equation after removal of the *TIP*. Inset: plot of χ_M vs. *T* from 0 to 15 K fit to the Bleaney-Bowers equation.

Table 4.16. Magnetic properties derived from Bleaney-Bowers fits to Cu magnetic data. Data for **2e**, and **3a** were not measured due to low chemical purity, whereas there was insufficient quantity of **4a** to accurately measure the magnetic susceptibility.

Complex	*g*-value		*J* / cm^{-1}		*TIP* / cgs	$^{\dagger}R$
	$\chi_M T$ vs. *T*	χ_M vs. *T*	$\chi_M T$ vs. *T*	χ_M vs. *T*		
1e	2.05	2.04	-0.78	-0.76	-165×10^{-6}	
3b	2.34	2.28	-1.34	-1.40	-304×10^{-6}	0.9986
3c	2.01	1.96	-1.52	-1.63	-326×10^{-6}	0.9998
3d	2.14	2.13	-1.46	-1.44	-198×10^{-6}	0.9998
4b	2.08	1.93	-1.81	-1.60	-153×10^{-6}	0.9986
4c	2.14	2.03	-1.59	-1.45	-67×10^{-6}	0.9998
4d	1.90	1.81	-1.62	-1.49	27×10^{-6}	0.9962

†Residual adjusted mean-square fit of data to the Bleaney-Bowers equation.

The calculated *g*-values are all in the range of 1.9 to 2.3, which are in general agreement with square-planar Cu(II) compounds.[1,8,9] The *J* values are small, ranging between approximately -0.8 and -1.6 cm^{-1}. These values are equivalent to those measured in Chapter 3, and are expected due to the nature of the orientation of the magnetic orbitals (**Section 3.2.8**). Potential magneto-structural correlation trends of

the Cu1···O1′ distance, Cu1-O2-Cu1′ angle Cu1···Cu′ distance with the value of *J* calculated from the $\chi_M T$ vs. *T* plots are displayed in **Figure 4.29**. As with the compounds in Chapter 3, there is a correlation of *J* with the Cu1-O2-Cu1′ bridging angle (aside from the **3d** data at *J* = -1.47 cm^{-1}), and weaker correlations with the interatomic distances. However, the correlations from Chapter 3 do not fit with those from this chapter, and it is likely that single crystal magnetic data would need to be collected before any proper correlations could be formulated.

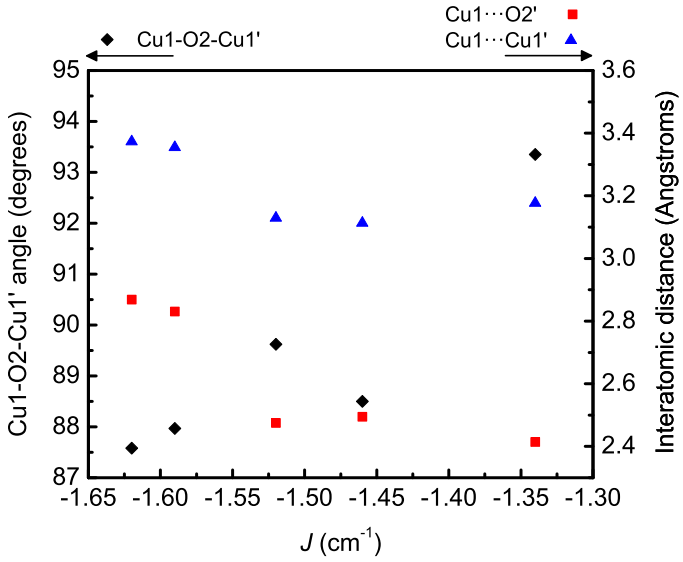

Figure 4.29. Correlations of various structural data with the values of J obtained from magnetic fitting for all compounds where structural data were available.

4.3 Conclusions

The synthesis and characterisation of a new family of heteroleptic square-planar Cu catecholate complexes with solubilising diimine ligands has been presented in this chapter. The presence of the solubilising functionality on the diimine ligand allowed the electronic influence of the series of halogenated catechol ligands to be further investigated, as well as allowing the LUMO energy level to be shifted depending on the nature of the diimine substituent.

The electronic properties of these complexes were analysed by the techniques of electronic absorption spectroscopy, electrochemistry and computational DFT calculations. It was seen that as the donor ability of the catecholate was increased ash the HOMO-LUMO gap decreased, and as the donor ability of the catecholate was reduced through addition of halogen-atom substituents on the aromatic ring the HOMO-LUMO gap increases. This also increases the stability of the complexes towards environmental oxidations that ultimately would lead to their decomposition. The DNbpy ligand resulted in a more destabilised LUMO and a larger HOMO-LUMO gap, whereas the DECbpy ligand had a stabilising effect on the LUMO energy and therefore resulted in a smaller HOMO-LUMO gap. Ultimately these results have proved the degree of tunability that can be achieved with these structures.

Thin-film processing did not yield favourable results due to the inability to form concentrated solutions. Future work will focus on enhancing this solubility by further modifications of the diimine ligand and improving the interacting with the substrate with further surface-modifying layers.

Crystal structures were obtained for five of the compounds in this chapter. The compounds of DNbpy were the more strongly dimerised than the DECbpy, which is represented by the shorter Cu···O′ and Cu···Cu′ distances. The influence of the catechol halogenation was also seen, with these intermolecular distances increasing with an increasing size and number of halogen atom substituents. Therefore, the catechol substituents are seen to have a structure influence as well as an electronic one.

4.4 Experimental

Mass spectrometry of the DNbpy compounds did not often yield the molecular ion peaks when using the techniques of fast-atom bombardment (FAB)

and electrospray ionisation (ESI). In all spectra either the species $[Cu(DNbpy)_2+H]^+$ or $[Cu(DNbpy)_2]^+$ was found, likely as a consequence of the ionisation conditions.

2,2'-Bipyridine-4,4'-dicarboxylic acid (DCAbpy). To an aqueous solution of potassium permanganate (11 g in 190 ml H_2O) was added 4,4'-dimethyl-2,2'-bipyridine (2g, 0.011 mol) and the mixture heated under reflux until the permanganate decolourised leaving a colourless mixture and black, manganese dioxide precipitate. After filtration the filtrate was extracted with diethyl ether (3 × 50 ml). Concentrated hydrochloric acid (4 ml) was added to the aqueous phase and stirred for 1 h to precipitate the product. The white product (2.5 g, 93%) was collected by filtration and dried under dessication for 1 d. The product was used for the synthesis of DECbpy (see below) without characterisation.

4,4'-Diethoxydicarbonyl-2,2'-bipyridine (DECbpy). To a mixture of DCAbpy (2.5 g, 8.3 mmol) in absolute ethanol (400 ml) was added concentrated sulfuric acid (5 ml). The mixture was refluxed under an atmosphere of nitrogen until a clear, pink solution and no solid remained (less than 50 h). Water (200 ml) was added and a white precipitate formed. Ethanol was removed by rotary evaporation and the pH adjusted to neutral with NaOH solution. The crude product (1.9 g, 62%) was filtered, washed with water and recrystallised from ethanol, forming white needles (0.9 g, 29%). ^{1}H-NMR (250 MHz, $CDCl_3$) δ:1.34 (6H, t, J = 7 Hz, CH_3); 4.36 (4H, q, J = 7 Hz, CH_2); 7.81 (2H, d, J = 6 Hz, aryl H on C_5 and $C_{5'}$); 8.76 (2H, d, J = 6 Hz, aryl H on C_6 and $C_{6'}$); 8.84 (2H, s, aryl H on C_3 and $C_{3'}$).

3,5-Di-^{t}butylcatecholato(2,2'-bipyridyl)Cu(II), [Cu(^{t}Bu$_2$cat)(bpy)] (1e). To a stirred solution of $CuSO_4 \cdot 5H_2O$ (0.249 g, 1 mmol) in deionised water (5 ml), was added a mixture of 3,5-di-t-butylcatechol (0.156 g, 1 mmol) plus 2,2'-bipyridine (0.180 g, 1 mmol) in EtOH (5 ml) with 2N equivalents of potassium hydroxide solution (in deionised water) under an N_2 atmosphere. A dark violet precipitate immediately formed on mixture of both solutions. The precipitate was filtered under vacuum and washed with deionised water and acetone, yielding a solid dark purple

product (0.410 g, 94%). Calculated (found) for $C_{24}H_{28}CuN_2O_2$: C, 65.51 (65.83); H, 6.41 (5.59); N, 6.37 (5.82). MS (+FAB): *m/z* 439.3 ($[M]^+$, 70%), 375.1 ($[Cu(bpy)_2]^+$, 25%).

Note that the remaining compounds were synthesised using slightly modified versions of the procedure for **1e**.

3,5-Di-^{t}butylcatecholato(1,10-phenanthrolino)Cu(II), [Cu(^{t}Bu$_2$cat)(phen)] (2e). Dark indigo solid (0.447 g, 96 %). Calculated (found) for $C_{26}H_{28}CuN_2O_2$: C, 67.29 (64.62); H, 6.08 (4.94); N, 6.04 (5.84). MS (+FAB): *m/z* 463.4 ($[M]^+$, 70%), 375.1 ($[Cu(bpy)_2]^+$, 25%).

Catecholato(4,4'-dinonyl-2,2'-bipyridyl)Cu(II), [Cu(cat)(DNbpy)] (3a). The procedure is modified by using acetone to dissolve the DNbpy ligand instead of EtOH. A tan solid was produced (0.348 g, 60%). Calculated (found) for $C_{16}H_8Cl_4CuN_2O_2$: C, 70.37 (67.72); H, 8.34 (7.70); N, 4.83 (4.92). MS (+FAB): *m/z* 879.5 ($[Cu(DNbpy)_2]^+$, 74%), 471.2 ($[M\text{-cat}]^+$, 100%).

4,5-Dibromocatecholato(4,4'-dinonyl-2,2'-bipyridyl)Cu(II), Cu(Br$_2$cat)(DNbpy)] (3b). The synthesis produced a mustard yellow precipitate that turned dark brown on drying under vacuum (0.550 g, 75 %). Calculated (found) for powder $C_{34}H_{46}Br_2CuN_2O_2$: C, 55.33 (53.88); H, 6.28 (3.63); N, 3.80 (3.63). The crude product was impure by elemental analysis, so was recrystallised from a 9:1 mixture of MeCN:EtOH over a period of 1 d. The crystals were large, dark blocks that were red brown under the light of a microscope. Calculated (found) for $C_{34}H_{46}Br_2CuN_2O_2$: C, 55.33 (55.24); H, 6.28 (6.01); N, 3.80 (3.73). MS (+ESI): *m/z* 879.56 ($[Cu(DNbpy)_2]^+$, 100%) 736.99 ($[M^+]$, 7%), 502.78 ($[M\text{-}Br_2cat+MeO]^+$, 38%).

Tetrachlorocatecholato(4,4'-dinonyl-2,2'-bipyridyl)Cu(II), [Cu(Cl$_4$cat)(DNbpy)] (3c). Mustard yellow solid (0.694 g, 97 %). The crude product

was not pure by elemental analysis, so was recrystallised by slow diffusion of EtOH into a DCM solution of the crude product over a period of days. Yellow brown crystals suitable for single-crystal XRD were produced (0.485 g, 70 %). Calculated (found) for $C_{34}H_{44}Cl_4CuN_2O_2$: C, 56.87 (56.95); H, 6.18 (5.28); N, 3.90 (3.85). MS (+ESI): *m/z* 914.41 ($[Cu(DNbpy)_2(OH)(OH_2)]^+$, 100%), 879.62 ($[Cu(DNbpy)_2]^+$, 52%) 715.64 ($[M^+]$, 6%), 409.55 ($[(DNbpy)+H]^+$, 34%).

Tetrabromocatecholato(4,4'-dinonyl-2,2'-bipyridyl)Cu(II), [Cu(Br$_4$cat)(DNbpy)] (3d). Dark brown solid (0.761 g, 85 %). Calculated (found) for $C_{34}H_{44}Br_4CuN_2O_2$: C, 45.58 (45.71); H, 4.95 (4.98); N, 3.13 (3.22). Crystals suitable for single crystal XRD were grown by slow evaporation of a dilute solution of **3d** in acetone over a period of days, yielding orange brown needles.

Catecholato(4,4'-diethoxycarbonyl-2,2'-bipyridyl)Cu(II), [Cu(cat)(DECbpy)] (4a). The synthesis of the DECbpy compounds was carried out on a 0.1 mM scale due to the availability of the DECbpy ligand, and was modified from the general procedure by using THF to dissolve the DECbpy ligand. The product residue from vacuum filtration washed with H_2O followed by acetone only once the residue appeared dry, yielding dark brown powder of **4a** (34 mg, 73%) (Calculated (found) for $C_{22}H_{20}CuN_2O_6$: C, 55.99 (56.16); H, 4.27 (4.19); N, 5.94 (6.04).

4,5-Dibromocatecholato(4,4'-diethoxycarbonyl-2,2'-bipyridyl)Cu(II), [Cu(Br$_2$cat)(DECbpy)] (4b). Dark brown solid (34 mg, 72%). Calculated (found) for $C_{22}H_{18}Br_2CuN_2O_6$: C, 41.96 (42.44); H, 2.88 (1.95); N, 4.45 (3.73) for the powder product.

Tetrachlorocatecholato(4,4'-diethoxycarbonyl-2,2'-bipyridyl)Cu(II), [Cu(Cl$_4$cat)(DECbpy)] (4c). Magenta solid (43 mg, 71%). Calculated (found) for $C_{22}H_{18}Cl_4CuN_2O_6$: C, 43.34 (43.31); H, 2.64 (2.60); N, 4.59 (4.49). Red single

crystals suitable for XRD were produced by slow diffusion of a DMF solution of **4c** layered on top of DCM in a plastic centrifuge tube over a period of days.

Tetrabromocatecholato(4,4'-diethoxycarbonyl-2,2'-bipyridyl)Cu(II), [Cu(Br$_4$cat)(DECbpy)] (4d). Solid dark red-brown product (62 mg, 78%). Calculated (found) for $C_{22}H_{18}Br_4CuN_2O_6$: C, 33.55 (33.64); H, 2.05 (2.15); N, 3.56 (3.65). Orange-brown single crystals suitable for XRD were produced by recrystallisation of a dilute solution of **4b** in DMF over a period of 1 d.

4.4.1 Surface treatments

The Au FET substrates were cleaned by soaking in sequential solvents of chloroform, acetone and IPA (15 min each). Prior to surface treatments, the substrates were UV/ozone treated (2 min). HMDS treatment was carried out by placing one drop of pure HMDS onto the interdigitated electrodes of the FET in a glovebox and leaving for 20 min. The FET substrates were rotated at 2000 rpm for 90 seconds using a spin coater to remove excess HMDS, washing with 1 ml of 1,1,2-TCE. OTS treatment involved soaking FET substrates in a 10 mM solution of OTS in toluene for 24 h. The substrates were rinsed in the same manner as with the HMDS treatment.

4.4.2 X-ray crystallography

The structure refinements of **3d**, **4c** and **4d** were carried out by the author, and **3b** and **3c** were carried out by Dr. Gary Nichol of the School of Chemistry crystallography service.

Single crystal data were collected on an Agilent Technologies SuperNova diffractometer using Cu Kα radiation and graphite monochromator at 120 K for all compounds except **3c**, which was collected using Mo Kα radiation. Data collection, cell refinement and data reduction were carried out using CrysAlis PRO[13] software.

The structures **3b**, **3d** and **4c** were solved using SIR92 direct methods,[14] and **3c** and **4d** were solved using the program SUPERFLIP,[15] giving the positions of all non-hydrogen atoms. The structures **3d**, **4c** and **4d** were refined using CRYSTALS[16] software and the CAMERON[17] structure visualiser, and **3b** and **3c** were refined using SHELXTL software.[18] All refinements used a full-matrix least-squares refinement procedure, with non-hydrogen atoms refined anisotropically with hydrogen atoms placed at calculated positions. Full details of the structure refinement are given in **Table 4.17**. Molecular graphics were constructed using Mercury[19] software.

The structures of **3c** and **3d** both exhibited positional disorder in the nonyl chains that is common for this type of fragment, whereas these chains were fully ordered in the structure of **3b**. This was handled with a two-part disorder model for both chains. For **3c**: C(22) to C(25) have a refined major:minor occupancy ratio of 0.690:0.310(13); C(26) to C(34) a ratio of 0.679:0.321(7). Bond distance restraints were used in modelling both instances of disorder. For **3d**: One alkyl chain was completely split with C(35) to C(52) refined to a 0.6:0.4 major:minor occupancy ratio. Restraints were placed on both alkyl chains with C-C bond lengths of 1.5 Å.

The diffraction data were weak for **3b** but were suitable for structure determination. Unlike the other DNbpy complexes, the long alkyl chains in **3b** were fully ordered. H atoms were observed in a difference Fourier map, but were geometrically constrained during refinement. However, there were two large residual peaks found in the Fourier map after structure refinement was complete. These peaks were adjacent to atoms C3 and C6 in the catecholate aromatic ring: one peak was approximately 3 e.Å^{-3} in size located 1.65 Å from C3; the second is approximately 5 e.Å^{-3} in size located 1.69 Å from C6. There was no obvious crystallographic origin of these peaks, and although the measured diffraction pattern was weak, it was good and showed no indication of missed twinning. There is no obvious chemical cause of these peaks either, with elemental analysis, MS and ^{1}H- and ^{13}C-NMR of the Br_2cat ligand confirming its purity. A model was created in which each residual peak was modelled as Br, with the occupancy refined to mimic

possible contamination by tri-brominated ligand. This disordered model refines to give R1 = 0.0267, wR2 = 0.0673, with Br occupancies of ~3% (for a Br bonded to C3) and 7% (for a Br bonded to C6) but with approximate C—Br distances of 1.65 and 1.68 Å respectively, which is approximately 0.25 Å shorter than Br1—C5 and Br2—C4. The synthesis of 4,5-dibromocatechol involves reaction of one mole of catechol with two moles of molecular bromine,[20] with higher molar equivalents of bromine leading to tribromination. Therefore it is likely that a small portion of 3,4,5-tribrominated catechol, undetected by the techniques described, may exist in the 4,5-dibromocatechol starting material. This is opposed to the potential existence of 3,4-dibromocatechol, which can not be synthesised using the method described.

Table 4.17. Crystallographic data and structure refinement details.

	3b	3c	3d	4c	4d
Chemical formula	$C_{68}H_{92}Br_4Cu_2N_4O_4$	$C_{68}H_{88}Cl_8Cu_2N_4O_4$	$C_{68}H_{88}Br_8Cu_2N_4O_4$	$C_{22}H_{16}Cl_4CuN_2O_6$	$C_{22}H_{16}Br_4CuN_2O_6$
Crystal size / mm^3	0.29 × 0.09 × 0.03	0.34 × 0.10 × 0.05	0.44 × 0.04 × 0.04	0.27 × 0.05 × 0.03	0.21 × 0.04 × 0.03
Crystal colour, shape	Orange blade	Yellow blade	Orange blade	Red blade	Orange block
Fw	1476.18	1436.10	1791.72	609.74	787.52
Crystal system	Triclinic	Monoclinic	Monoclinic	Monoclinic	Triclinic
Space group	*P*-1	$P2_1/c$	$P2_1/c$	*C*2/*c*	*P*-1
a / Å	8.56279(19)	20.7675(15)	20.7607(3)	35.2093(7)	8.2373(3)
b / Å	9.5585(2)	8.4434(4)	8.4879(1)	7.02320(9)	9.2476(4)
c / Å	20.7935(5)	19.3291(12)	19.8075(3)	21.2635(4)	16.5878(7)
α / °	78.270(2)	90	90	90	91.875(3)
β / °	85.820(2)	95.764(7)	94.777 (1)	119.117 (2)	102.963(3)
γ / °	86.9447(18)	90	90	90	103.436(3)
V / Å^3	1660.62(7)	3372.2(4)	3478.24(9)	4593.62(18)	1192.87(9)
Z	1	2	2	8	2
Calc. density / g cm^{-3}	1.476	1.414	1.711	1.763	2.192
μ / mm^{-1}	3.988	0.998	6.522	6.024	9.53
T / K	120	120	120	120	120
Radiation, λ / Å	Cu-Kα, 1.54184	Mo-Kα, 0.71073	Cu-Kα, 1.54184	Cu-Kα, 1.54184	Cu-Kα, 1.54184
θ range / °	4.3 to 76.2	3.1 to 25.0	4.3 to 74.1	2.9 to 74.0	2.7 to 73.8
Index ranges	h -8 to 10	h –24 to 24	h -25 to 25	h -43 to 43	h -10 to 9
	k -12 to 12	k –10 to 9	k -8 to 10	k -8 to 8	k -10 to 11
	l -26 to 26	l –22 to 21	l -24 to 24	l -26 to 26	l -20 to 20
Refinement method	Full-matrix least-squares on F^2	Full-matrix least-squares on F^2	Full-matrix least-squares on F^2	Full-matrix least-squares on F^2	Full-matrix least-squares on F^2
Absorption correction	Gaussian	Analytical	Gaussian	Gaussian	Spherical
T_{min}, T_{max}	0.39, 0.89	0.73, 0.96	0.26, 0.77	0.57, 0.84	0.59, 1.00
Structure solution	Direct methods	Charge-flip	Direct methods	Direct methods	Charge-flip
R_{int}	0.019	0.057	0.041	0.032	0.047
Collected	29032	24723	27280	34517	19073
Independent	6867	5892	6933	4635	4729
Observed $[I > 2\sigma(I)]$	6517	4621	5660	4240	4147
Reflections used	6867	5892	6904	4616	4709
Parameters / restraints	374 / 0	510 / 197	259 / 27	316 / 0	316 / 0
R, R_w $[I > 2\sigma(I)]$	0.0483, 0.1248	0.0466, 0.1086	0.0731, 0.1449	0.0244, 0.0462	0.0278, 0.0526
R,[a] R_w (all data)[b]	0.0499, 0.1262	0.0655, 0.12200	0.0845, 0.1607	0.0268, 0.0481	0.0336, 0.0562
GOF	1.06	1.034	1.027	1.040	0.933
$\Delta\rho_{max}$, $\Delta\rho_{min}$ (e Å^{-3})	4.95, -0.67	0.53, –0.58	2.29, –2.06	0.37, –0.41	0.64, –0.69

[a] $R = \Sigma||F_o| - |F_c||/\Sigma|F_o|$. [b] $R_w = [\Sigma w(|F_o| - |F_c|)^2/\Sigma w|F_o|^2]^{1/2}$.

4.5 References

(1) Buchanan, R. M.; Wilsonblumenberg, C.; Trapp, C.; Larsen, S. K.; Greene, D. L.; Pierpont, C. G. *Inorganic Chemistry* **1986**, *25*, 3070.

(2) Brown, D. G.; Hughes, W. J.; Knerr, G. *Inorganica Chimica Acta* **1980**, *46*, 123.

(3) Brown, D. G.; Vogel, G. C. *Inorganic Chemistry* **1978**, *17*, 1367.

(4) Brown, D. G.; Beckmann, L.; Ashby, C. H.; Vogel, G. C.; Reinprecht, J. T. *Tetrahedron Letters* **1977**, *18*, 1363.

(5) Miller, T. R.; Dance, I. G. *Journal of the American Chemical Society* **1973**, *95*, 6970.

(6) Benedix, R.; Vogler, A. *Inorganica Chimica Acta* **1993**, *204*, 189.

(7) Zuleta, J. A.; Bevilacqua, J. M.; Proserpio, D. M.; Harvey, P. D.; Eisenberg, R. *Inorganic Chemistry* **1992**, *31*, 2396.

(8) Hasty, E. F.; Colburn, T. J.; Hendrickson, D. N. *Inorganic Chemistry* **1973**, *12*, 2414.

(9) Inman, G. W.; Hatfield, W. E.; Drake, R. F. *Inorganic Chemistry* **1972**, *11*, 2425.

(10) Turki, M.; Daniel, C.; Záliš, S.; Vlček Jr., A.; van Slageren, J.; Stufkens, D. J. *Journal of the American Chemical Society* **2001**, *123*, 11431.

(11) Magyar, R. J.; Tretiak, S. *Journal of Chemical Theory and Computation* **2007**, *3*, 976.

(12) Handa, S.; Miyazaki, E.; Takimiya, K. *Chemical Communications* **2009**, 3919.

(13) *CrysAlis PRO*; Agilent Technologies UK Ltd: Yarnton, England, 2011.

(14) Altomare, A.; Cascarano, G.; Giacovazzo, C.; Guagliardi, A.; Burla, M. C.; Polidori, G.; Camalli, M. *Journal of Applied Crystallography* **1994**, *27*, 435.

(15) Palatinus, L.; Chapuis, G. *Journal of Applied Crystallography* **2007**, *40*, 786.

(16) Betteridge, P. W.; Carruthers, J. R.; Cooper, R. I.; Prout, K.; Watkin, D. J. *Journal of Applied Crystallography* **2003**, *36*, 1487.

(17) Watkin, D. J.; Prout, K.; Pearce, L. J.; Chemical Crystallography Laboratory, University of Oxford: Oxford, UK, **1996**.

(18) Sheldrick, G. M. *Acta Crystallographica* **2008**, *A64*, 112.

(19) Macrae, C. F.; Bruno, I. J.; Chisholm, J. A.; Edgington, P. R.; McCabe, P.; Pidcock, E.; Rodriguez-Monge, L.; Taylor, R.; van de Streek, J.; Wood, P. A. *Journal of Applied Crystallography* **2008**, *41*, 466.

(20) Kohn, M. *Journal of the American Chemical Society* **1951**, *73*, 480.

5. Half-sandwich cobalt diamido complexes

5.1 Introduction

Ferrocene is a very well-known organometallic compound due to its facile reversible one-electron oxidation process, which has led to its popularisation as an internal standard for electrochemical reactions.[1] The structure of ferrocene is a central Fe(II) ion that is complexed by two cyclopentadienyl (Cp) ligands to produce an 18 e^- complex. It is a stable yet relatively volatile crystalline compound with a sublimation temperature around 398 K at a pressure of 1 atmosphere. It is these two normally unrelated properties that prompted the investigations in this chapter of organometallic compounds. As described in Chapter 1 and subsequent chapters, reversible redox activity is a highly sought after characteristic for functional materials, as it can be used to confirm the energetics and stability of electron transfer processes. In addition, compounds that will readily sublime at low temperatures allow them to be vapour processed into thin films for electronic applications at reduced cost.

The cobalt and nickel analogues of ferrocene are called cobaltocene and nickelocene respectively, and this class of compound can be referred to as metallocenes. Nickelocene is a paramagnetic compound, and Fourmigue et al. have investigated their derivatives with the ever popular dithiolene ligands (described in Chapter 1).[2-5] Due to the non-innocence of these complexes they can form fundamentally interesting neutral radical species. Cobaltocene has a sublimation temperature around RT and is very reactive due to its 19 valence-electron count. Half-sandwich derivatives of cobaltocene with simple 1,2-disubstituted phenyl chelates were synthesised by Heck[6,7] and others[8,9] in the 1960s, but were not pursued beyond their chemical characterisation. Brill investigated the structure and bonding within these structures in the 1980s,[10-14] and Fourmigué furthered these investigations into the structure and reactivity of dithiolene derivatives.[15-18]

The electronic properties of a pair of half-sandwich complexes of cobalt with 1,2-bidendate aromatic chelates have been investigated in this chapter. The CpCo unit is chelated by two N-donor groups of either 1,2-diamidobenzene (DAbnz) or 1,2-diamidonaphthalene (DAnap). The two compounds that are discussed throughout this chapter are shown in **Scheme 5.1**. Compound **7a** has been synthesised previously amongst a series of other derivatives in the literature,[7] but the electronic characterisation was limited to the absorption spectra. The electronic properties of the two compounds herein were studied by the electrochemistry, electronic absorption spectroscopy and TD-DFT calculations. Novel crystal structure data is also presented. In addition to the molecular and structural characterisation, thin-film characterisation and field-effect transistor measurements are presented and discussed. By comparison of the two compounds, the influence of the increased conjugation of the chelating ligand is determined.

Scheme 5.1. Compounds presented in this chapter.

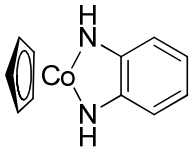

7a

CpCoDAbnz

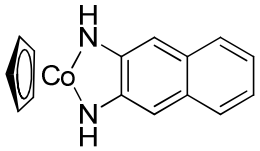

7b

CpCoDAnap

5.2 Results and discussion

5.2.1 Remarks on synthesis

The general synthetic route to compounds in this chapter was derived from the method of Heck,[7] who described the synthesis of benzene-1,2-diamidocyclopentadienylcobalt(III) (CpCoDAbnz) amongst other chelates of 1,2-

disubstituted benzene where the chelating moiety is a combination O, S and NH. The study was of purely synthetic purposes, and there was no further study on the molecules beyond their chemical characterisation.

5.2.2 Structure

Despite the very high solubility of both compounds in organic solvents, single crystals suitable for XRD were not able to be grown by conventional solution-phase techniques. The only feasible method was that of slow evaporation, however crystalline material only formed outside the mother liquor and so the edges were imperfect. In addition, the crystals form too rapidly resulting in multifaceted small growths. The crystal structure of **7a** was determined from powder diffraction (**Section 5.2.3**). The structure of **7b** was obtained by vacuum sublimation in a tube furnace.

The molecule **7b** crystallises in the orthorhombic *P*bca space group with four molecules per asymmetric unit and 32 molecules per unit cell. The unit cell and asymmetric unit for **7b** is displayed in **Figure 5.1**. The packing of molecules in the structure of **7b** can be seen in more detail from the different perspectives of the unit cell in **Figure 5.2**. The unit cell is very long in the *c*-axis due to the gradual rotation of the molecules with respect to the LS plane defined by the Co centre and DAnap ligand, resulting in a repeat of eight molecules. With the perpetual undulation exhibited in this direction, the orientation of the molecules changes by 180° with respect to the direction the Cp ring is facing every four molecules. This is explained in more detailed below. These chains are orientated to each other in the *a*-axis in a herringbone packing motif with respect to the LS plane. The herringbone packing style is prominent in organic structures that display good charge-transfer properties as detailed in Chapter 1. Close contacts between H-atoms and the centroids of rings present in the molecule of between 3.0 and 3.6 Å are displayed in **Figure 5.3**. The unique orientation of molecules, with a lack of dimerisation within the unit cell, may translate to the observation of charge-transport properties.

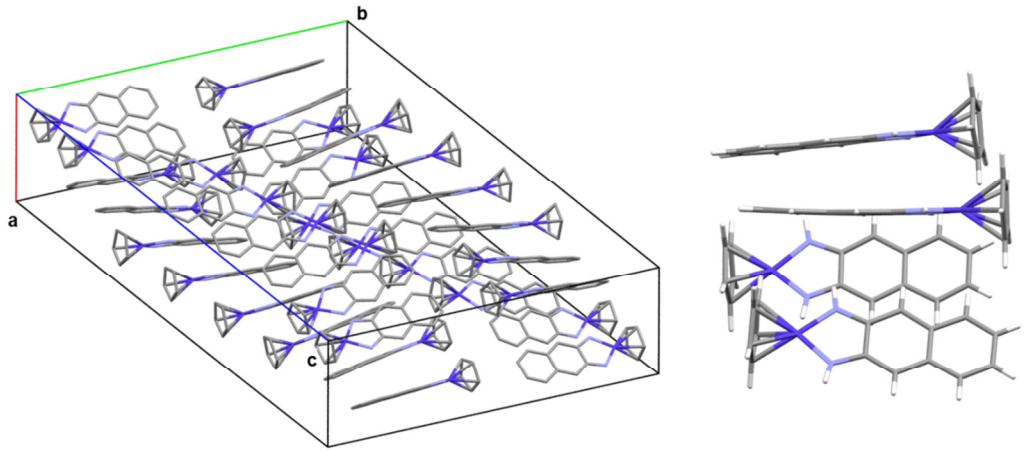

Figure 5.1. Unit cell (left) and asymmetric (right) of 7b. H-atoms are omitted from the unit cell diagram for clarity.

The intermolecular short contacts and angles of **7b** are displayed in **Figure 5.3**. The intermolecular distances displayed are between the H atoms and the centroids of one of the 4 rings present in the structure (the Cp ring, the metalocycle and the two in the naphthalene unit). Aside from those between the H atoms and the Cp ring, there is little directionality to these interactions, but they occur at distances between 3.0 and 3.6 Å. The angles between the LS plane of the molecules involved in these interactions along the *a*-axis is 57.3°. The angle between LS planes of molecules along the long *c*-axis shows variation, with an average of approximately 6.7° between planes of molecules that have Cp rings facing in the same direction (head-to-head). Every four molecules, the angle between these planes becomes approximately zero when the molecules face head-to-tail. From this point the molecular planes repeat the same rotation but in the opposite direction. This results in an undulating rotation of approximately ±20° in this direction.

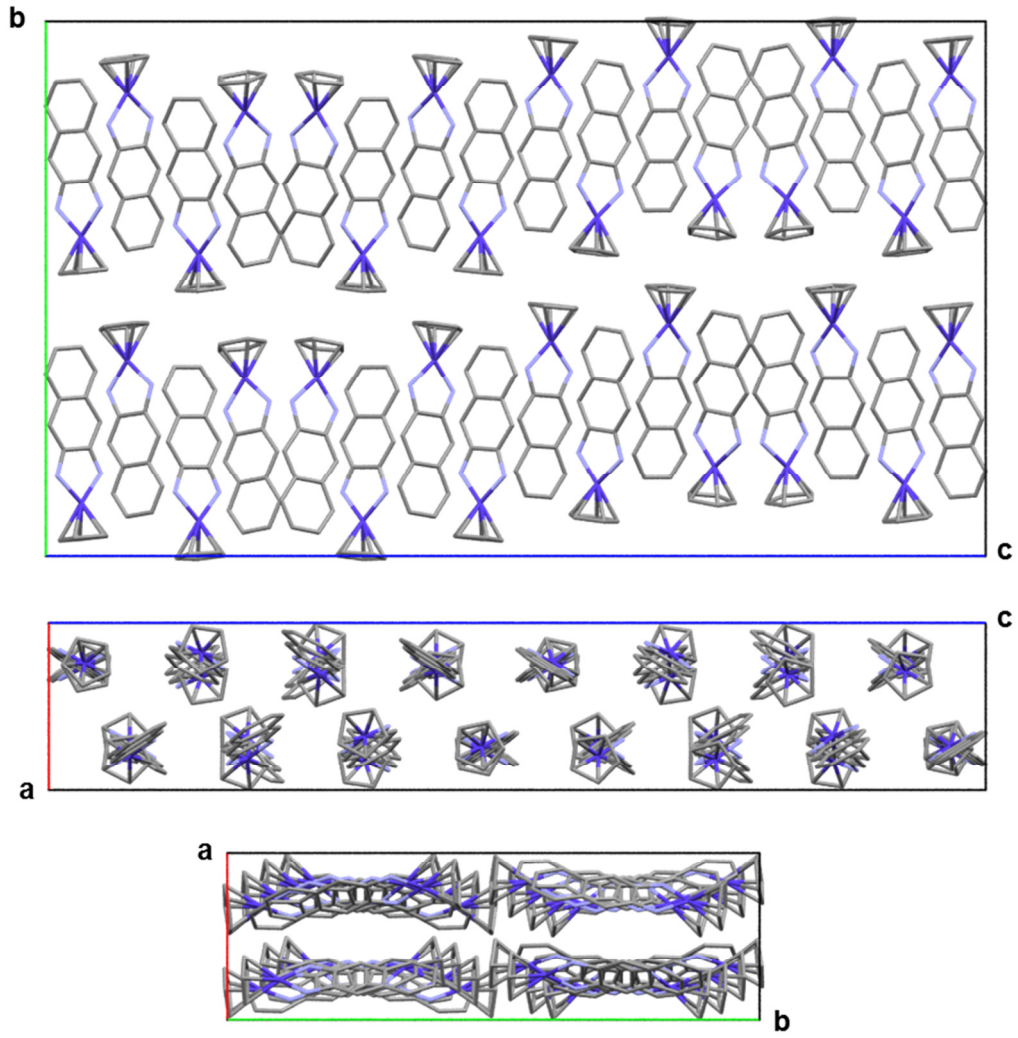

Figure 5.2. Unit cell of **7b** from different perspectives: looking down the *a*-axis (top) at one layer of molecules; looking down the *b*-axis (middle); looking down the *c*-axis (bottom). H-atoms are omitted for clarity.

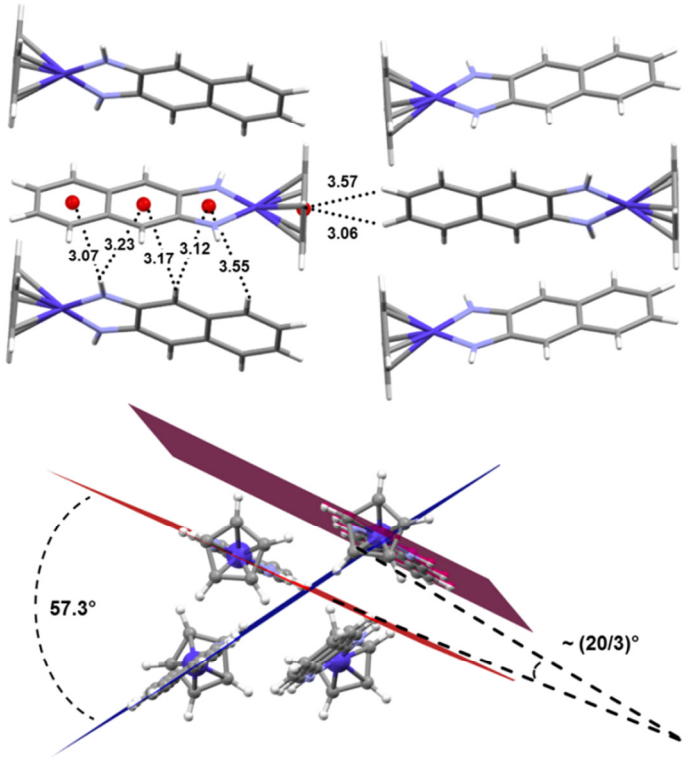

Figure 5.3. Intermolecular distances between molecular stacks (top) and angles between adjacent molecular LS planes in the asymmetric unit (bottom) of **7b**. The red spheres represent the centroids of rings.

5.2.3 Powder X-ray diffraction

Room-temperature PXRD measurements were carried out on **7a** and **7b** initially to confirm the phase and purity of the bulk material, with the data subjected to Rietveld refinements. Initial cell parameters for the refinement of **7b** were taken from the single-crystal structure obtained at 120 K. The experimental data and Rietveld fits are displayed in **Figure 3.7**, with the calculated cell parameters presented with comparison to single-crystal values in **Table 3.6**.

The quality of the PXRD data of **7b** was not as good as for **7a**, with fewer and less intense peaks. This is unsurprising given the size and low symmetry of the unit cell. In addition, the crystal structure was diffracted at 120 K whereas the powder data were collected at RT, therefore by correcting for thermal displacements

the data can be confirmed to be of the same phase of the crystal structure. The confirmation of the powder phases of both compounds is crucial to the validation of any conclusions drawn between the solid-state structure and the origin of the intense NIR absorption discussed in **Section 5.2.4**.

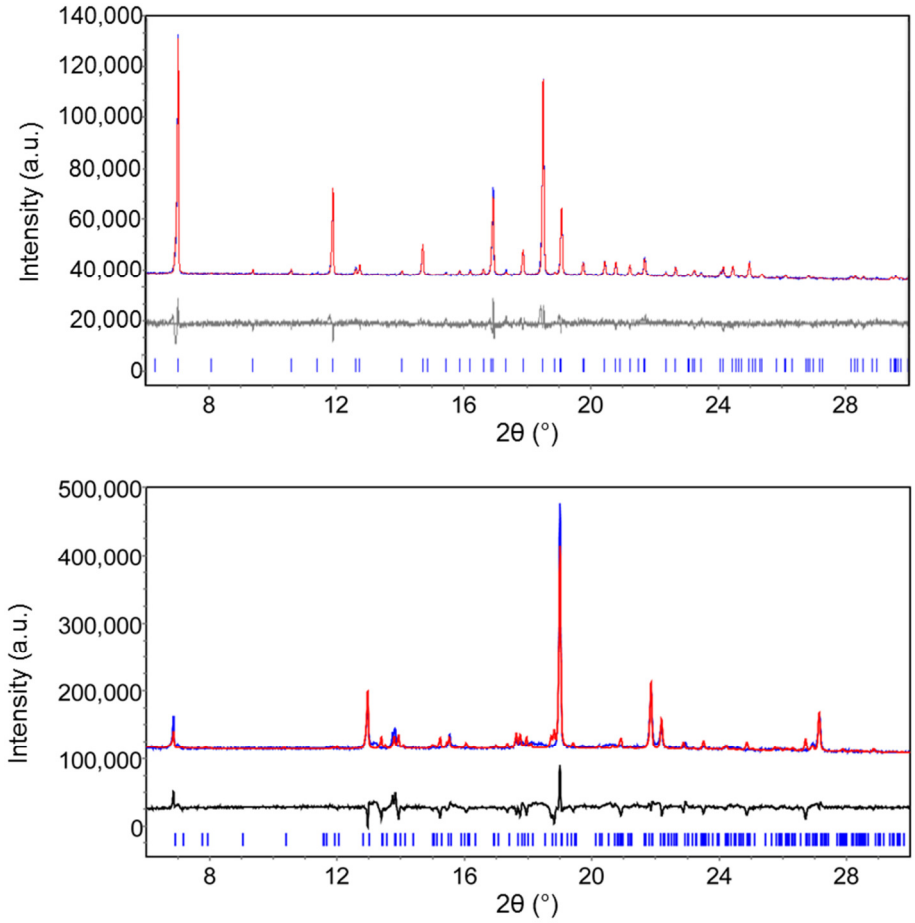

Figure 5.4. Rietveld fits for **7a** (top) and **7b** (bottom). Observed data (blues line) at 298 K are compared with the calculated patterns (red lines). The difference between the two patterns (grey/black lines) are also shown along with the predicted Bragg peaks for the calculated space groups (blue tick marks).

Table 5.1. Unit cell parameters and reliability factors obtained from Rietveld refinement of powder data of **7a** and **7b**.

	7a		**7b**	
	Powder	**SC**[†]	**Powder**	**SC**
Space group	$P2_1/n$	$P2_1/n$	*P*bca	*P*bca
a / Å	17.8129(9)	17.817(5)	8.1071(5)	8.0581(4)
b / Å	8.8612(9)	8.865(2)	25.5678(5)	25.6103(14)
c / Å	12.4825(3)	12.479(3)	45.4773(6)	45.069(2)
α / °	90	90	90	90.0
β / °	94.6973(4)	94.70(2)	90	90.0
γ / °	90	90	89.4290(4)	90.0
V / Å^3	*1963.750(5)*	1964.4(6)	9426.112(4)	9300.9(8)
Z		8		32
λ (Å)	1.5418	1.5418	1.5418	1.5418
2θ range (°)	2-30	3-45	6-30	3-27.5
R_p (%)	5.67		13.98	
R_{wp} (%)	8.17		26.18	
R_{exp} (%)	5.13		2.95	
χ^2 (GoF)	1.592		8.885	

[†]From Rheingold.[12]

Due to the quality of the PXRD data of **7a**, a full structural model could be formulated by fitting the data with the constraint of the molecular coordination supplied from a geometry-optimised structure from DFT calculations (**Section 5.2.6**). There was a crystal structure of **7a** in the literature,[12] but it lacked full information. Therefore Rietveld refinements were carried out on **7a** using the structural parameters taken from the literature as initial cell parameters.

7a crystallises in the monoclinic $P2_1/c$ space group with two molecules per asymmetric unit and only eight molecules per a unit cell (**Figure 5.5**). The two molecules in **7a** are aligned head-to-head with respect to the orientation of the Cp ring in the asymmetric unit, but exist at an angle of 78.8° between the LS planes (**Figure 5.6**). The crystal structure of **7a** is distinct from that of **7b**, but does display a similar interaction between individual molecules in the structure. The intermolecular short contacts between ring centroids and H-atoms are of a similar magnitude to those of **7b** between 3.0 and 3.5 Å. The overall packing of the structure is notably

different from that of **7b** however, with an orientation between the molecules that is less simple to define.

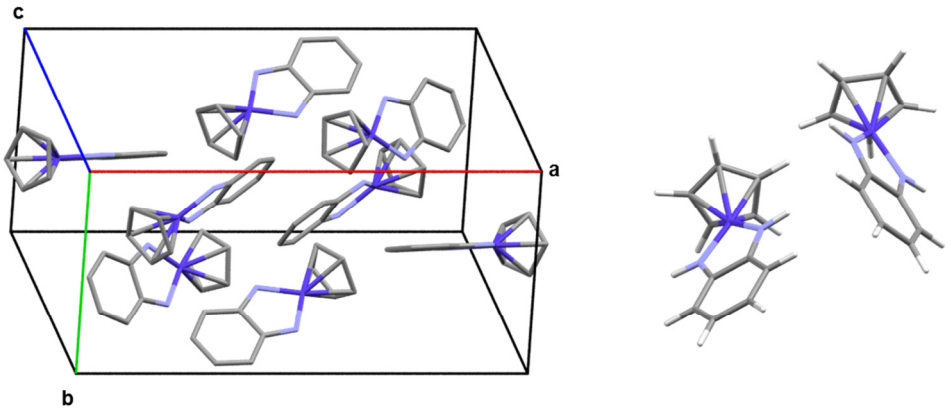

Figure 5.5. Unit cell (left) and asymmetric (right) of **7a**. H-atoms are omitted from the unit cell diagram for clarity.

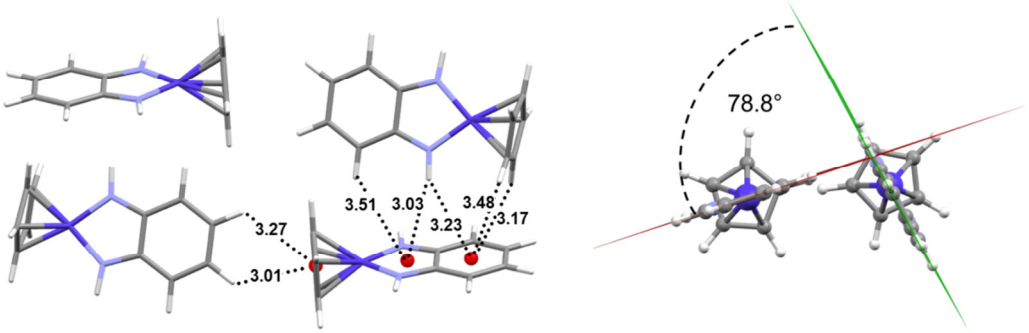

Figure 5.6. Intermolecular distances between molecular stacks (left) and angles between adjacent molecular LS planes in the asymmetric unit (right) of **7a**.

It should be emphasised that obtaining a unit cell with complete atomic positions from PXRD data is not commonplace for molecular structures, but was enabled in this instance by the rigidity of the molecule that possessed very few degrees of freedom, minimising the number of parameters to be fit. Given the quality of the raw PXRD data and that of the Rietveld fit, one should place confidence in the in the structure obtained by this method. The structure of **7a** calculated herein was essentially identical to that the literature, with the only deviation in the unit cell parameters in the third decimal place. Therefore, contrary to confirming a novel

crystal structure, the presence of an identical structure in the literature has verified this as a valid method for predicting fully-resolved crystal structures.

5.2.4 Electronic absorption spectroscopy

The solution absorption spectra of both **7a** and **7b** are shown in **Figure 5.7** (left). Each compound displays an intense CT absorption in the visible region of the spectrum, with molar absorptivities of 24,840 and 29,820 mol^{-1} dm^3 cm^{-1} for **7a** and **7b** respectively. The peak position shows a bathochromic shift from 520 nm in **7a** to 560 nm in **7b**. No significant solvatochromic behaviour was observed for this visible absorption peak, studied in organic solvents ranging in polarity from hexane to dimethylformamide. However, both compounds also display a NIR absorption band, which is also redshifted in peak position from 740 nm for **7a** to 940 nm for **7b**. This absorption is very weak in comparison to the absorptions in the visible region, so much so that it could be missed if not for careful observation. Indeed, for **7a** this absorption peak is not reported at all by Heck.[7] This NIR peak displays negative solvatochromism for **7b**, which is displayed in **Figure 5.7** (right), where the absorption peak position is blueshifted with increasing solvent polarity (hypsochromic shift) from 975 nm in hexane to 908 nm in DMF. The same behaviour is not observed for the NIR peak of **7a**. Both sets of peaks obey the Beer-Lambert law, indicating that the NIR peak is not due to aggregation effects.[19]

Analogues of these compounds in the form of CpNi(dithiolene) compounds have reported strong NIR absorptions in the range of 700 to 1000 nm, with molar absorptivities of between approximately 1000 and 5000 mol^{-1} dm^3 s^{-1} in the solution spectra.[2] The authors ascribe this transition as having origins based on the HOMO, which is located on the dithiolene part of the molecule. No solid-state spectra have been presented in their analysis however, so one can not compare the same phenomena. Furthermore, these compounds are radicals, and so will possess a different electronic structure than those presented in this thesis.

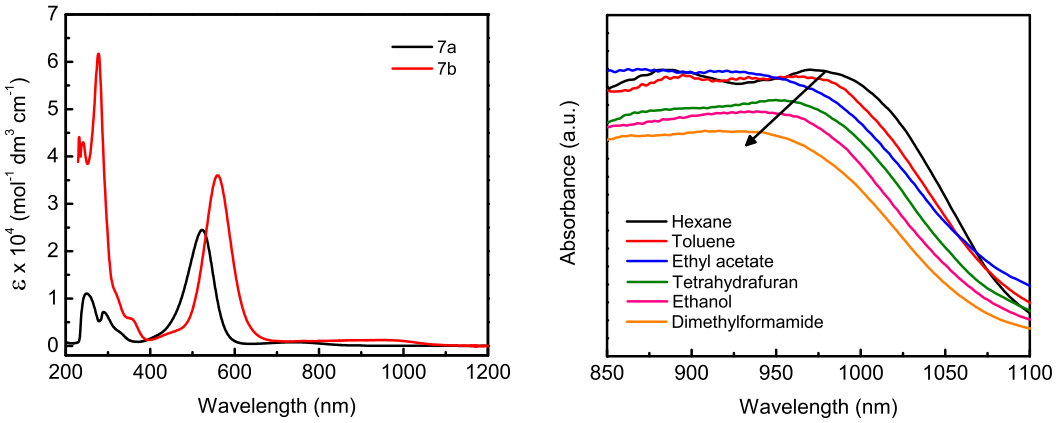

Figure 5.7. Left: solution UV-Vis-NIR absorption spectra of **7a** (black line) and **7b** (red line). Right: negative solvatochromism of the NIR peak of **7b**; there is a hypsochromic shift from a peak maxima position of 975 nm in hexane to 908 nm in DMF. There is a second peak observable at lower values of wavelength (*ca*. 880 nm) in the low-polarity solvents of hexane, toluene and ethyl acetate.

The reflectance spectra (**Figure 5.8** (left)) reveal a very interesting feature of these compounds in the solid state. The weak NIR absorptions from the solution spectra appear with equal or greater intensity to the visible peaks from the solution spectra. Comparing with the NIR absorptions from the solution spectra, the peak positions have shifted from 740 nm to 780 nm for **7a** and from 940 to 1082 nm in **7b**. The electronic absorption spectra for vacuum-deposited thin films of **7b** on HMDS- and OTS-treated quartz glass were measured and compared to the powder reflection spectrum (**Figure 5.8** (right)). The thin film of **7a** was not able to be deposited (**Section 5.4.1.2**). The thin-film absorptions of **7b** for both surface treatments are similar to that of the powder diffuse reflectance spectrum, but show fine structure to both the high- and low-energy absorption peaks. The low-energy peak has a shoulder on the high-energy side, which may help deconvolute this absorption in that it may arise from more than one transition. Indeed, this transition is assigned to two transitions from the TD-DFT calculations for **7b** (**Section 5.2.6.1**), corresponding to HOMO to LUMO and HOMO-2 to LUMO transitions.

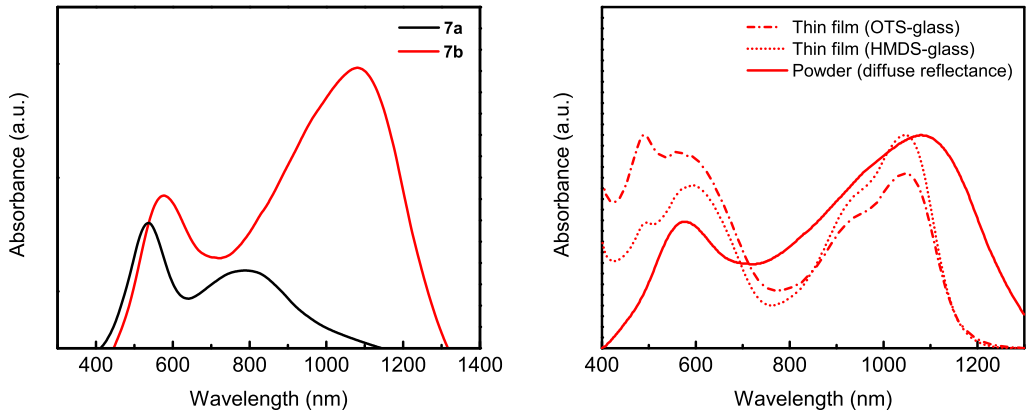

Figure 5.8. Left: diffuse reflectance spectra of **7a** (black line) and **7b** (red line) in the visible/NIR spectral region from 350 to 1400 nm. Right: comparison of thin films of **7b** with the diffuse reflectance spectrum of a polycrystalline sample.

Table 5.2. Peak absorption details from the electronic spectra of **7a** and **7b**.[†]

	Absorption maximum, λ_{max} (nm)					
	Solution				Diffuse reflectance	
7a	249	290	523 [24,500]	740 [650]	536	788
7b	241 [36,100]	278 [49,800]	560 [29,820]	940 [560]	576	1082

[†]The numbers in square brackets represent the molar extinction coefficient measured in units of mol^{-1} dm^3 cm^{-1}. E_{gap} is calculated from the λ_{onset} for diffuse reflectance.

It may be the case that it is not the NIR peak that is intense, rather the visible peak that has weakened from solution to the solid state. Normalising the intensities of the absorptions in the UV region observed in the thin-film with that in solution, one can standardise the relative intensities of the other absorptions (**Figure 5.9**). This assumption is reasonable because the absorptions in the UV correspond primarily to intraligand-based transitions from more core-like orbitals, therefore these transitions should not change drastically between the solution and solid states. This comparison shows that the visible absorption is at a significantly lowered intensity in the solid state, whilst the NIR absorption is only intense in the solid state. This result proves that the intense NIR absorption is not a consequence of scaling.

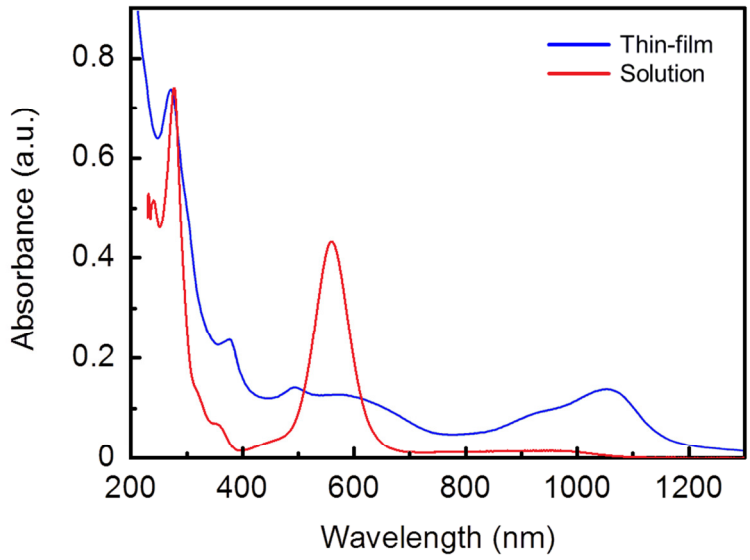

Figure 5.9. Comparison of the absorption spectra of **7b** of a thin film on HMDS-treated quartz glass (blue line) and of a THF solution (red line). The y-axis has been normalised to the height of the UV absorption peak that occurs around 280 nm.

5.2.5 Electrochemistry

The redox activity of **7a** and **7b** was analysed through the techniques of CV and DPV. These compounds were specifically chosen for investigation with redox activity in mind, because the presence of facile redox processes has positive implications for potential charge transfer in the solid state. In addition, analysis of the energies of the electrochemical processes will provide insight into the electronic structure of these materials, and possibly into the nature of the NIR absorption band.

Experiments were carried out with 0.1 M $TBABF_4$ in acetonitrile, using the standard 3-electrode system described in Chapter 2 (**Section 2.2.4**). The potentials were measured with respect to Ag/AgCl and corrected *vs*. the Fc/Fc^+ redox couple that occurs at $E_{1/2}$ = 0.562 V and with ΔE = 110 mV for both **7a** and **7b**. Cyclic voltammograms of the compounds each display one oxidation and one reduction process in the electrochemical range of -2.0 to 2.0 V *vs*. Ag/AgCl (**Figure 5.10**), with the measured electrochemical values present in **Table 4.7**. The oxidation process occurs at very similar half-wave potentials of -0.13 and -0.10 V for **7a** and **7b** respectively. This process is electrochemically reversible for **7a** (**Figure 5.11**

(right)), whereas it is electrochemically irreversible for **7b**. Close inspection of the oxidative scan reveals a small, second anodic process immediately following the first in **7b**, which is the likely cause of the irreversible nature and is confirmed from DPV analysis (**Section 5.2.6**). The first reduction process occurs at the more separated half-wave potentials of -1.83 and -1.52 V for **7a** and **7b** respectively. On first examination the processes appear electrochemically reversible for both compounds, and examination at different scan rates indicates that the peak potentials do not shift: the magnitude of ΔE stays at a relatively constant value with increasing scan rate, at approximately 90 mV for **7a** and 100 mV for **7b**. ΔE for ferrocene was measured at 110 mV, therefore these processes may be regarded as electrochemically reversible.

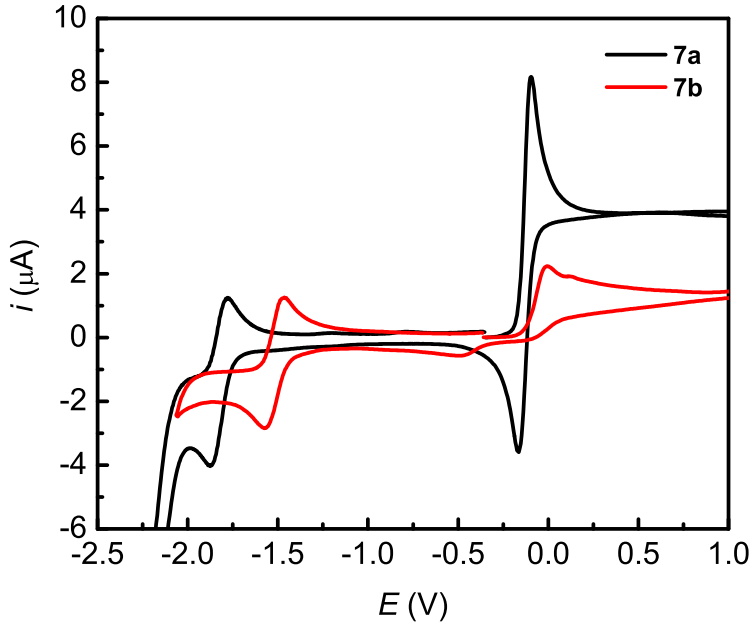

Figure 5.10. Cyclic voltammograms of **7a** (pink) and **7b** (purple) in MeCN with 0.3 M $TBABF_4$ supporting electrolyte in the range of electrochemical activity. Both voltammograms were oxidative scans swept from zero with respect to Ag/AgCl reference electrode and subsequently referenced *vs.* Fc/Fc^+.

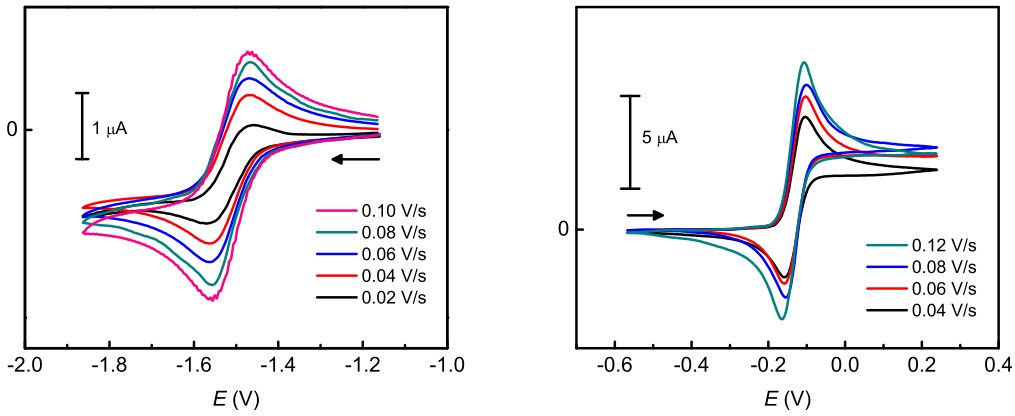

Figure 5.11. Scan rate study of the first reduction potential of **7b** (left) and the first oxidation potential of **7a** scan rate (right). The arrows indicated the direction of initial scan. The first reduction potential of both complexes is electrochemically reversible, whereas the first oxidation process is only electrochemically reversible for **7a**.

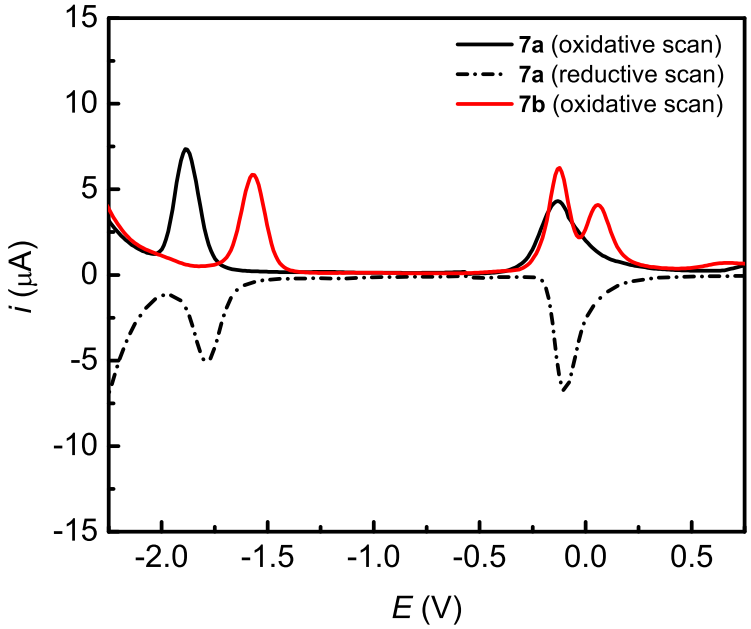

Figure 5.12. Differential-pulse voltammograms of **7a** and **7b** in MeCN with 0.3 M $TBABF_4$ supporting electrolyte in the range -2.25 to 0.75 V. Potentials are referenced *vs.* Fc/Fc^+. The solid lines represent the scan from negative to positive potentials (oxidative) and the dot-dash line represents the scan from positive to negative potentials (reductive).

Table 5.3. Selected electrochemical values observed from CV for **7a** and **7b** in MeCN with 0.3 M $TBABF_4$ supporting electrolyte.[†] Scan rate = 0.1 V s^{-1}. Potentials are referenced *vs*. Fc/Fc^+.

Complex	$E_{1/2}^{red}$ (V)	ΔE (mV)	$\lvert i_{pa}/i_{pc} \rvert$	$E_{1/2}^{ox}$ (V)	ΔE (mV)	$\lvert i_{pa}/i_{pc} \rvert$	E_{gap} (eV)
7a	-1.83[B]	90	0.61	-0.13[A]	70	1.13	1.70
7b	-1.52[A]	100	1.04	-0.10[C]	*n/a*	*n/a*	1.32

[†]Definition of terms in the table are given in Chapter 2. For processes defined as irreversible, $E_{1/2}^{red/ox} = (E_p + E_{p/2})/2$ and $\Delta E_{p/2} = (E_p - E_{p/2})$, where $E_{p/2}$ is the half-peak potential. [A]Electrochemically-reversible redox process. [B]Partially-reversible redox process (presence of redox activity within 200 mV of the peak potential). [C]Electrochemically-irreversible redox processs.

Table 5.4. Selected electrochemical values observed from DPV for **7a** and **7b** in MeCN with 0.3 M $TBABF_4$ supporting electrolyte.[†] Potentials are referenced *vs*. Fc/Fc^+.

Complex	$E_{1/2}^{red}$ (V)	ΔE (mV)	$\lvert i_{pa}/i_{pc} \rvert$	$E_{1/2}^{ox}$ (V)	ΔE (mV)	$\lvert i_{pa}/i_{pc} \rvert$	E_{gap} (eV)
7a	-1.84[B]	99	1.44	-0.12[A]	33	0.64	1.70
7b	-1.57[B]	*n/a*	*n/a*	-0.13[C]	235	22.70	1.44

[†]For processes defined as irreversible, $E_{1/2} = E_p$. [A]Electrochemically-reversible redox process. [B]Partially-reversible redox process. [C]Electrochemically-irreversible redox processs.

From the calculated $E_{1/2}$ values for the oxidation and reduction processes, one can calculate the electrochemically determined energy gap, which often corresponds directly to the HOMO-LUMO gap. This can then be compared with the estimates of the optical band gap determined from the onset of the low-energy band in the absorption spectra. One can also estimate the energy of the HOMO experimentally from the oxidation potential from electrochemistry and referencing it with respect to the energy level of the HOMO of ferrocene, which is calculated to occur at 4.8 eV below the vacuum level.[20] The equation for this estimation is:

$$E_{HOMO} = -(E_{1/2}^{ox} - E_{1/2}^{Fc}) - 4.8 \text{ eV} \qquad \textbf{Equation 5.1}$$

where $E_{1/2}^{ox}$ is the potential for the first oxidation process and $E_{1/2}^{Fc}$ is the potential for the Fc/Fc^+ redox couple. The calculated values of E_{HOMO} and the experimentally determined HOMO-LUMO gaps derived from DPV (E_{gap}^{DPV}) and optical spectroscopy (E_{gap}^{Abs}) are compared in **Table 5.5** with values derived computationally

from DFT. The estimated HOMO-LUMO gaps of 1.70 and 1.44 eV for **7a** and **7b** respectively compare reasonably well to those estimated from the onset of the respective absorption bands in the solution UV/Vis absorption spectra of 1.43 and 1.15 eV. The energy levels of the HOMOs determined from electrochemistry of -4.92 and -4.93 eV for **7a** and **7b** respectively compare very favourably with the values of -4.93 and -4.95 eV calculated from DFT methods (**Section 5.2.6**). The HOMO-LUMO gap predicted from DFT ($E_{\mathrm{gap}}^{\mathrm{DFT}}$) is significantly greater than the gaps determined by the other methods. However, this is due to the error in the estimation of the energy of the virtual orbitals which is fundamentally more difficult.

Table 5.5. Frontier orbitals and band gap energies determined by various methods.[†]

	E_{HOMO} (V)	$^{‡}E_{\mathrm{HOMO}}^{\mathrm{DFT}}$(eV)	$^{‡}E_{\mathrm{gap}}^{\mathrm{DFT}}$ (eV)	$E_{\mathrm{gap}}^{\mathrm{DPV}}$ (eV)	$E_{\mathrm{gap}}^{\mathrm{Abs}}$ (eV)
7a	-4.92	-4.93	2.80	1.70	1.43
7b	-4.93	-4.95	2.41	1.44	1.15

[†]$E_{\mathrm{HOMO}} = -(E_{1/2}^{\mathrm{ox}} - E_{1/2}^{\mathrm{Fc}}) - 4.8$ eV, $E_{\mathrm{gap}}^{\mathrm{DFT}}$ = electrochemical band gap calculated from the difference in the oxidation (E_{HOMO}) and reduction (E_{LUMO}) peak potential values, $E_{\mathrm{gap}}^{\mathrm{Abs}}$ = optical band gap determined by onset of NIR absorption band from solution. [‡]Calculations optimised with a polarisable continuum solvent model with MeCN.

5.2.6 DFT calculations

Single-molecule gas-phase calculations were used to determine the ground state molecular geometry as well as the position of the frontier orbitals of the molecules. The geometry optimisation generated the predicted T-shaped geometry typical of this class of molecules, with the planar Cp and diamine ligands perpendicular to each other. Solvent interactions were represented by running calculations with the PCM with acetonitrile as the solvent to allow for better comparison with the experimental data. As in the other chapters, the B3LYP hybrid DFT functional and the 6-31G(d,p) basis set were used for all atoms apart from Co, which used the LANL2DZ pseudopotentials to model core electrons. TD-DFT analysis was carried out using the PCM-optimised structures and the same level of theory.

An energy level diagram for the solvent-optimised structures together with a graphical representation of the molecular orbital locations is presented in **Figure 5.13**, with the percentage occupancies of the HOMO and LUMO shown in **Table 3.8**. The frontier orbitals are significantly delocalised over the entire molecule of **7a**. This is an ideal feature for charge transfer applications, as it promotes the potential orbital overlap and also improves stability of charge-transfer states in the solid state due to lower reorganisation energies.[21] Unfortunately this compound has yet to be processed into a suitable thin film for solid-state conductivity measurements like that which was done for **7b** (**Section 5.2.7**). The orbital locations of the LUMO of **7b** are similar to that of **7a**, with significant contributions from the Co centre and the diamido ligand of approximately 47 and 36 % respectively. The HOMO orbital on the other hand has a small Co contribution relative to the LUMO, with the majority contribution to the orbital coming from the more delocalised diamido of DAnap.

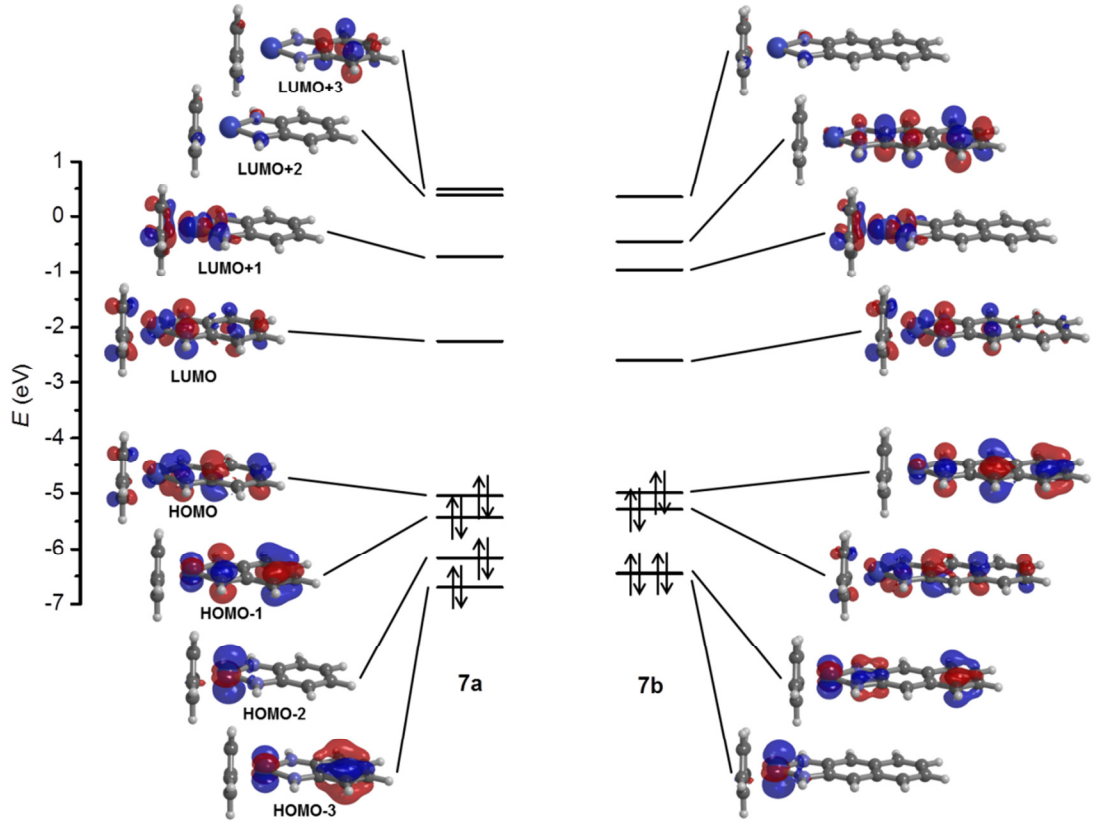

Figure 5.13. Orbital energy diagram with graphical representation of the calculated orbital positons.

Table 5.6. Calculated percentage contributions to selected molecular orbitals of Co complexes.

Complex	Orbital	Energy (eV)	Orbital locations (%)		
			Co	Diamine	Cp
7a	HOMO	-5.05	32.57	53.88	13.54
	LUMO	-2.25	44.08	40.91	15.02
7b	HOMO	-4.95	13.10	84.89	2.02
	LUMO	-2.55	46.81	36.23	17.00

5.2.6.1 TD-DFT

The TD-DFT calculations were carried out to determine the origin of the observed transitions in the electronic spectra, and in particular, the origin of the NIR peak in the experimental spectra. The calculated absorption spectra (modelled with acetonitrile solvent) are compared with the experimental spectra of **7a** and **7b** in acetonitrile solution (**Figure 5.14**). There is a good qualitative agreement between observed and experimental spectra, with the main transitions being predicted. The UV and visible absorption peaks are calculated to occur at higher energies than in the experimental spectra, whereas the NIR absorption is predicted to occur at lower energies. The majority contributions to the main transitions observed in the absorption spectrum are presented in **Table 4.15**. The absorption in the visible region of the spectrum is predicted to be mainly HOMO → LUMO in nature in **7a** and HOMO-1 → LUMO in nature in **7b**. This assignment is reversed for the predicted low-energy NIR transition, with major contributions from HOMO-1 → LUMO in **7a** and from HOMO → LUMO in **7b**. This assignment agrees with the orbital diagrams (**Figure 5.13**), which show that the HOMO and HOMO-1 orbitals switch over from **7a** to **7b**. The HOMO and LUMO orbitals are similar in shape for **7a**, whereas it is the HOMO-1 and LUMO that are similar in **7b**.

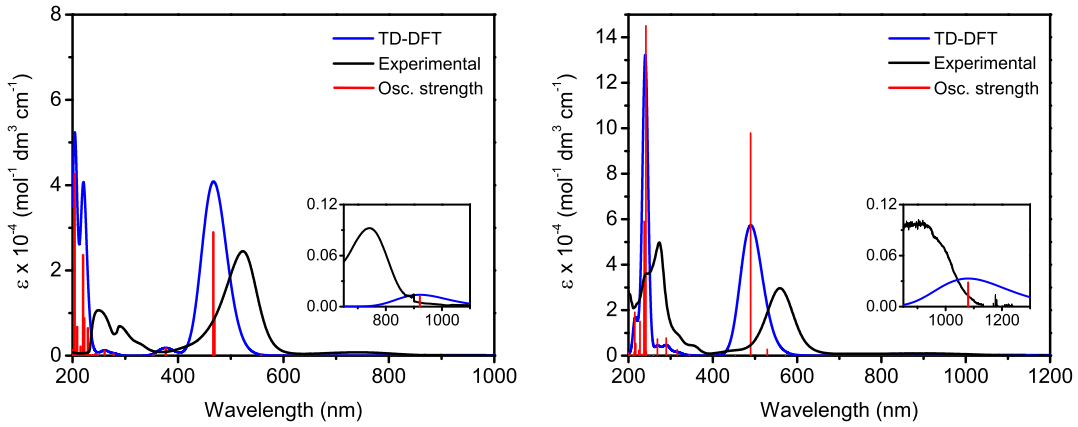

Figure 5.14. TD-DFT calculated absorption spectra (blue lines) with oscillator strengths (red vertical lines) of **7a** (left) and **7b** (right), compared with the experimental solution spectra (black lines). The full-width half-maximum (FWHM) values used for the calculated spectra were 2500 cm^{-1}.

Table 5.7. Calculated TD-DFT excitation energies and assignments of low-energy transitions and experimental absorption maxima from solution spectra.[†]

Complex	Energy (cm^{-1})		Majority orbital contribution
	Experimental	TD-DFT	
7a	40,161	49,049 (0.533)	HOMO-1 → LUMO+6 (50%)
	34,483	45,434 (0.295)	HOMO-4 → LUMO+1 (49%)
			HOMO-1 → LUMO+9 (23%)
	19,120 [24,500]	**21,414 (0.362)**	**HOMO → LUMO (77%)**
			HOMO-2 → LUMO+1 (17%)
	13,514 [650]	**10,855 (0.002)**	**HOMO-1 → LUMO (63%)**
			HOMO-3 → LUMO (25%)
7b	41,494 [36,100]	45,985 (0.036)	HOMO → LUMO+7 (58%)
	35,971 [49,800]	42,175 (0.211)	HOMO-3 → LUMO+2 (45%)
			HOMO-1 → LUMO+5 (23%)
		42,176 (0.394)	HOMO-1 → LUMO+5 (42%)
			HOMO-3 → LUMO+2 (25%)
	17,857 [29,820]	**20,420 (0.653)**	**HOMO-1 → LUMO (99%)**
	10,638 [560]	**9,260 (0.004)**	**HOMO → LUMO (53%)**
			HOMO-2 → LUMO (34%)

[†]Molar absorptivities (mol^{-1} dm^3 cm^{-1}) of experimental absorptions are given in square brackets and calculated oscillator strengths of calculated absorptions are given in parentheses.

5.2.7 Thin-film processing

In order to study the conducting properties of the compounds thin films were prepared. The compounds are extremely soluble in a wide range of organic solvents, which was an incentive for attempting to process films by spin coating. As mentioned in Chapter 4, a high solution concentration is a prerequisite for producing high-quality films from this method. Extensive testing was carried out in solutions of various organic solvents at concentrations close to saturation, spin-coating the solutions onto FET substrates. However, no success was had in producing films using this method. It was found that the molecules did not adhere strongly enough to the surface of the substrate, and instead spun off the surface still in solution. Future work in solution processing will focus more on the technique of drop casting to create polycrystalline films,[22] as these compounds readily precipitate as crystalline material from the slow evaporation of organic solvents. However, these compounds were initially designed with vapour processing in mind, which is discussed below.

5.2.7.1 Vapour processing

Vapour deposition of **7a** and **7b** was carried out in a vacuum chamber, the experimental details of which are given in **Section 5.4.1.2**. The substrates that were to be deposited onto included BCBG FET substrates with interdigitated Au source-drain electrodes to test the field-effect mobility of the compounds. Interdigitated electrode gaps of L = 2, 5, 10, 20 and 50 μm were used. Quartz glass substrates were also included to measure the thin-film absorption properties.

Despite an estimated film thickness of 1000 nm being registered by the quartz crystal microbalance (QCM), there was little evidence of **7a** visible on the surface of the substrates during deposition. On close inspection, there was minimal and non-uniform coverage on the substrates, whereas there was much material deposited around the inside of the vacuum chamber. The QCM surface was coated with a thick, dark red layer of material, which explains why it was registering a thick layer being formed. It is hypothesised that the high relative volatility of the molecules prevents a

suitable vapour pressure from being established to deposit uniform films. This is validated by the fluctuations observed in the deposition rate.

Successful deposition was achieved with **7b**, which formed purple films on all substrates. The general surface coverage and uniformity of the films was good by examination under an optical microscope (**Figure 5.15**). Overall, the OTS-treated substrates yielded more uniform films. However, the position of the substrates within the chamber can have an influence on the nature of the films. Furthermore, only one successful deposition of **7b** onto treated FET substrates was carried out during this thesis, so presumptions about which treatment favours high-quality thin films cannot be made.

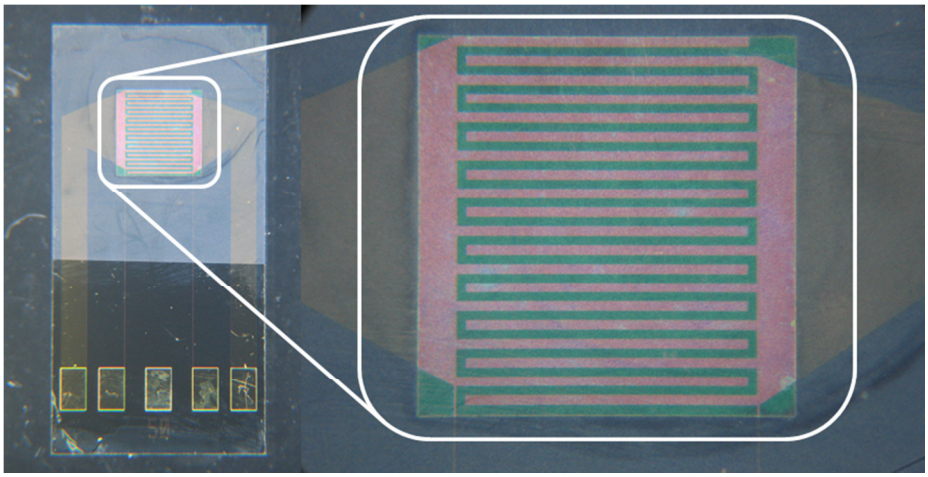

Figure 5.15. Optical microscope image of vapour-deposited film of **7b** on 50×50 μm Au FET. On the right side of the image one can see the interdigitated Au S-D electrodes coated with the purple film of **7b**.

5.2.8 FET measurements

The transfer and output characteristics of vapour-deposited thin films of **7b** were measured, with a range of FET substrates with different channel lengths. Two pairs of depositions and FET measurements were carried out, the first by the author and the second by Dr. Simon Dalgleish of the Kunio Awaga research group in Nagoya University. For each deposition, only one FET for every channel length and

surface treatment procedure was analysed, so the results have not been verified by the process of duplication and should not be considered to be the best achievable with the materials used.

For the first set of measurements, FET substrates with Au S-D electrodes were used that were surface treated with either OTS or HMDS prior to vapour deposition. OTS-treated substrates with channel lengths of 2, 10 and 20 µm and HMDS-treated substrates with channel lengths of 5 and 10 µm are presented in

Figure 5.16 and **Figure 5.17** respectively. The other FET measurements are not given due to unsuitable device characteristics.

For the second set of measurements, FET substrates with Pt S-D electrodes were used, with channel lengths of 5, 20 and 50 µm. Substrates that had either no surface treatment, OTS treatment or HMDS treatment were tested. The OTS-treated devices did not display any influence of the applied gate voltage (no gate effect). This can be rationalised by the presence of a thick, white insulating siloxane layer that formed as a result of trace moisture present during the surface treatment. This is verified by a clouding of the toluene solution used to treat the substrates. The HMDS-treated FETs performed better than the non-treated ones (the results of which are not discussed from this point). The transfer and output characteristics of these devices are displayed in **Figure 5.18**.

The FET measurements of **7b** exhibit hole-transport behaviour with both Au and Pt S-D electrodes, which is consistent with the electrochemical results of a facile one-electron oxidation. Measurements at positive values of V_G did not produce any meaningful response, indicative of negligible electron transport. The relevant characteristics derived from all of the given measurements are compared in **Table 5.8**. The transfer characteristics measure how the S-D current (I_D) varies in response to a changing V_G at a constant value of V_D. All the values represented in **Table 5.8** have been extracted from graphs of the transfer characteristics: the current on/off ratio (I_{on}/I_{off}) is calculated from the values of I_D when the device is “on” at V_G = -60

V and when the device is "off" at V_G = 0 V. The threshold voltage (V_T) is determined by extrapolating to the intercept a straight line fitted to the linear regime in the plot of the square root of I_D against V_G. The field-effect mobility is calculated from the linear regime of the transfer characteristics, $\mu_{lin} = (\partial I_D/\partial V_G)\cdot(L/C_i W V_D)$.

Comparing the different surface modifications of the FET substrates, better results are achieved with the HMDS treatment where smaller values of V_T and relatively larger μ_{lin} are observed. The improvements are not drastic however and are still in the same order of magnitude. The same is observed when comparing the results from different metal electrodes of HMDS-treated substrates: the significant difference is in the I_{on}/I_{off} values, with those measured in the Pt FETs being much higher. The Pt FET with a gap length of 5 μm has a I_{on}/I_{off} value that is 3 orders of magnitude higher than what is observed in the equivalent Au FET. This trend can be explained from the higher I_{off} value in the Au devices resulting in a smaller $I_{on}/I_{off,}$ which itself can be explained by two potential causes. The first is that due to experimental limitations, the Au FETs were not measured immediately after vapour deposition of the thin films, therefore increasing the potential exposure to air.[23] The second potential cause is of a fundamental rather than environmental origin, as a result of the higher workfunction of Au (-5.1 eV) as compared to Pt (-6.35 eV).[24] The Au workfunction is therefore closer in energy to the calculated HOMO energy level in **7b** of -4.93 eV from electrochemistry and -4.95 eV from DFT. This means that the HOMO level may be more easily doped with holes without the application of applied gate voltage.

General trends observed from all measurements are that the effective mobility and the threshold voltage both increase with increasing electrode gap length. This is likely the result of a decrease in contact resistance at larger gap lengths: contact resistance is high when the gap length of the electrodes is comparable with the morphological scale of the polycrystalline material such as grain size and boundaries.[25] The correlations for the Pt FETs are visualised in **Figure 5.19**, which also confirms the linear dependence of the on/off ratio decreasing the gap length.

This may also be a result of lower contact resistance, or explained by the fact that the FETs measurements were carried out in order of gap length. Therefore the FETs with the largest gaps were the last to be tested and hence more susceptible to atmospheric conditions that would raise the size of I_{off}. Further depositions would need to be carried out to confirm either hypothesis. The threshold voltage is also known to be dependent on environmental factors and additionally to the thickness of the semiconducting layer and the nature of the dielectric surface:[26] a thicker semiconducting layer results in a higher charge injection barrier at the electrode interface. The thickness of the semiconducting layer deposited onto the Pt FETs, which have the lowest V_T measured, was less than that deposited onto the Au FETs. The application of different organosilane SAMs has been demonstrated to shift V_T in FETs due to modification of the dielectric surface dipole.[27] From the results obtained for the Au FETs, V_T is lower for the HMDS-treated FETs than for the OTS-treated ones.

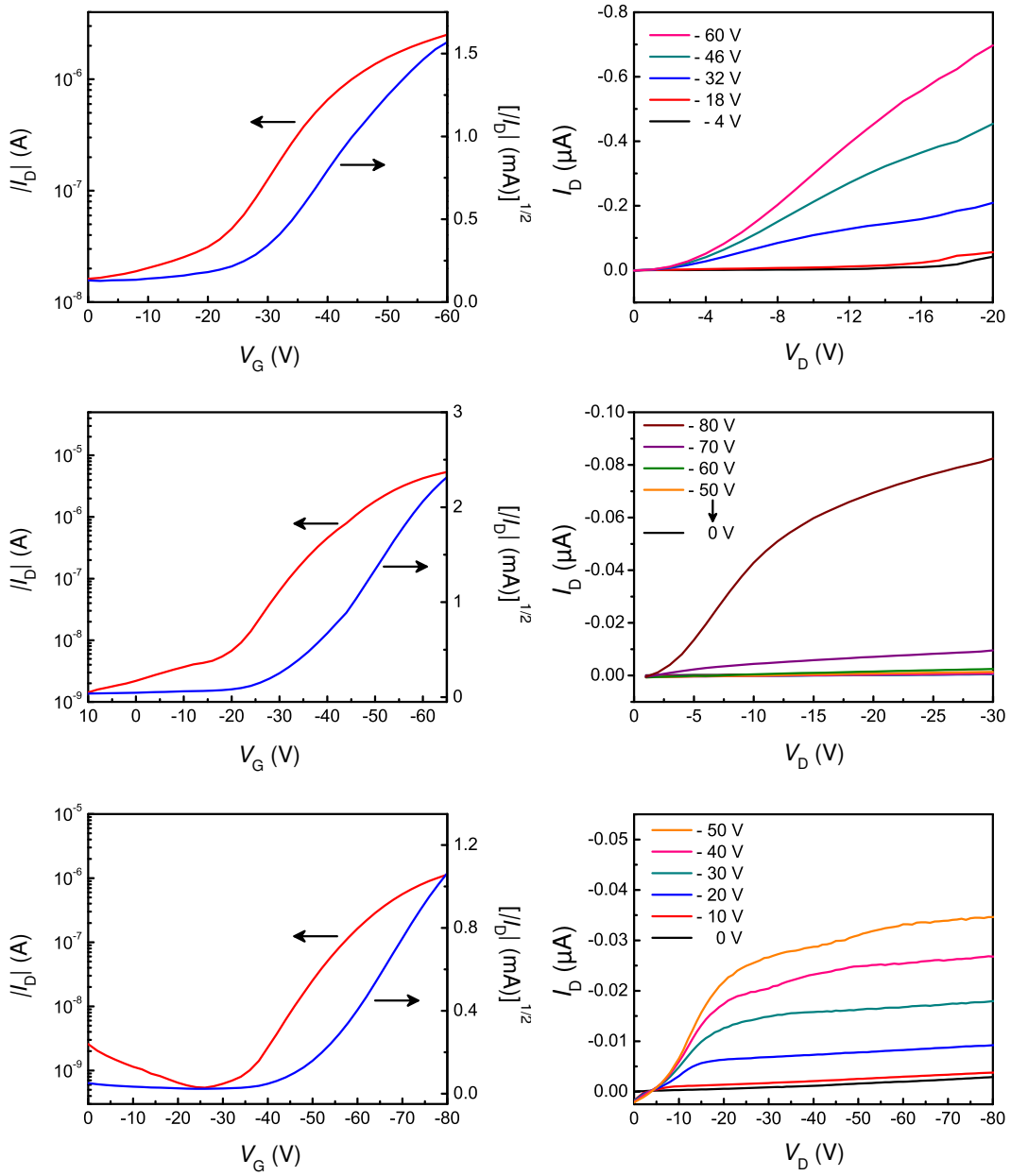

Figure 5.16. Transfer (left) and output (right) characteristics of FET measurements carried out using BCBG OTS-treated FETs with interdigitated Au electrodes, with gap length, L = 2 μm (top), 10 μm (middle) and 20 μm (bottom).

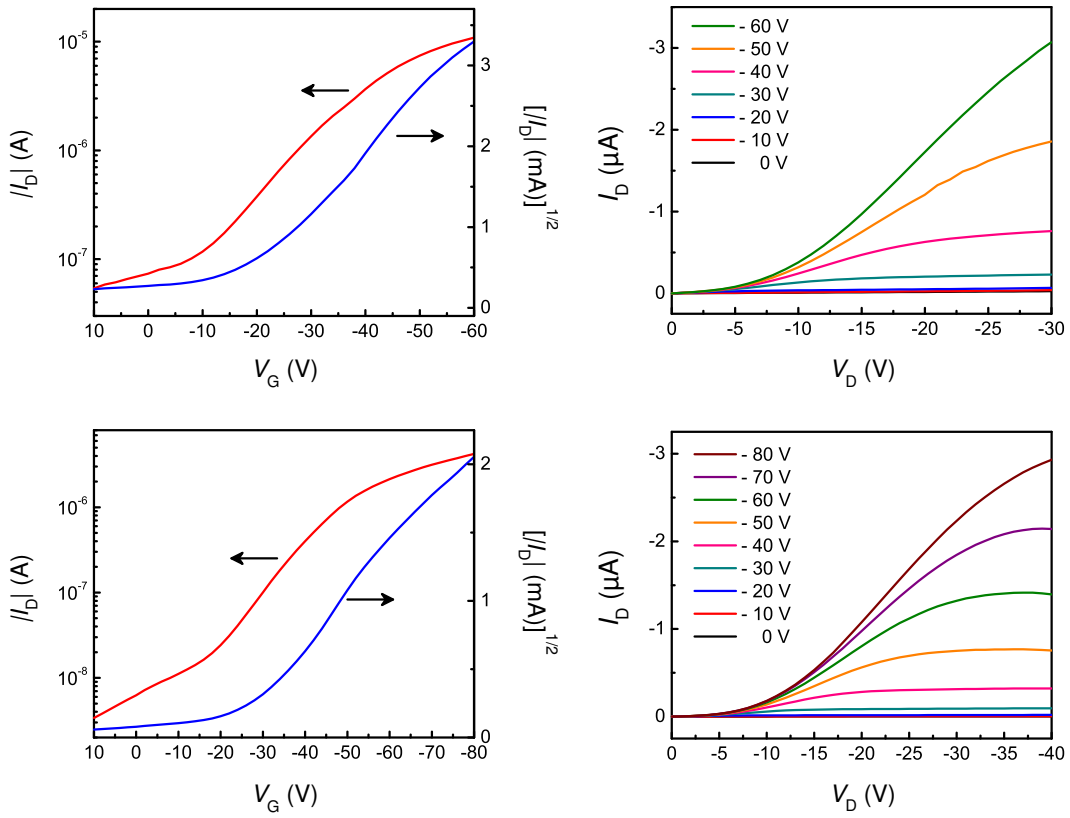

Figure 5.17. Transfer (left) and output (right) characteristics of FET measurements carried out using BCBG HMDS-treated FETs with interdigitated Au electrodes, with gap length, L = 5 (top) and 10 (bottom).

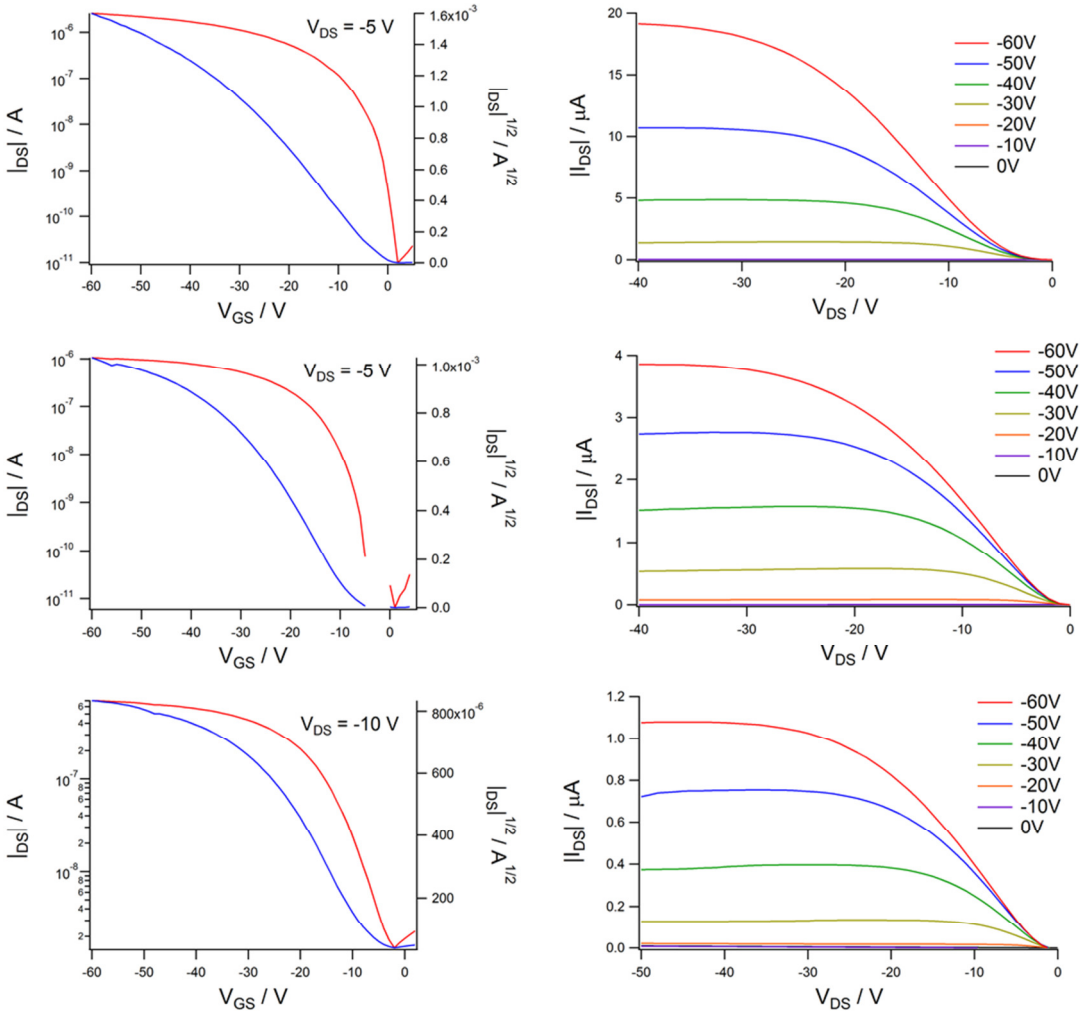

Figure 5.18. Transfer (left) and output (right) characteristics of FET measurements carried out using BCBG HMDS-treated FETs with interdigitated Pt electrodes, with gap length, L = 5 (top), 20 (middle) and 50 (bottom).

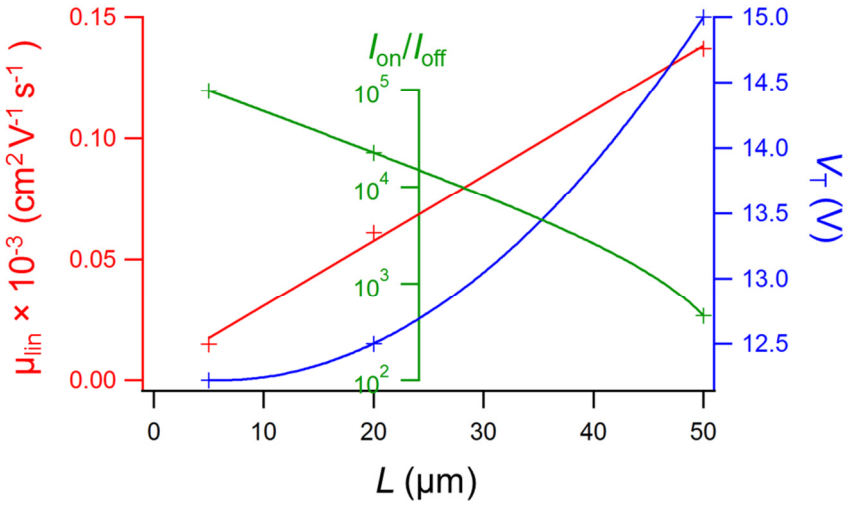

Figure 5.19. Electrode gap-length (L) dependence of μ_{FET}, I_{on}/I_{off} ratio and V_T for vapour-deposted films of **7b**. Measurements were carried out by Dr. Simon Dalgleish at Nagoya University in Japan.

Table 5.8. FET results of all measurements carried out on thin films of **7b**.

Treatment (electrodes)	Gap length (μm)	I_{on}/I_{off}	V_T (V)	μ_{lin} ($cm^2\ V^{-1}\ s^{-1}$)
OTS (Au)	2	0.02×10^4	-25	1×10^{-6}
	10	0.20×10^4	-32	8×10^{-6}
	20	0.21×10^4	-47	1×10^{-5}
HMDS (Au)	5	0.02×10^4	-18	2×10^{-5}
	10	0.03×10^4	-25	5×10^{-5}
HMDS (Pt)[†]	5	1.00×10^5	-12	2×10^{-5}
	20	3.50×10^4	-13	6×10^{-5}
	50	6.50×10^2	-15	1×10^{-4}

[†]Measurements carried out on FETs deposited at Nagoya University by Dr. Simon Dalgleish.

5.2.8.1 Scanning electron microscopy (SEM)

Scanning electron microscopy was used to provide detail of the surface morphology of the films of **7b** deposited from the vapour phase. The images are shown in **Figure 5.20**, where the light surface is the Au electrodes and the grey surface is the gap between the electrodes of surface-treated SiO_2 dielectric. The images indicate that the films deposited onto HMDS-treated FET substrates are more crystalline than those deposited on the OTS-treated FET substrates. This may

provide a rationale for the slightly higher effective mobilities observed on the HMDS-treated FETs, although again, further studies would be needed to verify this. The grain size of the crystallites in the film on top of the HMDS substrate is relatively small, of the order of less than one micron.

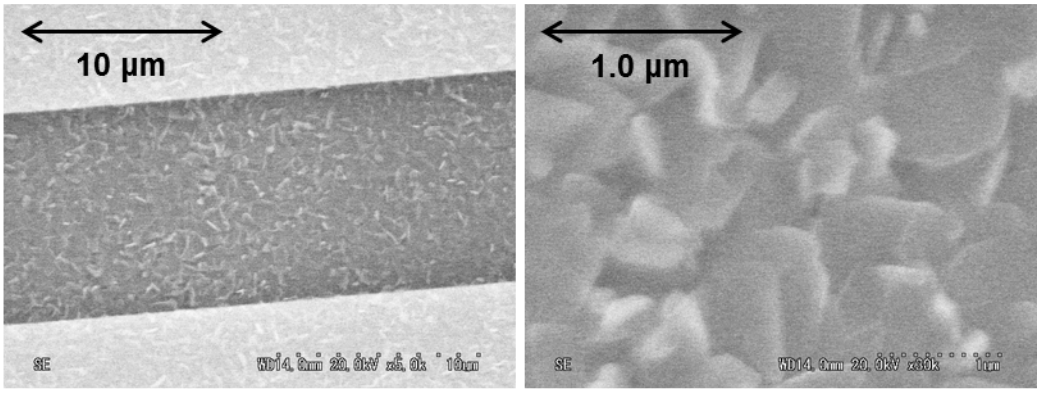

Figure 5.20. SEM images of an HMDS-treated 10 µm gap Au FET.

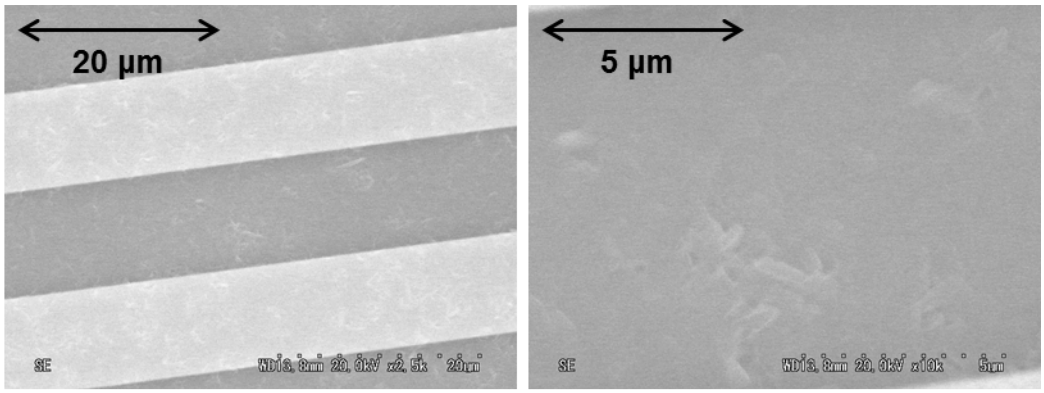

Figure 5.21. SEM images of an OTS-treated 10 µm gap Au FET.

5.3 Conclusions

A pair of half-sandwich complexes of Co(III) with 1,2-diamino-substituted aromatic ligands were prepared. The electronic structure of these complexes was examined using absorption spectroscopy, electrochemistry and DFT calculations. The complexes possess a NIR absorption peak in the solution spectra that

corresponds to a HOMO or HOMO-1 to LUMO transition, which becomes very intense in the solid state. The origins of this intensity are still being investigated, but it remains an interesting feature of these materials that may prove to have applications in optoelectronic devices.

Crystals of **7b** were grown by vacuum sublimation and the structure was determined by X-ray crystallography, which was compared with the structure of **7a** determined from Rietveld refinement of a model against PXRD data. The PXRD data confirmed the phase purity of the bulk polycrystalline material and the Rietveld refinements confirmed that the measured phases were the same as in the single-crystal structures obtained. Therefore conclusions about the solid-state properties of these compounds can be compared to the determined structures. The structure of **7a** and **7b** are notably different, with **7b** displaying a unique undulation propagated along the *c*-axis of approximately ±20° between LS planes of adjacent sets of four molecules. This structural property may have a strong influence on the solid-state charge transfer properties given comparison to other structural features of molecular semiconductors.

Initial assessment of the formation and analysis of thin films of compound **7b** was carried out in regard to electronic characterisation and the solid-state conductivity in devices. The thin-film absorption spectrum is characteristic of that seen in the bulk polycrystalline material from diffuse reflectance spectroscopy.
Further studies will be carried out on the photoconductive properties of thin films of these materials to assess their applicability.

The FET characteristics of these thin films were found to exhibit *p*-type semiconductivity, with a highest FET mobility of approximately 10^{-4} cm^2 V^{-1} s^{-1}. The measured mobilities are comparable to those achieved for other transition metal-based compounds. The surface treatment of the FET substrates was seen to have an effect on the FET parameters, with the HMDS-coated FETs resulting in higher measured mobilities than the OTS-coated FETs. SEM images of the thin films show

that the HMDS treatment led to films with a greater degree of crystallinity, which may help explain the improved performance. With further testing and optimisation of the experimental parameters, higher mobilities are to be expected.

Overall, this class of compounds is the first of its kind to display FET characteristics, and from the preliminary studies are promising candidates for future investigations. Future work is proposed for changes to the molecular structure that may lead to better FET characteristic and a better understanding of the observed NIR absorptions. Proposed ligand modifications of the chelating aromatic ligand include donor or acceptor substituents to tune the frontier orbitals as well as modifications to increase the conjugation and promote intermolecular interactions.

5.4 Experimental

Diiodocarbonylcyclopentadienylcobalt(III) ($CpCo(CO)I_2$). Synthesis derived from the method of King.[8] Dicarbonylcyclopentadienylcobalt(I), $CpCo(CO)_2$ (1.0 g, 5.67 mmol), was weighed out using a tared syringe and dissolved in MeOH (20 ml) under N_2. Iodine (1.41 g, 5.67 as I_2) was added to the stirred solution over 20 min, resulting in the evolution of CO and formation of a black precipitate. The mixture was concentrated to half volume on a rotary evaporator before filtering under vacuum. The black residue was extracted into DCM (100 ml) and evaporated to dryness to give a black, microcrystalline product (1.915 g, 83%). Calculated (found) for $C_6H_5CoI_2O$: C, 17.76 (17.79); H, 1.24 (1.14); N, 0.00 (0.00).^{1}H-NMR (500 MHz, $CDCl_3$): δ 5.69 (5H, s). ^{13}C-NMR (500 MHz, $CDCl_3$): δ 89.42 (5 × *C*H). MS (+ESI): *m*/*z* 437.31 ($[M+CH_3OH]^+$, 100%). IR (KBr, cm^{-1}) ν 2924 (w), 2360 (s), 2335 (s), 2063 (s), 1869 (w), 1844 (w), 1791 (w), 1772 (w), 1734 (m), 1716 (m), 1699 (m), 1684 (m), 1670 (w), 1653 (s), 1635 (m), 1616 (w), 1576 (w), 1558 (s), 1541 (s), 1522 (m), 1506 (s), 1489 (w), 1473 (w), 1456 (m), 1437 (w), 1419 (m), 1396 (w), 1070 (m), 1043 (m), 837 (s), 667 (m), 600 (m).

Benzene-1,2-diamidocyclopentadienylcobalt(III) (CpCoDAbnz). Synthesis derived from that of Heck.[7] $CpCo(CO)I_2$ (0.812 g, 2 mmol) and 1,2-diaminobenzene (0.213 g, 2 mmol) were dissolved in dry DCM (10 ml) and stirred at RT for 3 h. The mixture was filtered under vacuum to yield crude iodo(benzene-1,2-diamido)cyclopentadienylcobalt(III) iodide, a black solid (0.968 g, 99%). This crude intermediate was suspended in diethyl ether (Et_2O, 25 ml) and added to a separating funnel with a solution of NaOH (2g, 0.05 ml) in H_2O (20 ml). The layers were shaken vigorously, resulting in the organic layer turning very dark red in colour. The aqueous phase was removed and the organic phase washed twice with water (2 × 25 ml). The diethyl ether solution was evaporated to dryness on a rotary evaporator, producing a black crystalline solid with a green hue (0.372 g, 81%). Calculated (found) for $C_{11}H_{11}CoN_2$: C, 57.40 (57.50); H, 4.82 (4.76); N, 12.17 (12.10). ^{1}H-NMR (500 MHz, $CDCl_3$): δ 5.02 (5H, s), 6.96 (4H, m), 9.57 (2H, s). ^{13}C-NMR (500 MHz, $CDCl_3$): δ 75.61 (5 × *C*H), 116.97 (2 × *C*H), 120.15 (2 × *C*H), 151.83 (2 × *C*q). MS (+ESI): *m*/*z* 231.13 ($[M+H]^+$, 100%), 196.79 ($[Co(DAbnz)+CH_3OH]^+$, 25%), 182.78 ($[Co(DAbnz)+H_2O]^+$, 24%). IR (KBr, cm^{-1}) ν 3466 (s, br), 3432 (s, br), 1638 (s), 1472 (w), 1412 (w), 1372 (m), 1340 (w), 1302 (w), 1198 (w), 1108 (m), 1048 (w), 1000 (m), 914 (w), 816 (m), 744 (s), 670 (w), 656 (w), 574 (w).

Naphthalene-2,3-diamidocyclopentadienylcobalt(III) (CpCoDAnap). The synthesis was the same as above for CpCoDAbnz, yielding a black solid with a dark blue hue (1.231 g, 94 %). Calculated (found) for $C_{15}H_{15}CoN_2$: C, 64.30 (64.37); H, 4.68 (4.77); N, 10.00 (10.05). ^{1}H-NMR (500 MHz, $CDCl_3$): δ 7.170 (2H, AA'BB' m), 7.540 (2H, AA'BB' m), 9.760 (2H, s). ^{13}C-NMR (500 MHz, $CDCl_3$): δ 74.07 (5 × *C*H), 107.34 (2 × *C*H), 119.82 (2 × *C*H), 125.10 (2 × *C*H), 126.89 (2 × *C*q), 150.34 (2 × *C*q). MS (+ESI): *m*/*z* 281.13 ($[M+H]^+$, 100%), 311.30 ($[M+CH_3OH]^+$, 48%). IR (KBr, cm^{-1}) ν 3466 (s, br), 3432 (s, br), 3326 (s), 3044 (w), 2962 (w), 2920 (w), 1636 (s), 1396 (m), 1344 (m), 1262 (w), 1162 (m), 1108 (m), 1050 (m), 1002 (m), 946 (w), 850 (s), 810 (s), 742 (m), 674 (m), 580 (w), 528 (w).

5.4.1 Thin-film processing

5.4.1.1 Surface treatments

The FET and quartz glass substrates were cleaned by soaking in sequential solvents of chloroform, acetone and IPA (15 min each). Prior to surface treatments, the substrates were UV/ozone treated (2 min). HMDS treatment was carried out by dropping pure HMDS onto the glass surface or the interdigitated electrodes of the FET in a glovebox and leaving for 20 min. The substrates were rotated at 2000 rpm for 90 seconds using a spin coater to remove excess HMDS, washing with 1 ml of 1,1,2-TCE. OTS treatment involved soaking the substrates in a 10 mM solution of OTS in toluene for 24 h. The substrates were rinsed in the same manner as with the HMDS treatment. The substrates used in the second deposition of **7b** were annealed at 150 °C for 1 h prior to deposition.

5.4.1.2 Vapour deposition

Vapour deposition of both compounds was carried out in a vacuum chamber. The material to be sublimed was placed in a ceramic crucible at the bottom of the chamber, which is heated by resistance coils to induce sublimation. The substrates to be coated are attached to a plate at the top of the chamber, facing the material to be sublimed. The height of the plate above the deposition material can be adjusted. An estimate of the deposition temperature was obtained by a thermocouple placed inside the crucible. The growth rate and estimated thickness was monitored using a quartz crystal microbalance (QCM) based on the density of the material. The pressure of the vaccuum chamber for each deposition was approximately 4×10^{-4} Pa. **7a** was deposited at an estimate growth rate of 0.4-0.6 Å s^{-1} to a thickness of 180 nm. The first deposition of **7b** was carried out at a pressure of 4.0×10^{-4} Pa and an estimated growth rate of 0.4 ± 0.1 Å s^{-1} to a thickness of 100 nm. The devices were tested over 24 h after the deposition. The second deposition of **7b** was carried out at a rate of 0.2 ± 0.1 Å s^{-1} to a thickness of 50 nm. The devices were tested immediately after opening the PVD chamber.

5.4.1.3 FET measurements

The FET substrates were composed of BGBC, interdigitated, Au S-D electrodes. Interdigitated electrode gaps of L = 2, 5, 10, 20 and 50 μm were tested. The FET substrates were washed, ozone treated and coated with either HMDS or OTS prior to deposition of the active layer (**Section 5.4.1.1**). Thin films of vapour-deposited **7b** of approximately 100 nm thickness (by QCM) were produced for the first deposition, and 50 nm thickness of the second deposition. The current-voltage characteristics were measured using a Keithley 2636A sourcemeter controlled using Labtracer 2.0 software, and were carried out in darkness and under vacuum. The thin films were imaged by a Hitachi S-4300 scanning electron microscope.

5.4.2 X-ray crystallography

The data collection and structure refinement of **7b** was carried out Yoshiaki Shuku at Nagoya University. The diffraction data were measured with Mo-Ka radiation (λ = 0.71070 Å) on a Rigaku AFC10 Saturn-70 CCD diffractometer at 123 K. Data collection, cell refinement and data reduction were carried out using CrystalClear (version 2.0) software.[28] The structures were solved using SIR97[29] direct methods, giving the positions of all non-hydrogen atoms. The structures were refined using SHELX[30] software and the CrystalStructure (version 4.0) structure visualiser[31] and using a full-matrix least-squares refinement procedure on F^2, with non-hydrogen atoms refined anisotropically and hydrogen atoms placed at calculated positions. Full details of the structure refinement are given in **Table 5.9**. Molecular graphics were constructed using Mercury[32] software.

Table 5.9. Crystallographic data and structure refinement details.

	7b
Chemical formula	$C_{15}H_{13}CoN_2$
Crystal size / mm^3	0.10 × 0.07 × 0.05
Crystal colour, shape	Green block
Fw	280.21
Crystal system	Orthorhombic
Space group	*P*bca
a / Å	8.0581(4)
b / Å	25.6103(14)
c / Å	45.069(2)
α / °	90.0
β / °	90.0
γ / °	90.0
V / Å^3	9300.9(8)
Z	32
Calc. density / g cm^{-3}	1.601
μ / mm^{-1}	14.60
T / K	123
Radiation, λ / Å	Mo-Kα, 0.71070
θ range / °	3.02 to 27.5
Index ranges	h -10 to 10
	k -32 to 32
	l -58 to 58
Refinement method	Full-matrix least-squares on F^2
Absorption correction	Multi-scan
T_{min}, T_{max}	0.87, 0.93
Structure solution	Direct methods (Sir97)
R_{int}	0.082
Collected	85427,
Independent	10467
Observed [$I > 2\sigma(I)$]	9902
Reflections used	10467
Parameters / restraints	649 / 0
R, R_w [$I > 2\sigma(I)$], GOF	0.082, 0.139, 1.33
$\Delta\rho_{max}$, $\Delta\rho_{min}$ (e Å^{-3})	0.44, -0.48

$^a R = \Sigma||F_o| - |F_c||/\Sigma|F_o|$. $^b R_w = [\Sigma w(|F_o| - |F_c|)^2/\Sigma w|F_o|^2]^{1/2}$.

Powder XRD was carried out using the in-house Bruker D8 Advance Powder X-ray diffractometer by Mark Senn, who also carried out the Rietveld refinements of the measured powder diffraction data. The diffractometer was operating in capillary mode with monochromated Cu-Kα1 radiation (λ = 1.54046 Å). The data were collected over a range of 6 to 40° over a period of 10 hours. The Rietveld refinements were carried out using TOPAS software.[33]

5.5 References

(1) Gagne, R. R.; Koval, C. A.; Lisensky, G. C. *Inorganic Chemistry* **1980**, *19*, 2854.

(2) Nomura, M.; Cauchy, T.; Geoffroy, M.; Adkine, P.; Fourmigué, M. *Inorganic Chemistry* **2006**, *45*, 8194.

(3) Grosshans, P.; Adkine, P.; Sidorenkova, H.; Nomura, M.; Fourmigué, M.; Geoffroy, M. *The Journal of Physical Chemistry A* **2008**, *112*, 4067.

(4) Fourmigué, M.; Cauchy, T.; Nomura, M. *Crystal Engineering Communications* **2009**, *11*, 1491.

(5) Nomura, M.; Cauchy, T.; Fourmigué, M. *Coordination Chemistry Reviews* **2010**, *254*, 1406.

(6) Heck, R. F. *Inorganic Chemistry* **1965**, *4*, 855.

(7) Heck, R. F. *Inorganic Chemistry* **1968**, *7*, 1513.

(8) King, R. B. *Inorganic Chemistry* **1966**, *5*, 82.

(9) Joh, T.; Hagihara, N.; Murahashi, S. *Bulletin of the Chemical Society of Japan* **1967**, *40*, 661.

(10) Miller, E. J.; Brill, T. B. *Inorganic Chemistry* **1983**, *22*, 2392.

(11) Miller, E. J.; Brill, T. B.; Rheingold, A. L.; Fultz, W. C. *Journal of the American Chemical Society* **1983**, *105*, 7580.

(12) Rheingold, A. L.; Fultz, W. C.; Brill, T. B.; Landon, S. J. *Journal of Chemical Crystallography* **1983**, *13*, 317.

(13) Miller, E. J.; Rheingold, A. L.; Brill, T. B. *Journal of Organometallic Chemistry* **1984**, *273*, 377.

(14) Miller, E. J.; Landon, S. J.; Brill, T. B. *Organometallics* **1985**, *4*, 533.

(15) Fourmigué, M.; Perrocheau, V. *Acta Crystallographica Section C* **1997**, *53*, 1213.

(16) Guyon, F.; Lucas, D.; Jourdain, I. V.; Fourmigué, M.; Mugnier, Y.; Cattey, H. *Organometallics* **2001**, *20*, 2421.

(17) Nomura, M.; Fourmigué, M. *Journal of Organometallic Chemistry* **2007**, *692*, 2491.

(18) Nomura, M.; Fourmigué, M. *Inorganic Chemistry* **2008**, *47*, 1301.

(19) Pasternack, R. F.; Huber, P. R.; Boyd, P.; Engasser, G.; Francesconi, L.; Gibbs, E.; Fasella, P.; Cerio Venturo, G.; Hinds, L. d. *Journal of the American Chemical Society* **1972**, *94*, 4511.

(20) Wu, T.-Y.; Sheu, R.-B.; Chen, Y. *Macromolecules* **2004**, *37*, 725.

(21) Newman, C. R.; Frisbie, C. D.; da Silva, D. A.; Bredas, J. L.; Ewbank, P. C.; Mann, K. R. *Chemistry of Materials* **2004**, *16*, 4436.

(22) Mas-Torrent, M.; Durkut, M.; Hadley, P.; Ribas, X.; Rovira, C. *Journal of the American Chemical Society* **2004**, *126*, 984.

(23) Jurchescu, O. D.; Baas, J.; Palstra, T. T. M. *Applied Physics Letters* **2004**, *84*, 3061.

(24) *Modern Physics*; 3rd Ed ed.; Tipler, P. A.; Llewellyn, R. A., Eds.; W. H. Freeman, 1999.

(25) Reese, C.; Bao, Z. *Advanced Functional Materials* **2009**, *19*, 763.

(26) Małachowski, M.; Żmija, J. *Opto-Electronics Review* **2010**, *18*, 121.

(27) Pernstich, K. P.; Haas, S.; Oberhoff, D.; Goldmann, C.; Gundlach, D. J.; Batlogg, B.; Rashid, A. N.; Schitter, G. *Journal of Applied Physics* **2004**, *96*, 6431.

(28) Corporation, R.; 2.0 ed.; Rigaku Corporation: Toyko, Japan, 2009.

(29) Altomare, A.; Burla, M. C.; Camalli, M.; Cascarano, G. L.; Giacovazzo, C.; Guagliardi, A.; Moliterni, A. G. G.; Polidori, G.; Spagna, R. *Journal of Applied Crystallography* **1999**, *32*, 115.

(30) Sheldrick, G. M. *Acta Crystallographica* **2008**, *A64*, 112.

(31) Corporation, R.; 4.0 ed.; Rigaku Corporation: Toyko, Japan, 2010.

(32) Macrae, C. F.; Bruno, I. J.; Chisholm, J. A.; Edgington, P. R.; McCabe, P.; Pidcock, E.; Rodriguez-Monge, L.; Taylor, R.; van de Streek, J.; Wood, P. A. *Journal of Applied Crystallography* **2008**, *41*, 466.

(33) Coelho, A. *Journal of Applied Crystallography* **2003**, *36*, 86.